Schmisseur

REPORT DOCUMENTATION PAGE

Form Approved
OMB No. 0704-0188

PLEASE DO NOT RETURN YOUR FORM TO THE ABOVE ORGANIZATION.

1. REPORT DATE *(DD-MM-YYYY)*	2. REPORT TYPE	3. DATES COVERED *(From - To)*
8/31/2009	Final	June 1, 2004 to May 31, 2009

4. TITLE AND SUBTITLE
Hypersonic transition and turbulence with non-equilibrium thermochemistry

5a. CONTRACT NUMBER

5b. GRANT NUMBER
FA9550-04-1-0425

5c. PROGRAM ELEMENT NUMBER

6. AUTHOR(S)
Sharath Girimaji, Rodney Bowersox, Simon North, Helen Reed, Joanna Austin, Gregory Elliott, Robert Lucht and Lishi Luo

5d. PROJECT NUMBER

5e. TASK NUMBER

5f. WORK UNIT NUMBER

7. PERFORMING ORGANIZATION NAME(S) AND ADDRESS(ES)
Texas A&M University, College Station, TX
University Of Illinois, Urbana Champagne, Il
Purdue University, West Lafayette, IN
Old Dominion University, Norfolk, VA

8. PERFORMING ORGANIZATION REPORT NUMBER

9. SPONSORING/MONITORING AGENCY NAME(S) AND ADDRESS(ES)
AFOSR (John Schmisseur)
875 North Randolph Street
Arlington, VA 22203

10. SPONSOR/MONITOR'S ACRONYM(S)

11. SPONSOR/MONITOR'S REPORT NUMBER(S)
AFRL-OSR-VA-TR-2013-0903

12. DISTRIBUTION/AVAILABILITY STATEMENT

20130919117

13. SUPPLEMENTARY NOTES

14. ABSTRACT

The objective of the completed MURI project was to develop various fundamental building blocks required for assembling a reliable predictive capability for hypersonic turbulent flows in Non-Thermochemical-Equilibrium (NTE). A coordinated three pronged approach addressing fundamental characterization, physics comprehension and computational prediction of hypersonic NTE turbulent flows has been completed. The main contributions from the completed works are: (1) development of a modular theoretical and computational framework for addressing NTE turbulence; (2) identification of the fundamental physical mechanisms that render NTE turbulence different from standard incompressible turbulence; (3) compilation of experimental and numerical databases in homogeneous and canonical flows that highlight non-equilibrium and compressibility effects; (4) proposal of closure models at various degree of sophistication; (4) development of new laser diagnostic techniques developed specifically for characterization of hypersonic NTE turbulence; and (6) preliminary integration of numerical methods and turbulence models for efficient CFD simulations. Overall, the completed work has resulted in crucial improvements for hypersonic turbulence predictions.

15. SUBJECT TERMS
Hypersonics, turbulence, non-equilibrium flows

16. SECURITY CLASSIFICATION OF:			17. LIMITATION OF ABSTRACT	18. NUMBER OF PAGES	19a. NAME OF RESPONSIBLE PERSON
a. REPORT	b. ABSTRACT	c. THIS PAGE			Sharath S. Girimaji
					19b. TELEPHONE NUMBER *(Include area code)* 979-845-1674

Abstract

The objective of the completed MURI project was to develop various fundamental building blocks required for assembling a reliable predictive capability for hypersonic turbulent flows in Non-Thermochemical-Equilibrium (NTE) state. A coordinated three-pronged approach addressing fundamental characterization, physics comprehension and computational prediction of hypersonic NTE turbulent flows has been completed. The main contributions from the completed works are: (1) development of a modular theoretical and computational framework for addressing NTE turbulence; (2) identification of the fundamental physical mechanisms that render NTE turbulence different from standard incompressible turbulence; (3) compilation of experimental and numerical databases in homogeneous and canonical flows that highlight non-equilibrium and compressibility effects; (4) proposal of closure models at various degree of sophistication; (4) development of new laser diagnostic techniques developed specifically for characterization of hypersonic NTE turbulence; and (6) preliminary integration of numerical methods and turbulence models for efficient CFD simulations. Overall, the completed work should result in crucial improvement in the predictive capabilities.

Executive Summary

The objective of the MURI project was to develop fundamental building blocks required for assembling a reliable predictive capability for hypersonic turbulent flows with Non-Thermochemical-Equilibrium (NTE) effects. A three pronged approach addressing fundamental characterization, physics comprehension and computational prediction of hypersonic NTE turbulent flows has been completed. A summary of the important scientific and technological accomplishments is given below, and a more detailed description is reported in this document.

Task 1: Establishment of facilities, diagnostics and plasma characterization

A large portion of the effort was focused on developing the experimental tools necessary to properly characterize the salient flow physics. The specific tasks and accomplishments were:

(1) Development of advanced laser diagnostics: Three new major diagnostic achievements were accomplished to fully characterize turbulent flows with NTE effects.

(2) RF-Plasma facilities for NTE turbulence experiments and diagnostic development: Four new facilities were developed used for fundamental studies and diagnostic development.

(3) RF-Plasma facility for hypersonic shear layer NTE experiments. The TAMU National Aerothermochemistry Laboratory was established. This facility houses the Actively Controlled Expansion (ACE) hypersonic tunnel, which was developed for this study.

(4) Plasma characterization: A suite of modern diagnostics was used to characterize the vibrational state of the nitrogen; the only excited major species within the plasma. New models developed for high collision energy molecular-molecular energy transfer rate.

Task 2: Perform Fundamental Studies

A fundamental framework for describing the thermodynamics-flow interaction was developed. The hypersonic flow effects were categorized into high-speed effects (characterized by gradient and turbulent Mach numbers) and high temperature effects (characterized by heat-release parameter). Both numerical and physical experiments were performed to characterize the effect of these hypersonic effects on the basic turbulence processes. The specific tasks were:

(a) Development kinetic schemes and numerical procedure for NTE flows: For describing non-continuum hypersonic phenomenon, Boltzmann-equation based physical framework and numerical schemes were developed.

(b) Perform DNS of isotropic NTE Turbulence flows: Several numerical simulations were performed to characterize the effect of heat release, turbulent Mach number, body force (magneto-hydro-dynamics) and transport property variations on energy exchange and dissipative processes.

(c) Linear and non-linear theories: Linear RDT (rapid distortion theory) and non-linear HEE (Homogenized Euler equation) theories for compressible turbulence were developed. Based on the linear analysis, the first complete explanation for the three-stage behavior of kinetic energy in high Mach number homogeneous shear flows was developed.

(d) Perform isotropic and homogeneous NTE turbulence physical experiments. An extensive investigation of the coupling between NTE and decaying mesh turbulence was performed to characterize the basic NTE-turbulence coupling mechanisms. The database is available for model verification and validation.

Task 3: Free Shear-Layer Experiments and Model Development

Both numerical and physical experiments were performed to provide model validation data.

(a) Experiments of free shear layer NTE-turbulence. An innovative Shock-Induced-Shear-Layer experiment was conceived as canonical flow with well defined boundary conditions. The model was designed, constructed and preliminary tests were performed. The detailed turbulence studies were not accomplished prior to this report as the tunnel compressor failed resulting in 1-year delay. The experiments were underway at the time of this document.

(b) Investigation of hypersonic transition in free-shear layer experiments. Progress was continued on the development of physics-based linear stability theory (LST) and nonlinear parabolized stability equation (NPSE) tools including non-equilibrium thermo-chemistry. The initial application of LST to the SISL flow field found unstable flow and provided early qualitative results for this project aiding in experiment design.

(c) RDT, realizability and fixed-point analysis of NTE-turbulence: Based on the results of RDT study, a new pressure-strain correlation model valid for a wide range of Mach numbers was developed. High Mach number model for pressure-dilatation was also proposed. These models are based on the finding that inertia dominates over pressure at very high Mach numbers and there is an inertia-pressure balance around a Mach number of unity. Based on DNS study, it was proposed that the slow pressure-strain correlation be retained in the low-Mach number form for solenoidal fluctuations. It was suggested that the slow pressure-strain correlation model for dilatational fluctuations must be modified to include acoustic rather than eddy turn-over timescale.

(d) *Development of RANS models for NTE-turbulence.* A new internal energy based modeling framework was established to model the turbulent heat flux. An algebraic equilibrium model was validated for Mach numbers from 0.02 to 11.8. Corresponding thermal and mechanical non-equilibrium models were developed, and the necessary validation experiments were underway at the time of this document. A new variable-C_{μ} model valid over a wide Mach number range was proposed based on the RDT findings and resulting pressure-strain correlation model. It was shown that the dissipation equation is unaffected by viscosity perturbations.

Task 4: CFD Integration and testing with available databases

Preliminary model validation efforts have been accomplished in high Mach number mixing layers and flows over cavities. In addition, the equilibrium energy flux model has been validated against the existing high Reynolds number data from the literature.

In summary, this AFOSR MURI project has resulted in the production of new knowledge that should significantly improve the accuracy in the numerical prediction of hypersonic non-equilibrium turbulent flows. A state-of-the-art hypersonic laboratory has also been developed. To date, the project has already produced over 60 journal/conference publications and 20 advanced degrees.

Table of Contents

Chapter 1
Introduction

Technical feasibility of hypersonic flight, to an important degree, depends on our ability to understand and predict transition and turbulence in hypersonic flows in the presence of non-equilibrium thermo-chemistry (Anderson, 1989; Vincenti and Krueger, 1965) effects. The presence of strong shock waves results in excitation of internal energy modes which relax back to the equilibrium state at a timescale larger than the flow transit timescale. Furthermore, the thermo-chemical relaxation timescales can be of the same order, or even larger, than the characteristic turbulence timescales. Hence, strong coupling between the non-equilibrium thermo-chemistry and the turbulence can be expected. Much research has been done on non-equilibrium hypersonic laminar flows especially in the context of aero-braking of re-entry vehicles using continuum computational fluid dynamics (CFD) and molecular-dynamics methods such as direct-simulation Monte Carlo (DSMC) -- e.g., the work of NASA Langley Aerothermodynamics Branch. However, works addressing non-equilibrium effects on turbulent flows have been very limited. With few notable exceptions, all transition and turbulence investigations of hypersonic non-equilibrium flows have been restricted to straight-forward extensions of standard turbulence concepts and model closures. Unfortunately, many of the standard turbulence modeling paradigms are not valid in the presence of non-equilibrium effects. This requires re-visiting the fundamental turbulence modeling tenets and modifying them appropriately to account for the novel effects. In order to do that, the physical effects of non-equilibrium thermochemistry on turbulence must be qualitatively and quantitatively established. There have been limited experiments focusing on the basic effects of non-equilibrium thermochemistry on high-Mach number turbulence. This is due to the inherent difficulties in designing and building such facilities as well as lack of appropriate diagnostic techniques which are accurate at very high speeds. Throughout the report, NTE-turbulence will refer to turbulence evolving under the influence of non-thermochemical-equilibrium (NTE) effects.

NTE-Turbulence modeling status prior to MURI Project: Previous and many of the current large-scale NTE-turbulence computations in industry and government laboratories typically employ two-equation, or even lower-order, turbulence models that invoke the Boussinesq approximation with simple compressibility and *ad hoc* length-scale corrections. Non-equilibrium effects are treated with simple relaxation equations for vibrational and electronic energies. The effect of turbulent fluctuations on the chemical source term is usually neglected. Lastly, constant turbulent Prandtl, Schmidt and Lewis number assumptions are routinely invoked. This current state-of-affairs has proven to lack the physics required to develop efficient hypersonic vehicles, with system goals of compensating, or alleviating, the detrimental effects of turbulence along the external flow path, while enhancing the benefits along the internal path. For example, scramjet computations performed in NASA Langley in 2002 (Baurle) showed that the predicted propulsion performance depends strongly on the value of the assumed Schmidt number. Specifically, it was shown that the predicted engine performance varied from flame-out to full engine un-start over a small and representative Schmidt number range of 0.25-0.75.

MURI project objectives and accomplishments: The overarching objective of the MURI project was to develop the fundamental building blocks required for assembling a reliable predictive capability for hypersonic turbulent flows in Non-Thermochemical-Equilibrium (NTE) state. A coordinated three-pronged approach focusing on characterizing, understanding and predicting hypersonic NTE turbulent flows was followed. The main contributions from the completed works are: (1) development of a modular theoretical and computational framework for addressing NTE turbulence; (2) identification of the fundamental physical mechanisms that render NTE turbulence different from standard incompressible turbulence; (3) compilation of experimental and numerical databases in homogeneous and canonical flows that highlight non-equilibrium and compressibility effects; (4) proposal of closure models at various degree of sophistication; (4) development of new laser diagnostic techniques developed specifically for characterization of hypersonic NTE turbulence; and (6) preliminary integration of numerical methods and turbulence models for efficient CFD simulations. Through the remainder of this document we will detail the advances made during the course of MURI project.

1.1 Research Framework

We start with a brief description of the various key features of the research.

Turbulence closure modeling: Any attempt at physics-based closure modeling must start with a clear understanding of the basic NTE-turbulence processes. In standard turbulence, central to our understanding of physics and model development is the Kolmogorov paradigm: energy is produced in the large scales due to shear production, and it cascades unchanged through the inertial scales until it is dissipated in the isotropic small scales. At the most fundamental level, the non-equilibrium effects are likely to modify the spectral cascade by introducing an energy capacitance and rendering invalid the Kolmogorov paradigm. The energy capacitance in the inertial scales caused by non-equilibrium effects is due to production/consumption of turbulent kinetic energy due to large density, pressure and temperature fluctuations. This production – much like the baroclinic torque production – will inject energy into or divert energy away from the cascade at all scales of motions. Further, anisotropy of small scales is quite common in the presence of body forces (rotating and buoyancy driven flows). We also anticipate that transition will play a more central role in non-equilibrium hypersonic flows than in sub-sonic flows. As a consequence of these changes, the turbulent transport can change significantly rendering standard modeling inadequate. For addressing the immediate and near-term needs, NTE turbulence models are developed within the continuum Navier-Stokes framework.

Kinetic-theory based approach: Any long-term strategic plan for hypersonic flow must include treatment of turbulence over a wide range to Knudsen numbers and non-equilibrium effects. However, at the current stage of development, turbulence modeling can be performed with any degree of reliability only in the continuum Navier-Stokes framework. With long-term goals in mind, we have also developed kinetic-theory based description and computational schemes such as Gas-Kinetic Method (GKM). This permits the study of NTE phenomena which cannot be done efficiently with Navier-Stokes equations.

Thermochemistry reduction: NTE effects can be most precisely treated by considering each significant quantum level as a different species undergoing vibrational and electronic exchange

(quantum-resolved approach). This approach is too complicated for practical computations. At the extreme lies the lumped-system approach. In the approximate *lumped-system* approach only the average (first moment) of the vibrational energy distribution is considered. While computationally viable, this approach does not possess the required degree of accuracy. During the MURI project, we developed the advanced quasi-steady state assumption (A-QSSA) which represents a reasonable compromise between physical fidelity and computational feasibility.

Optical Diagnostics for NTE Flows: NTE turbulence involves strong coupling between the kinematic and thermochemical states of the flow. Hence, characterization will require the development and usage of advanced laser diagnostics for simultaneous optical measurement of the instantaneous kinematic and thermochemical flow properties with sufficient spatial resolution and sample sets to establish reliable turbulent statistical moments. Important advances have been made in this regard.

NTE facilities and Experimentation: Hypersonic flight introduces thermally induced NTE. However, it is difficult and costly to duplicate true hypersonic flight conditions in ground test facilities with sufficiently long run times for reliable measurement of turbulent statistical moments. The Air Force (AFRL/VAAA) is currently simulating high-temperature NTE effects using cold flow. Along the same lines, we use a plasma-generator to produce NTE flow. The primary reason for the cold flow approach is it produces flows with the salient NTE effects while permitting experiments in long duration wind tunnels with well controlled flow conditions, which are necessary for meaningful statistical measurements. The progress made in this area is also reported in detail.

1.2 Broad Categorization of Tasks

In the research proposal, the research was sub-divided into the following broad tasks. Important areas in each task are identified.

1. Establishment of facilities and development of diagnostics:

a) Advanced laser diagnostic techniques to fully characterize NTE turbulence.
b) RF-plasma facility for fundamental NTE-turbulence experiments.
c) RF-plasma facility for hypersonic free-shear layer NTE-turbulence experiments.
d) Characterization of excited states/RF plasma for inflow condition specification.

2. Fundamental studies

a) Development of kinetic schemes and numerical procedures for NTE-flows.
b) DNS of isotropic and homogeneous NTE-turbulence.
c) Experiments of isotropic and homogeneous NTE-turbulence flows.

3. Free shear-layer experiments and model development

a) Experiments of free-shear layer NTE-turbulence.
b) Investigation of hypersonic transition in free-shear layers.
c) RDT, realizability and fixed-point analysis of NTE-turbulence.
d) Development of RANS models for NTE-turbulence.

4. CFD integration, testing and validation

a) Preliminary integration and testing of data bases against available data.

1.3 Research Roadmap

A three-step multi-disciplinary research plan that combines theory, computation and experiment, given in Fig. 1, was formulated to meet the research objectives given in Section 1.2. The three basic building block steps of the research process are aligned along the center of the flowchart. Also indicated at each step are the additional multidisciplinary research requirements.

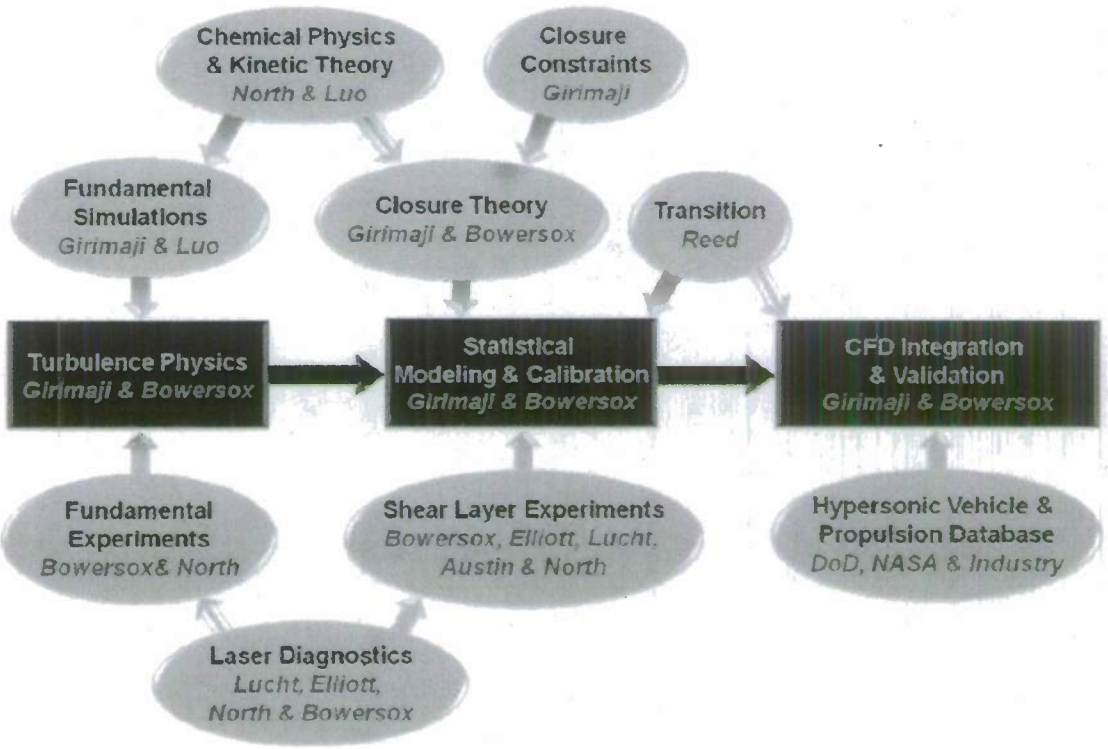

Fig. 1.3.1 Multidisciplinary Research Plan

The progress made in the various tasks and sub-tasks are given in the next two Chapters. Reports on the theoretical and computational investigations are given in Chapter 2 and experimental/diagnostic efforts are described in Chapter 3. Each section in these chapters comprises of a key task and is a complete report of that effort. The authors contributing to each section are also identified. We conclude in Chapter 4 with a listing of students and publication resulting from the MURI project.

Chapter 2
Progress in Theory and Computation

2.1 NTE Framework and Thermochemistry Reduction

Sharath Girimaji, Texas A&M University

Even in its most benign manifestation in incompressible, isothermal, single-Newtonian fluid, turbulence is a nearly intractable phenomenon that was quite justifiably labeled as '*The last unsolved problem in classical physics*' by Nobel-prize winning physicist Richard Feynman. Similar statements regarding the intricacies of turbulence have been made by noted scientists such as Horace Lamb and Albert Einstein. In hypersonic flight applications of interest to Air Force and NASA, the already complex turbulence problem is further exacerbated by various effects arising due to compressibility, heat release and non-thermochemical-equilibrium (NTE) state. Any reasonable effort toward developing hypersonic turbulence computational building blocks must start with a clear understating of the influence of non-thermochemical-equilibrium on various turbulence processes. The objective of this section is two-fold: (1) Establishment of the framework of interaction between non-equilibrium thermodynamics and turbulence; and, (ii) Development of non-equilibrium thermochemistry computational strategies. We will demonstrate in the first part that NTE affects turbulence only via a few select parameters. This allows for modular treatment of thermochemistry and turbulence provided the interaction parameters are matched appropriately. Thus, throughout the MURI project this modular approach was followed.

2.1.1 Thermochemistry-Flow Interaction

In hypersonic flight applications, turbulence occurs in a medium (air) in which the constituent molecules can be at different quantum energy levels. Under these conditions, the tenets of equilibrium thermodynamics breaks down and a more complex approach that identifies different quantum levels individually is called for. The most general treatment calls for considering collections of molecules at different quantum energy levels as separate species even though their chemical compositions may be identical – this is the so-called master equation approach. In most practical situations further simplifications may be possible – e.g., Landau Teller (LT) model. In our initial considerations to establish the NTE turbulence framework, we will follow the master equation description. However, for practical calculations we will invoke LT model or other intermediate-level models as mentioned in the introduction.

We will now start with NTE description in which collections of molecules at different energy levels – even if they belong to the same chemical species – are treated as individual entities. In order to establish the precise nature of the influence of non-equilibrium thermochemistry on turbulence, the interplay between mass conservation, species balance, momentum balance, energy balance and state equations must be established. We seek a general framework of thermochemistry-turbulence interaction with clear identification, characterization and parameterization of the manner by which air chemistry and relaxation from quantum non-equilibrium individually and collectively affect the evolution of velocity field perturbations. In Figure 2.1.1 we show the interactions between the various conservation/balance and state equations. The species balance equation contains the

chemical reaction and quantum relaxation physics represented by appropriate kinetic mechanisms. The mixture law provides the transport properties of multi-fluid mixture that feeds into the momentum conservation equation. The chemical reactions and quantum relaxation result in heat release/absorption. The energy budget finally yields the energy incumbent in the molecular translational motion. Then, utilizing the calorific equation of state (CEOS), the temperature of each species in the mixture can be found. Finally, using the equation of state (EOS) the mixture pressure is determined. This is the pressure that appears as the driving force in the momentum equation.

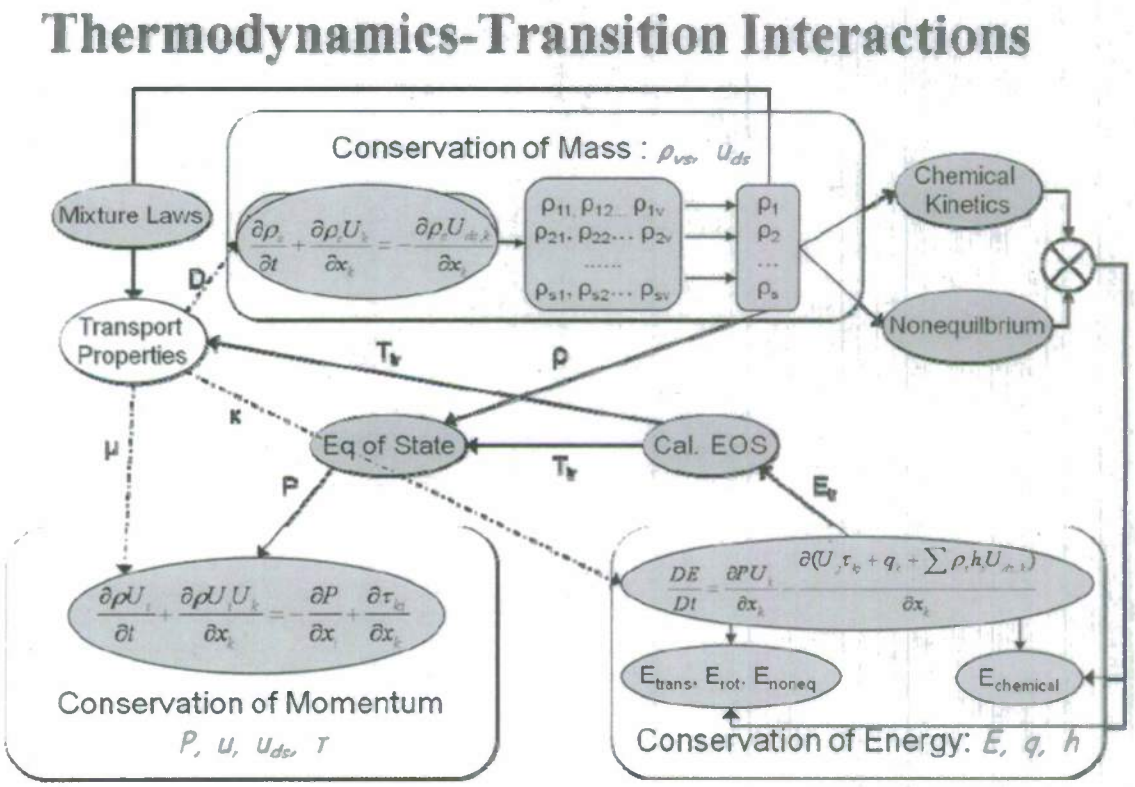

Fig. 2.1.1 Flow chart of interaction between conservation equations

In Fig. 2.1.2 the interplay between different physical phenomena is shown. While the focus in Fig. 2.1.1 was on how NTE effects influence turbulence, the objective of Fig. 2.1.2 is to establish the effect of turbulence on NTE state. It is shown that in average sense, turbulence increases the scalar fluxes in the mass balance equation resulting in more rapid mixing to the various species. Further, turbulence modifies the average temperature via the pressure dilatation term (pressure work).

Turbulence/Non-equilibrium Interaction

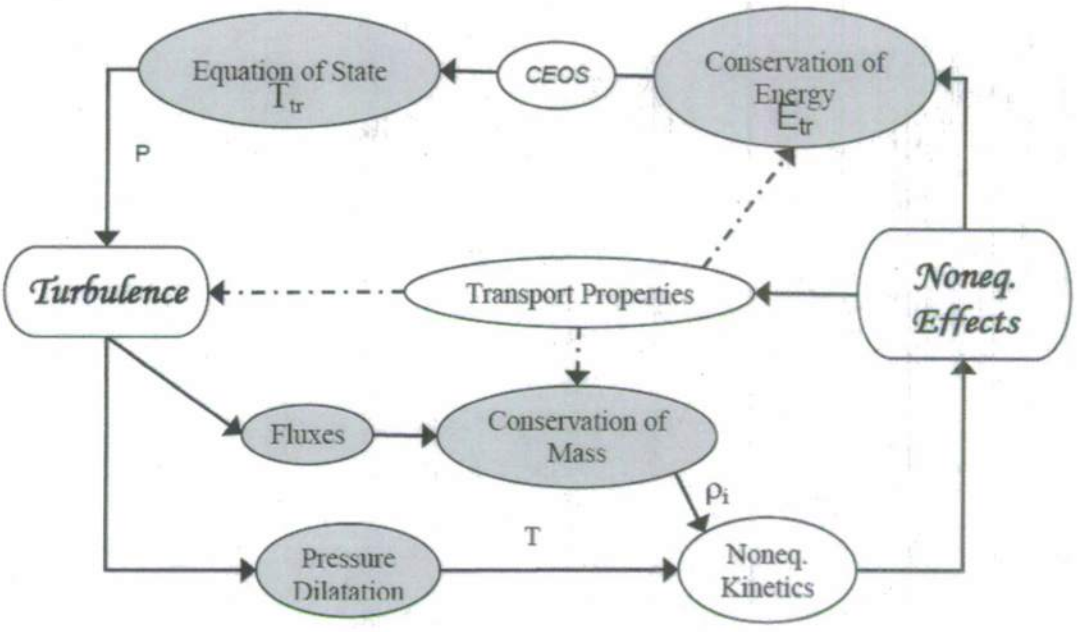

Fig. 2.1.2 Interplay between various phenomena

Overall, close examination of the interplay between various conservation equations and physical processes reveal the following:

1. Physics of NTE turbulence is identical to that of reacting flows. Thus the analytical and computational framework for NTE turbulence can be identical to that of turbulent reacting flows.
2. In general, all of the strategies and techniques devised for turbulent reacting flows can be applied with suitable adaptations for hypersonic NTE turbulence.
3. The adaptations must account for the fact that hypersonic NTE turbulence operates at vastly different speed, pressure, temperature and enthalpy regimes than low-speed turbulent combustor flows.
4. Turbulence and NTE effects interact only via the pressure/temperature field and transport properties.

Based on our experience with turbulent combustion and the above observations, we suggest that NTE-turbulence be treated in a modular fashion. The three important processes -- thermodynamics, multi-species molecular mixing and turbulence – can be treated individually so long as the interaction parameters are appropriately matched. The functions of the three modules can now be formulated.

1) ***Thermodynamic module:*** The function of this module is to account for air and non-equilibrium chemistry to yield species densities (mass fractions) and pressure/temperature profiles.
2) ***Mixture Law***: This module must provide the mixture transport properties as a function of mixture composition, pressure and temperature.

3) ***Turbulence module***: Given the pressure/temperature/density fields and transport properties, the function of this module is to provide models for unclosed turbulence terms in the statistical description.

Such a modular approach may not address higher-order interactions. Experience in turbulent combustion has shown that higher order effects may not be very important for engineering applications. If necessary, such effects should be addressed in future works. Numerical issues are also of crucial importance, but that falls outside the scope of this project.

2.1.2 Thermochemistry Module

As mentioned in the Introduction, two general approaches representing the extremes in computational complexity are available for computing non-equilibrium thermochemistry: the *Master-equation* approach and *Landau-Teller* model.

'The Master Equation' approach is the most detailed description and it involves the following:

1) Collection of molecules at each quantum state is considered individually.

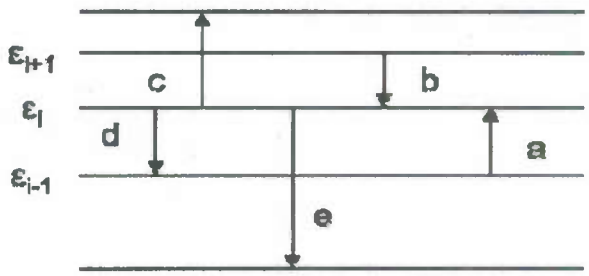

Fig. 2.1.3 Internal states.

2) The evolution of number density of each state is described using the complete transition probability matrix.

$$\frac{dN_i}{dt} = \left(\sum_{j \neq i} k_{j,i} N_j - \sum_{j \neq i} k_{i,j} N_i \right)_{V,V} + \left(\sum_{j \neq i} k_{j,i} N_j - \sum_{j \neq i} k_{i,j} N_i \right)_{V,T}$$

$$e_v = \sum_j N_j \varepsilon_j \;\Rightarrow\; \frac{de_v}{dt} = \sum_j \frac{dN_j}{dt} \varepsilon_j = \sum_i \sum_{j \neq i} k_{j,i} N_j \varepsilon_j - \sum_i \sum_{j \neq i} k_{i,j} N_i \varepsilon_i$$

3) Soling such a set of equations is computationally infeasible owing to the degree of detail.
4) This problem similar to that of full chemistry calculation in turbulent combustion.

Thus, the Master Equation approach is nearly impossible for a full turbulent flow computation with several million grid points considered over several thousand time steps. Some level of simplification is necessary.

The **Landau-Teller** model represents the other extreme. Invoking a set of simplifications shown schematically below, the Master equation representation is reduced to a single step calculation.

$$\frac{de_v}{dt} = \sum_i \sum_{j \neq i} k_{j,i} N_j \varepsilon_j - \sum_i \sum_{j \neq i} k_{i,j} N_i \varepsilon_i$$

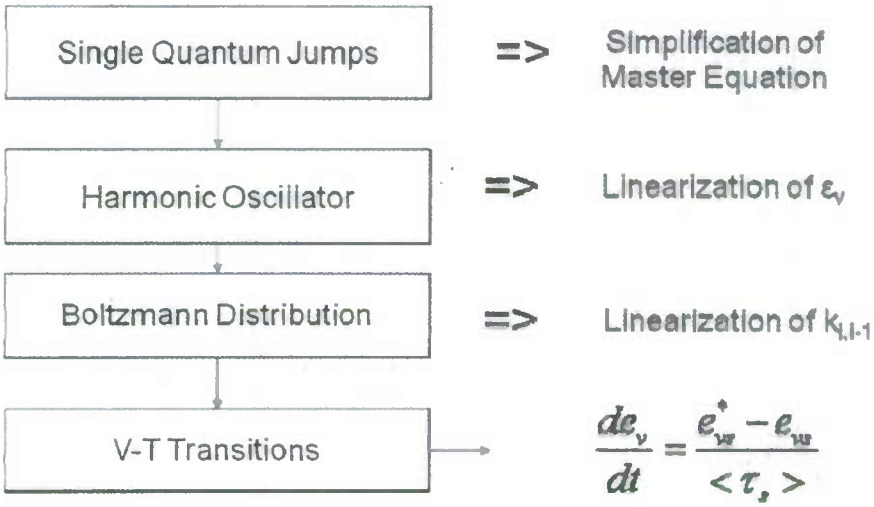

Fig. 2.1.4 Simplifications for the Master equation

While computationally trivial, the approximations invoked make this model unsuitable for many high-fidelity calculations.

The reduced thermo-chemistry approach

Motivation: Based on the foregoing discussion, it is clear that a method that represents a reasonable compromise between physical-fidelity and computational-feasibility must be developed. A similar need in the turbulent combustion research community has lead to the development of the so-called *reduced-chemistry* approach. Such an approach would be ideal for hypersonic NTE-turbulence calculations as well.

Objective: Our objective is to develop a reduced thermo-chemical kinetic mechanism that offers a reasonable compromise between accuracy and computational viability – which we call the *reduced thermo-chemistry* approach.

Approach: This development will be along the lines of a reduced chemistry approach in turbulent combustion. The approach developed here is called the Advance Quasi-Steady State Approximation (A-QSSA).

Reference:

Manuscript under preparation:
S. S. Girimaji: 'Advanced QSSA method for reducing large chemical kinetic systems'.

Since this article is not yet available, we present an extended summary here. The development is in the more general context of reduction of large dynamical systems. The example studied is a highly relevant case of Hydrogen-Air reacting flow.

2.1.3 Advanced-QSSA Approach

Reducing a large dynamical system with many degrees of freedom to a smaller system with minimal loss of accuracy is vital in many fields of engineering and science. In the field of turbulent combustion, it is nearly impossible to compute any practical problem without such reduction. Dynamical system reduction is widely employed in two different areas: simplification of full chemical kinetics to a much smaller reaction set [1-5, 7-14] and derivation of algebraic stress model from the more detailed Reynolds stress closure equations [6]. An exhaustive survey of the many chemistry reduction schemes proposed in literature can be found in [11]. Reduction procedures can be broadly classified into two categories: local and global reduced systems. Global reduction in general can be performed in a mathematically rigorous fashion and the procedures are well developed [11, 13]. The mathematical rigor comes at the expense of increased computational burden making many global methods prohibitive for most practical three-dimensional unsteady turbulence simulations. Moreover, global description of reduced system is unnecessary as most practical systems only access a limited portion of the phase space. Local system reductions, such as the classical quasi-steady state assumption (QSSA), lack the mathematical rigor of global schemes but continue to be widely used due to their computational viability and conceptual clarity. Local approaches in general and the QSSA in particular suffer from two important weaknesses: (i) unreliable accuracy, especially far from equilibrium; and (ii) crucial dependence on the correct *a priori* identification of slow and fast species which is often very difficult.

The motivation for this study comes from the fact that improvements to QSSA by incorporating some of the formalism of the global methods can have a significant impact on practical computations. The objectives of this paper are to (i) identify important physical and mathematical characteristics that must be preserved during reduction and (ii) develop an advanced QSSA reduction procedure that preserves the proposed characteristics. Concurrent to this work, constraints of somewhat similar nature were also advocated in [13] in the context of global manifold reduction.

Consider the chemical evolution of species concentration z_i in a well-stirred reactor:

$$\dot{\mathbf{z}} = F_z(\mathbf{z}) \tag{1}$$

where, $\mathbf{z}$ is the composition vector of the mixture. In mathematical terms, this equation set constitutes an autonomous, dissipative dynamical system, with one globally attracting hyperbolic fixed point and disparate timescales [15]. In problems of interest here, the full set of variables can be partitioned into fast ($\mathbf{x}$) and slow ($\mathbf{y}$) variables:

$$\mathbf{z} = (\mathbf{x}, \mathbf{y}); \quad \dot{\mathbf{x}} = F_x(\mathbf{x}, \mathbf{y}); \quad \dot{\mathbf{y}} = F_y(\mathbf{x}, \mathbf{y}). \tag{2}$$

The objective of system reduction is to determine lower the dimensional manifold (LDM) $\mathbf{y}_r$ such that

$$\mathbf{x}_r = \mathbf{x}_r(\mathbf{y}_r); \text{ and } \dot{\mathbf{y}}_r = F_y(\mathbf{x}_r, \mathbf{y}_r). \tag{3}$$

Successful reduction requires that the reduced algebraic-differential $(\mathbf{x}_r, \mathbf{y}_r)$system provide a reasonable approximation of kinetics of the fully differential $(\mathbf{x}, \mathbf{y})$ system. This is complicated by the fact that the identities of fast and slow variables are not known *a priori* and may vary as a

function of state $\mathbf{z}$. Global reduction procedures develop $\mathbf{x}_r(\mathbf{y}_r)$ by integration over a substantial portion of the $\mathbf{y}_r$-space. On the other hand, in the local reduction methods, $\mathbf{x}_r(\mathbf{y}_r)$ is obtained in a point-wise manner. Point-wise reduction entails further simplifying assumptions. In [5], the local reduction criterion is

$$\left| F_x\left(\mathbf{x}_r\right|_{\mathbf{y}_r}\right) \tag{4}$$

The most popularly used local reduction simplification is the quasi-steady state approximation (QSSA) in which the fast species are taken to be in dynamical equilibrium with the slow ones:

$$\dot{\mathbf{x}}_r(\mathbf{y}_r) \approx 0, \text{ leading to } \mathbf{x}_r = \mathbf{x}_r(\mathbf{y}_r). \tag{5}$$

One of our objectives is to enhance the QSSA for improved behavior in these aspects.

Clearly, the fidelity of local reduction is highly dependent on the assumptions underlying the reduction procedure. Some of the procedures fail to guarantee even elementary properties for the reduced system. We now present three physical and mathematical consistency conditions that will ensure that the reduced representation possesses the most elementary properties.

(i) *Physical realizability:* The reduced system must be mathematically realizable, much like the realizability constraint in turbulence modeling [6]. For example, temperature must always be positive and the species mass fraction must be in the range (0, 1). Current reduction procedures do satisfy this requirement to various degrees. For example, in [3], this constraint is fully satisfied. However, in QSSA only the sum of mass fractions is constrained to be unity but the requirement that any individual mass fraction must be positive is not formally enforced. In fact, small negative numbers for mass fractions are encountered during computation and these are arbitrarily reset to zero. This violation can be of sizable magnitude if the evolution rate of the discarded variable is not small.

(ii) *Kinetic realizability or consistency:* The reduced-system solution trajectory in composition space must be a realizable trajectory of the full system. This constraint is not currently enforced in any of the reduction schemes and the physical realizability alone cannot guarantee this behavior. This requirement is crucial for preserving important physical characteristics of the full system such as compliance with the laws of thermodynamics and conservation principles.

(iii) *Mathematical consistency:* The mathematical character of the reduced system must be consistent with that of the full system. Even the more sophisticated methods lead to reduced systems that can be mathematically inconsistent with the parent full system. For example, the reduced system can be multi-valued whereas the full system is clearly single-valued.

All the proposed constraints can be satisfied if the reduced LDM is mandated to be an invariant manifold of the full system. It is also widely recognized [3, 5] and indeed formally proven [15] that only the slow timescales of the system will be active along the LDM. Thus, we define reduced LDM as being the slowest invariant manifold given the retained state variables.

If the required LDM is in fact a invariant manifold, then we must have the phase velocity of $\mathbf{x}$ trajectory in the full system be equal to that along the reduced manifold:

$$F_x(\mathbf{x}_r, \mathbf{y}_r) = \frac{\partial \mathbf{x}_r}{\partial \mathbf{y}_r} F_s(\mathbf{x}_r, \mathbf{y}_r) \tag{6}$$

A similar equation is routinely used in fluid mechanics to construct streamlines from a vector field and also proposed in [15]. This approach is tantamount to identifying the slowest streamline in phase-space given the values of the retained variables. If along the manifold x and y are nearly orthogonal it is easy to see that $(\partial \mathbf{x}_r/\partial \mathbf{y}_r) \approx 0$. Under these special conditions, equation (6) would lead to $\dot{\mathbf{x}} = \dot{\mathbf{x}}_r \approx 0$, leading to the rigorous mathematical justification of the QSSA. For more general cases, we need a better approximation. Different approaches can adopt different approximation even if they start from eq. (6) [15]. We propose two possible approximations: (i) linear approximation about equilibrium (LAE) point or any other reference point; and (ii) locally-linear approximation (LLE), which is linearization about the local point of interest. The terms globally-linear and local-linear approximations are not be confused with global and local reduced manifolds. Both approximations pertain to local reduction.

Globally-linear approximation: We will first develop this for a single retained variable and then discuss the extension to multiple retained variables. For a single retained variable, we can write from the invariant manifold equation

$$\frac{d\mathbf{x}_r}{d\mathbf{y}_r} = \frac{\dot{\mathbf{x}}}{\dot{\mathbf{y}}}\frac{\dot{\mathbf{x}}}{\mathbf{x}_r - \mathbf{x}_0} = \frac{\dot{\mathbf{y}}}{\mathbf{y}_r - \mathbf{y}_0} = \frac{1}{\tau(\mathbf{x},\mathbf{y})}\frac{\dot{\mathbf{x}}[\mathbf{x}_r,\mathbf{y}_r]}{\dot{\mathbf{y}}[\mathbf{x}_r,\mathbf{y}_r]} \approx \frac{\mathbf{x}_r - \mathbf{x}_0}{\mathbf{y}_r - \mathbf{y}_0} \tag{7}$$

Thus in principle, knowing one reference point$(\mathbf{x}_0, \mathbf{y}_0)$, the remainder of the reduced LDM can be constructed. If we linearize the system about the reference point, along any invariant manifold we must have

$$\frac{\dot{\mathbf{x}}[\mathbf{x}_r,\mathbf{y}_r]}{\dot{\mathbf{y}}[\mathbf{x}_r,\mathbf{y}_r]} \approx \frac{\mathbf{x}_r - \mathbf{x}_0}{\mathbf{y}_r - \mathbf{y}_0} \tag{8}$$

leading to (valid for any discarded variable)

$$\frac{\dot{\mathbf{x}}}{\mathbf{x}_r - \mathbf{x}_0} = \frac{\dot{\mathbf{y}}}{\mathbf{y}_r - \mathbf{y}_0} = \frac{1}{\tau(\mathbf{x},\mathbf{y})} \tag{9}$$

The physical meaning of the approximation is quite simple. Along the one-dimensional slow manifold, one timescale (the slowest one) controls the evolution of *all* variables. The evolution rate of each variable depends upon its degree of departure from equilibrium. Thus, the exponential relaxation rates of all variables to their respective equilibrium values are the same. (In contrast, with QSSA, the evolution rates of the discarded variables are zero). With this method, *any one of the system variables can be chosen to monitor the progress in the evolution of the system*. Such a variable can be called the retained variable or, more descriptively, the progress variable. Very importantly, unlike the traditional QSSA, eq. (9) is symmetric in all variables. Thus, any invariant manifold determined from eq. (9) will be independent of the choice of the retained variable. Although the equilibrium point is the most obvious choice for the reference point, other choices can also be considered. Thus, the globally-linear model can be specialized to the problem on hand.

Extension of this procedure to higher-dimensional manifolds is fairly straight forward. Define a new dynamical system $(\mathbf{x}_t, \mathbf{y}_t)$ by eliminating the contribution to the evolution rate by the first (one-dimensional) slow manifold: $\mathbf{x}_t = \dot{\mathbf{x}} - \dot{\mathbf{x}}_1$; $\mathbf{y}_t = \dot{\mathbf{y}} - \dot{\mathbf{y}}_1$. Subscript 1 denotes the contribution of the first one-dimensional reduced manifold. The one-dimensional slow-manifold of the new system can then be found as before. This procedure can be used consecutively to

construct a multi-dimensional slow manifold. Other methods of determining multi-dimensional manifolds are also possible.

Locally-linear approximation: A more accurate and a little more computationally intensive approximation can be obtained by linearizing about the local retained variables. On the invariant manifold, Jacobian of the discarded variables obtained from the full system must match that obtained from the reduced system. This concept forms the basis of the locally-linear approximation. Consider a dynamical system with n discarded variables and N retained variables.

Differentiating the left hand side of eq. (6) along the invariant manifold with respect to a retained variable, we get

$$\frac{d\dot{x}_i}{d\dot{y}_j^r} = \sum_{k=1}^{n} \frac{\partial \dot{x}_i}{\partial x_k^r} \frac{\partial x_k^r}{\partial y_j^r} + \frac{\partial \dot{x}_i}{\partial y_j^r}; \qquad \frac{d\dot{y}_i}{d\dot{y}_j^r} = \sum_{k=1}^{n} \frac{\partial \dot{y}_i}{\partial x_k^r} \frac{\partial x_k^r}{\partial y_j^r} + \frac{\partial \dot{y}_i}{\partial y_j^r}. \tag{10}$$

Here the reduced manifold is represented with superscript r rather than subscript to distinguish it from tensor indices. Similar differentiation of the right hand side of eq. (6) leads to (for all i and j)

$$\frac{d\dot{x}_i}{d\dot{y}_j^r} = \sum_{k=1}^{N} \left(\frac{d}{d\dot{y}_j^r} \left(\frac{\partial x_i^r}{\partial y_k^r} \right) \dot{y}_k + \frac{\partial x_i^r}{\partial y_k^r} \frac{d\dot{y}_k}{d\dot{y}_j^r} \right) \tag{11}$$

Equations (10 and 11) must be consistent yielding

$$\sum_{k=1}^{n} \frac{\partial \dot{x}_i}{\partial x_k^r} \frac{\partial x_k^r}{\partial y_j^r} + \frac{\partial \dot{x}_i}{\partial y_j^r} = \sum_{k=1}^{N} \left(\frac{d}{d\dot{y}_j^r} \left(\frac{\partial x_i^r}{\partial y_k^r} \right) \dot{y}_k + \frac{\partial x_i^r}{\partial y_k^r} \frac{d\dot{y}_k}{d\dot{y}_j^r} \right) \tag{12}$$

If the manifold is assumed to be locally linear, we get

$$\sum_{k=1}^{n} \frac{\partial \dot{x}_i}{\partial x_k^r} \frac{\partial x_k^r}{\partial y_j^r} + \frac{\partial \dot{x}_i}{\partial y_j^r} = \sum_{k=1}^{N} \frac{\partial x_i^r}{\partial y_k^r} \frac{d\dot{y}_k}{d\dot{y}_j^r} \tag{13}$$

Equations (13) can be solved numerically for a locally-linear estimate of $(\partial x_i^r / \partial y_j^r)$ from which the needed reduced-manifold relationship $\mathbf{x}_r(\mathbf{y}_r)$ can be determined. The numerical effort required will be no more than that needed for other procedures such as ILDM.

For linear systems, both of the simplifications proposed in this paper are exact. The traditional QSSA on the other hand, even with the most judicious choice of slow variables, can have large errors even in linear systems. The error can be catastrophically large if a fast variable is chosen as the retained one. In the algebraic Reynolds stress modeling context, the dangers of choosing the wrong retained variable in QSSA-type reduction is discussed in detail in [6]. With the present methods, the choice of a fast variable as the retained variable does not affect the accuracy of the reduction. In non-linear systems the linear approximations for $(\partial \mathbf{x}/\partial \mathbf{y})$ does not lead to a linear slow-manifold, much like the traditional QSSA does not lead to a constant value of the discarded variable. The advantage of the globally-linear method (GLM) over QSSA in algebraic Reynolds stress reduction is very clearly demonstrated in [6]. Here, we will present a similar demonstration for chemical kinetics.

Results obtained from the new schemes and traditional QSSA are now presented for a typical chemical kinetics problem. We consider a 14-reaction/7-species full chemical kinetic set for the comparison. The full set comprises of seven variables: temperature (T) and six species ($O_2, O, H_2, H, OH, and\ H_2O$) concentrations. For details regarding the evolution equations and full chemical kinetic set the reader is referred to Girimaji [5]. We consider the evolution of a hydrogen (15%

by atomic mass fraction) and oxygen (85% by atomic mass fraction) mixture from various initial conditions of same total enthalpy. The full-kinetics evolution trajectories of H_2 mass fraction from various initial states are shown in Fig. 2.1.5 as a function of temperature with solid lines. The equilibrium value of H_2 mass fractions is 0.060. The line on to which the various trajectories converge is easily identified as the reduced manifold of the full system. The temperature-based QSSA manifold (+ symbol) shows good agreement with the true reduced manifold while the O_2-based QSSA manifold (square symbol) shows very poor agreement. Traditional QSSA manifolds based on other retained variables show agreements of various degrees in between. *The retained-variable independent globally-linear model (GLM) manifold (◊) is in excellent agreement with the true reduced manifold, demonstrating one of its major advantages of GLM over QSSA method.* In Fig. 2.1.6 we present a similar result for H_2O mass fraction (equilibrium value of approximately 0.55). The new method is again better than the best QSSA result. The results for other species also show similar trend.

In Fig. 2.1.7, we try to reproduce one specific H_2 trajectory of the full-system using two-dimensional manifold models. Two-dimensional GLM reduced manifold (+ symbol), captures the true trajectory (solid-line) extremely well. The best QSSA two-dimensional manifold (square symbol) captures the general trend of the trajectory but is in error by about 15%. Other 2D-QSSA manifolds are in considerably worse agreement with data. In most practical devices, it is important to capture the ignition stage (in the vicinity of $1000\,°K$) accurately. For such applications, the degree of error incurred with the traditional QSSA may be a major disadvantage. For applications in which some degree of error is permissible, one can also consider a 1D-GLM manifold based on initial condition as the reference point. This manifold (x symbol) does reasonably well in predicting the trajectory during the early stages of evolution and is nearly as accurate as the equilibrium-reference point 1D-GLM (diamond symbol) during the latter stages. The 1D-QSSA manifold (not shown) is completely wrong except in the vicinity of equilibrium. The marked improvement of the initial-state-based 1D-GLM manifold over equilibrium-based 1D-GLM manifold at early stages of evolution demonstrates one of the most attractive features of GLM. *The GLM reduction can be customized, depending upon the application on hand, by appropriately choosing the reference state.*

In Fig. 2.1.8, a similar comparison is shown for H_2O mass fraction. Again, the 2D-GLM (+) captures the selected trajectory exceedingly accurately, markedly better than the best 2D-QSSA (square). Other 2D-QSSA based on other slow species choices perform much worse. The 1D-GLM based on initial condition as reference point (x) is only slightly worse than the best 2D-QSSA. The 1D-GLM based on equilibrium reference point (diamond) is much worse.

Conclusion: In this section, some fundamental requirements of reduced mechanisms are sketched and two alternate approximations to the traditional QSSA are proposed. They have the following important attributes which are lacking with the traditional approach: (i) improved accuracy; (ii) insensitiveness to the choice of retained and discarded variables; and, (iii) possibility of customizing the invariant manifold calculation for a specific situation by choosing appropriate reference point.

References

[1] N. Peters and B. Rogg (Editors). Reduced kinetic mechanisms for applications in combustion systems. Springer-Verlag, New York (1993).

[2] M. Smooke (Editor). Reduced kinetic mechanisms and flames. Springer-Verlag, Berlin (1992).
[3] U. Maas, and S. B. Pope, Combustion and Flame, **88**, 239 (1992).
[4] S. H. Lam, and D. A. Goussis. International Journal of Chemical Kinetics, **26**, 461-486 (1994).
[5] S. S. Girimaji, Physical Review Letters, **82**, 11, pp. 2282-2285, (1999).
[6] S. S. Girimaji, Theoretical and Computational Fluid Dynamics, **14**, pp. 259 - 281 (2001).
[7] S. J. Fraser, Journal of Chemical Physics, **88**, pp. 4732, (1988).
[8] M. J. Davis and R. T. Skodje, Journal of Chemical Physics, **111**, pp. 859 (1999).
[9] T. Turanyi, New Journal of Chemistry, **14**, No. 11, pp. 795, (1990).
[10] F. C. Christo, A. R. Masri, E. M. Nebot, Combustion and Flame, **59**, No. 2-3, pp 177, (1995).
[11] H. G. Kaper and T. J. Kaper, Physica D, **165**, 66 - 93 (2002).
[12] S. S. Girimaji and C. Brau, Theoretical and Computational Fluid Dynamics, **17**, No. 3, 171-188 (2004).
[13] A.N. Gorban, I.V. Karlin: Invariant Manifolds for Physical and Chemical Kinetics, Lecture Notes in Physics. Springer, New York (2005).
[14] E. Josyula and W. F. Bailey, AIAA 2005-5204, 38th AIAA Thermophysics Conference, 6 - 9 June 2005, Toronto, Ontario Canada (2005).
[15] N. Kazantzis and C. Kravaris. Personal communication.

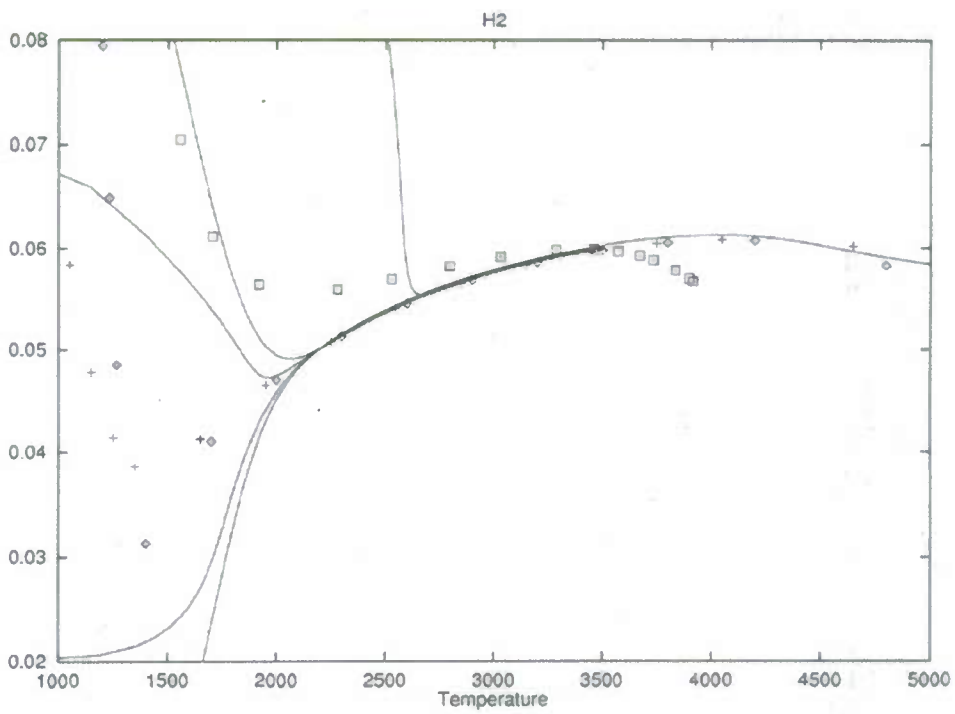

Fig. 2.1.5 State-space evolution of H_2 as a function of temperature. Solid-lines correspond to different trajectories of the full system and symbols to one-dimensional model calculations from various models. (+) – QSSA manifold based on temperature; (square) – QSSA manifold based on O_2; (diamond) – GLM manifold.

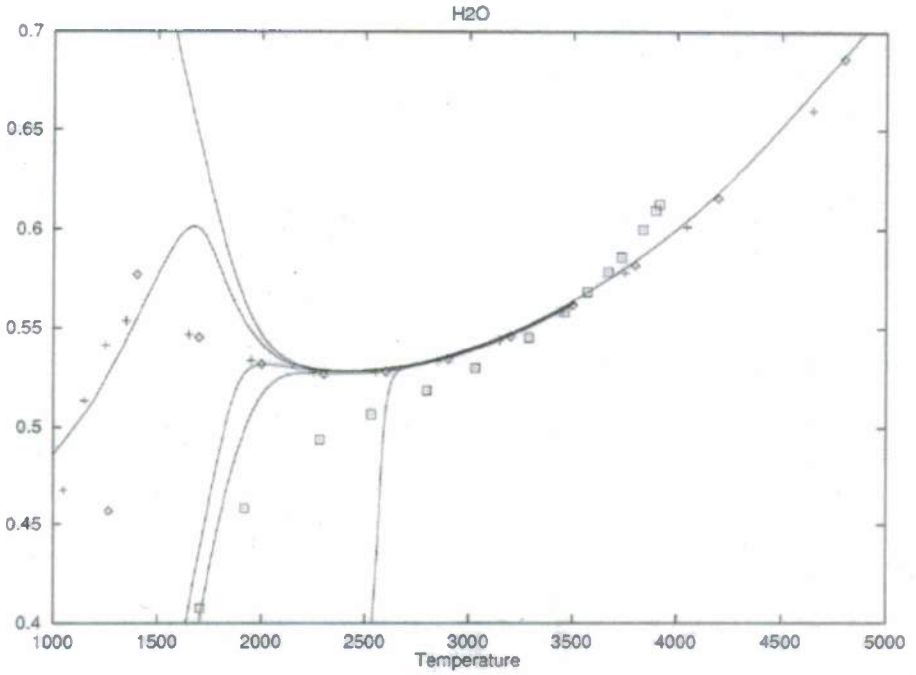

Fig 2.1.6 State-space evolution of H_2O as a function of temperature. Same legend as fig. 2.1.5.

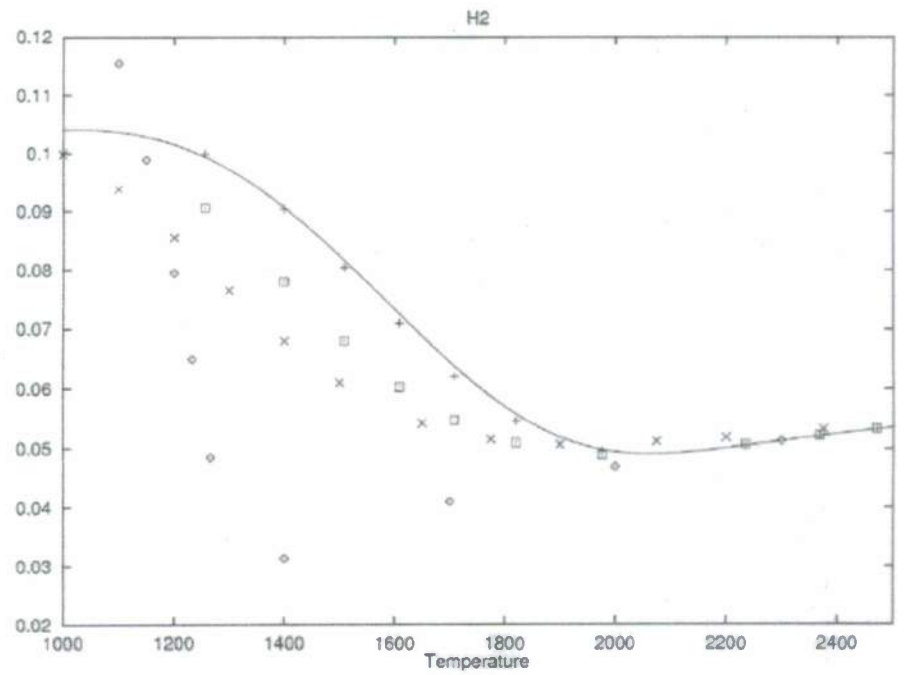

Figure 2.1.7 Trajectory of H_2 mass fraction as a function of temperature. Solid line represents one selected full trajectory of the system. (+) – GLM two-dimensional manifold; (square) – QSSA two-dimensional manifold; (x) – GLM one-dimensional manifold with initial state as reference point; (diamond) – GLM one-dimensional manifold with equilibrium state as reference point.

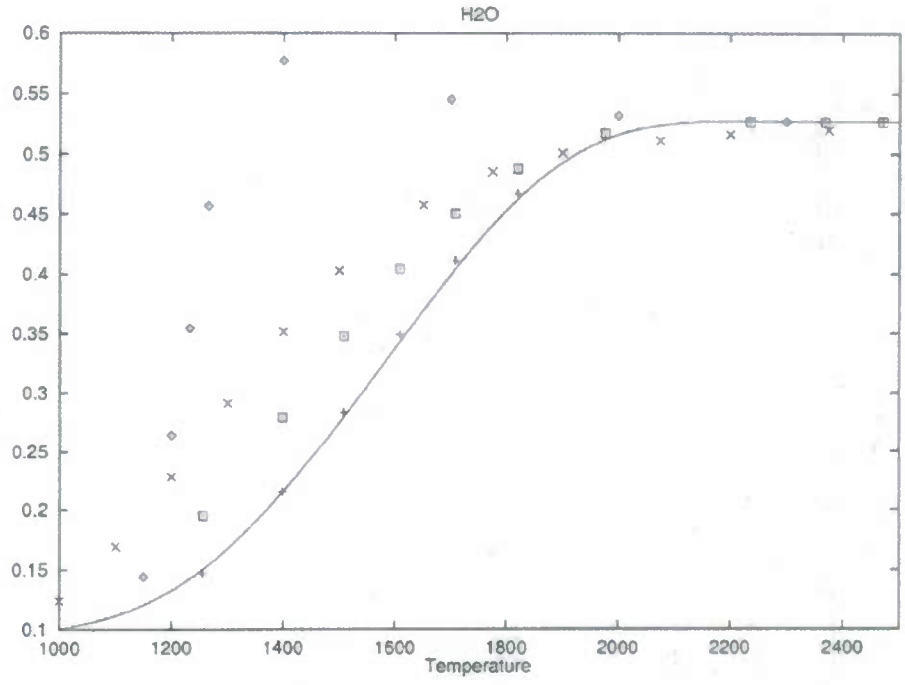

Fig 2.1.8 Trajectory of H_2O mass fraction as a function of temperature. Same legend as Fig. 2.1.7.

2.2 NTE-turbulence: Simulations, analyses, modeling and preliminary computations

The work described in this section represents one of the most important functions of the research performed under the MURI grant. The three-step – understanding, modeling and computing – NTE-turbulence research approach outlined in the Introduction is executed here. We start with the acknowledgement that direct numerical simulation (DNS) of all of the relevant conservation and state equations, even if known and valid, is computationally not viable in the flows of interest. The only practical approach for the foreseeable future involves solving modeled turbulence equations with substantially reduced degrees of freedom. Thus, the goal is to develop physics-based turbulence models of high level of fidelity starting from first principles.

NTE-turbulence closure modeling can be attempted at many different levels of sophistication. While the more sophisticated closure levels are of higher physical fidelity, these models are also less computationally viable for device-scale computations. The low-order models on the other hand tend to be empirical at best and *ad hoc* at worst. The best compromise between physical fidelity and computational viability can be achieved by the method outlined in Fig 2.2.1. Second moment closure is the lowest modeling level at which the NTE effects of large pressure, temperature and transport property fluctuations along with the electromagnetic (plasma) body force effects can be modeled from first principles. Once the second moment closure model is developed, then lower-order models can be systematically derived by invoking a series of clearly stated simplifications. Thus, our goal is to develop a range of compatible models of different degrees of sophistication. We now outline the various steps involved.

Step 1: Establishment of thermodynamics-turbulence interaction Framework
The modular turbulence-thermodynamics framework outlined in Section 2.1.1 is adopted.

Step 2: Model development Roadmap
The model development approach is outlined in Fig. 2.2.1. We seek to develop turbulence models at the second moment closure level first and then adapt the models for hybrid simulations. We start with the Favre-averaged Navier-Stokes equations for multi species mixture:

$$\tau^T_{ij,t} + (\tilde{u}_k \tau^T_{ij})_{,k} = -\tau^T_{ik}\tilde{u}_{j,k} - \tau^T_{jk}\tilde{u}_{i,k} - \overline{u_i^{''}}(-\tilde{p}_{,j} + \tilde{\tau}_{jk,k}) + (\overline{p_{,j}^{''}u_j^{''}}) + (\overline{p_{,j}^{''}u_i^{''}})$$
$$- \sum_n \left[f_{b(n)i}\overline{\rho u_j^{''} Y_{(n)}^{''}} + f_{b(n)j}\overline{\rho u_i^{''} Y_{(n)}^{''}} \right] + \left[(\overline{\rho u_i^{''} u_j^{''} u_k^{''}}) + (\overline{\tau_{ik}^{''} u_j^{''}} + \overline{\tau_{jk}^{''} u_i^{''}}) \right]_{,k}$$
$$+ \overline{\tau_{ik}^{''} u_{j,k}^{''} + \tau_{jk}^{''} u_{i,k}^{''}}$$

We identify the various terms that require closure modeling. Based on the findings of previous and current studies, it is recognized that pressure-strain correlation and pressure-dilatation are most crucial effects that alter the nature of turbulence in high-Mach number flows. We perform fundamental studies to understand the physics of these flows and develop closure models at several levels of sophistication. For example, the rapid pressure-strain correlation model is identified as one of the most important contributors to the so-called Langley curve effect. The interactions between the various thermodynamic and fluid dynamic processes are identified as given in Section 2.1. The NTE-turbulence interaction parameters are:

1) Gradient Mach number – M_g
2) Turbulent Mach number – M_t
3) Heat-release coefficient
4) Viscosity-variation ratio
5) Integral scale Reynolds number – Re_L
6) Taylor scale Reynolds number –Re_l
7) Magnetic Interaction parameter – N

Step 3: Physics investigation studies

1) The linear physics -- rapid pressure-strain correlation and pressure-dilatation -- as a function of the above NTE-turbulence interaction parameters are studied using rapid distortion theory (RDT).
2) The non-linear physics – slow pressure-strain correlation and pressure-dilatation – as a function of the interaction parameters is examined using appropriately formulated DNS and Homogeneous Euler Equation (HEE).
3) Body force physics – electromagnetic-flow interaction -- is investigated using DNS.

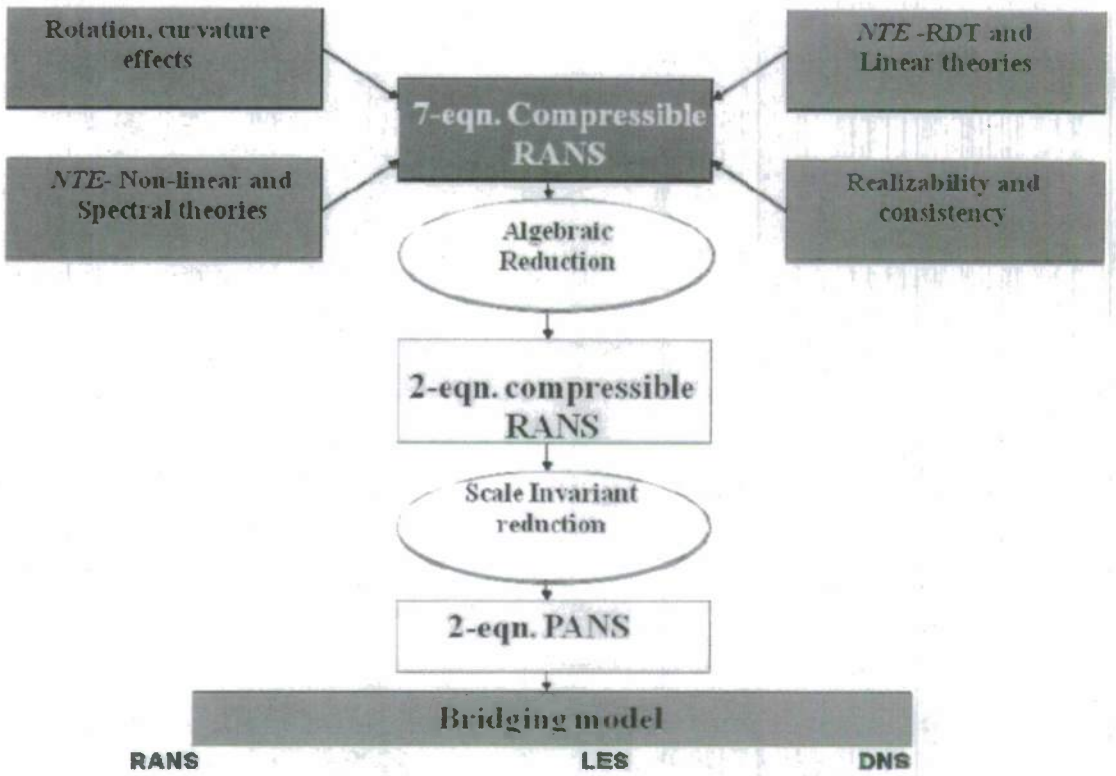

Fig. 2.2.1 Turbulence model development approach

Step 4: High-speed turbulence closure model proposals
Based on the outcomes of the studies in Step 3, we propose turbulence closure models for pressure-strain correlation and pressure dilatation.

Step 5: Averaging Invariance of compressible Navier-Stokes equations
Once the second-moment closure modeling is complete, we derive the hybrid closure models employing the averaging invariance property of Navier-Stokes equations. While the averaging invariance property of incompressible Navier-Stokes equation is well known, the compressible version is not yet formally established. This development is one of the many fundamental contributions of this study.

Step 6: Model verification and validation
Then the models will be verified at various levels of sophistication and fidelity. Only some preliminary studies have been completed at this stage. The results will be presented at the end of this section.

Through the remainder of this section we present the important outcomes from the various studies aimed at executing this model development plan. Details can be found in various theses, journal papers and conference presentations listed in Chapter 4.

2.2.1 DNS Studies

2.2.1.1 Heat release effects

References: A detailed discussion of this topic can be found in the PhD thesis and journal papers of K. C. Lee from the list above.

Motivation: In hypersonic flows, the evolution of turbulence is much more complicated than in incompressible or low Mach number flows. The fundamental argument of energy cascade that, at very high Re, the energy of turbulence is produced in energy-containing range, transferred through inertial range, and converted to heat in dissipation range, may not be valid. Turbulent kinetic (mechanical) energy can be produced in the inertial range or even in the dissipation range in hypersonic flows, by transfer from thermal field depending on the length scales of temperature field. Furthermore, as molecules at different excited states in hypersonic flows relax to ground state, heat will be released into the flow. Thus the effect of heat release on turbulence evolution needs to be understood.

Objective: Several DNS studies were conducted to explore the effect of heat release on various aspects of return-to-isotropy, non-linear pressure-dilatation, solenoidal dissipation and dilatational dissipation effects.

1) Decaying isotropic turbulence with temperature fluctuations.
2) Temperature-difference (heat release) driven turbulence.
3) Decay of fully dilatational turbulent field.
4) Return to isotropy in presence of temperature fluctuations.
5) Active/passive thermal mixing in compressible turbulence.
6) Turbulence decay under the influence of viscosity fluctuations.

We also examine the energy exchange mechanism between kinetic and internal energy in compressible homogeneous isotropic turbulence with heat release.

Approach: The macroscopic governing equations for compressible flow are the continuity, momentum, energy equation, and the equation of state as follow.

$$\frac{\partial \rho}{\partial t}+\frac{\partial(\rho u_j)}{\partial x_j}=0$$

$$\rho\left(\frac{\partial u_i}{\partial t}+u_j\frac{\partial u_i}{\partial x_j}\right)=-\frac{\partial p}{\partial x_i}+\mu\frac{\partial^2 u_i}{\partial x_k \partial x_k}+(\lambda+\mu)\frac{\partial}{\partial x_i}\left(\frac{\partial u_k}{\partial x_k}\right)$$

$$\rho\left(\frac{\partial e}{\partial t}+u_j\frac{\partial e}{\partial x_j}\right)=k\frac{\partial^2 T}{\partial x_k \partial x_k}-p\frac{\partial u_k}{\partial x_k}+\lambda\left(\frac{\partial u_k}{\partial x_k}\right)^2+\mu\left(\frac{\partial u_i}{\partial x_j}+\frac{\partial u_j}{\partial x_i}\right)\frac{\partial u_j}{\partial x_i}+\rho\dot{q}$$

$$p=\rho RT$$

where e is internal energy, μ is shear viscosity , λ is the bulk viscosity, $\dot{q}$ is the heat source, T is the temperature, p is the pressure, and k is the diffusivity of fluid. All simulations are performed in a periodic box which has the resolution of 64^3 to 128^3. The initial homogenous isotropic random velocity and temperature fields are generated by the same random procedure

but at different wavenumbers in order to generate different length scales. After setting all the initial conditions, the flow is allowed to evolve and results are gathered after each time step.

Results and discussion: Here we present a small selection of results from the various studies. For more detailed discussion, please check the references given above.

Study 1: The objective of this study is to examine the effect of length scale of heat release. For this purpose three cases are studied: (1) HIT (Homogeneous Isotropic Turbulence) in which the temperature length scale is larger than the velocity scale, (2) HIT in which the velocity length scale is larger, and (3) HIT with two different species corresponding to two different excited states of the same elementary species.

In Case 1, in which T-field length scale is larger, the evolution of k is much different from the one with constant T field. The energy transfer from thermal (internal) to kinetic modes is oscillating with a non-zero mean. The pressure work plays main role in generating this oscillations as shown in Fig. 2.2.2. Considering the net effect of the pressure work, it transfers the energy from internal energy to kinetic energy. The increase of internal energy in Fig. 1a is due to the dissipation which includes both bulk and shear dissipation as shown in Fig. 1b. When the length scale of T diminishes, the oscillation of k is also reduced as shown in Fig. 2.2.3. However, there is still a net energy transfer from e to k. Compared with Case 1 , the magnitude of pressure work and bulk dissipation in Case 2 is relatively small, while the magnitude of shear dissipation is relatively large.

Case 1	Case 2	Case 3
 Velocity	 Velocity	 Velocity
 Temperature	 Temperature	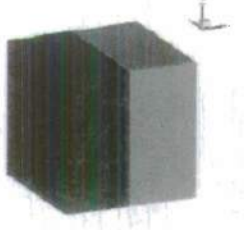 γ

Table 2.2.1 Simulation cases

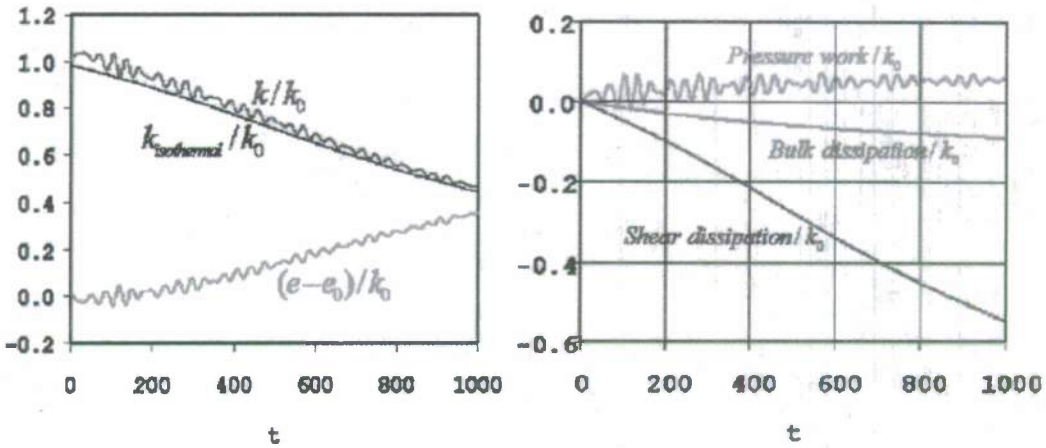

(a) Kinetic energy (b) Energy budget

Fig. 2.2.2 Case 1: $l_T(0) > l_u(0)$

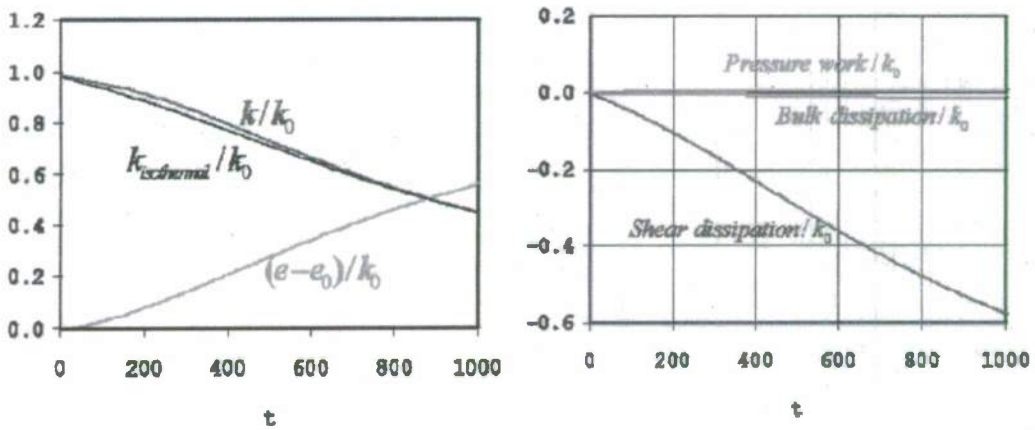

(a) Kinetic energy (b) Energy budget

Fig. 2.2.3 Case 2: $l_T(0) < l_u(0)$

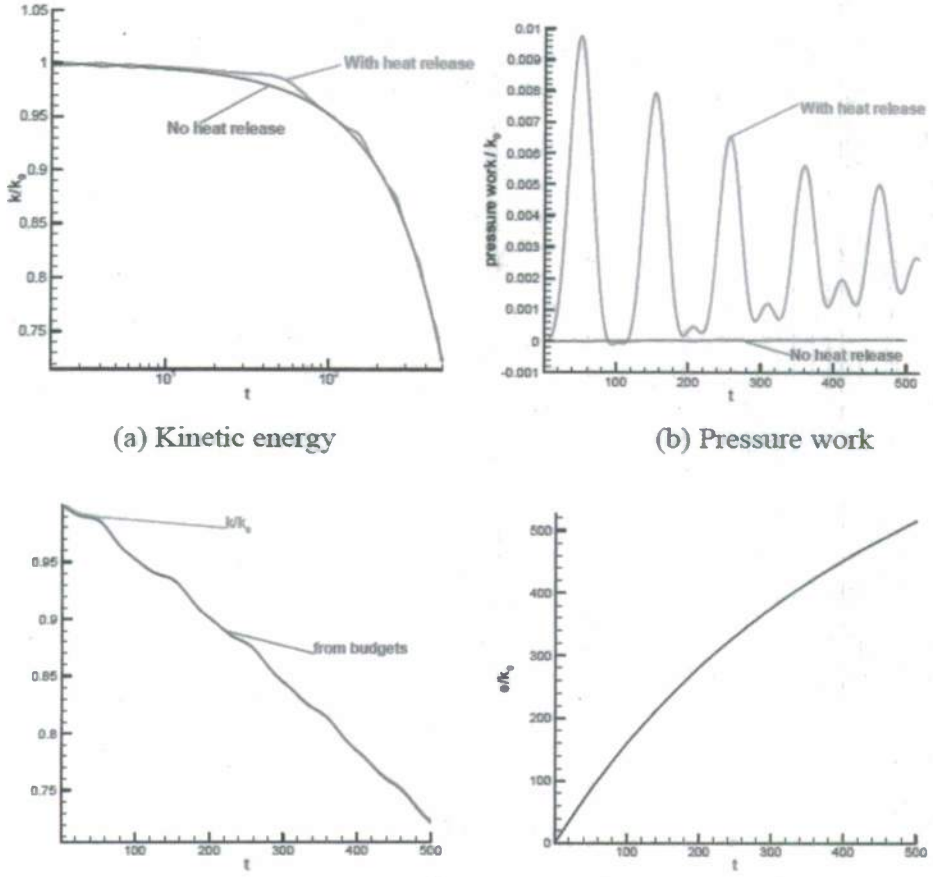

(a) Kinetic energy (b) Pressure work

(c) Kinetic energy budget (d) Internal energy

Fig. 2.2.4 Case 3: Mixing between different γ

Figure 2.2.4 summarizes the most important results in Case 3. As shown in Fig. 3a, the most salient feature in the evolution of k in heat release case is that k does not evolve smoothly as in the HIT without heat release. To better understand this, we study the mechanism of energy transfer into k. The pressure work in the k-budget is shown in Fig. 2.2.4. It can be seen clearly that pressure work adds energy into k, and the oscillatory behavior of pressure work explains the manner of k evolution. The pattern of the evolution of pressure work itself is of great interest in this study. In order to understand the variation of pressure work, we examined the position of interface (PI) between two species in this case. We found that although the heat is released smoothly into the system, the variation of PI is not smooth. At initial stage, the mean speed of interface is zero. When the system evolves, the excited species in the left half of system is relaxed to the background states and heat is released into this portion. This causes the increase of T on the left side, upsetting the balance of pressure between the left and right sides. The expansion of the left half makes the interface at the middle of domain move to the right. This part of the phenomenon is easy to understand. However, as shown in Fig. 2.2.4, the movement of interface is not smooth. It slowly moves to right first, then fast, and then slowly again. During

some periods, the interface stays at almost the same position. This phenomenon will be studied in more detail in the future.

To verify the numerical results, we compare the kinetic energy obtained from budget equation with the one directly computed using the definition of $(\frac{1}{2}u_i u_i)$. It is shown that those two results agree very well in Fig. 2.2.4. In Fig. 2.2.4, the evolution of internal energy is also given. It is seen that amount of energy transferred from the internal energy is much larger than the initial kinetic energy.

Study 2: The main objective of this study is to examine the cascade process in initially solenoidal turbulence in the presence of small temperature fluctuations. We compare isothermal decay with that in the presence of temperature fluctuations. The primary conclusion is that when the temperature fluctuations are of the order of 5%, the compressibility effects and dilatational dissipation are quite negligible (Fig. 2.2.5). When the fluctuations are larger, then the effects can be significant.

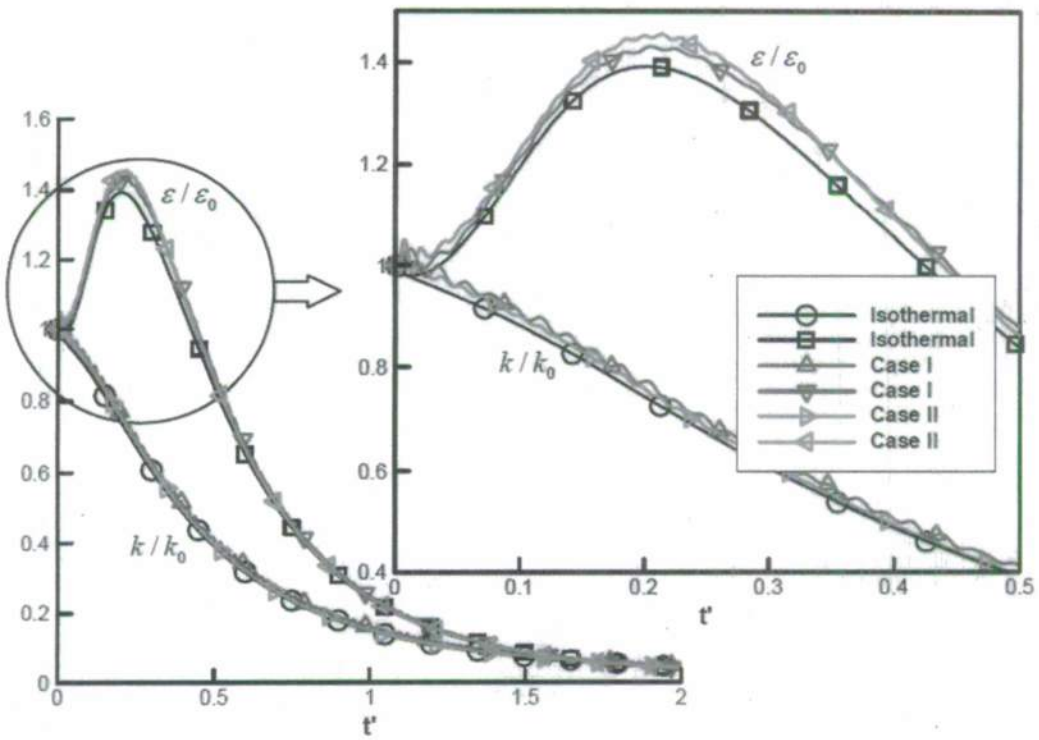

Fig. 2.2.5 Decaying isotropic turbulence with and without temperature fluctuations

Study 3: In this case turbulence is generated purely by heat release. We study the energetics in such a flow which tends to be mostly dilatational.

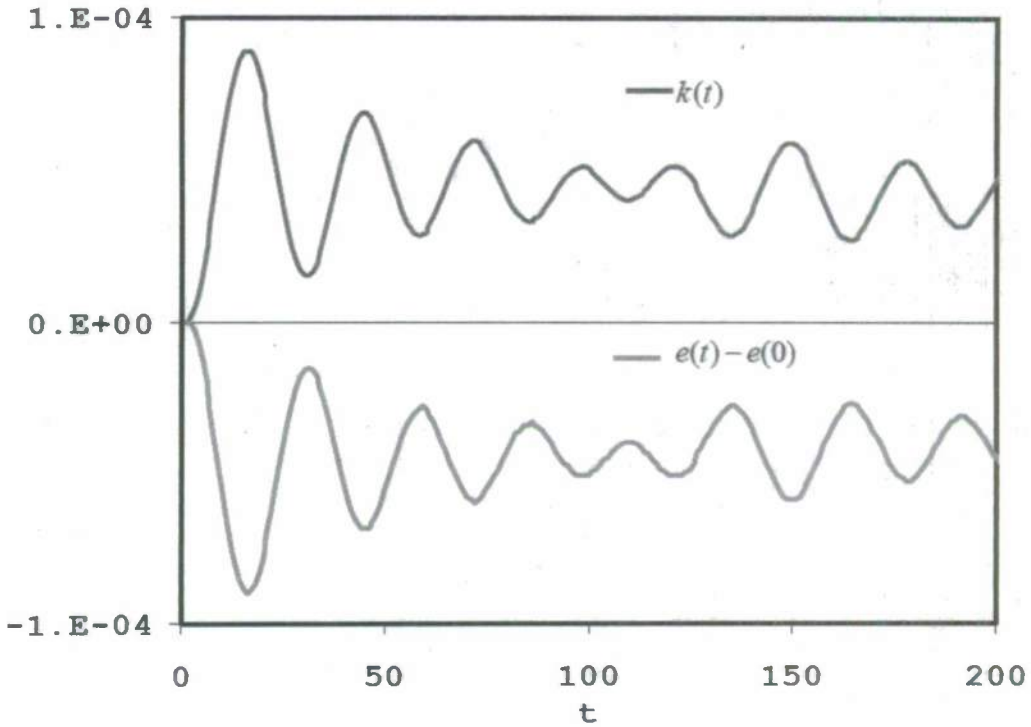

Fig 2.2.6 Evolution internal and turbulent kinetic energy

It is clear from the figure that the evolution of turbulence is very different in this case. Initially, the turbulent kinetic energy is zero and it is quickly generated at the expense of internal energy. It can be shown that the velocity fluctuations generated are dilatational in nature. The pressure-work (pressure-dilatation correlation) is the mechanism responsible for this energy transfer. After the initial growth in turbulent kinetic energy, there is a dynamic exchange between the kinetic and internal mode. Overall, the kinetic energy decays more slowly than is typical in initially solenoidal turbulence cases.

Study 4: The objective of this study is to examine the decay of purely compressible isotropic fluctuations. From the previous study it is evident that dilatational velocity dynamics is quite different from that of solenoidal velocity dynamics. To directly compare the two cases, we now study evolution of turbulence decay from initially randomly distributed dilatational fluctuations. This offers a more controlled examination of the behavior dilatational turbulence making possible a direct comparison with solenoidal turbulence decay. From Fig. 2.2.7, the difference between solenoidal and dilatational turbulence decays are quite evident. From the dissipation plot it is clear that the dilatational field does not experience any gradient steepening typically seen in solenoidal turbulence. In solenoidal turbulence, the dissipation increases initially due to energy cascade to small scales before decaying under the influence of viscous effects. Such initial rise is completely absent in the dilatational case. The presented results clearly call for careful modeling of the dilatational velocity field.

Study 5: The goal here is to study the return to isotropy process in the presence of small temperature fluctuations. One of the primary unclosed terms in second moment turbulence closures is slow (non-linear) pressure-strain correlation. We would like to investigate the physics of this term in the presence of small temperature fluctuations. Return to isotropy trajectories with and without temperature fluctuations are plotted in the Lumley invariant triangle in Figures 2.2.8a and 2.2.8b. It is clearly evident that when the temperature fluctuations are small, the return-to-isotropy process is only slightly affected when compared to the isothermal case. It must be pointed out that the dilatational field induced by the temperature fluctuations is rather small in this case. The small-amplitude oscillations in the trajectory are due to the effect of pressure-dilatation which transfers back-and-forth small amount of energy from one component to the other. We do, however, expect larger dilatational fields to be larger if the temperature fluctuations are larger. Thus in the presence of large amounts of heat release, it remains to be seen how the return-to-isotropy process will be affected. The will be investigated in a later study.

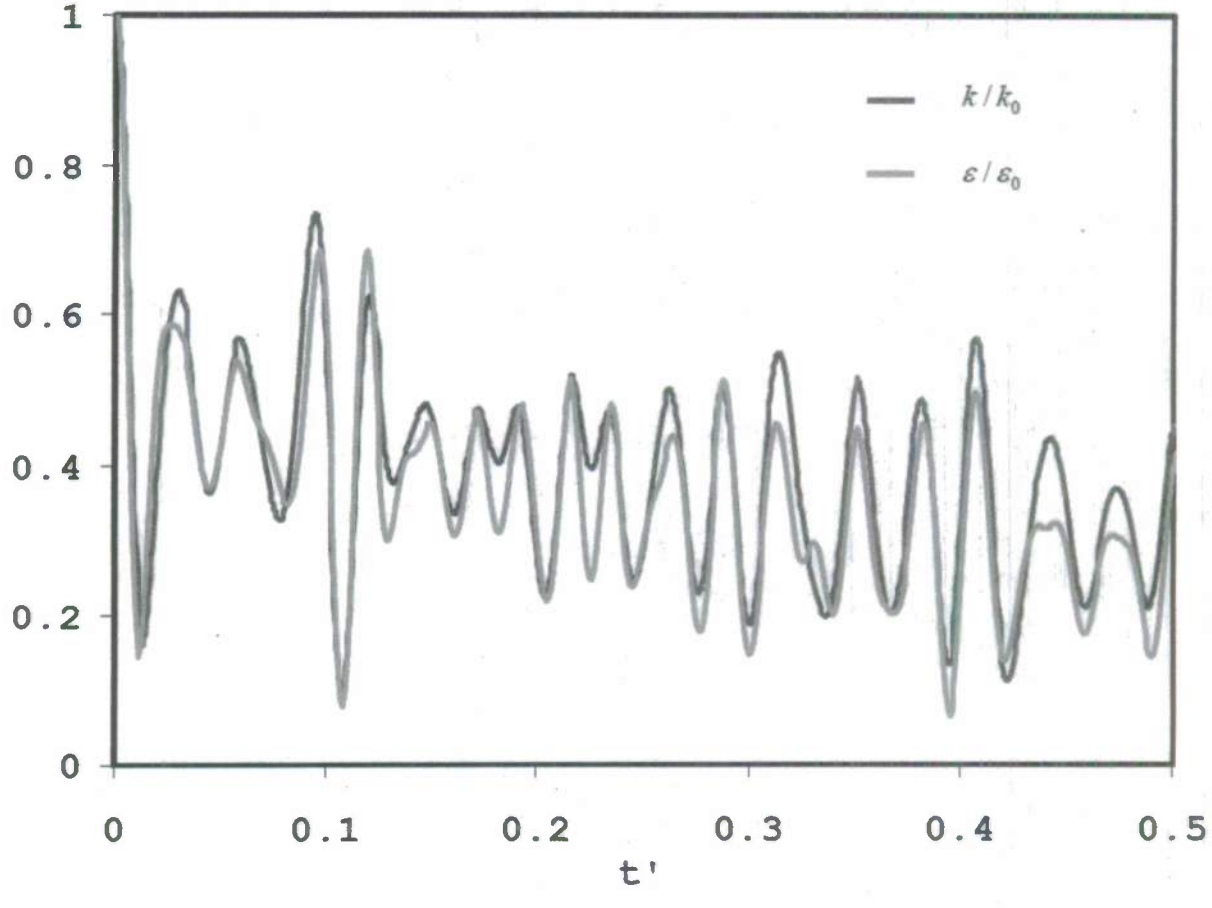

Fig. 2.2.7 Evolution of kinetic energy and dissipation in dilatational turbulence

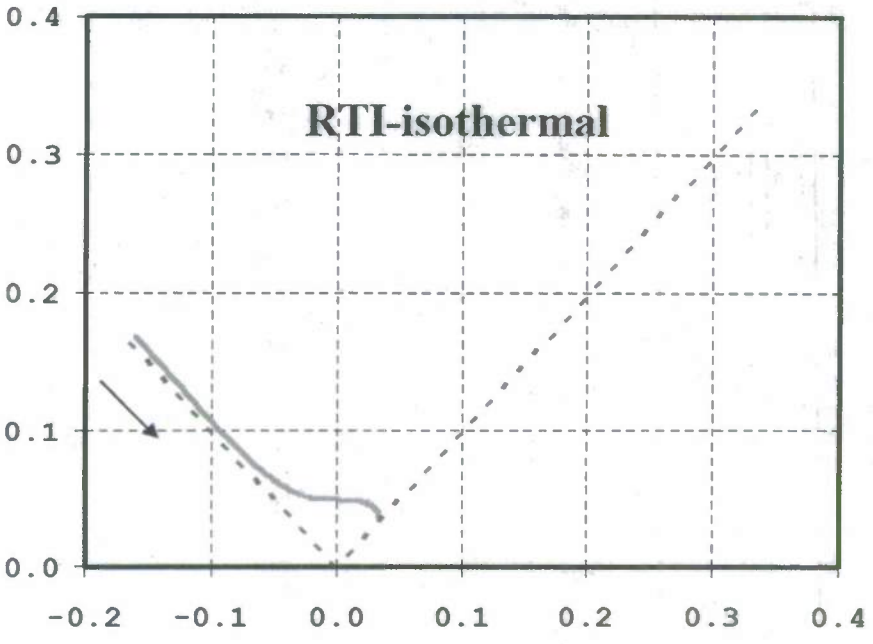

Fig. 2.2.8a Isothermal return to isotropy trajectory

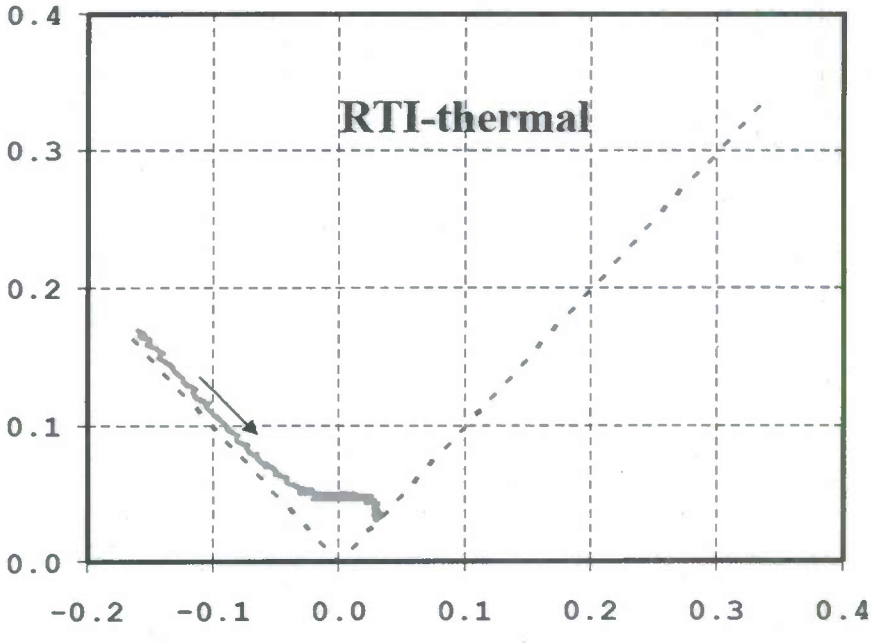

Fig. 2.2.8b Return-to-isotropy in the presence of small temperature fluctuations

Study 6: The main motivation of this study is to examine how the momentum-energy equation coupling affects the thermal mixing process.

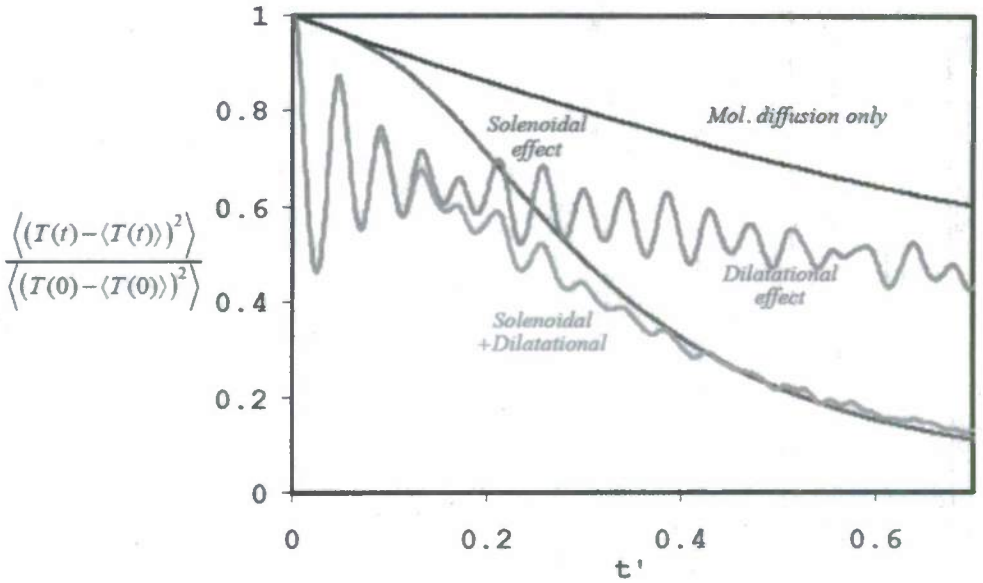

Fig. 2.2.9. Role of various effects in turbulent mixing.

In this work, the roles of molecular diffusion, solenoidal stirring and dilatational stirring are clearly delineated. It appears that the dilatational stirring occurs at the acoustic time scale. Although the overall effect of the dilatational field is to enhance mixing when acting alone, there is considerable amount of un-mixing (un-stirring) indicated by the increase in temperature variance. The solenoidal stirring scales with the turbulence time scale and there is no evidence of any un-mixing. When both dilatational and solenoidal velocity fields act together, the former trends dominate at early times and latter trend at latter times.

2.2.1.2 Variable transport properties effects

References:

1. K. C. Lee: 'Heat Release effects on turbulence', Ph.D. Thesis (2007)
2. K. C. Lee, S. S. Girimaji and J. Kerimo, 'Validity of Taylor's dissipation-viscosity independence postulate in variable-viscosity turbulent fluid mixtures', ***Physical Review Letters,*** Vol. 101, Issue 7, (2008)

Motivation: In non-equilibrium flow, it is anticipated that viscosity will be a strong function of space depending on the local composition of the gas and temperature. Therefore, it is important to assess the effect of variable viscosity on the various turbulence phenomena.

Objective: Most importantly, this study provides a basis for examining one of the most important tenets of turbulence modeling – the Taylor postulate. According to this postulate, dissipation should be independent of viscosity rendering the dissipation equation independent of any viscous terms.

Approach: We perform decaying turbulence simulations in a periodic box. The viscosity in one half of the box is five times that in the other half. The initial turbulence field is isotropic and density and temperature are taken to be constant throughout the box. Such a study will isolate the effect of variable transport coefficient on turbulence decay.

Results: The referenced paper presents a series of results that demonstrate the validity of Taylor's postulate even in flows with steep spatial gradients in viscosity. Here we present just two sample results.

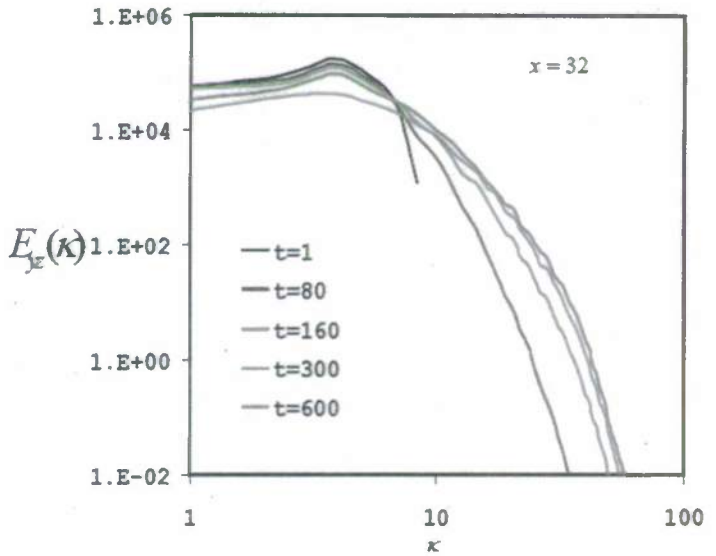

Fig. 2.2.10a Spectral evolution in low viscosity region

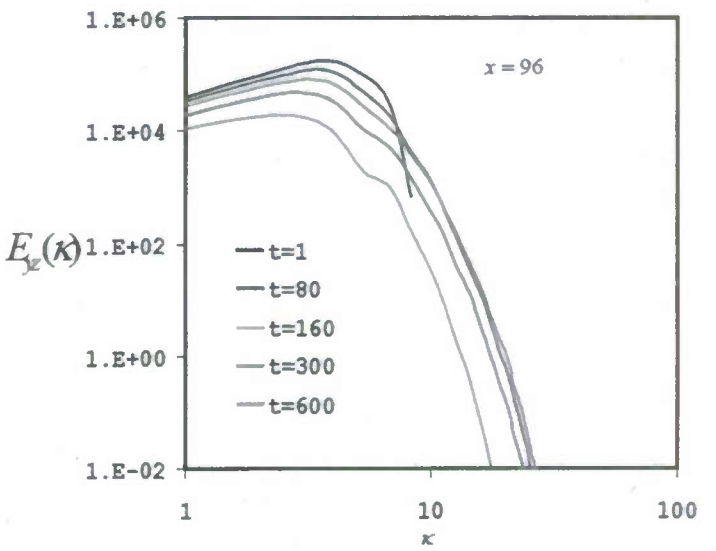

Fig. 2.2.10b Spectral evolution in high viscosity region

As mentioned earlier, we find that, at long enough times, the value of dissipation does indeed become independent of local viscosity and the size of the small scales are indeed proportional to the viscosity value. These points are well demonstrated in Fig. 2.2.10. In Fig. 2.2.10a, the turbulence spectrum evolution in the low viscosity region is shown. In Fig. 2.2.10b, the spectral evolution in a high viscosity region is given. It is clear that a wider range of scales are energetic in the low viscosity region. The most important outcome of the study is that, to leading order, the effect of variable viscosity can be neglected in modeling turbulent fluxes in non-equilibrium flows, provided the Reynolds number is high enough.

2.2.1.3 Effect of charged flow: MHD turbulence

References:

1. B. M. Riley. 'MHD effects in jets and turbulence,' MS thesis (2006).
2. B. M. Riley, J. C. Richard and S. S. Girimaji, 'Magnetic field effects on axis-switching and instabilities in rectangular plasma jets,' to appear in ***Flow, Turbulence and Combustion*** (2008). Published online November 2008 DOI 10.1007/s10494-008-9182-y
3. B. M. Riley, J. C. Richard and S. S. Girimaji, 'Assessment of magneto-hydrodynamic Lattice-Boltzmann schemes in turbulence and rectangular jets,' ***(IJMPC) Computational Physics and Physical Computation***, Vol. 19, No. 8 (2008) pp. 1211 - 1220.

Motivation: At very high speeds and shock strengths, turbulence is affected by not only heat release --- via thermodynamic interaction parameters and transport coefficient variations -- but also by electromagnetic forces that arise due to the generation of plasma. It is therefore important to examine the physics of Magneto-hydrodynamic (MHD) turbulence.

Objective: The purpose of this sequence of studies is to examine the effect of constant and fluctuating magnetic fields on various turbulence mechanisms -- especially the energy exchange between magnetic and turbulence fields.

Approach: A series of MHD laminar jet flow computations and decaying turbulence simulations were performed.

Results: For a detailed discussion we refer the reader to the published work. Here, we present only the important outcomes:

1. Magnetic field can profoundly affect the stability of the flow field – it can have stabilizing or destabilizing effects.
2. Magnetic field can affect the spectral anisotropy of the flow, but does not appear to affect the variation anisotropy significantly.
3. The role of Lorentz force is predominantly to enforce equi-partition between turbulent kinetic and turbulent magnetic energies.
4. Under certain conditions, the approach to equi-partition between kinetic and magnetic energies is however not monotonic. There can be wild fluctuations away from equi-partition. In all the cases observed in this study, all of the turbulent energy was contained in the kinetic form and very little in the magnetic form during these fluctuations.

2.2.1.4 Velocity gradients in compressible turbulence

References:

1. K. C. Lee, S. S. Girimaji and J. Kerimo. 'Effect of compressibility on turbulent velocity gradients and small-scale structure,' ***Journal of Turbulence,*** 9 (10), 1-18 (2009).
2. S. Suman and S. S. Girimaji. 'Velocity gradient invariants and topology in compressible turbulence,' submitted to ***Journal of Turbulence***, 2009.

Motivation: Velocity-gradient dynamics and associated small-scale structure hold the key to understanding many turbulence processes such as material-element deformation, scalar/temperature mixing, energy cascade and intermittency. Understanding velocity gradient dynamics is crucial for modeling these turbulence processes.

Objective: The objective of this study is to study the difference between the velocity gradient dynamics and small-scale structure in incompressible and compressible turbulence. Of particular interest is the role of pressure which now evolves according to an evolution equation (energy conservation equation) rather than the Poisson equation.

Approach: We perform DNS of decaying isotropic compressible turbulence at various turbulent Mach numbers. Then the small-scale structure is examined conditioned on the local value of dilatation. Heat release effects are also examined.

Results: All the results are well documented in the papers listed above. The most important results are now summarized:

1) The small-scale structure is a strong function of local normalized dilatation, but independent of flow Mach number and Reynolds number. This is an important finding for closure modeling.
2) The small-scale structure at extreme dilatations (both contracting and expanding) is spherical.
3) The possible local stream topologies are greater in number for compressible turbulence than incompressible turbulence. The preferred topology is a strong function of normalized dilatation.

2.2.2 Rapid distortion (Linear) analysis of compressible turbulence

Although turbulence is eminently a non-linear process, linear theories can provide very useful insight as well. In fact, linear terms play a forcing role and the non-linear processes respond to this linear forcing. In turbulence literature, the linear analysis is given the name rapid distortion theory (RDT). In previous literature, RDT for incompressible and compressible turbulence always used the Reynolds-averaged reference field and un-weighted fluctuations as small parameters. Under the MURI project, we developed the following:

1) Extension of compressible RDT to arbitrary reference fields.
2) Detailed analysis of Reynolds-RDT equations for the case of compressible shear flow.
3) Proposal of pressure-strain correlation model based on RDT studies.
4) Extension of RDT to Favre-averaged reference fields.

Here we will report the progress in two sub-sections: Reynolds-averaged RDT and Favre-averaged RDT

2.2.2.1 Reynolds-averaged RDT

References:

1) H. Yu and S.S. Girimaji, 'Extension of compressible ideal gas rapid distortion theory to general mean velocity gradients,' ***Physics of Fluids,*** Vol. 19, 4, (2007).
2) T. Lavin, S. Suman, S. S. Girimaji and H.Yu. 'Rapid distortion analysis of compressible ideal-gas shear turbulence: Role of pressure-strain correlation,' submitted to ***Theoretical and Computational Fluid Dynamics***, 2009
3) M.S. Thesis of Tucker Lavin (2007).

Solution Procedure: We begin by considering the ideal gas equation (1 eqn.) and the inviscid conservation equations (mass, momentum and energy – 5 eqns.):

$$\frac{\partial \rho}{\partial t}+U_j\frac{\partial \rho}{\partial x_j}=-\rho\frac{\partial U_j}{\partial x_j}$$

$$\frac{\partial U_i}{\partial t}+U_j\frac{\partial U_i}{\partial x_j}=-\frac{1}{\rho}\frac{\partial P}{\partial x_i}$$

$$\frac{\partial T}{\partial t}+U_j\frac{\partial T}{\partial x_j}=-(\gamma-1)T\frac{\partial U_j}{\partial x_j}$$

$$P=\rho RT$$

These equations are developed with the following steps:

1) Normalization
2) Decomposition into mean and fluctuating parts (e.g. $U=\overline{U}+u'$)
3) Derivation of the equation for the fluctuating flow.
4) Linearization by ignoring the all nonlinear terms followed by homogenization.

The ensuing linear fluctuating flow equations (in which the assumptions of homogenous turbulence are applied) are then transformed into Fourier space for conditional-average analysis. The wave-vector is determined by:

$$\frac{d\kappa_i}{dt}+\kappa_k\frac{\partial \overline{U}_k}{\partial x_i}=0$$

For each given wave vector, we have the following the equations for Fourier coefficients:

$$\frac{d\hat{\rho}}{dt}=-i\overline{\rho}\kappa_k\hat{u}_k-\frac{\partial \overline{U}_k}{\partial x_k}\hat{\rho}$$

$$\frac{d\hat{u}_i}{dt}=-\hat{u}_k\frac{\partial \overline{U}_i}{\partial x_k}-\frac{i\alpha_0}{M_{a0}^2}\hat{T}\kappa_i-\frac{i\alpha_0\overline{T}}{M_{a0}^2\overline{\rho}}\hat{\rho}\kappa_i$$

$$\frac{d\hat{T}}{dt}=-i(\gamma-1)\overline{T}\hat{u}_k\kappa_k-(\gamma-1)\frac{\partial \overline{U}_k}{\partial x_k}\hat{T}$$

These are combined to produce 25 equations that must be simultaneously solved over 4096 wave numbers (in Fourier space) and then averaged to obtain the final results.

Moment Equations: Reynolds-averaged fluxes of interest are found by solving the following 25 equations (in tensor notation) for each wave-vector:

$$\frac{dR_{ij}}{dt} = -R_{kj}\frac{\partial \overline{U}_i}{\partial x_k} - R_{ik}\frac{\partial \overline{U}_j}{\partial x_k} + \frac{i\alpha_0}{M_{a0}^2}(L_j\kappa_i - L_i^*\kappa_j) + \frac{i\alpha_0\overline{T}}{M_{a0}^2\overline{\rho}}(M_j\kappa_i - M_i^*\kappa_j)$$

$$\frac{dM_i}{dt} = i\overline{\rho}\kappa_k R_{ki} - \frac{\partial \overline{U}_k}{\partial x_k}M_i - M_k\frac{\partial \overline{U}_i}{\partial x_k} - \frac{i\alpha_0}{M_{a0}^2}A\kappa_i - \frac{i\alpha_0\overline{T}}{M_{a0}^2\overline{\rho}}C\kappa_i$$

$$\frac{dL_i}{dt} = i(\gamma-1)\overline{T}R_{ki}\kappa_k - (\gamma-1)\frac{\partial \overline{U}_k}{\partial x_k}L_i - L_k\frac{\partial \overline{U}_i}{\partial x_k} - \frac{i\alpha_0}{M_{a0}^2}B\kappa_i - \frac{i\alpha_0\overline{T}}{M_{a0}^2\overline{\rho}}A^*\kappa_i$$

$$\frac{dA}{dt} = i\overline{\rho}\kappa_k L_k^* - i(\gamma-1)\overline{T}M_k\kappa_k - \gamma\frac{\partial \overline{U}_k}{\partial x_k}A$$

$$\frac{dB}{dt} = -2(\gamma-1)\frac{\partial \overline{U}_k}{\partial x_k}B + i(\gamma-1)\overline{T}\kappa_k(L_k^* - L_k)$$

$$\frac{dC}{dt} = -2\frac{\partial \overline{U}_k}{\partial x_k}C + i\overline{\rho}\kappa_k(M_k^* - M_k)$$

where, $R_{ij} \equiv <\hat{u}_i^*\hat{u}_j \mid \vec{\kappa}>$, $L_j \equiv <\hat{T}^*\hat{u}_j \mid \vec{\kappa}>$, $M_j \equiv <\hat{\rho}^*\hat{u}_j \mid \vec{\kappa}>$, $A \equiv <\hat{\rho}^*\hat{T} \mid \vec{\kappa}>$, $B \equiv <\hat{T}^*\hat{T} \mid \vec{\kappa}>$, $C \equiv <\hat{\rho}\hat{\rho}^* \mid \vec{\kappa}>$, $a=\alpha_0/M_{a0}^2$, $b=\left(\alpha_0/M_{a0}^2\right)\left(\overline{T}/\overline{\rho}\right)$, $c=(\gamma-1)\overline{T}$, $\alpha_0 = P_0/\rho_0 c_{s0}^2$ and $M_{a0} = U_0/c_{s0}$. The physical values of these fluxes are then obtained by summing over all wave-vectors. The primary term of interest is the R_{ij} term, but the influence of the other terms requires that all 25 equations must be solved, as shown in Fig. 2.2.11.

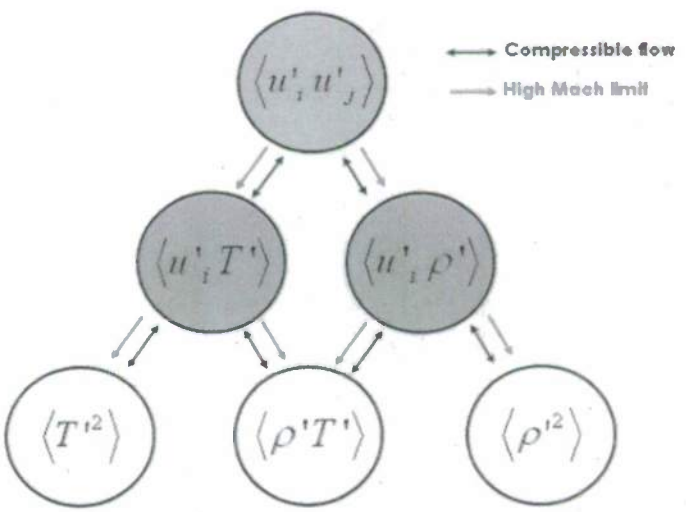

Figure 2.2.11 - Reynolds stress interaction

Key Results: To validate the above analysis, we compare our results against the known limits of incompressibility and high Mach limit. A plot of the non-dimensionalized kinetic energy compared to incompressible RDT is shown in Fig. 2.2.12 for the homogenous shear flow case.

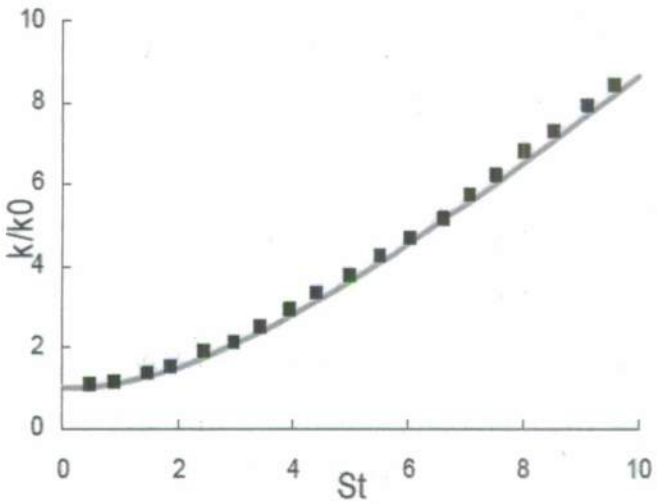

Figure 2.2.12 - Kinetic energy comparison: line - compressible RDT; points - incompressible RDT

Other mean flow cases – plain strain, axi-symmetric expansion and contraction – were also applied and compared to incompressible results, as seen in Fig. 2.2.13.

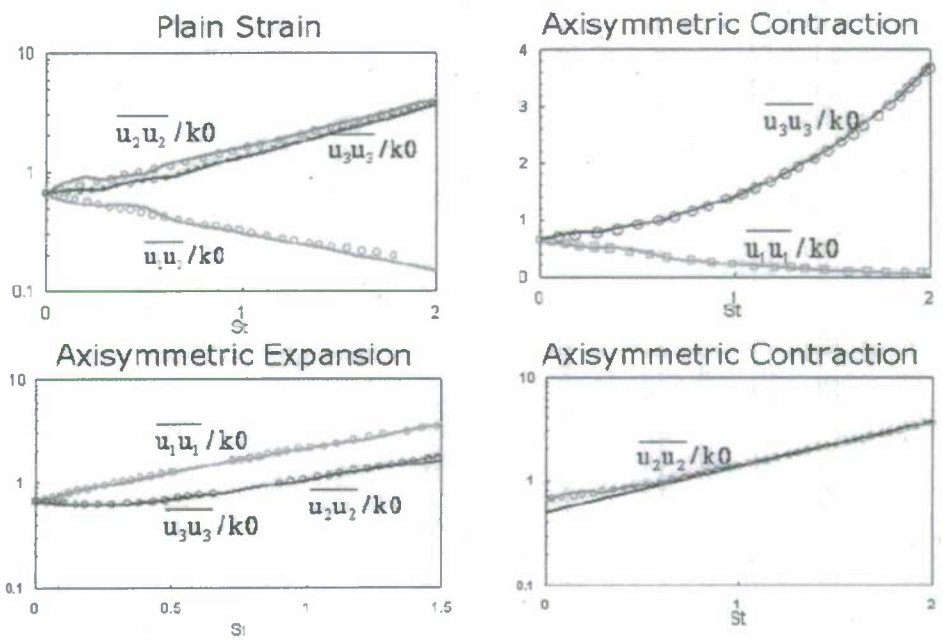

Figure 2.2.13 - Flow regime comparison: line - compressible RDT; points - incompressible RDT

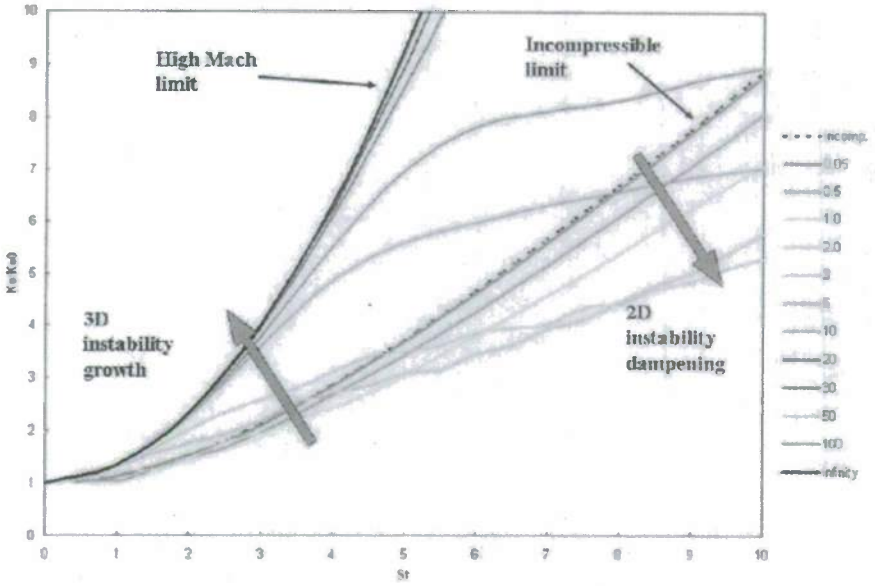

Figure 2.2.14 - Mach number progression of kinetic energy

Also of interest is how the flow behaves as Mach number approaches infinity. This progression as it affects kinetic energy can be seen in Fig. 2.2.13. Of note in this figure is the difference between the trends below and above Mach 3. Previous theory projected that, as Mach number (and, thus, the level of compressibility) increases, the kinetic energy plot would continue to move downward due to decreasing two-dimensional instability effects. However, it was known from theory that the high Mach limit was well above the incompressibility limit. This research shows that, at approximately Mach 3, the effect of increasing three-dimensional instability becomes predominant and accounts for the higher kinetic energy plot.

Other terms of importance are shown to approach the theoretical limit as Mach number goes to infinity. Parameter growth rates are shown in Fig. 2.2.14 as they range from the incompressible limit to the high Mach limit.

Conclusions of R-RDT study: Our compressible RDT analysis adequately captures the features at incompressible and high Mach number limits. Comparisons show good agreement with incompressible RDT calculations with different types mean flows. High Mach number limits are also well predicted by our RDT calculations. Most importantly, it is shown that the turbulence is stabilized at intermediate Mach numbers due to compressibility effects. This observation and further investigation of the underlying physics leads to the rapid pressure-correlation models outlines in a later sub-section.

2.2.2.2 Favre-averaged RDT

Reference:

1) S. Suman, S. S. Girimaji, H. Yu and T. Lavin. 'Rapid distortion theory for density weighted fluctuations,' submitted to ***Journal of Fluid Mechanics***, 2009.

2) **S. Suman, S. S. Girimaji and R. Bertsh.** 'Homogeneously-sheared compressible turbulence at the rapid distortion limit: Interaction between velocity and thermodynamic fluctuations,' submitted to ***Flow, Turbulence and Combustion***, 2009.

$$\Lambda = \frac{1}{Sk}\frac{dk}{dt}$$

$$\Gamma = \frac{1}{S<\rho T>}\frac{d<\rho T>}{dt}$$

$$\Pi = \frac{1}{S<T^2>}\frac{d<T^2>}{dt}$$

$$\Phi = \frac{1}{S<\rho^2>}\frac{d<\rho^2>}{dt}$$

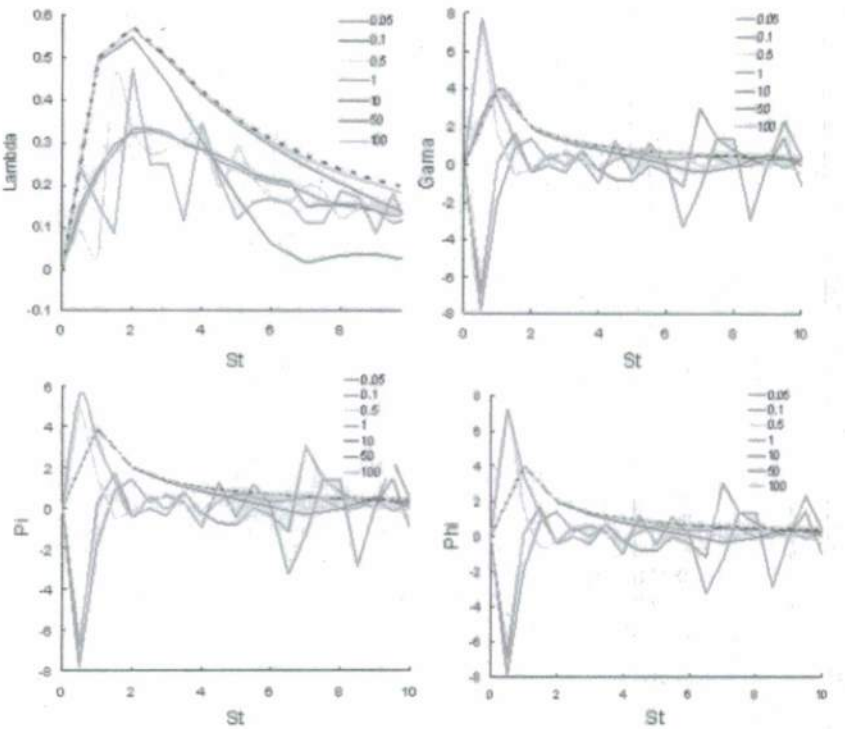

Figure 2.2.15 - Non-dimensional growth rates (high Mach limit): dashed line – high Mach limit

Motivation: Near all of the practical compressible turbulence calculations are performed using Favre-averaged Navier-Stokes equations. The model development is however guided by Reynolds-averaged RDT. As Reynolds and Favre-averaged RDT can potentially lead to large differences, it is imperative to develop Favre-RDT.

Objective: The objective of this project is to derive and analyze the linear Favre-RDT equations to aid in compressible turbulence closure model development.

Approach: Primary variables of interest are: $\langle \rho u_i'' u_j'' \rangle$, $\langle \rho T u_i'' \rangle$, $\langle \rho''^2 \rangle$ and $\langle \rho' u_i'' \rangle$. To obtain these values, many other terms must be included in the calculation. This is the first known attempt by any research group to obtain such values for compressible flows. Preliminary derivation shows that 128 equations that must be simultaneously solved, an inherently more complex problem to solve, but a methodology which will ultimately yield the results that are more telling about the flow. The details can be found in the reference listed above. Here we will summarize the conclusions.

Key results and Conclusions:

1) The difference between R-RDT and F-RDT stresses is small at small gradient Mach Numbers and substantial at large gradient Mach number.
2) The difference between R-RDT and F-RDT thermodynamic statistics is large at all gradient Mach numbers.
3) F-RDT captures the key polytropic index behavior precisely whereas R-RDT behavior is completely incorrect.
4) The qualitative aspects of F-RDT and R-RDT in terms of equi-partition between dilatational kinetic and internal energies are similar.

The overall inference is that for high-Mach number flows with heat release, F-RDT must be used for guiding turbulence closure models rather than R-RDT.

2.2.3 Non-linear analysis of velocity-gradients

Turbulence is dominantly a non-linear flow phenomenon. As mentioned in the previous sub-section, the driving force is the linear production term. The non-linear processes represent the fluctuating field response to the forcing. Here, we present two models for the non-linear processes

2.2.3.1 Homogenized Euler Equation

References:

1) S. Suman and S.S. Girimaji, 'Homogenized Euler Equation: a model for compressible velocity gradient dynamics,' ***Journal of Fluid Mechanics***, Vol. 620, pp. 177-194 (2009)
2) R. Bikkani and S. S. Girimaji, 'Role of pressure in velocity gradient dynamics,' ***Physical Review E***, Vol. 75, 3 (2007)

Motivation and Objectives: In this work we seek insight into the major non-linear processes in turbulence. We study the evolution of the velocity gradient tensor in a compressible flow field wherein density and temperature variations are expected to influence turbulence. An insight into the structure of the velocity gradient in turn offers valuable information about dilation, energy cascading direction and vortex stretching tendencies of the flow field. The inviscid assumption not only simplifies the governing equations, but it renders the results more attributable to the combined effects of compressibility and the non-linear inertial term. Furthermore, all higher spatial derivatives of the velocity gradients are neglected to close the set of equations.

Approach: The details are given in the listed references. We present a short description of the methodology. We start with a definition of the various terms and equations used in this analysis.

Symbols

ρ : Density T : Temperature u_i : Velocity component R: Gas Constant

$$A_{ij} = \frac{\partial u_i}{\partial x_j} \qquad \frac{\partial^2 (\ln \rho)}{\partial x_i \partial x_j} (= B_{ij})$$

$$\frac{\partial (\ln \rho)}{\partial x_i} (= C_i) \qquad \frac{\partial^2 T}{\partial x_i \partial x_j} (= D_{ij}) \qquad \frac{\partial T}{\partial x_i} (= E_i)$$

$$\varepsilon = \sqrt{A_{mn}A_{mn}} \qquad a_{ij} = \frac{A_{ij}}{\varepsilon} \qquad R_c = \frac{1}{\varepsilon}\frac{d\varepsilon}{dt}$$

Evolution Equations

$$\frac{dA_{ij}}{dt} = -A_{kj}A_{ik} - \left(B_{ij}RT + E_i C_j R + D_{ij}R\right) \qquad (1) \quad 9 \text{ Equations}$$

$$\frac{dT}{dt} = -T(\gamma-1)A_{ii} \qquad (2) \quad 1 \text{ Equation}$$

$$\frac{dB_{pq}}{dt} = -A_{ip}B_{iq} - A_{iq}B_{pi} - \underline{\frac{\partial^2 A_{ip}}{\partial x_i \partial x_q} - E_i\frac{\partial A_{ip}}{\partial x_q}} \qquad (3) \quad 6 \text{ Equations}$$

$$\frac{dC_i}{dt} = -A_{ji}C_j - C_i(\gamma-1)A_{ii} - \underline{T(\gamma-1)\frac{\partial A_{kk}}{\partial x_i}} \qquad (4) \quad 3 \text{ Equations}$$

$$\frac{dD_{pm}}{dt} = -A_{km}D_{pk} - \frac{\partial A_{jp}}{\partial x_m}C_j - A_{jp}D_{jm} - D_{pm}(\gamma-1)A_{ii} - \underline{C_p(\gamma-1)\frac{\partial A_{ii}}{\partial x_m} - C_m(\gamma-1)\frac{\partial A_{ii}}{\partial x_p}} \qquad (5) \text{ 6 Eqns.}$$

$$\underline{-T(\gamma-1)\frac{\partial^2 A_{ii}}{\partial x_p \partial x_m}}$$

$$\frac{dE_p}{dt} = -A_{ip}E_i - \underline{\frac{\partial A_{ip}}{\partial x_i}} \qquad (6) \quad 3 \text{ Equations}$$

All underlined terms have been neglected.

Solution procedure:

1) Each evolution equation represents the rate of change of the relevant quantity following a fluid element (Lagrangian reference frame).
2) All 28 ordinary differential equations are integrated simultaneously using fourth order Runge-Kutta technique. Computation is done with non-dimensionalized velocity gradients, a_{ij}, as A_{ij} diverges in finite time. Time marching is pursued until a_{ij} reaches its asymptotic state.
3) Initial conditions for the 28 quantities are obtained from the DNS database of a compressible, turbulent flow field so that each participating term in the evolution equation of A_{ij} asserts its influence realistically.
4) Independent computations are performed for several sets of initial conditions ('several particles').

Key Results:

1) Both compression and expansion have been observed for compressible turbulence. Almost 10 percent of the particles expand ($a_{ii}>0$) while the majority of the particles

contract (a_{ii}<0). Fig. 2.2.16 shows the variation of dilatation with normalized time for a few particles representing the sets of expanding and contracting particles.

2) All the expanding particles are observed to be undergoing reverse energy cascading in asymptotic state as indicated by the small negative value of R_c (Fig. 2.2.17). The contracting particles, in contrast, exhibit forward energy cascading throughout. This correlation between dilation and the direction of energy cascading in asymptotic state has been observed for all the particles without an exception.

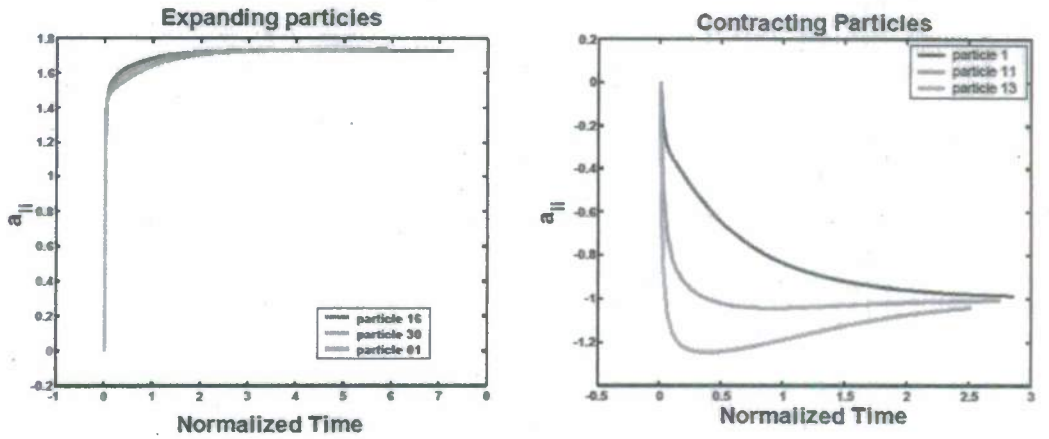

Fig. 2.2.16 Variation in particle dilatation.

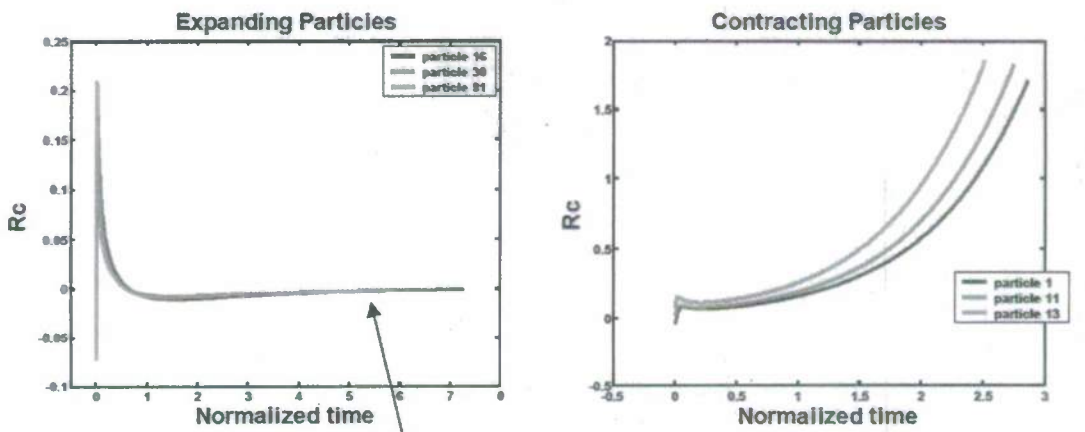

Fig. 2.2.17 Variation in R_c : Indication of the direction of energy cascading

3) Fig. 2.2.18 plots the contribution of the triple moment term $\left(-\frac{A_{mn}A_{kn}A_{mk}}{\varepsilon^2}\right)$ to R_c and the variations suggest that the internal geometry itself may be the dominant factor –as compared to the density and temperature gradient terms- deciding the energy cascade direction for a particle.

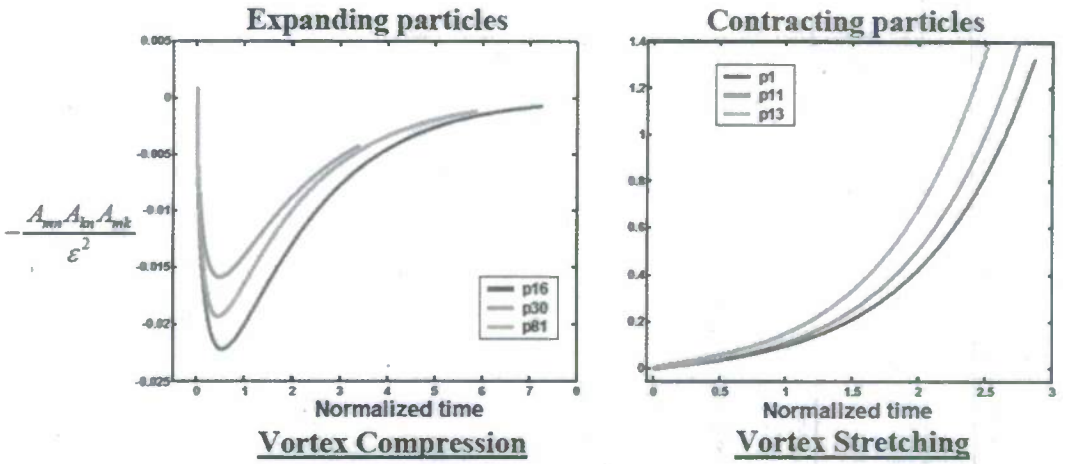

Fig. 2.2.18 Contribution of the triple moment term to R_e

4) The asymptotic principal strain rates for the particles show close agreement with the analytical solutions of the Burgers equation. Fig. 2.2.19 substantiates this claim for the expanding particles. Similar agreement has been observed for the contracting particles.

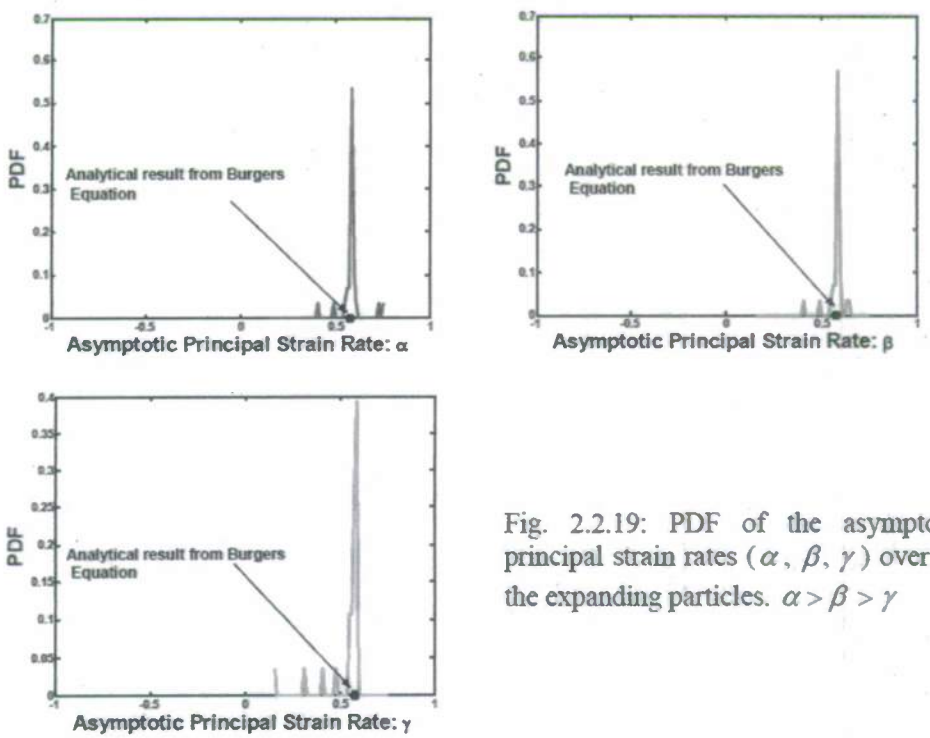

Fig. 2.2.19: PDF of the asymptotic principal strain rates (α, β, γ) over all the expanding particles. $\alpha > \beta > \gamma$

5) Fig 2.2.20 plots the alignment tendencies of the vorticity vector with the principal strain rates. For expanding as well as contracting particles, this tendency seems equi-probable with respect to α and β. This behavior is different from that observed in the

incompressible turbulence field where the asymptotic vorticity vector shows a distinctly higher preference to align with β.

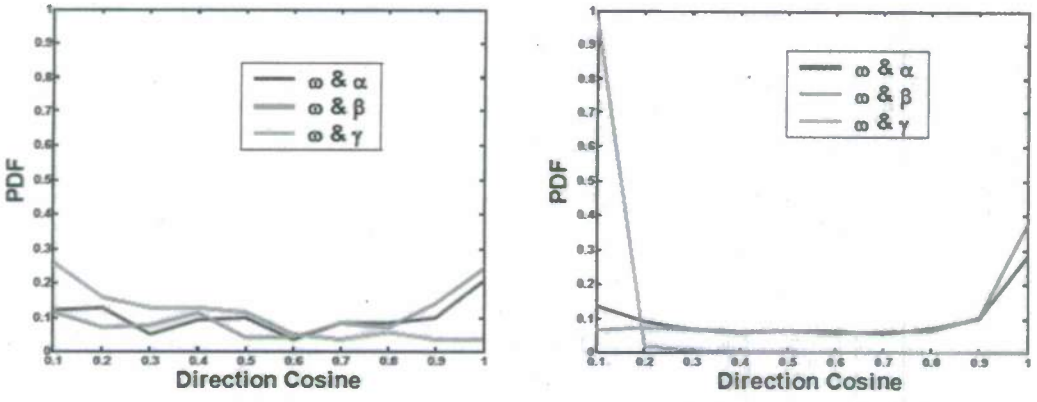

Fig. 2.2.20 Orientation of vorticity vector with respect to the principal strain rates

Conclusions: The main conclusions of the study are:

1) The solenoidal part of the velocity field agrees well with known features of incompressible turbulence cascade physics. The magnitude of strain rate eigen-values and the orientation between the strain rate eigen-vectors and vorticity vector are well captured.
2) The dilatational part of the velocity field is in good agreement with the solution of Burgers equation which can be considered as the infinite Mach number limit of Navier-Stokes equation. The flow physics in this case is dominated by the formation of shocklets.
3) It is shown that with increasing Mach numbers, the turbulence cascade mechanism goes from that is dominated by vortex stretching to one that is controlled by self-straining. Thus, it appears that there is a clear difference in the cascade mechanisms of incompressible and hypersonic turbulence.

Notwithstanding the simplifying assumptions made in the beginning, this study has highlighted some of the important compressible turbulence features which are in contrast with the known incompressible turbulence behavior. The accumulated knowledge and understanding are expected to help development of better dissipation models for compressible flow fields.

2.2.3.2 Enhanced Homogenized Euler Equation (E-HEE)

Reference: Sawan Suman, Ph.D. Thesis (2009) and manuscript (under preparation).

Motivation: While the homogenized Euler equation (HEE) reproduces many aspects of compressible velocity-gradient dynamics seen in DNS, it does not account for two important effects: (i) pressure effects in controlling dilatation and (ii) viscous and other transport effects. These phenomena are crucial for accurately capturing all compressibility effects.

Objective: The objective of this work is to systematically account for the (i) behavior of the trace of the pressure Hessian and (ii) all transport effects.

Approach: The pressure Hessian trace evolution is modeled with a simple exponential relaxation model. This guarantees that the trace approaches the value specified by the Poisson equation with a time scale that is inversely proportional to the Mach number. At small Mach numbers, the trace almost instantly takes the Poisson value leading to incompressible flow dynamics. At large Mach numbers, however, the relaxation is slow and compressibility effects come into play. The transport term is modeled using an IEM (Interaction by Exchange with Mean) model. Such an approach has been very successful in many incompressible flow applications and in principle should be valid for compressible flows as well.

Key results: The important results presented in the references are summarized here:

1) The evolution of kinetic energy and dissipation is well reproduced by the model.
2) The dilatation kinetic energy is qualitatively captured.
3) The behavior of the skewness and flatness are captured well at early times. At large times, the variance decreases more rapidly that the skewness or flatness.

Future work must address the asymptotic behavior.

2.2.4 Averaging Invariance of compressible flows

Reference:

Suman and S. S. Girimaji. 'Averaging invariance property of Favre-filtered compressible Navier-Stokes equation,' Submitted, 2009

Motivation and objective:

Filter invariance property of Navier-Stokes equation is critical for hybrid-calculations and has been shown for incompressible flows by Germano (1992). Extension of this compressible Navier-Stokes (cNS) is rendered difficult due to the increase in the flow The goal of this work is to formalize the filter-invariance property of cNS in its most general form.

Approach: The details are given in the above paper. Here we present a brief summary starting with the evolution equations of relevance.

This requires the definition of two types of generalized central moments (GCM): density weighted GCM and mixed GCM

$$\tau_D(\phi_1,\phi_2) \triangleq \{\phi_1\phi_2\} - \{\phi_1\}\{\phi_2\}$$

$$\tau_M(\phi_1,\phi_2) \triangleq \{\phi_1\phi_2\} - \{\phi_1\}\langle\phi_2\rangle$$

Now, starting from the instantaneous equations, the scale invariant compressible Navier-Stokes equations can be derived.

Summary and conclusions: In summary, the filter-invariance property of compressible Navier-Stokes equation has been demonstrated and the specific forms of the generalized moments have been identified.

2.2.5 Closure Model Development (S. S. Girimaji)

References: MS thesis of Tucker Lavin and manuscripts under preparation.

Motivation: Pressure-strain and pressure-dilatation closure models hold the key to the success of a compressible turbulence CFD calculation.

Objective: The objective of this work is to develop high-fidelity closure models using the insight developed by the physics investigation studies.

Approach: Previously we have performed a thorough analysis and pre-modeling of the various physical processes of importance in compressible turbulence. We will use the rapid distortion studies in the development of the rapid pressure correlations. For slow pressure correlations, we use the insight gained from the DNS studies of decaying anisotropic compressible turbulence with and without heat release.

In Fig. 2.2.21 we summarize the thermodynamics-flow interaction as gleaned from our RDT and DNS studies.

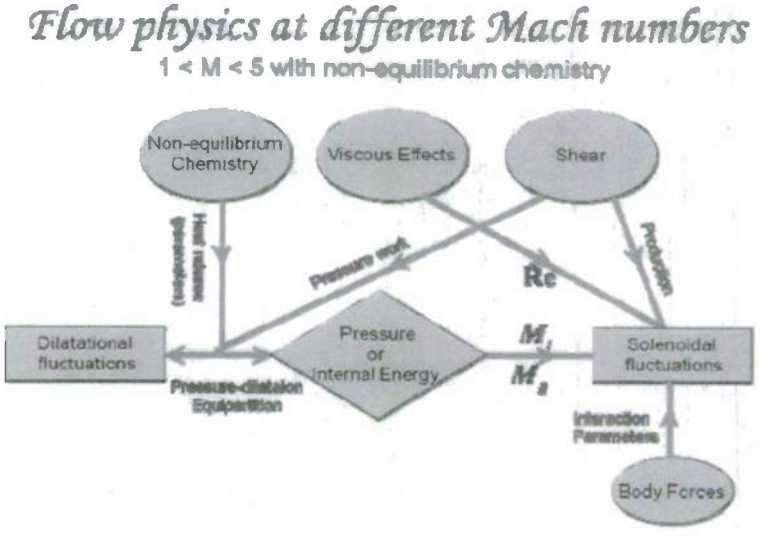

Fig. 2.2.21 Thermodynamics-Flow interactions

The actions of the various physical processes are clearly identified. It is evident that heat release and other high speed effects (an in a non-equilibrium hypersonic flow) produces only dilatational kinetic energy. Further there is equi-partition between dilatational kinetic energy and incremental internal energy contained in pressure/temperature fluctuations. The role of pressure-dilatation is merely to bring about this equi-partition. Heat release and other high speed effects modify the solenoidal energy only via the action of pressure. The behavior of pressure and its effect on the solenoidal velocity field depends on the Mach number.

Rapid pressure-strain correlation model proposal: From the RDT study, we propose the following model (Table 2.2.2) for rapid pressure-strain correlation at different Mach number regimes.

Rapid Pressure Modeling suggestions from physics study

Hypersonic Mach numbers $\tau_{shear} \ll \tau_{acoustic}$

$\langle ps_{ij} \rangle \approx \langle pd \rangle \approx 0$

Supersonic Mach numbers $\tau_{shear} \approx \tau_{acoustic}$

$\langle ps_{12} \rangle \approx P_{12} \rightarrow \langle u_1 u_2 \rangle$;.....$\langle pd \rangle \approx -\langle ps_{22} \rangle \rightarrow$ *equipartion*

Subsonic Mach numbers $\tau_{shear} \approx \tau_{acoustic}$

$\langle ps_{12} \rangle \approx 0 \rightarrow \langle u_1 u_2 \rangle - (-)ve$;.....$\langle ps_{11} \rangle \approx -\langle ps_{22} \rangle \rightarrow \langle u_2 u_2 \rangle \approx 0$

Table 2.2.2 Rapid pressure effects in various Mach number regimes

Slow Pressure-strain closure model proposal: Based on our DNS studies (Ph.D. thesis of Lee and papers therein), we suggest the following:

1) Even in the presence of heat release, the effect of slow pressure-dilatation is to bring about equi-partition between dilatational kinetic energy and incremental internal/potential energy.
2) Even at high turbulent Mach numbers, the solenoidal portion of the turbulence field returns to isotropy at eddy-turn over time scale.
3) The dilatational fluctuations return to isotropy at a rate dictated by the Mach number or acoustic timescale.

2.2.6 Preliminary RANS and PANS computations

Our goal is to develop turbulence closure models employing the model proposals resulting from our physics investigation studies. These models can be at several different levels of sophistication. High-fidelity models are under development and that will proceed beyond the MURI dates. Our preliminary computations are based on a low-level model. Here we employ a realizable two-equation model and incorporate the most basic compressibility effects. The realizability-based compressible flow two-equation model (developed as a part of Lakshmipathy's thesis) is given by:

$$C_\mu = 0.12 \qquad for\ C_{comp}\frac{Sk^{3/2}}{a\varepsilon} \geq 5.0$$

$$C_\mu = 0.0 \qquad for\ 1.5 \leq C_{comp}\frac{Sk^{3/2}}{a\varepsilon} < 5.0$$

$$C_\mu = MIN\left(2.0\left(\frac{\varepsilon}{kS}\right)^2, 0.09\right) \qquad for\ C_{comp}\frac{Sk^{3/2}}{a\varepsilon} < 1.5$$

from which the turbulent viscosity is computed using:

$$\nu_t = \rho C_\mu \frac{k^2}{\varepsilon}$$

This C_μ modification calls for a corresponding modification in the transport coefficients to preserve the log-law slope and boundary layer thickness:

$$\sigma_\varepsilon = \frac{\kappa^2}{\sqrt{C_\mu}(C_{\varepsilon 2} - C_{\varepsilon 1})}$$

where κ=0.41, $C_{\varepsilon 1}$=1.44, $C_{\varepsilon 2}$=1.92

This model predicts the M=2.2 and 7.2 boundary layers very accurately. In these cases, the compressibility effects are quite minor and indeed the modification is not invoked much. This is consistent with known physics and model performance.

Next we attempt to compute medium and high-speed mixing layers Figures 2.2.22 to 2.2.27. In the medium speed case, the compressibility effects are minimal and both the standard and

modified models produce adequate agreement. However, in the higher speed case the stabilizing effect of compressibility comes into play. The standard model predicts very rapid mixing whereas the experimental data shows much slower mixing than the medium speed case. As seen from the figures, the modified model qualitatively captures the observed behavior. While further model calibration is needed, the qualitative features of the model are in excellent agreement with compressibility turbulence physics. In the future we plan to (i) develop more sophisticated algebraic stress models and (2) perform a more thorough validation study. All comparisons are with the experimental data of Goebel and Dutton (1991).

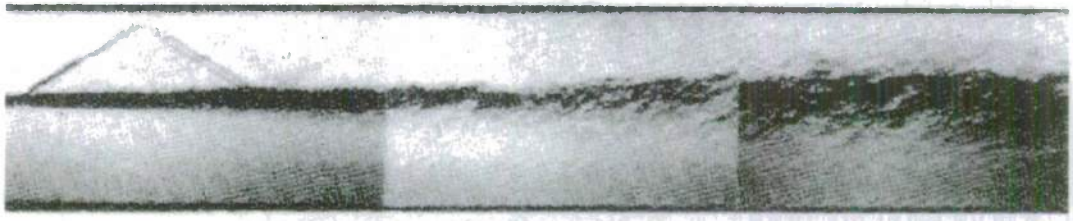

Fig.2.2.22 Schlieren Image of High-Speed Mixing Layer. Case-3 Goebel and Sutton (1991)

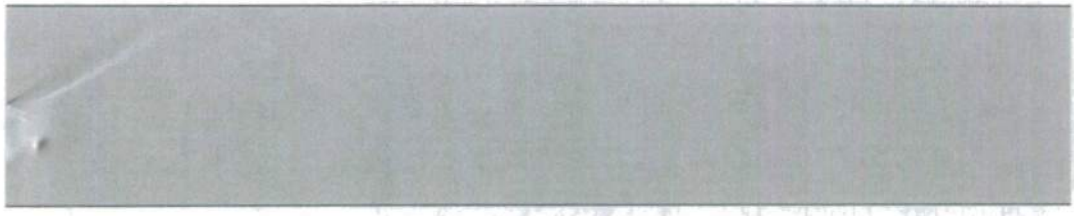

Fig. 2.2.23 Standard model Schlieren (mixing too rapid)

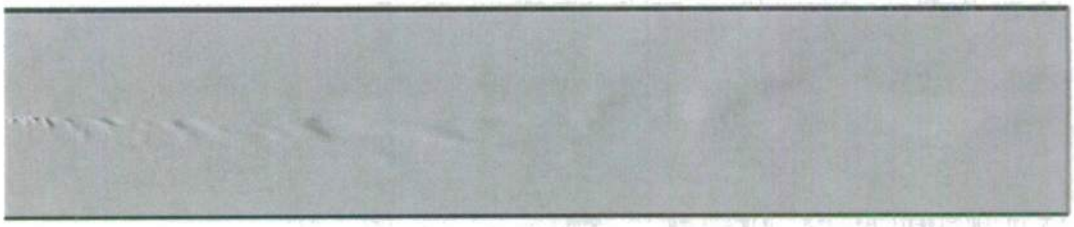

Fig. 2.2.24 Modified model Schlieren (reasonable mixing rate)

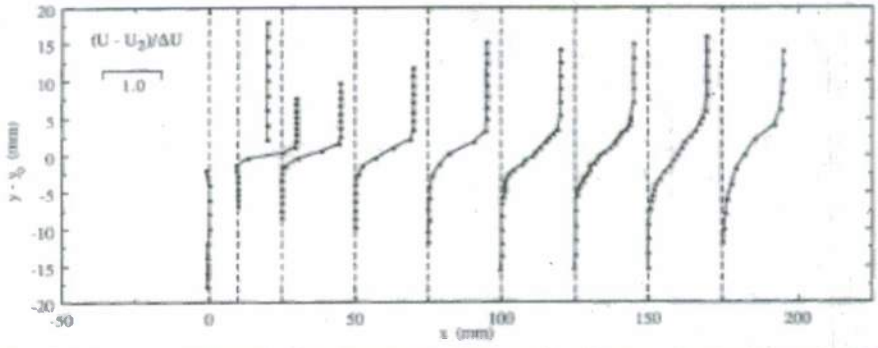

Fig. 2.2.25 Experimental Development of normalized mean streamline velocity

Fig.2.2.26 Standard model normalized mean streamlines (poor agreement)

Fig. 2.2.27 Modified model normalized mean streamlines (reasonable agreement)

2.2.7 Kinetic Theory Scheme for turbulence simulations

References:

1) S. S. Girimaji, 'Boltzmann kinetic equation for filtered fluid turbulence,' ***Physical Review Letters,*** Vol. 99, 3 (2007)
2) J. Kerimo and S.S. Girimaji, 'DNS of decaying isotropic turbulence with Boltzmann BGK approach,' ***Journal of Turbulence,*** Volume 8, Issue 46, Pages 1-16, (2007)

Motivation: This represents the most novel aspect of the MURI research. The motivation comes from the fact that many hypersonic flow problems are not amenable to continuum description and hence cannot be represented by the Navier-Stokes equations.

Objectives: Our goals are:

1) To develop a description of turbulence using the Boltzmann equation. Recall that the Boltzmann kinetic theory description of fluid motion is valid for continuum and non-continuum regimes.
2) Develop a Boltzmann-based CFD solver that can potentially incorporate non-continuum effects such as the lack of closed-form constitutive relation as well as moderate rarefied effects.

Accomplishments: The theoretical accomplishment is detailed in the Physical Review Letters paper shown above. This represents the first derivation of a complete kinetic theory description of turbulence. The second paper represents the first demonstration of the use of one class of Boltzmann-BGK CFD approach for computing turbulent flows. Much progress was made in this area and they are detailed in Section 3.

2.2.8 Turbulent energy flux model development for hypersonic flow (Bowersox)

The objective of this task was to develop a new framework for algebraic energy flux truncation modeling for high-speed shear flows. The flows are divided into following two classes:

(1) Flows in mechanical and thermal equilibrium, with caloric imperfections [follows from Bowersox (2009)]. The primary focus of this effort was to establish and validate the mechanics of energy flux modeling for hypersonic flows with relatively mild thermal effects. Hypersonic flow up to Mach 11.8 was examined.

(2) Thermal non-equilibrium flows in mechanical equilibrium (follows from Bowersox (2009a) and Bowersox et al (2008)). The primary goals of this effort are to determine the extent that thermal non-equilibrium alters the transport of turbulence and to examine the feasibility of extending the energy flux modeling mechanics to include thermal non-equilibrium flow.

A brief overview of the model development is presented below. Additional details are available in Bowersox (2009, 2009a), Bowersox et al (2008) and Fuller et al (2009).

Nomenclature

a	Speed of sound
a_1	Bradshaw-Townsend constant
a_{ik}	Algebraic energy flux turbulence model parameter
A^+	van Driest constant (=26.0)
b_i	Algebraic energy flux turbulence model parameter
B^+	Heat flux damping constant (=12.0)
C_μ	Turbulence modeling constant
C_p	Specific heat at constant pressure
C_v	Specific heat at constant volume
D	Turbulence diffusion
$D_{(n)(m)}$	Diffusion coefficient
$D[\overline{\rho}()]/Dt$	$\equiv[\overline{\rho}()]_{,t}+[\overline{\rho}()\tilde{u}_k]_{,k}$
$D[\overline{\rho()}]/Dt$	$\equiv[\overline{\rho()}]_{,t}+[\overline{\rho()}\tilde{u}_k]_{,k}$
e	Internal energy
d	van Driest Damping function, $1-e^{x_2^+/A^+}$
d_T	Turbulent Prandtl number correction factor, $1-e^{x_2^+/B^+}$
$\overline{\rho e'' u''_{k,k}}$	Energy dilatation
f_μ	Near wall (Low Reynolds Number) turbulence model correction
F_{Bi}	Body force vector
h	Enthalpy
$h^o_{f(n)}$	Heat of formation of fpecies n
$I_{(n)}$	Ionization energy of species n
$J_{(n)i}$	Mass diffusion vector of species n
$J^T_{(n)i}$	Turbulent mass diffusion of species n

q_i	Molecular heat flux vector ($=-kT_{,i}$)
q_i^T	Turbulent heat flux vector ($\equiv \overline{\rho h'' u_i''}$)
q_0^{0-0}	Energy exchange mechanism per unit mass
Q_0^0	Total energy exchange ($=\sum_m \rho_{(n)} q_{(n)}^{(m)-0} + Q_{rad(n)}^0$)
Q_{rad}	Energy exchange due to radiation
k	Thermal conductivity
k^T	Turbulence kinetic energy ($\equiv \overline{\rho u_k'' u_k''} / 2\overline{\rho}$)
p	Pressure
Pr_T	Turbulence Prandtl number
Pr_T^∞	Turbulence Prandtl number away from wall effects
R	Gas constant
S	Third order source/sink terms
t	Time
T	Temperature
u_i	Velocity component or vector
$u_{(\cdot)i}$	Molecular diffusion velocity
u_*	Friction velocity ($=\sqrt{\tau_w / \rho_w}$)
$\overline{u_i''}$	Mean Favre velocity fluctuation ($\equiv -\overline{\rho' u_i'} / \overline{\rho}$)
$\overline{u_i'' u_{k,k}''}$	Velocity dilatation
V	Turbulence moments involving molecular transport
x_i	Cartesian coordinates in indicial notation
W	Rate of energy exchange
Y	Mass fraction

Greek

δ_{ij}	Kronecker delta function
ε	Turbulence kinetic energy dissipation
ε_{ij}	Turbulence shear stress dissipation
γ	Ratio of specific heats ($=\overline{C}_p / \overline{C}_v$)
κ	Logarithmic velocity profile slope
κ_T	Logarithmic temperature profile slope
μ	Molecular viscosity
μ_T	Turbulent (eddy) viscosity
ϑ_i^T	Turbulence energy flux ($\equiv \overline{\rho e'' u_i''}$)
θ	Momentum thickness
ρ	Density
$\overline{\rho' u_{k,k}''}$	Density dilatation

τ_{ij}	Molecular shear stress $\{\mu[(u_{i,j}+u_{j,i})-\frac{2}{3}\delta_{ij}u_{k,k}]\}$
τ_{ij}^{T}	Turbulence Shear stress $(\equiv-\overline{\rho u_i'' u_j''})$
τ_{e^-}	Pressure gradient term time scale
τ_w	Wall shear stress
τ_u	Turbulence kinetic energy time scale $(=k/\varepsilon)$
τ_{vib}	Vibration-to-translation relaxation time scale
τ_ϑ	Energy flux time scale
σ_{ij}	$=-p\delta_{ij}+\tau_{ij}$
σ_ϑ	Algebraic energy flux model constant
σ_{e^-}	Algebraic energy flux model constant
$\dot{\omega}_{(n)}$	Mass source term for species n
ξ_1	Energy flux dissipation
$\tilde{\psi}_{,k}$	Defined mean flow gradient $(\equiv\tilde{e}_{,k}-\overline{p}\overline{\rho}_{,k}/\overline{\rho}^2)$
Υ_{ij}^{T}	Density strain $(=\overline{\rho' u_{i,j}''}+\overline{\rho' u_{j,i}''})$

Superscripts

(ex)	External energy mode
(in)	Internal energy mode
$()'$	Reynolds (time-averaged) fluctuation
$()''$	Favre (mass-weighted time averaged) fluctuation
$\overline{\ }$	Reynolds mean flow property
$\tilde{\ }$	Favre mean flow property

Subscripts

(e)	Electron
(h)	Heavy particles
i,j,k ...	Indicial notation
$,i$	Gradient in the x_i-direction
(n)	Species n
rad	Radiation
w	Wall condition
∞	Free stream value
$()()$	Indicial notation not implied
$()_o$	Stagnation property $[=()+\frac{1}{2}u_k u_k]$

2.2.8.1 Thermal equilibrium model

A description of the energy flux model derivation and validation is presented. Since the focus of this section is flows in thermochemical equilibrium; species and internal state sub- and superscripts are omitted from the nomenclature.

Transport equations

Most high-speed simulations are based on the Favre (1969) averaged conservation equations. For flows in thermochemical equilibrium, the two moments that require models are the turbulent shear stress $\tau_{ij}^T = -\overline{\rho u_i'' u_j''}$ and heat $q_i^T = \overline{\rho h'' u_i''}$; this is the case when the turbulent kinetic energy $k^T = \frac{1}{2}\overline{u_i'' u_i''}$ equation is combined with the averaged static energy equation to eliminate the dissipation and pressure fluctuation terms and the diffusion and convection of k^T are negligible in the resulting mean equation.

The modeling was performed on the energy flux $\vartheta_i^T = \overline{\rho e'' u_i''}$ transport equation. This choice over enthalpy was based on the elimination of ambiguous terms, such moments with the unsteady pressure. Also, the internal energy has proven to be the natural variable when characterizing the internal state of molecules. The energy flux is related to the turbulent heat (enthalpy) flux through the definition of the enthalpy as $q_i^T = \vartheta_i^T + \overline{p'u_i''} + \overline{p}\overline{u_i''}$. Taking moments between the energy and momentum equations resulted in the following transport equation

$$D\vartheta_i^T / Dt = \tau_{ik}^T \tilde{e}_{,k} - \vartheta_k^T \tilde{u}_{i,k} - \overline{\overline{p}(u_i'' u_{k,k}'')} - [\overline{(p'u_i'')} + \overline{u_i''}\,\overline{p}]\tilde{u}_{k,k} + \overline{p'e_j''} - \overline{e''}\,\overline{p}_{,j} + \overline{u_i''}(\overline{\tau}_{ik}\tilde{u}_{i,k} - \overline{q}_{m,m}) + \overline{e''}\,\overline{\tau}_{ik,k}$$
$$+\overline{\tau}_{ki}\overline{(u_i'' u_{k,j}'')} + \overline{(\tau_{ki}' u_i'')}\tilde{u}_{i,k} - \overline{(p'u_i'' u_{k,k}'' - \tau_{ki}' u_i'' u_{k,j}'')} - \overline{(p'e'')}_{,j} + \overline{\rho u_i'' e'' u_k''} + \overline{q_k' u_i'' - \tau_{ik}' e''})_{,k} - \overline{\tau_{ik}' e_{,k}''} + \overline{q_k' u_{i,k}''} \quad (1)$$

In this expression, the material on the left hand side is $D\vartheta_i^T / Dt \equiv \vartheta_{i,t}^T + (\vartheta_i^T \tilde{u}_k)_{,k}$; the over bar denotes a time-averaged quantity; the over tilde denotes a Favre averaged quantity, the superscript T denotes a turbulence moment; The double and single primes denotes a fluctuating quantity under Favre averaging and time averaging, respectively. The variables are defined as follows: ρ is the density; u_i is the velocity vector; p is the pressure; $\overline{\tau}_{ik}$ is the molecular shear stress tensor; e is the internal energy; h is the enthalpy, and $\overline{q}_k$ is the molecular heat flux vector. The physical interpretation of the terms in Eq. (1) follows from Launder (1988). The exceptions are compressibility terms; specifically, the third, fourth and sixth terms. Simplifications to eliminate the pressure fluctuations were performed using state equations.

For thermally perfect gases in thermal equilibrium with caloric imperfections, the caloric equations of state are functions of translational temperature. For most gases, $C_v' / \overline{C}_v << e'' / \tilde{e}$. Hence, $e'' \simeq \overline{C}_v T''$, where $\overline{C}_v$ is the value of the specific heat at the mean temperature $\tilde{T}$. Thus, the mean and fluctuating thermal equations of state reduce to

$$\overline{p} = (R / \overline{C}_v)\overline{\rho}\tilde{e} \quad ; \quad p' = (R / \overline{C}_v)(\tilde{e}\rho' + \rho e'') \quad (2)$$

Modeling simplifications

Simplifications to the energy flux transport equation

Equation (1) was simplified as follows. First, a model was derived for velocity dilatation by taking a moment of the fluctuating conservation of mass equation. Neglecting unsteady and third order terms, and simplifying with the identity $\overline{\rho}\overline{u_i''}+\overline{\rho u_i''}=0$, resulted in $\overline{\rho u_i'' u_{k,k}''} \simeq -\overline{\rho u_i'' u_k''}\overline{\rho}_{,k}/\overline{\rho}$ $+\tilde{u}_k\overline{\rho u_{,k}''}$, where $\tilde{u}_k\overline{\rho u_{,k}''}$ is expected to be small for shear layer flows. Neglecting this term ensured Galilean invariance. The resulting velocity dilatation model is

$$\overline{\rho u_i'' u_{k,k}''} \simeq \tau_{ik}^T \overline{\rho}_{,k}/\overline{\rho} \tag{3}$$

This relation is equivalent to the leading term in the Ristorcelli (1993) model. Comparison of Eq. (3) to the DNS, shown in Fig. 2.2.28(a), indicated the approximations were reasonable. Second, the term in the square brackets on the first line was reduced with the state equation to

$$\overline{p'u_i''} = -\overline{p}\overline{u_i''} + (R/\overline{C}_v)\vartheta_i^T \tag{4}$$

Third, the pressure scrambling term $\overline{p'e_j''}$ was estimated to be of second order diffusion by using the Eq. (2) to write $\overline{p'e_j''} = R[\overline{\rho}\overline{e''e_j''} + \tilde{e}\overline{\rho'e_j''}+]/\overline{C}_v$. The first term is a gradient of the energy variance. The second term was also shown to be proportional to gradients of statistical moments by approximating the internal energy and density fluctuations with a Taylor series; noting that $\overline{\rho'e''} = \overline{\rho'e'} = -\overline{\rho}\overline{e''}$ and assuming that statistical moments were approximately homogeneous. Thus, grouping the molecular correlations, triple correlations, diffusion and dissipation terms into $V_i^{\vartheta^T}$, $S_i^{\vartheta^T}$, $D_i^{\vartheta^T}$, and $\overline{\rho}\varsigma_i^{\varepsilon}$, respectively, Eq. (1) was written as

$$D\vartheta_i^T/Dt = \tau_{ik}^T\left(\tilde{e}_{,k} - \overline{p}\overline{\rho}_{,k}/\overline{\rho}\right) - \vartheta_k^T\tilde{u}_{i,k} - (R/\overline{C}_v)\vartheta_i^T\tilde{u}_{k,k} - \overline{e''}\,\overline{p}_{,i} + V_i^{\vartheta^T} + S_i^{\vartheta^T} + D_i^{\vartheta^T} + \overline{\rho}\varsigma_i^{\varepsilon} \tag{5}$$

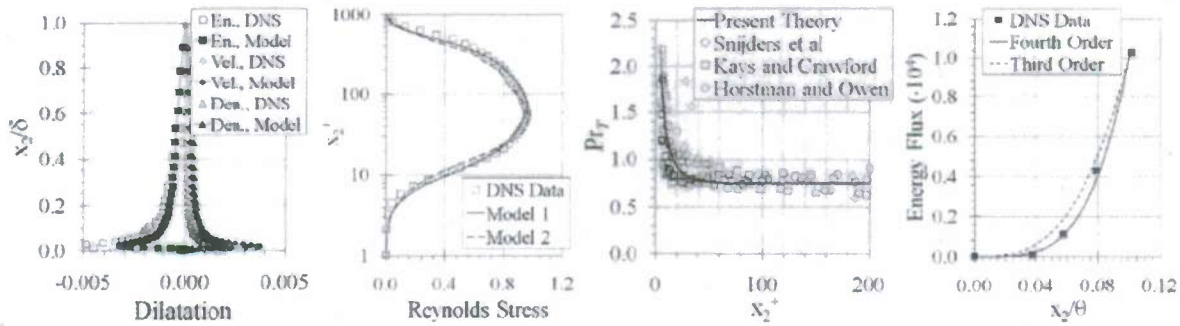

(a) (b) (c) (d)

Fig 2.2.28 Supporting evidence for model simplifications. (a) Comparison of the present velocity, energy and density dilatation models [Eqs. (3), (11)] to the DNS data of Pirozzoli et al (2004); (b) Comparison of the Reynolds stress correlations [Model 1: Eq. (15), Model 2: Eq. (17)], normalized by the wall shear stress, to DNS data; (c) Comparison of the modified turbulent Prandltl number [Eq. (18)] to the experimental data of Snijders et al (1983), Kays and Crawford (1993, includes flat plate, pressure gradient and blowing data) and Horstman and Owen (1972); (d) Near wall behavior of the energy flux, normalized by free stream values.

Algebraic energy flux model

An algebraic model for the energy flux was obtained by truncating Eq. (5) the following Girimaji and Balachandar (1998). To accomplished this, an energy flux correlation coefficient was defined $F_i = \vartheta_i^T / [(\overline{\rho} k^T)^{1/2} (\overline{\rho e''^2})^{1/2}]$. The weak equilibrium assumption implies that $DF_i / Dt = 0$. In this limit, it is also appropriate to assume that the molecular, triple, diffusion and dissipation terms are negligible. Performing the operations led to the following model

$$\vartheta_i^T / \tau_\vartheta \approx \tau_{ik}^T \tilde{\psi}_{,k} - \vartheta_k^T \tilde{u}_{i,k} - (R / \overline{C}_v) \vartheta_i^T \tilde{u}_{k,k} - \overline{e''} \overline{p}_{,i} \tag{6}$$

where

$$\tilde{\psi}_{,k} = \tilde{e}_{,k} - \overline{p}\overline{\rho}_{,k} / \overline{\rho}^2 = \tilde{h}_{,k} - \overline{p}_{,k} / \overline{\rho} \tag{7}$$

In Eq. (6), $\tau_\vartheta^{-1} = \frac{1}{2}[(P^{k^T} - \overline{\rho}\varepsilon) / \overline{\rho} k^T + (P^{\overline{e''^2}} + \overline{\rho}\chi) / \frac{1}{2}\overline{\rho e''^2}]$, where $P^{(\cdot)}$ denotes the production and χ is the dissipation rate for the energy fluctuation variance $\overline{e''^2}$. To build an algebraic model, the system was further simplified by interpreting τ_ϑ as an average of the relaxation time-scales of the kinematic and thermal variance fluctuating motions. Assuming that the thermal and kinetic energy fluctuation velocity scales were common resulted in $\tau_\vartheta \approx \sigma_\vartheta k^T / \varepsilon$, where σ_ϑ was added as an adjustable constant. With this simplification, Eq. (6) was reduced to

$$a_{ik} \vartheta_k^T = b_i \tag{8}$$

where

$$a_{ik} = \left[\tau_\vartheta^{-1} + (R / \overline{C}_v)\tilde{u}_{m,m}\right]\delta_{ik} + \tilde{u}_{i,k} \quad ; \quad b_i = \tau_{ik}^T \tilde{\psi}_{,k} - \overline{e''} \overline{p}_{,i} \tag{9}$$

Equation (8) was explicitly solved for ϑ_i^T via Cramer's rule. The determinant was approximated as τ_ϑ^{-3} for shear flows with a principal strain-rate; this helped to insure numerical stability.

To account for the second term on the right-hand-side of b_i in Eq.(9), a transport equation was derived for $\overline{e''}$ from the conservation of energy. The resulting equation is given by

$$D\overline{\rho e''} / Dt = -\overline{\rho}\tilde{e}_{,k}\overline{u_k''} + \vartheta_{k,k}^T - \overline{\rho u_k'' e_{,k}''} - \tau_{ik}^T \tilde{u}_{i,k} - \left(\overline{p\rho' u_{k,k}''} + \tilde{u}_{k,k}\overline{\rho' p'}\right) / \overline{\rho} + M \tag{10}$$

On the left-hand-side of this expression, $D\overline{\rho e''} / Dt \equiv (\overline{\rho}\overline{e''})_{,t} + (\overline{\rho}\tilde{u}_k\overline{e''})_{,k}$. The production and redistribution terms were listed on the right-hand-side; the molecular fluctuation terms were grouped in M. The second and third terms on the right-hand-side were expressed as $\vartheta_{k,k}^T - \overline{\rho u_k'' e_{,k}''} \approx \vartheta_k^T \overline{\rho}_{,k} / \overline{\rho} + \overline{\rho e'' u_{k,k}''}$ with the product rule. The approximation indicates that third order terms were neglected. To close the model, energy and density dilation models were derived following the arguments that led to Eq. (3).

$$\overline{\rho e'' u_{k,k}''} \simeq -\vartheta_k^T \overline{\rho}_{,k} / \overline{\rho} \quad ; \quad \overline{\rho' u_{k,k}''} \simeq \overline{u_k''} \overline{\rho}_{,k} \tag{11}$$

For the density dilatation, the fluctuating conservation of mass equation was multiplying by ρ' and averaged. A comparison these models to DNS data, shown in Fig. 2.2.28(a), indicated that the models were qualitatively correct. An algebraic model was derived for Eq. (10) by recalling that $\overline{\rho}\overline{e''} = -\overline{\rho' e''}$, which allowed for the definition of a correlation coefficient. Performing the operations led to $(\overline{\rho}\overline{e''}) \approx -[\tau_{ik}^T \tilde{u}_{i,k} + (\overline{\rho}\tilde{e}_{,k} + \overline{p}\overline{\rho}_{,k} / \overline{\rho})\overline{u_k''}]\tau_{e''}$, where $\tilde{u}_{k,k}\overline{\rho' p'}$ and M

were neglected. To close this term, a truncation model for the mean Favre velocity fluctuation was derived from the conservation of momentum. The transport equation is given by

$$D\overline{\rho}\widetilde{u_i''}/Dt = -\overline{\rho}\tilde{u}_{k,j}\widetilde{u_k''} + \overline{\rho u_i'' u_{k,k}''} - (\tau_{ik}^T\overline{\rho}_{,k} - \overline{p'\rho_{,j}'} - \overline{\tau_{ki,k}'\rho'})/\overline{\rho} + [(\overline{\rho' u_i'' u_k''} + \overline{p'\rho'})_{,k} + \overline{\rho}_{,k}\overline{\rho' u_i'' u_k''}/\overline{\rho}]$$

The second and third terms cancel under the assumptions that led to Eq. (3). Following the arguments that led to Eq. (5), the forth term was reduced to second order diffusion. Since, all three terms in this expression are diffusion, the algebraic truncation is is $(\tau_u \cdot \tilde{u}_{k,j} + \delta_{ik})\widetilde{u_k''} \approx D_u$, where D_u denotes the second order diffusion and third order source terms. This result suggested that the mean Favre fluctuation was of the order of diffusion for flows that meet the assumptions leading to Eq. (3). Thus, neglecting this term in the mean energy fluctuation equation resulted in the following expression for b_i

$$b_i = \tau_{ik}^T\tilde{\psi}_{,k} + \tau_{ki}^T\tilde{u}_{1,k}\overline{p}_{,j}\tau_{e^*}/\overline{\rho} \tag{12}$$

where $\tau_{e^*} \approx \sigma_{e^*} k^T/\varepsilon$, and σ_{e^*} is a mechanical non-equilibrium modeling constant.

The model constant σ_ϑ

To set the constant σ_ϑ, the model was examined in the logarithmic overlap region of a zero pressure gradient turbulent boundary layer. For a boundary layer flows, where the principal strain rate is given by $\tilde{u}_{1,2}$, the model reduces to

$$\vartheta_1^T \simeq \tau_{12}^T\tilde{h}_{,2}\tau_\vartheta - \tau_{22}^T\tilde{h}_{,2}\tilde{u}_{1,2}\tau_\vartheta^2 \quad ; \quad \vartheta_2^T \simeq \tau_{22}^T\tilde{h}_{,2}\tau_\vartheta \tag{13}$$

Combining Eq. (4) with $q_i^T = \vartheta_i^T + \overline{p'u_i''} + \overline{p}\widetilde{u_i''}$ resulted in $q_i^T = \gamma\vartheta_i^T$, where $\gamma = \overline{C}_p/\overline{C}_v$. Thus, in the near wall region, the energy equation reduces to

$$\vartheta_2^T \approx q_{wall}/\gamma \tag{14}$$

The time scale was estimated as $\tau_u = \mu_T / f_\mu C_\mu \rho k^T$, where f_μ is a near wall correction and C_μ is a constant set to 0.09. This relation results from the turbulence viscosity associated with k-ε models [Jones and Launder (1972)]. The Bradshaw et al (1967) model was used to further simplify the time-scale estimate. The relation was multiplied by the van Driest damping factor d to extend the applicability closer to the wall; i.e.

$$\tau_{12}^T \approx a_1 d\overline{\rho}k^T \tag{15}$$

In the above relation, $d = 1 - e^{-x_2^+/A^+}$, $y^+ = \rho_w u_\tau y/\mu_w$, $u_\tau = (\tau_w/\rho_w)^{1/2}$ and $A^+ = 26.0$. This relation is compared to DNS data in Fig. 2.2.28(b). With this, $\tau_u = a_1 d/f_\mu C_\mu \tilde{u}_{1,2}$. The gradient $\tilde{\psi}_{,2}$ was evaluated in the logarithmic region as $\tilde{h}_{,2} = -h_\tau/\kappa_T x_2$. Also, in the logarithmic region, $\tilde{u}_{1,2} = u_\tau/\kappa x_2$, and d and f_μ are both $\simeq 1$. Noting that $h_\tau/u_\tau = q_w/\tau_w$, then the energy flux relation was reduced to $\vartheta_2^T \approx -(\tau_{22}^T/\tau_w)(\kappa/\kappa^T)(a_1\sigma_\vartheta/C_\mu)\, q_{wall}$. The first factor was written as $-\tau_{22}^T/\tau_w = 1/\overline{u_2'^{+2}}$, which is approximately constant at 0.75 – 0.85 within the logarithmic region. Thus, equating this ϑ_2^T expression to Eq. (14) resulted in $\sigma_\vartheta \approx (C_\mu/\gamma a_1)(\kappa^T/\kappa)(1/\overline{u_2'^{+2}})$, where

$\kappa_T / \kappa \approx 1.1 - 1.2$ for gases, and $a_1 = 0.27 - 0.30$ for high Reynolds number boundary layers [Barrett and Hollingsworth (2003)]. With these values, $\gamma\sigma_\vartheta \approx 0.25 - 0.32$. Comparing with Launder's (1988) low-speed model, it is readily seen that C_T is equal to $\gamma\sigma_\vartheta$.

Discussion of the model

To better understand the differences between the present and gradient diffusion models, the two were set equal el for boundary layer flows. The analysis was facilitated by writing the turbulence viscosity as $\mu_T = f_\mu C_\mu \tau_{12}^T \tau_u / a_1 d$; this relation stemmed from the arguments in the previous section. Performing the operations led to

$$\mathrm{Pr}_T = -(\tau_{12}^T / \tau_{22}^T)(C_\mu / \gamma\sigma_\vartheta a_1)(f_\mu / d) \tag{16}$$

This expression was simplified with the following empirical relation

$$\tau_{12}^T / \tau_{22}^T \approx -C / d \tag{17}$$

where C is a constant and d is the van Driest damping factor. The van Driest damping factor was included to incorporate the correct near wall asymptotic behavior; that is, $u_1' \sim x_2$ and $u_2' \sim x_2^2$ [Lai and So (1990)]. With this behavior, $\tau_{12}^T / \tau_{22}^T \sim x_2^{-1}$ as $x_2 \to 0$. The van Driest damping factor has the correct asymptotic behavior near the wall; that is d scales with x_2 as $x_2 \to 0$. The constant C is nominally 0.6 to 0.8 for a number of shear flows. A comparison of Eq. (17) to DNS data, given in Fig. 1b, demonstrated that the model produced the correct behavior across the boundary layer including the near wall region. For this comparison, C was set to 0.68. The second factor in Eq. (16) is a constant, which is near unity for diatomic gases. Hence, a modified turbulent Prandtl number was derived as

$$\mathrm{Pr}_T \simeq \mathrm{Pr}_T^\infty / d_T \tag{18}$$

where, $\mathrm{Pr}_T^\infty \equiv CC_\mu / \gamma\sigma_\vartheta a_1$, which is a constant in the range of 0.6 – 1.0 for diatomic gases. The term in the denominator of Eq. (18) is given by quotient $d_T = d^2 / f_\mu$. Since f_μ is an empirical function used to correct the eddy viscosity near the wall, it was believed that this formulation may result in non-physical behavior. Hence, the following model was proposed: $d_T = 1 - e^{-y^+/B^+}$, where B^+ was selected at 12.0 to the data in Fig. 2.2.28(c). Also, based on the comparison, Pr_T^∞ was set to 0.75. The agreement between the model, labeled Present Theory, and the data was considered qualitatively good. Physically, these arguments suggest that the near wall behavior of the gradient diffusion and truncation models differ. Specifically, q_2 in the gradient diffusion model goes as x_2^3 as $x_2 \to 0$, where q_2 goes as x_2^4 for the truncation models. Applying a Taylor series to the enthalpy fluctuations in the near wall region indicates that the near wall scaling of q_2 goes as $f_1 x_2^3 + f_2 x_2^4$ [Abe & Suga (2000)]. Since the prefactor f_1 is proportional to the mean enthalpy gradient, the first term is zero for adiabatic wall flows. A comparison to DNS data supported the x_2^4 dependency (Fig. 2.2.28(d)). Apparently, based on the comparisons in Section 5, the latter term scaling also prevails for flows with heat transfer. Modifying Pr_T via eq. (18) produced the x_2^4 behavior.

Comment toward mechanical non-equilibrium

Mechanical non-equilibrium often results from streamline curvature driven pressure gradients, shock/expansion wave boundary layer interactions or surface roughness [Ekoto et al (2009)]. To appreciate the role of the pressure gradient terms, the model was simplified for the case of a two-dimensional variable pressure gradient boundary layer as follows

$$\mathcal{P}_1^T = [\tau_{12}^T(\tilde{h}_{,2} + \tau_\vartheta \tilde{u}_{1,2}\overline{p}_{,1}/\overline{\rho}) - \tau_{11}^T\overline{p}_{,1}/\overline{\rho}]\tau_\vartheta - (\tau_{22}^T\tilde{h}_{,2} - \tau_{12}^T\overline{p}_{,1}/\overline{\rho})\tilde{u}_{1,2}\tau_\vartheta^2 \quad ; \quad \mathcal{P}_2^T = (\tau_{22}^T\tilde{h}_{,2} - \tau_{12}^T\overline{p}_{,1}/\overline{\rho})\tau_\vartheta$$

To arrive at this form, it was assumed that the principal strain rate $\tilde{u}_{1,2}$ was much larger than the extra strain-rates and $\overline{p}_{,2} \approx 0$. The relative magnitude of the axial pressure gradient to the enthalpy gradient is apparent in the above expressions. Hence, quantifying the non-dimensional parameter $B \equiv \overline{\rho}^{-1}\overline{p}_{,1}/\tilde{h}_{,2}$ is sufficient to characterize the relative importance of the pressure gradient. For many shear layer problems, $B << 1$. For example, B varied from ~10^{-5} to ~10^{-3} for the largest pressure gradient studied by Huora and Nagano (2006), corresponding to a Clauser (1956) pressure gradient parameter of 4.0. Hence, the pressure gradient terms in Eqs. (7) and (12) were assumed negligible for most problems. An exception includes the possible strong gradients associated with high-speed flow. Moreover, at hypersonic conditions, the thermal gradients are reduced as the boundary layer thickness is increased with the Mach number. For the hypersonic expansion study of Bloy (1975), B was crudely estimated at ~0.1. The high Mach pressure gradient limitations of the present model require further study and calibration of σ_ϑ requires a specifically designed high Mach number experiment. Developing experiments for this validation purpose requires careful consideration as the energy flux relationship, and hence the model calibration, depends strongly on knowledge of the Reynolds shear stress. A comment towards extending the model to include pressure gradients and realistic hypersonic surface topologies is given in Section III.

Simulation methods

The above described equilibrium model provides the model basis, and extensions to include thermal and mechanical non-equilibrium effects are discussed in Sections II and III. However, before this, it was deemed necessary to examine the performance of the model with available data from the literature.

Heat flux models

The present algebraic model [Eqs. (8), (9) and (12)] with $\gamma\sigma_\vartheta = 0.28$], the present modified gradient diffusion model [Eq. (18), with $\mathrm{Pr}_T^\infty = 0.75$, $B^+ = 12$] and the standard gradient diffusion model, with $\mathrm{Pr}_T = 0.9$, were examined. The constants were set as follows: σ_ϑ was calibrated with the low-speed boundary layer (first) test case; Pr_T^∞ and B^+ were chosen based on Fig. 1c, and Pr_T was set to the value recommended by Launder (1976).

Reynolds stress model

Since the goal of the present study was the advancement of the heat flux model, the test cases were limited to zero pressure gradient flows, where an established two layer model for the Reynolds shear stress ($\tau_{12}^T = \mu^T \tilde{u}_{1,2}$) was available. The transverse normal stress τ_{22}^T was computed from the Reynolds stress with the empirical model described in Section 3.4; the quotient d^2 / f_μ was modeled as d_T. In the inner region, the turbulence viscosity was computed with Prandlt's (1904) mixing length model and the van Driest (1956) near wall damping function; that is, $\mu_i^T = \overline{\rho}\kappa^2 x_2^2 d^2 \tilde{u}_{1,2}$. In the outer region, Clauser's (1956) model was used with the Klebanoff (1955) intermittency correction; that is, $\mu_o^T = C_C \overline{\rho} U_e \delta_k^* \cdot [1 + C_K (x_2 / \delta)^{n_k}]^{-1}$, where δ_k^* is the kinematic displacement thickness. The model constants were set to established values in the literature. Specifically, $\kappa = 0.41$, $A^+ = 26.0$, $C_C = 0.018$, $C_\mu = 0.09$, $a_1 = 0.28$, $C = 0.68$, $n_K = 6.0$ and $C_K = 1.2$ [this constant was re-tuned to match Pirozzoli et al (2004) and Horstman and Owen (1972)]. The heat flux model time-scale was computed as described in Section 3.3.

Gas models

For the test cases presented here, the medium was air or helium. The air model was based on a mole fraction composition of 78% N_2, 21% O_2 and 1.0% Ar. The temperature dependency of the specific heats was computed following Vincenti and Kruger (1961). The enthalpy was computed with a curve fit that matched the theory to within ±0.12%. The viscosity was computed following Roy and Blottner (2006). The molecular thermal conductivity was computed as $k = \mu C_p / Pr$, where the molecular Prandtl number Pr was set to 0.71. Helium was treated as a calorically perfect gas. The viscosity was computed following Miller and Maddalon (1970). The molecular Prandtl number was set to 0.69.

Finite difference methods

The model assessment was performed using the two-dimensional boundary layer equations [Prandtl's (1904)]. An upwind finite difference scheme was used for the axial x1 derivatives, and central differences were used for the transverse x2 derivatives. To produce a stable solution, a downwind difference was used for the transverse mass flux in the conservation of mass equation. Variable grid spacing was used. A space-marching, predictor-corrector solution procedure was employed, where for the predictor step, the coefficients in the finite difference equations were evaluated using the solution from the previous plane. For the corrector step, the coefficients were evaluated with the results from the predictor step. The above algorithm was not fully implicit, where treating the turbulence a source reduced the stability of the program.

The solutions were initiated with a parallel flow laminar similarity solution at an axial location of 1.0% of the plate length or the transition location if provided. This was found to increase stability. An extrapolation boundary condition was used for the upper boundary. For the lower boundary, a no-slip, isothermal wall was enforced. The solutions were marched until the predicted momentum thickness matched that of the test case.

Grid convergence was ensured, where solutions were run on the following grids 7500 × 50, 15000 × 75 and 25000 × 100. The maximum difference between solutions on these grids was

0.25%, which was deemed acceptable for the model comparison studies. Consistency was validated with exact laminar similarity solutions, where solutions agreed to within 0.3%.

Model evaluation results

The model evaluation results are shown in Figs. 2.2.29 for zero pressure gradient boundary layers over a Mach number range of 0.02 to 11.8. The model constants for the shear stress and heat flux were fixed to the same values for all of the simulations. The primary model development test bed was the DNS data of Pirozzoli et al. (2004) shown in Figs. 2.2.29(a) and (b). The mean velocity profiles (Figs. 2.2.29(a)) for all of the models were in excellent agreement with the data. The constant turbulent Prandtl model temperature, $\theta = (T_w - \overline{T})/(T_w - T_\infty)$, results agreed well with the DNS data in the outer region. However, in the region between $x_2^+ = 10$ and 200, θ was under predicted, where the largest difference was about 15 percent. The temperature profiles for the modified turbulent Prandtl and the four algebraic models were within 3 percent of the DNS data across the entire boundary layer. Similar trends were observed when evaluating the models for the Mach 2.8 adiabatic wall experiments described in Bowersox (1996).

The comparisons of the modeled energy to the DNS data are given in Fig. 2.2.29(b). In addition to the numerical simulations, the model formulations were directly evaluated with the DNS data; these data are also included in Fig. 2.2.29(b). Focusing on the DNS evaluations (labeled DE), the Abe-Suga (2000) and Launder (1988) axial results agreed well with the data for

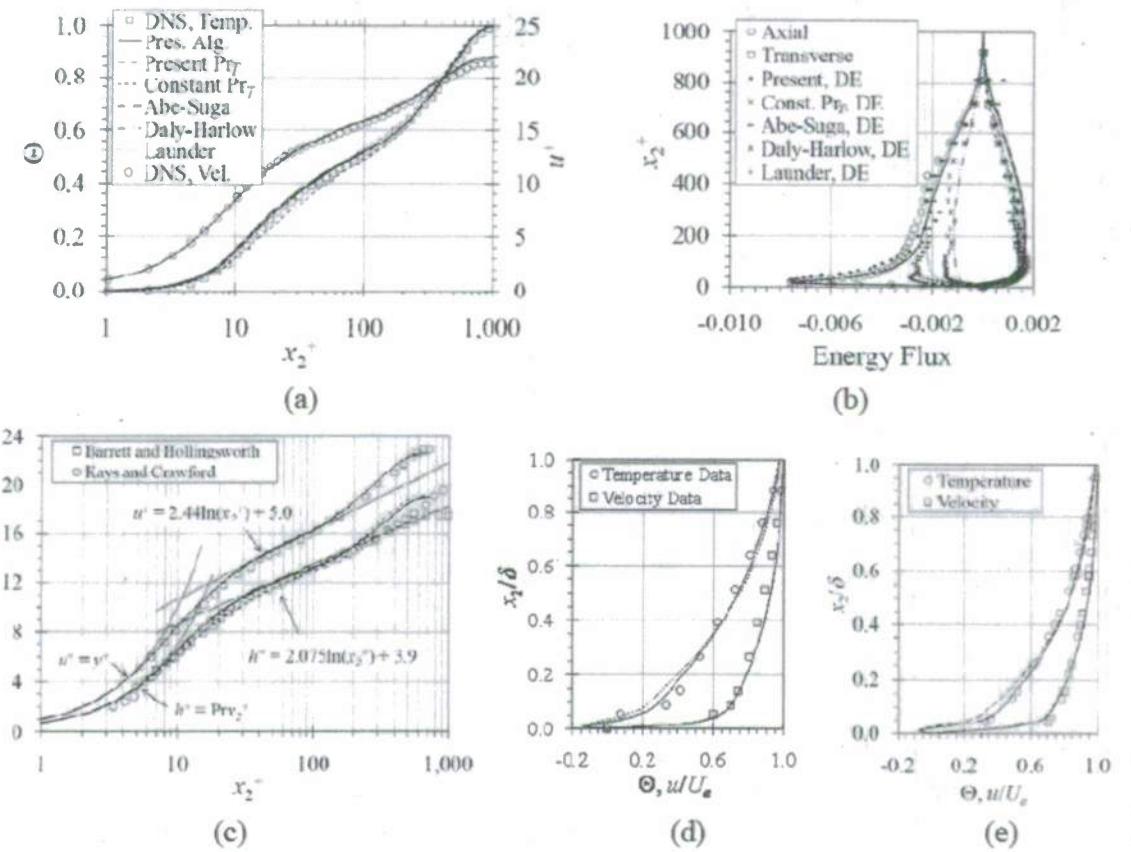

Figure 2.2.29 Model comparison. (a) DNS data of Pirozzoli et al (2004), M = 2.25, Air, T_w/T_{aw} = 0.52, Re_θ = 4,000. (b) DNS energy flux normalized by free stream conditions [legend continued from (a), DE indicates model evaluated with DNS data directly] (c) Low-speed boundary layer with heat transfer [Barrett and Hollingsworth (2003) and Kays and Crawford (1993)]. (d) M = 7.1, Air, T_w/T_{aw} = 0.52, Re_θ = 10,500 [Horstman and Owen (1972)], and (e) M = 11.8, He, T_w/T_{aw} = 0.56, Re_θ = 18,000 [Watson (1978)].

x_2^+ greater than about 100. Below this region, the models did not capture the observed peak. Abe-Suga (2000) showed slightly better results in this region as the model was adjusted to depend on the axial shear stress. The Daly-Harlow (1970) model under predicted the axial u_x across the boundary layer. Following the arguments in presented above, the near wall scaling for q_1 goes as x_2^3 for adiabatic wall flows. To achieve this scaling, the modeled axial component for the present model was divided by $1-e^{x_2^+/B_1^+}$, where B_1^+ was selected at 95 to capture the near wall peak shown in Fig. 2.2.29(b). This factor asymptotes to unity near x_2^+ = 250. With this correction, the present model agreed well with the data across the entire boundary layer. The corresponding numerical simulation axial results shown in Fig. 2.2.29(b) followed the trends established by the DNS model evaluations. The differences between the models for the transverse component were subtle, and the corresponding differences in the temperature profiles were the result of the near wall behavior described above. Similar agreement was seen for the experiments in Bowersox (1996).

The present and gradient diffusion models were also compared to the low-speed data of Barrett & Hollingsworth (2003) and Kays & Crawford (1993) in Fig. 2.2.29(c). The velocity profiles for the three models were in excellent agreement with the data. The present model temperature results were approximately 10 percent higher than the constant turbulent Prandtl model in the x_2^+ = 10 and 200 region. However, the experimental data spanned the model differences. The models were compared to the hypersonic data of Horstman & Owen (1972) and Watson (1978) in Figs. 2.2.29(d) and (e), respectively. The constant turbulent Prandtl number model temperature predictions were up to 20 percent off in the x_2/δ = 0.05 to 0.35 region of the boundary layer. The temperature profiles with the present models were in much better agreement across the entire boundary layer.

The Reynolds analogy was estimated for the present model as $2St/C_f \approx \kappa^T/\kappa$, where the Stanton number and skin friction coefficient are given by $q_w/\rho_e U_e(h_w - h_{aw})$ and $\frac{1}{2}\rho_e U_e^2$, respectively. The observed range of κ^T/κ is 1.1 to 1.2, which is consistent with a large volume of empirical data across a wide speed range [e.g., see Cary (1970)].

2.2.8.2 Toward modeling thermal non-equilibrium flows in mechanical equilibrium

The primary second-order moments that require modeling for thermochemical non-equilibrium are the Reynolds shear stress tensor $\tau^T_{(h)ij}$, the energy flux vectors $\mathcal{J}^{T(\alpha)}_{(h)i}$, $\mathcal{J}^{T(\alpha)}_{(e)i}$ and $\mathcal{J}^{T(i)}_{(n)i}$, and the turbulent species diffusion vector $J^T_{(n)i}$; the latter is omitted for flows without chemical reactions, which is the case described here. As indicated in the introduction, relaxation of an internal mode has the potential to alter the basic state of turbulence. However, this has yet to be shown

definitively. Experimental results from our laboratory are presented below that confirm the coupling. Hence, the algebraic models described in Section II were extended to include thermal non-equilibrium effects. The thermal non-equilibrium energy flux model derivation is a direct extension of the model derivation in the previous sections. The primary differences are (1) energy is split into an external mode and the various internal modes and (2) the state equation modifications to the resultant equation are extend to include thermochemical effects. The resulting algebraic models are written for thermal non-equilibrium.

Decaying mesh turbulence with vibrational non-equilibrium

Decaying mesh turbulence with vibrational non-equilibrium was studied to better appreciate the role of thermal non-equilibrium on the transport of turbulence. The basic question to be addressed was: *Does thermal non-equilibrium alter the basic transport of turbulence?*

To answer this question, the transport equation set was reduced to appropriate form for one-dimensional nearly homogeneous flow, where it is assumed that the mean velocity gradient, and Reynolds shear stresses are negligible.[1] To accomplish this, the Reynolds stress tensor and energy flux transport equations were re-derived and simplified with the appropriate state equations. Assuming that $\rho_{(e)} / \rho_{(h)} \ll 1$, which implies that $\rho \approx \rho_{(h)}$, simplifies the operations because this assumption allows the conservation of mass to be written as $\rho_{(h),t} + \left(\rho_{(h)} u_k\right)_{,k} = 0$ to eliminate terms when taking the moments.[2] The resulting equations for the energy fluxes and Reynolds axial stresses are summarized below:

$$\frac{D\mathcal{G}^{T(m)}_{(n)1}}{Dt} \approx \tilde{Y}_{(n)} \tau^{T}_{(h)11} \tilde{e}^{(m)}_{(n),1} + \rho_{(n)} \overline{q^{n(m)}_{(n)} u^{n}_{i}} - \frac{\tilde{Y}_{(n)} \tilde{R}_{(h)}}{\tilde{C}^{(tr)}_{v(h)}} \rho_{(n)} \overline{e^{n(\alpha)}_{(h)} e^{n(m)}_{(n),1}}$$

$$\frac{D\mathcal{G}^{T(\alpha)}_{(h)1}}{Dt} \approx \tau^{T}_{(h)11} \tilde{e}^{(\alpha)}_{(h),1} + \rho_{(h)} \overline{q^{n(\alpha)}_{(h)} u^{n}_{i}}$$

$$\frac{D\tau^{T}_{(h)(i)(i)}}{Dt} \approx \frac{2\tilde{R}_{(h)}}{\tilde{C}^{(\alpha)}_{v(h)}} \mathcal{G}^{T(\alpha)}_{(h)(i),(i)} + \overline{\rho}\varepsilon_{(i)(i)} - \frac{2\tilde{R}_{(h)}}{\tilde{C}^{(tr)}_{v(h)}} \overline{\rho e^{n(\alpha)}_{(h)} u^{n}_{(i),(i)}}$$

$$\frac{D\overline{\rho}k^{T}}{Dt} \approx -\frac{\tilde{R}_{(h)}}{\tilde{C}^{(\alpha)}_{v(h)}} \frac{\partial \mathcal{G}^{(\alpha)T}_{(h)1}}{\partial x_1} - \overline{\rho}\varepsilon$$

The parentheses on the coordinate direction subscript i in the Reynolds stress equation where added to indicate that summation was not implied. The postulated mechanism for the coupling between the internal energy and the turbulence transport is as follows. The molecular relaxations acts as a source or sink for $\mathcal{G}^{T(m)}_{(n)1}$ via the production (first term on the right-hand-side of the first equation above), which in-turn couples into the external energy flux through the exchange terms, and ultimately into the axial stresses and turbulent kinetic energy through the first terms on the right-hand-sides of the last two equations.

---

[1] This assumption is overly simplistic, but the underlying exchange mechanism is readily discerned.

[2] This assumption is not required to derive the transport equation.

A series of experiments were conducted as part of this project at *Texas A&M University* to provide an empirical database to aid in understanding and model turbulent flows with thermal non-equilibrium. In the first experiment, decaying mesh turbulence is coupled to a Capacitively-Coupled-RF (CCRF) plasma [Palm et al (2003)]. Plasma generation in long duration cold flow facilities was chosen so that large sample sets, for statistically converged measurements could be acquired with conventional laser diagnostics. Palm et al (2003) have shown that radio frequency plasma generators are effective at producing controllable degrees of molecular non-equilibrium of air. Following Kimmel (2003) and Palm et al (2003), a 2500W Cesar 1325 RF generator (13.56MHz) was used to produce vibrational temperatures on the order of 1200 - 2000K, while the translation and rotational temperatures remain close to room temperature. The experiments were designed to couple the plasma generator to basic turbulent flows so that the salient transport mechanisms could be interrogated. That is the, the turbulence and vibrational excitation decay rates were selected to be one the same order of magnitude. The results are described in Chapter 3. The experiments demonstrated that the decay rate of the turbulence was altered by the presence of the plasma. The Townsend-Batchelor (1943) exponent was observed to increase from 0.92 to 1.25 as the plasma power was increased from 0 to 300 W. Examination of the axial stress profiles showed that the transverse stress was unaffected, which suggested that transverse axial stress dissipation was unaffected and that $\overline{\rho e_{(h)}^{\prime\prime(\alpha)} u_{2,2}^{\prime\prime}}$ was negligible. If the flow is incompressible, then $\overline{\rho e_{(h)}^{\prime\prime(\alpha)} u_{k,k}^{\prime\prime}}$ is zero. Thus, it is reasonable to drop this term from each of the axial stress components. This simplifies the interpretation of the results and provides confidence in the proposed exchange mechanism.

Heavy particle energy flux models for thermal non-equilibrium flows

To arrive at the Favre averaged equations, the density weighting of the energy pools were defined in terms of the associated partial density. For example, $\tilde{e}_{(n)}^{(tn)} \equiv \overline{e_{(n)}^{(tn)} \rho_{(n)}} / \overline{\rho}_{(n)}$. With this definition, the usual advantages of Favre averaging remain prevalent. The mean density of species n is given by $\overline{\rho}_{(n)} = \overline{\rho} \tilde{Y}_{(n)}$. The energy flux is related to the turbulent heat flux by the definition of the enthalpy as $q_i^T = \mathcal{J}_i^T + \overline{p' u_i''} + \overline{p} \overline{u_i''}$.

It is assumed that each species in within the flow act as a thermally perfect gas. The thermal equation of state the mixture of is given by $p = \sum_{n \neq e} p_{(n)} + p_{(e)}$, where the heavy particle pressure is given by the first summation term. The heavy particle pressure is given by

$$p_{(h)} = \sum_{n \neq e} \rho_{(n)} R_{(n)} T = \frac{R_{(h)}}{C_v^{(\alpha)}} \rho_{(h)} e^{(\alpha)} \tag{19}$$

where $R_{(h)} = \sum_{n \neq e} Y_{(n)} R_{(n)}$. The corresponding equations for the each individual species are given by

$$p_{(n)} = \rho_{(n)} R_{(n)} T_{(n)} = \frac{R_{(n)}}{C_{v(n)}^{(\alpha)}} \rho_{(n)} e_{(n)}^{(\alpha)} \tag{20}$$

The state equations were Favre decomposed and used to simplify the resulting transport equations following the methods described in Section 2.2.4.

Transport equations for $\mathcal{J}^{T(ex)}_{(h)i}$ ($= \overline{\rho_{(h)} e^{n(ex)}_{(h)} u_i''} = \overline{\rho e^{n(ex)}_{(h)} u_i''}$) and $\mathcal{J}^{T(in)}_{(n)i}$ ($= \overline{\rho_{(n)} e^{n(in)}_{(n)} u_i''}$) were derived by taking moments between the energy and momentum equations. State equation simplifications were applied and algebraic truncation models were derived for both energy fluxes. The methods used were a direct extension of those described in Section 2.2.4.

The algebraic external energy flux model for molecular (thermal) non-equilibrium is similar to Eq. (8); that is

$$a_{ik} \mathcal{J}^{T(ex)}_{(h)k} = b_i \tag{21}$$

where

$$\tilde{\psi}_{,k} = \tilde{e}^{(ex)}_{(h),k} - \overline{p}\,\overline{\rho}_{(h),k} / \overline{\rho}^2_{(h)} = \tilde{h}_{(h),k} - \overline{p}_{,k} / \overline{\rho}_{(h)} \tag{22}$$

$$a_{ik} = \left[\tau_{\mathcal{J}}^{-1} + \tilde{R}_{(h)} / \tilde{C}^{(ex)}_{(h)v} \right] \delta_{ik} + \tilde{u}_{i,k} \tag{23}$$

$$b_i = \tau^T_{(h)ik} \tilde{\psi}_{,k} - \overline{e^{n(ex)}_{(h)}}\, \overline{p}_{(h),i} + \left\{ \overline{\rho_{(h)} u_i'' q^{n(ex)}_{(h)}} \right\} \tag{24}$$

The last term in b_i results from the energy exchange mechanism from the internal modes to the external model. Specifying a form for this term finalizes the model.

The algebraic internal energy flux model for species n for thermal non-equilibrium is given by

$$\left(\frac{\delta_{ik}}{\tau_{\mathcal{J}^{T(in)}_{(n)}}} + \tilde{u}_{i,k} \right) \mathcal{J}^{T(in)}_{(n)k} \approx \tilde{Y}_{(n)} \tau^T_{ik} \tilde{e}^{(in)}_{(n),k} + \overline{\rho_{(n)} q^{n(in)}_{(n)} u_i''} + \tilde{Y}_{(n)} \left[\frac{\overline{p}_{(h)}}{\overline{\rho}_{(h)}} \overline{\rho'_{(n)} e^{n(in)}_{(n),i}} - \frac{\tilde{R}_{(h)}}{\tilde{C}^{(tr)}_{v(h)}} \overline{\rho e^{n(ex)}_{(h)} e^{n(in)}_{(n),i}} \right] + \overline{\rho}_{(n)} \overline{q}^{(in)}_{(n)} \overline{u_i''} \tag{25}$$

To better see how the molecular time-scale inters into the equation, Eq. (25) is rewritten for the case of mild vibrational non-equilibrium, where the exchange between internal and external modes follows a Landau-Teller (1936) relaxation model. Assuming the last two terms are negligible for weak non-equilibrium (this implies that the argument in Section II may be reasonable here) results in the follow expression

$$\left[\left(\tau^{-1}_{\mathcal{J}^{T(ex)}_{(n)}} + \overline{\tau}^{(vib)-1}_{(n)} \right) \delta_{ik} + \tilde{u}_{i,k} \right] \mathcal{J}^{T(in)}_{(n)k} \approx \tilde{Y}_{(n)} \tau^T_{(n)ik} \tilde{e}^{(vib)}_{(n),k} + \mathcal{J}^{T(in)}_{(n)i,eq} / \overline{\tau}^{(vib)}_{(n)} \tag{26}$$

where $\tau^{(vib)}_{(n)} \approx C_{(n)1} e^{(C_{(n)2}/T_1)^{1/3}} / p$. Although this model is overly simplistic, it does clearly show how the molecular non-equilibrium couples into the internal energy flux, which in-turn couples into the external energy flux through the exchange terms.

Unfortunately, experimental data to validate the above modeling ideas for molecular non-equilibrium is apparently unavailable. Hence, the SISL experiments were designed and are underway to fill this void (see Chapter 3).

2.2.8.3 Conclusions

The objective of this study was to further develop algebraic models for the energy flux in high-speed shear flows. Algebraic truncation models were derived. The thermal equilibrium model appeared to provide significant improvements in the temperature predictions over the constant

turbulent Prandtl number model, when compared to experimental and DNS data over a Mach number range of 0.02 to 11.8. The improvements, up to 20 percent, occurred in the $x_2^+ = 10$ to 200 region of the boundary layer, and were most pronounced in the supersonic and hypersonic boundary layers. Analyses of the algebraic model resulted in a Reynolds analogy factor that was proportional to the ratios of the slopes of the temperature and velocity profiles in the logarithmic region of the boundary layer, which is consistent with numerous studies within the literature.

The inclusion of compressibility led to explicit pressure gradient dependency with the algebraic model. Analyses indicated that if $B \equiv \overline{\rho}^{-1}\overline{p}_{,1} / \tilde{h}_{,2}$ is small then the pressure gradient terms are negligible. For most flows, this parameter is very small, however for high-speed flow, this term may become significant. Additional experiments are required to better understand the pressure gradient limitations of the present models.

The algebraic model produced accurate predictions of the heat flux vector as compared to DNS results. An important inference from the analysis was that the near wall behavior of the algebraic model for q2 agreed with expected scaling, where the gradient diffusion model did not. This comparison led to a slight modification of the turbulent Prandtl number. Specifically, $\mathrm{Pr}_T \approx \mathrm{Pr}_T^{\infty} / d_T$, where Pr_T^{∞} is a constant near 0.75 and d_T is similar the van Driest damping function. The resulting model produced results that were in agreement with the algebraic model for the transverse component of the heat flux.

Relaxation of an internal mode was shown to alter the basic state of turbulence. Hence, algebraic models were derived to include thermal non-equilibrium effects. However, validation data for the models are lacking. Lastly, comments towards extending the models to include mechanical non-equilibrium relevant to hypersonic flow were presented.

References

1) Anderson, J., *Hypersonic and High Temperature Gasdynamics*, AIAA Education Series, DC, 1989.
2) Barrett, M. and Hollingsworth, K., "Heat Transfer in Turbulent Boundary Layers Subjected to Free-Stream Turbulence – Part 1: Exp. Results," *J. of Turbomach.,* Vol. 125, Apr., 2003, pp. 232 – 241.
3) Bertin, J., *Hypersonic Aerothermodynamics*, AIAA Education Series, DC, 1994.
4) Bloy, A., "The Expansion of a Hypersonic Turbulent Boundary Layer at a Sharp Corner," *JFM*, Vol. 67, part 4, 1975, pp. 647-655.
5) Bradshaw, P., Ferris, D. and Atwell, N., "Calculation of Boundary Layer Development Using the Turbulent Energy Equation," *Journal of Fluid Mechanics*, Vol. 28, Pt. 3, 1967, pp., 593-616.
6) Bowersox, R., "Extension of Equilibrium Turbulent Heat Flux models to High-Speed Shear Flows," *Journal of Fluid Mechanics*, Vol. 633, August, 2009, pp. 61-70.
7) Bowersox, R., "Algebraic turbulent energy flux models for hypersonic shear flows: Invited presentation," AIAA-2009-3724, AIAA 39th Fluid Dynamics Conference, San Antonio, TX, June 22-25, 2009a. *Progress in Aerospace Sciences*, In Review.
8) Bowersox, R., North, S. and Srinivasan,R., "High- Speed Free Shear Layers with Molecular Non-Equilibrium: An Example of the Fluids Information Triad (Invited)," AIAA-2008-685, 46th AIAA Aerospace Sciences Meeting and Exhibit, Reno, Nevada, Jan. 2008.

9) Candler, G., "Translation -Vibration – Dissociation Coupling in Non-equilibrium Hypersonic Flows," AIAA-1989-1739, AIAA, DC, 1989.
10) Cary, A., "Summary of Available Information on Reynolds Analogy for Zero-Pressure-Gradient, Compressible Turbulent-Boundary-Layer Flow," NASA TN D-5560, Washington DC, 1970.
11) Chien, K.-Y., "Predictions of Channel and Boundary-Layer Flows with a Low-Reynolds-Number Turbulence Model," *AIAA Journal*, Vol. 20, No. 1, 1982, pp. 33-38.
12) Clarke J. and McChesney M., *Dynamics of Real Gases*, Butterworths Scientific Publ., London, 1964.
13) Clauser, F., "The Turbulent Boundary Layer," *Advances in Applied Mechanics*, Vol. 14, Academic Press, New York, 1956.
14) Deiwert, S. and Candler, G., "Reacting Flows," *Special Course on Three-Dimensional Supersonic/Hypersonic Flows Including Separation*, AGARD Report No. 764, NASA Ames Research Center, Ames CA, 1989, pp. 8.1-8.28.
15) Ekoto, I., Bowersox, R., Beutner, T. and Goss, L., "Response of Supersonic Turbulent Boundary Layers to Local and Global Mechanical Distortions," *Journal of Fluid Mechanics*, Vol. 630, July, 2009, pp. 225-265.
16) Ekoto, I., Bowersox, R., Beutner, T. and Goss, L., "Supersonic Boundary Layers with Periodic Surface Roughness," *AIAA Journal*, Vol. 46, No. 2, Feb., 2008, pp 486-497.
17) Favre, A., "Statistical Equation of Turbulent Gases," in *Problems of Hydrodynamics and Continuum Mechanics*, SIAM, Philadelphia, PA, 1969.
18) Fuller, T., Hsu, A., Bowersox, R. and North, S., "The Effect of Vibrational Non-Equilibrium on the Decay of Grid Generated Turbulence," AIAA-2009-593, 47th AIAA Aerospace Sciences Meeting, Orlando, Florida, Jan. 5-8, 2009.
19) Girmaji, S. and Balachandar, S., "Analysis and Modeling of Bouyancy-Generated Turbulence Using Numerical Data," *Int. Journal of Heat and Mass Transfer*, Vol. 41, Nos. 6-7, 1998, pp. 915-929.
20) Gnoffo, P, Gupta, R. and Shin, J., "Conservation Equations and Physical Models for Hypersonic Air Flows in Thermal and Chemical Nnon-equilibrium," NASA Technical Paper 2867, Langley, VA, 1989.
21) Grabow and White, "A Surface Flow Approach for Prediction of Crosshatch Patterns," *AIAA J.*, Vol. 11, 1973.
22) Horstman, C. and Owen, F., "Turbulent Properties of a Compressible Boundary Layer," *AIAA J.* Vol. 10, No. 11, 1972, pp. 1418-1424.
23) Huora, T. and Nagano, Y., "Effects of Adverse Pressure Gradient on Heat Transfer in Thermal Boundary Layer," *Int. J. Heat and Fluid Flow*, Vol. 27, 2006, pp. 967-976.
24) Jones, W. and Launder, B., "The Prediction of Laminarization with a Two-Equation Model of Turbulence," *International Journal of Heat and Mass Transfer*, Vol. 15, 1972, pp. 301-314.
25) Kays, W. and Crawford, M., *Convective Heat and Mass Transfer, 3rd Ed.*, McGraw-Hill, New York, 1993.
26) Kimmel, R., AFOSR Contractors Meeting, San Destin, FL., Sept. (2003).
27) Klebanoff, P, "Characteristics of Turbulence in a Boundary Layer with Zero Pressure Gradient," NACA Report 1247, 1955.
28) Launder, B., "Heat and Mass Transport," in *Topics in Applied Physics, Turbulence*, ed. P. Bradshaw, Springer-Verlag, New York, 1976.

29) Launder, B., "On the Computation of Convective Heat Transfer in Complex Flows," *Trans. ASME*, Vol. 110, Nov. 1988, pp. 1112-1128.
30) Miller, C. and Maddolon, D., "Errors in Freestream Reynolds Number of Helium Wind Tunnels," *AIAA J.*, Vol. 8, No. 5, 1970, pp. 968-970.
31) Morkovin, M., "Effects of Compressibility on Turbulent Flows," *The Mechanics of Turbulence,* Gordon and Breach Science Publishers, New York, 1961.
32) Osipov, A., Uvarov, A. and Vinnichenko, N., "Influence of the Initial Vibrationally Non-equilibrium State of a Medium on the Structure of Von Karman Vortex Sheet," *Phys. Fuilds,* Vol. 18, 2006, p. 1 – 7.
33) Palm, P., Meyer, R., Plonjes, E., Rich, J. Adamovich, I., "Non-equilibrium Radio Frequency Discharge Plasma Effect on Conical Shock Wave: M = 2.5 Flow," *AIAA J.*, Vol. 41 No. 3, 2003, pp. 465-469.
34) Park, C., *Non-equilibrium Hypersonic Aerothermodynaamics*, John Wiley & Sons, New York, 1990.
35) Pirozzoli, S., Grasso, F. and Gatski, T., "Direct Numerical Simulation and Analysis of a Spatially Evolving Supersonic Turbulent Boundary Layer at M = 2.25," *Phys. of Fluids*, Vol. 13, No. 3, March 2004.
36) Pope, S., *Turbulent Flows*, Cambridge University Press, Cambridge, UK, 2000.
37) Prandtl, L., "Über Flüssigkeitbewegung bei sehr kleiner Reibung," *Proc. 3rd Int. Math. Congr.*, Heidelberg, 1904.
38) Ristorcelli, J., "A Presentation for the Turbulent Mass Flux Contribution to the Reynolds-Stress and Two-Equation Closures for Compressible Turbulence," NASA CR 191569/ICASE 93-88, NASA LaRC, Hampton VA, 1993.
39) Roy, C. and Blottner, F., "Review and Assessment of Turbulence Models for Hypersonic Flows," *Progress in Aerospace Sciences*, Vol. 42, 2006, pp. 469–530.
40) Scalabrin, L. and Boyd, I., "Development of an Unstructured Navier-Stokes Solver for Hypersonic Non-Equilibrium Aerothermodynamics," AIAA-2005-5203, AIAA, DC, 2005.
41) Snijders, A., Koppius, A, and Nieuwvelt, C., "An Experimental Determination of the Turbulent Prandtl Number in the Inner Boundary Layer for Air over a Flat Plate," *International Journal of Heat and Mass Transfer*, Vol. 26, No. 3, 1983, pp. 425-431.
42) Speziale, C., "Modeling of Turbulent Transport Equations," in *Simulation and Modeling of Turbulent Flows*, Ed. Gatski, T., Hussaini, M. and Lumley, J., Oxford University Press, New York, 1996.
43) Stock, "Patterns on Subiming and Liquifying Ablation Materials," *AIAA J.* 1975.
44) Tobak, "Hypothesis for the Origin of Cross-Hatching," *AIAA J.*, Vol. 8, 1970.
45) Townsend, A., Batchelor, G., "Decay of Turbulence in the Final Period," *Proceedings of the Royal Society of London. Series A, Mathematical and Physical Sciences*, Vol. 194, No. 1039, 1948, pp. 527-543.
46) Walters, R., Cinnella, P. and Grossman, B., "Characteristic-Based Algorithms for Flows in Thermochemical Non-equilibrium," *AIAA Journal*, Vol. 30, No. 5, 1992, pp. 1304-1313.
47) van Driest, E., "On Turbulent Flow Near a Wall," *J. Aero. Sci.*, Vol. 23, pp. 1007-1012, 1956.
48) Vincenti, W. and Kruger, C., *Introduction to Physical Gas Dynamics*, Krieger Publishing Company, Malabar, Florida, 1986.

2.3 Hypersonic transition (Reed)

With the goal of investigating hypersonic transition in shear layers, physics-based linear stability theory (LST) and nonlinear parabolized stability equation (NPSE) tools including non-equilibrium thermo-chemistry effects have been under development. These efforts have been related to two projects: SISL and hypersonic forebodies.

Considerable uncertainty exists regarding hypersonic flow transition due to the dearth of reliable experiments. The paper by Mack (1984) regarding the linear stability of compressible boundary layers remains the most complete description available. Mack's LST analysis of ideal-gas high-speed flows describes three major differences between supersonic and subsonic flow: the presence of a generalized inflection-point, the dominance of 3-D viscous disturbances, and the presence of high-frequency acoustic modes now named Mack modes. The dominance of 3-D viscous disturbances refers to the fact that at supersonic speeds, the 2-D viscous disturbances called Tollmien–Schlichting (TS) waves at lower speeds are not the most unstable viscous disturbances. Instead, oblique disturbances of the same general family are most amplified. These are called first-mode disturbances.

The acoustic instability discovered by Mack arises when the edge velocity is sufficiently fast that disturbances can propagate downstream at a subsonic speed relative to the boundary-layer edge velocity but supersonic relative to the wall. Such disturbances are inviscid acoustic waves that reflect between the solid wall and the relative sonic line. The lowest-frequency Mack mode, the so-called "second mode" becomes more unstable than the first mode for freestream Mach numbers above about 4. Whereas the first mode is stabilized by wall cooling, the second mode is destabilized via a decrease in the local sound speed and associated increase of the local relative Mach number. Accordingly, factors affecting the thermal boundary layer are critical to understanding the second-mode. The second mode is found in the experiments of Kendall (1975), Demetriades (1977), and Stetson et al. (1984). Beyond these experiments, there has never been a systematic effort to validate Mack's predictions or to investigate the conditions (roughness, bluntness, angle of attack, wall cooling, chemistry effects etc.) at which the first mode, second mode, transient growth or cross-flow dominate transition.

Beyond the additional Mack modes, hypersonic stability analyses are complicated for other reasons.

1) At hypersonic speeds, the ideal-gas assumption is invalid because certain molecular species dissociate due to aerodynamic heating and, in some instances, too few intermolecular collisions occur to support local chemical equilibrium.
2) The bow shock is close to the edge of the boundary layer and affects transition via the production of an entropy layer. Additionally, the finite shock thickness can be important and this suggests a PSE or DNS simulation approach is required.
3) Surface ablation can have a significant effect on stability via the introduction of roughness, varying surface properties, and localized blowing, all of which affect the thermal and/or momentum boundary layers.
4) The flow is highly 3-D in the neighborhood of drag flaps or fins, or when at angle of attack. 3-D boundary layers are susceptible to cross-flow which must be included in determining the appropriate transition physics. Cross-flow is ultra sensitive to roughness and freestream disturbances, and leads to important nonlinear effects across much of the transition zone.

2.3.1 Perfect-Gas Linear Stability Theory

The paper by Mack (1984) is the most complete description of compressible stability available anywhere. The linear stability analysis of high-speed perfect-gas boundary layers uncovers three major differences between it and the subsonic analysis: the presence of a generalized inflection-point, multiple acoustic modes (Mack modes), and the dominance of 3-D viscous disturbances. Stability analyses of high-speed, chemically-reacting boundary layers have largely been limited to simple geometries such as flat plates and axi-symmetric cones. In these cases, the 2-D boundary layers are subject to two inviscid instabilities. The first is vortical in nature and is due to a generalized inflection point in the boundary layer that represents a maximum in angular momentum. The second is an acoustic instability that occurs when there is a region of supersonic mean flow relative to the disturbance phase velocity. The first mode is distinguished from the second mode by using a local Mach number $\tilde{M}$, defined as the difference between the phase velocity of the disturbance c_r and the basic state velocity u, divided by the local sonic speed a.

$$\tilde{M} = (c_r - u)/a$$

If $\tilde{M} < 1$ everywhere within the boundary layer, then the first mode may be present. If $\tilde{M} > 1$ somewhere within the boundary layer, the flow is unstable to "Mack" modes. The lowest-frequency Mack mode, the so-called second mode, is found to be the dominant instability for Mach number greater than about 4; it is more unstable than either the 3-D first mode or any of the other higher modes. The second mode is a "subsonic" mode in that its structure exponentially decays with height in the inviscid region of the shock layer. The second mode is found in the experiments of Kendall (1975), Demetriades (1977), and Stetson et al.(1984) .

Mack (1984) provides additional insight to second-mode behaviour, discussing the effect of the thermal boundary layer. Mack observes that whereas the first mode is stabilized by cooling in air, the second mode is actually destabilized. The second mode is also found to be less stable with decreasing viscosity in air. This idea is related to the argument about cooling in that the viscosity of air increases with temperature. As temperature decreases, the local speed of sound decreases, which means local Mach number $\tilde{M}$ increases and the second mode, is more unstable.

Additionally Mack (1984) reasons that the behaviour of the second mode is influenced by the height of the boundary layer, which is affected by both wall cooling and viscosity. There is a strong tuning with the boundary-layer thickness, so that the frequency of the most amplified disturbance may be predicted from this flow parameter. In particular, the fluctuation wavelength is approximately twice the boundary-layer thickness. This implies that if the boundary-layer thickness is changed, for example by cooling, a corresponding and predictable change in frequency should be observed. A thinning of the boundary layer decreases the wavelength and thus increases the frequency, with the converse being true.

It is apparent from the discussion of Mack (1987) that the size of the region of relative supersonic flow is an important factor in determining second-mode behaviour. That is, the thickness of the region between the wall and the relative sonic line in which $\tilde{M} > 1$ and in which the second mode is unstable, determines the characteristics of the instability. The thermal boundary-layer profile affects both the viscosity and the local sonic speed (and thus $\tilde{M}$). Accordingly, particular attention should be given to the thermal boundary layer as a part of a second-mode investigation.

2.3.2 Validation

LST has been validated recently for 2-D high-speed flow by our group (Lyttle, Reed, et al. 2005) and is currently the method of choice in modeling streamwise instabilities.

As Schneider (2001) points out, accurate depiction of the growth of a second-mode instability wave over a circular cone at zero-angle of attack remains a challenge, both computationally and experimentally. The series of experiments performed by Stetson et al. (1984), who consider the growth of instabilities on right-circular cones (both sharp and blunted) at zero-angle-of- attack at Mach 8, serves as a benchmark for subsequent computations. Numerical comparisons to the observed growth of second-mode instabilities over the spherically blunted-cone are reported by Malik et al. (1990), Esfahanian (1991), Kufner et al. (1993), and Rosenbloom et al. (1999). Agreement with the experimentally observed growth rates can be described as qualitative.

The Stetson et al. (1984) geometry is a 7° half-angle right-circular cone, with a blunted nose of radius 3.81 mm. The total length of the model is just over 1 m (*s = 267*). The free-stream flow is Mach 8, with zero-incidence with respect to the cone's axis. The Reynolds number (based upon free-stream conditions and the nose radius) is 3.3×10^5. The focus of the experiment is the second-mode instability, which is thought to be dominant for high-speed flows over smooth, convex, axi-symmetric geometries in two-dimensional flow.

Schneider (2001) summarizes the Stetson experimental conditions very efficiently. Paraphrasing, the total pressure is 4.00 MPa; the total temperature is 750 K. Cone surface measurements are taken for pressure and temperature. Basic-state profiles are measured using total-temperature and pitot-pressure probes. Basic-state comparisons between experimentally determined profiles and computed profiles are discussed below. For the Stetson experiment, disturbances are measured using a series of four hot-wire anemometers. Starting at 0.254 m (s = 66:7), disturbance spectra are measured through 0.922 m (s = 242). The measured total-temperature spectra are shown in Fig. 2.3.5; it bears repeating that $\omega = 1$ corresponds to $f^* = 49.5$ kHz. The second-mode disturbances correspond to the spectral peaks that appear in the range $2.5 < \omega < 3$.

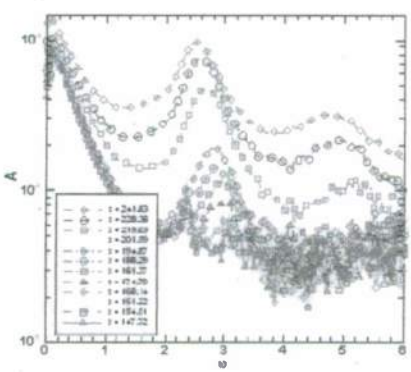

Fig. 2.3.1 Stetson experiment: measured disturbance spectra of total temperature

From Fig. 2.3.1, there follow some observations about the experiment. Firstly, Schneider (2001) notes that the experimental (free-stream) environment is not quiet, thus Fig. 1 shows the growth of broadband, uncontrolled disturbances that result from the free-stream noise. Secondly, one

notices the presence of a harmonic of the second-mode disturbance, starting at s = 215. This implies that non-linear interactions may be important downstream of s = 215. Summing up, the validity of comparing these experimental results with linear stability theory is limited by the free-stream disturbance environment and the possible presence of non-linear interactions.

Following Malik et al. (1990), many numerical investigators have chosen s = 175 as the place to make a comparison with the second-mode growth-rates reported by Stetson. As seen in Fig. 2.3.2, the numerically determined growth rates consistently peak roughly 60% higher than the peak growth-rate reported by Stetson. There have been a variety of theories to try to explain this discrepancy. Schneider (2001) points out that Stetson postulates that non-linearities are present at station 175, visible in Fig. 2.3.7b in Stetson et al. (1984). It has been pointed-out that the wall temperature at *s = 175* is not adiabatic, whereas the numerical (basic-state) models assume an adiabatic wall. Mack (1987) points out that the origin of the disturbances (receptivity) is not addressed by linear-stability theory - nor by the experiment. Furthermore, Mack (1987) points out that the experimentally determined growth rates are found using the y-locations that have the peak wide-band response - not with regard to the location of the peak of an individual frequency component. New experimental initiatives, led by Schneider et al. (2002) and Maslov (2001), address these issues.

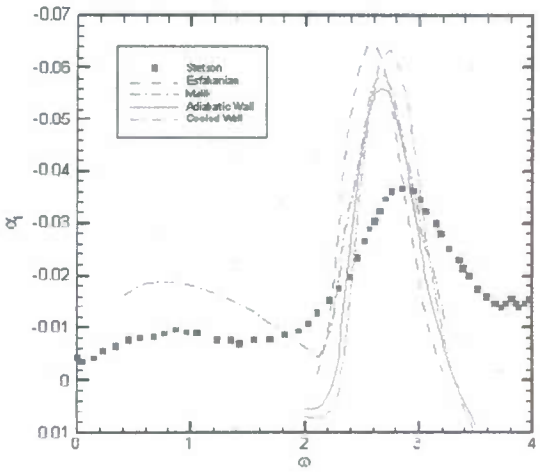

Fig. 2.32 Second-mode growth rates as functions of frequency at s=175.

Using a finite-volume code developed in-house, our group solves the Navier-Stokes equations for these conditions and uses the solutions to perform linear-stability analyses to determine the growth of second-mode disturbances. The traditional approach for numerically investigating the Stetson et al. (1984) case is to model the cone-wall as being adiabatic. This is the standard boundary-condition used by numerical investigators, and was the intent of the Stetson experiment. Per Schneider (2001), this assumption is not supported by the experimental evidence. The computed adiabatic wall temperature distribution is higher than the experimentally measured temperature distributions. Schneider further observes that, as consecutive experimental runs are made, the measured temperature distribution rises from run to run, until an equilibrium temperature distribution is reached. Schneider hypothesizes that the heat capacity of the model prevents the wall temperature from reaching the adiabatic value. Our group incorporates an option to use an experimentally determined wall-temperature distribution for the basic state.

Following the suggestion of Schneider (2001), comparisons are made of integrated growth-rates among the computations and the experiments. This may be a more appropriate comparison because the experiments measure the disturbance amplitudes, and then calculate the growth-rates based on the change in disturbance amplitudes. The integrated growth-rates, N-factors, depend on the two integration-endpoints s_0 and s_1, and are calculated as follows:

$$N = \ln\left(\frac{A_1}{A_0}\right) = \int_{s_0}^{s_1} -\alpha_i \, ds \tag{1}$$

To place the current results in the context of the Stetson experiment, the adiabatic-wall, cooled-wall, and Stetson N-factors are compared, using $s = 195$ as the reference location. The current results' agreement with the experimental results is best in the range of frequencies $2.4 < \omega < 2.8$. Examining the experimentally determined amplitudes from Fig. 2.3.1, this frequency range corresponds with those frequencies that are most-amplified in the experiment.

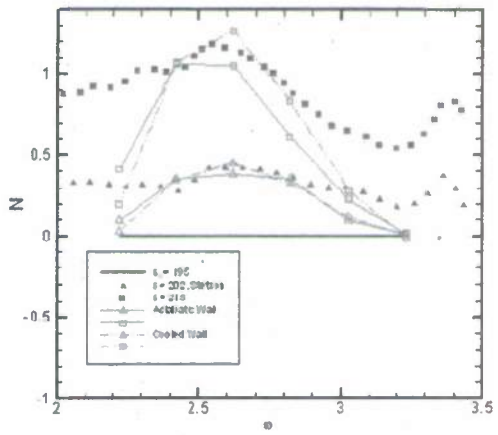

Fig. 2.3.3 Comparison of N-factors, s_0=195, Stetson case.

The N-factor curves for a series of individual disturbance waves are considered, using s = 195 as the reference location. It is surmised that if a discernible linear-growth region exists, the extent of such a region can be identified by choosing $s_0 = 195$. For example, the results for $\omega = 2.62$ are shown in Fig. 2.3.4, demonstrating the existence of a linear-growth region. The traditional under-prediction of growth-rates at s = 175 might also be explained by examining Fig. 2.3.4.

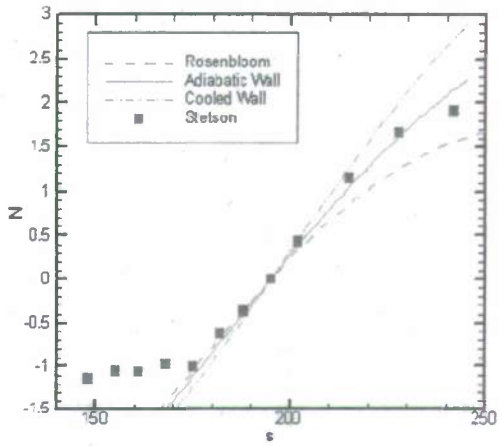

Fig. 2.3.4 N-factor comparison, ω=2.62, Stetson case.

In conclusion, our group proposes that linear-stability theory describes the growth of second-mode disturbances for $2.4 < \omega < 2.8$, and for the region $195 < s < 215$. The frequencies in this range correspond to the most-amplified second-mode frequencies. Upstream of $s = 195$, it is postulated that the amplified second-mode waves have not yet fully distinguished themselves from the noise. Indeed, the experimental N-factor curves suggest that the experimental-numerical disjoint at $s = 175$ may be attributed to signal-noise problems, rather than to non-linearity. For locations downstream of $s = 215$, perhaps non-linear interactions are important – behavior that cannot be captured using LST. Also, the agreement between the experiment and the current predictions appears better for the computations that use an experimentally determined wall-temperature distribution. Our group found similar successful second-mode validation with the Mach 6 spherically blunted cone experiments in the T-326 hypersonic blow-down wind tunnel at the Institute of Theoretical and Applied Mechanics in Russia- see Fig. 2.3.5.

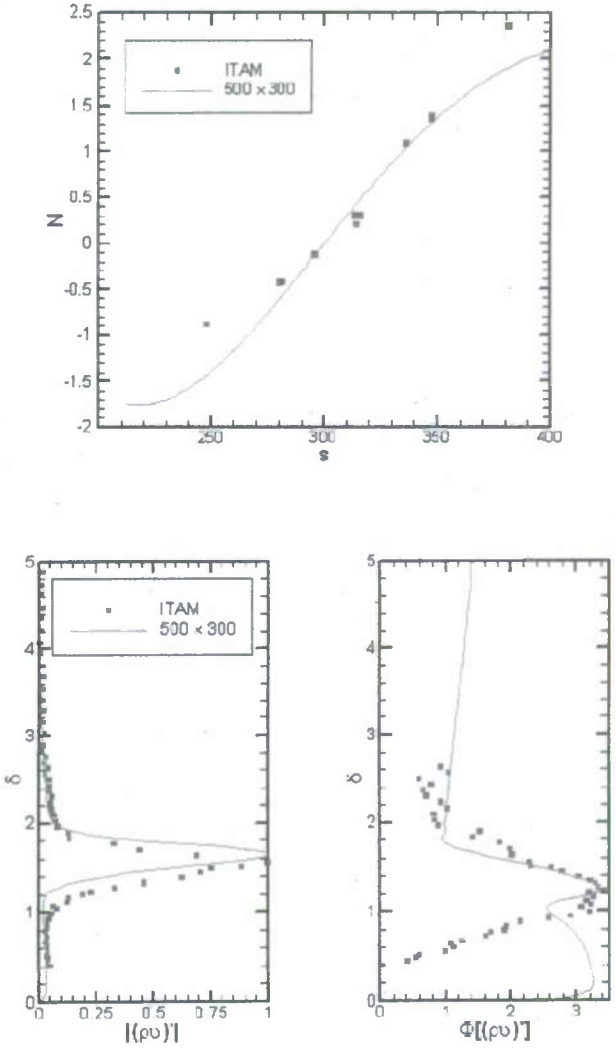

Fig. 2.3.5 Second-mode comparisons with ITAM experiments.

2.3.3 SISL

Our group also applied LST to the shock-induced shear layer project. The commercially available GASP code, which uses a structured, multi-block grid flow solver, was used to generate the basic state for a unit Reynolds number of 10,000,000 per meter. Fig. 2.3.6 shows results for a 1025×301 finite-volume scheme. The initial application of LST to this flow field found unstable flow and provided early qualitative results for this project aiding in experiment design.

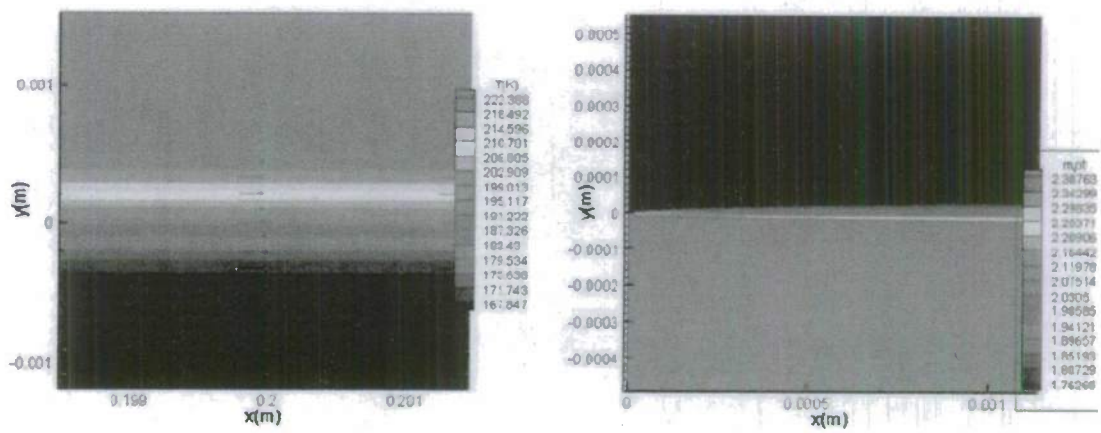

Fig 2.3.6 Basic-state modeling of the SISL flow field.

2.3.4 Chemical Reactions

For ideal-gas airflows, as are found in conventional (non-reacting) subsonic and supersonic flight, there is an accepted set of constitutive models. For the specific heat, $C_p = 3.5$; Sutherland's relationships are used for viscosity and thermal conductivity, using a Prandtl number of 0.72 (or perhaps 0.7). Compressible flows can be considered using this ideal-gas assumption so long as the temperature is within the calorically perfect range. Consider an amount of air at a pressure of 1 atm., as its temperature increases. The calorically perfect assumption begins to break down at 800 K, necessitating the use of a thermally perfect gas model for a frozen mixture of N_2 and O_2. The molecular oxygen begins to dissociate around 2500 K, necessitating the consideration of chemical reactions.

For flows where chemical reactions are important, additional constitutive models must be chosen. For each of the species, a relationship for the specific heat must be supplied. If a finite-rate reaction model is used, the reaction rates must be supplied for each reaction. As well, for the viscosity and thermal conductivity, models that take temperature and species composition into account must be provided.

If the flow is considered to be in thermal equilibrium, then there is a 'unique' temperature for all species and vibrational non-equilibrium is neglected. For a multiple-species gas mixture such as O_2, N2, O, N, NO (which has often been used for hypersonic flows – see Blottner et al. 1971, Prabhu et al. 1987), one usually assumes that each species satisfies a perfect gas relationship and Dalton's law of partial pressures applies for each species. The resulting equation of state for the gas mixture is

$$p = \rho R T \sum_{i=1}^{N} C_i / M_i$$

where R is the universal gas constant, and for the N species, the quantities C_i and M_i represent the mass concentration and molecular weight, respectively, of species i.

The governing equations for reacting flows are far more complicated due to the need to include species concentration equations for each species, coupled with the mixture mass continuity equation. In addition, chemical reactions introduce source terms in the energy

equation. In these source terms, the production rate of each species depends upon the chemistry model adopted: frozen (chemistry fixed – no reactions), equilibrium (infinite reaction rates), non-equilibrium (finite reaction rates). Models for each individual species' coefficients of specific heat and reaction rates are needed, and the viscosity and thermal conductivity are modelled using a mixture rule, which depends upon models for collision integrals for each species.

For the stability analysis, the governing Navier-Stokes equations are perturbed by decomposing the flow variables, species concentrations, transport and thermodynamic properties into a mean value (denoted by ~) and a fluctuation quantity (denoted by ')

$$u = \tilde{u} + u', \quad C_i = \tilde{C}_i + C_i', \quad \ldots$$

These forms are substituted into the full governing equations, and the equations governing the mean quantities are subtracted. The resulting disturbance equations are modelled and solved by linear stability, parabolized stability equation, or direct numerical simulation techniques.

For boundary conditions at the wall and at the edge of the computational domain, the following are suggested. At the wall, no-slip is applied to the shape function of the disturbances so that

$$\overline{u} = \overline{v} = \overline{w} = \overline{T} = 0, \quad at\ y = 0$$

If the surface material enhances the chemical reactions of the gas, the wall is called 'catalytic', and the species concentrations are determined by the corresponding equilibrium values so that

$$\overline{C}_i = 0, \quad i = 1, N \quad at\ y = 0$$

If no recombination takes place at the wall, the wall is called 'non-catalytic' and the mass flux is zero corresponding to

$$\partial \overline{C}_i / \partial y = 0, \quad i = 1, N \quad at\ y = 0$$

For a 'partially catalytic' wall, the mass flux is balanced by a prescribed catalytic rate for each species.

In the freestream (that is, the edge of the computational domain is inside the shock), Dirichlet boundary conditions are usually specified

$$\overline{u} = \overline{v} = \overline{w} = \overline{T} = \overline{C}_i = 0, \quad i = 1, N \quad as\ y \to \infty$$

If the oscillatory eigen-functions of supersonic modes are expected, then it is suggested to use a non-reflecting boundary condition. When the coordinate system for both the basic-state and stability analysis fit the body and bow shock as coordinate lines, linearized Rankine-Hugoniot shock-jump conditions are recommended for the disturbance boundary conditions.

For gas mixture in thermal and chemical non-equilibrium, a two-temperature model is used where the energy in the translational and rotational modes is characterized by the translational temperature T_T, and the energy of the vibrational modes is characterized by the vibrational temperature T_V. Thus five species equations, two momentum equations, and two energy equations are solved.

Malik (1989, 1990) and Malik & Anderson (1991) investigate the stability of an equilibrium-air boundary layer on an adiabatic flat plate. Malik et al. (1990) use the e^N method for the reentry-F experiments; the basic state was calculated by equilibrium-gas Navier-Stokes and PNS. Stuckert & Reed (1994) analyze the stability of a shock layer in chemical non-equilibrium and compared results with the flow assuming (1) local chemical equilibrium and (2) a perfect gas. Hudson et al. (1997) and Johnson et al. (1998) include chemical non-equilibrium and thermochemical non-equilibrium. Details are provided in the next several paragraphs.

Malik & colleagues conclude that reactions in equilibrium are stabilizing for the first mode and destabilizing for the second mode. Their thought is that this is most likely due to decreased temperatures in the boundary layer when the assumption of constant specific heat is removed and due to endothermic reactions which again, cool the boundary-layer and increase the region of relative supersonic flow. The Mach 10 adiabatic wall study also showed an unstable third mode, which did not appear in the perfect gas analysis. Third mode stability was found to depend on wall temperature and Mach number.

Stuckert & Reed (1994) consider a flow over a sharp cone, at zero incidence, with a freestream Mach number of 25, and include 5 species: O_2, N_2, O, N, and NO. The free-stream speed is high enough that non-equilibrium chemical reactions result from viscous heating in the boundary layer. Because the chemical reactions affect the temperature in the boundary layer (tending to cool it), and the second-mode disturbance is tuned to the boundary-layer thickness (which is affected by the cooling), they conclude that non-equilibrium chemistry has to be considered for stability analyses of this flow. Their coordinate system for both the basic-state and stability analysis fit the body and bow shock as coordinate lines. This eases the application of the linearized shock-jump conditions as the disturbance boundary conditions. At the surface of the cone, for the non-equilibrium calculations, the species mass fluxes were set to zero (non-catalytic wall), whereas for the equilibrium calculations the disturbances were assumed to be in chemical equilibrium. It is clear that the equilibrium and non-equilibrium solutions can differ significantly depending on the rates of the reactions relative to the time scales of convection and diffusion. For example, some of the equilibrium modes were determined to be supersonic modes, each of which was a superposition of incoming and outgoing amplified solutions in the inviscid region of the shock layer. (No similar solutions were found for the non-equilibrium shock layer.) The magnitudes of these modes oscillated with y in the inviscid region of the shock layer. This behaviour is possible only because the shock layer has a finite thickness. They are also unlike Mack's higher modes (except for the second) in that the disturbance-pressure phase for all of these supersonic modes changed most across the inviscid region of the shock layer. (The disturbance-pressure phase change for Mack's higher modes occurs across the viscous region of the flow, i.e. the boundary layer.) In fact, the disturbance-pressure phase change for all of these supersonic modes through the boundary layer is comparable to that of Mack's second mode.

Once again, the effect of the chemical reactions is to increase the size of the region of relative supersonic flow primarily by reducing the temperature in the boundary layer through endothermic reactions, increasing the density, and hence decreasing the speed of sound. This reduces the frequency of the higher modes; in particular, the most unstable one, the second mode. The higher modes in the reacting-gas cases are also more unstable relative to the corresponding perfect-gas modes. The first modes are, however, more stable.

Finally, the finite thickness of the shock layer has a significant effect on the first-mode solutions of all of the families. The effect on higher-mode, higher-frequency solutions does not seem to be as large as long as they are subsonic. This is perhaps what one would intuitively expect because the shock is likely 'stiff' and hence difficult to perturb with smaller-wavelength, larger-wave number, higher-frequency disturbances. However, the nonparallel effects are known to be large for first-mode solutions, and so a complete quantitative description of the effects of the finite shock-layer thickness needs either a PSE solution or a DNS analysis.

Modelling using non-equilibrium chemistry captures either of the limiting cases (frozen and equilibrium), but at significant computational cost. The important conclusion of Stuckert & Reed (1994) is that the complexity of the chemistry model one uses to model the flow can affect the stability prediction. Because transition prediction is well known to be influenced by all aspects of the flow, the conclusion is that one must consider all relevant physics.

Hudson et al (1997) conduct a numerical investigation into hypersonic flat-plate flows in thermochemical non-equilibrium. Their results confirm the dominance of the second-mode. Furthermore, they show that the effects of thermal-non-equilibrium are diminished as one advances downstream from the leading edge.

Johnson et al. (1998) follow this work by considering the linear stability of a high-speed flow, using a series of geometries that approximate an interceptor. One of the geometries they consider is a right-circular cone with a 21° half-angle. They consider a flow with a free-stream Mach number of 13.5; thermal and chemical non-equilibrium models are used. The cases they study include both a sharp cone and a spherically blunted cone with nose radius of 2.54 cm. They detail second-mode behaviour for both these cases, finding stable and unstable waves for the sharp-cone case, and finding only stable second-mode waves for the blunt-cone (for the distance that they consider). Among other results, these studies showed that thermochemical non-equilibrium was stabilizing for the second mode compared to chemical equilibrium and non-equilibrium. This result was attributed to the higher translational temperature, which is the result of decreased energy absorption by dissociation due to slow reaction rates. Another significant conclusion is that wall cooling effects dominate disturbance growth rates as compared to chemistry effects.

Chang et al. (1997) developed the linearized parabolized stability equations (LPSE) for reacting hypersonic flows considered 3 gas models: non-equilibrium with 5 species, equilibrium through a table look-up procedure, and perfect gas. They considered a Mach 20 flow over a 6° wedge and with the LPSE were able to account for the non-parallel effects. [Recall that Stuckert & Reed (1994) found supersonic disturbance modes for equilibrium flow with linear stability theory – these modes feature an oscillatory structure in the inviscid region of the shock layer.] For both equilibrium and finite-rate chemistry with LPSE, Chang et al. (1997) found amplifying supersonic modes with a relative phase velocity faster than the freestream sonic speed. These modes emerged just downstream of the unstable (subsonic) second-mode region and they generate dispersive waves that propagate into the freestream with a phase speed different from the corresponding acoustic wave and the wave structure decays at a finite distance outside the boundary layer. They determine that the Rankine-Hugoniot shock-jump conditions have little effect since the mode structure decays before the shock is reached. The unit Reynolds number for the wedge configuration was 9×10^5/ft and the wall temperature was constant at $T_w/T_{adiabatic} = 0.1$. The post shock Mach number is 12.5 with a shock angle (between the wedge and the shock) of 2.22°. Due to the presence of the supersonic modes, Chang et al. predicted the location of the onset of transition (that is, the location at which N-factor achieves a value of 10) to be 14 feet, 24 feet, and 39 feet if one uses the equilibrium, non-equilibrium, and perfect gas models, respectively – quite a difference. It is apparent that it is important to correctly model the chemistry and the global nature of the instabilities. Chang et al.(1997) also studied the effect of different mean-flow formulations on the stability results. Boundary-layer mean flows and parabolized Navier-Stokes mean flows give slightly different results but are qualitatively similar.

Apparent from this discussion, for chemically-reacting flows, a number of thermodynamics, reaction rates, and transport models must be used, and there are several available. Also these models have greater uncertainties than those describing ideal-gas flows. Our group (Lyttle & Reed 2005) considered different accepted thermodynamic models (for species specific heats), reaction rates, and transport models (mixture viscosity and thermal conductivity), with the goal of estimating the sensitivity of linear-stability predictions to the changes made to these models, within some given uncertainties. The selected geometry and flow conditions are the Mach 13.2 right-circular cone with a 21° half-angle (Johnson et al. 1998). For this investigation, five different simulations are made for the 'same' flow.

1) The first simulation serves as a baseline and uses the nominal constitutive relationships of Stuckert & Reed (1994).
2) For the second case, a different technique is used to model the species molar specific-heat coefficients. Stuckert & Reed use a cubic-spline technique. The alternative model uses a series of seventh-order polynomials for each of the species, as compiled by Palmer and Venkatapathy (1995). It is observed that small differences in the specific-heat curves translate to small differences in the composition curves.
3) For the third case, a different technique is used to model the mixture viscosity and thermal conductivity. The Blottner (1971) model uses a series of temperature-based curve-fits for these transport properties for each species. A mixture-rule is then used to find the mixture transport properties. This model is used by Johnson et al. (1998) and in many other investigations conducted by Prof. Candler's group. For the Stuckert & Reed model, collision integrals are determined using curve fits. These collision integrals are combined, using a mixture rule, to form the thermal conductivity of the mixture.
4) The fourth and fifth cases focus on the reaction rates for the dissociation of O_2. The uncertainty for these reaction rates is a factor of two. For the fourth case, the third-body efficiency factor for each O_2-dissociation reaction is multiplied by 0.5. For the fifth case, the third-body efficiency factor for each O_2-dissociation reaction is multiplied by 2.0.

	$\omega = 12.93, \beta = 0$		$\omega = 10.51, \beta = 0$	
Case	$\max(\alpha_i)$	$\frac{\max(\alpha_i)}{\max(\alpha_i)_{nominal}}$	$\max(\alpha_i)$	$\frac{\max(\alpha_i)}{\max(\alpha_i)_{nominal}}$
Nominal	-0.1844	1.000	-0.287416	1.000
Palmer & Venkatapathy cp	-0.2047	1.110	-0.297651	1.036
Blottner Transport	-0.2320	1.258	-0.311482	1.084
O_2 Rate Factor: 0.5	-0.1819	0.986	-0.287788	1.001
O_2 Rate Factor: 2.0	-0.1881	1.020	-0.286975	0.998

Table 2.3.1 Maximum second-mode growth-rates from different models

Table 2.3.1 demonstrates second-mode growth rates for the different cases at 2 different chordwise stations. Changing the model for the specific-heat has little effect on the basic-state flow profiles in this region. The largest change in the thermal profile is seen for the case where a different transport model is used. Considering the second-mode behaviour for each of these cases, the magnitude of change in the stability results correlates strongly with changes in the basic-state thermal boundary-layer profile. The choice of viscosity and thermal conductivity influenced the growth rates the most. Comparisons with the Goodwin (1995) model show that

the amount of disagreement between Stuckert and Blottner models is reasonable. It appears that the Goodwin model lies in between the two and agrees with the Stuckert model below 1000 K, and then asymptotes into the Blottner model at higher temperatures. The conclusion is that there exist appreciable differences among generally-accepted models.

It is recognized that a more robust study of the sensitivity of the stability predictions to these factors can be achieved by using a thermochemical non-equilibrium model as a baseline. Computational techniques, including direct numerical simulation (DNS) and non-linear parabolized stability equations (NPSE), are making tremendous strides, and are in some ways ahead of the experimental community's ability to validate the results (Schneider 2001). As these techniques are applied to flows in thermochemical non-equilibrium, the accuracy of the constitutive relationships should be considered. Perhaps one approach is for the numerical community to agree on a set of baseline models in order to remove a source of disagreement among results.

To summarize the results considering chemical effects:

1) All analyses confirm that the 2nd mode is most unstable
2) Most unstable 1st mode wave is oblique
3) Results of chemically reacting boundary layers show that chemistry / high-temperature effects alter the stability of the flow and must be included in any analysis
4) Different results for different mean flow and chemistry models
    a) Need experimental and flight guidance and validation
    b) Need consensus
5) Need experimental validation to ensure basic physics accurately modeled – quiet, well-documented tunnels and flight

2.3.5 Three-Dimensional Boundary Layers

As another project, our group is engaged with AFRL in developing computational solutions on hypersonic forebodies at angle-of-attack in collaboration with colleagues Candler and Johnson at Minnesota (STABL code), Schneider at Purdue (quiet tunnel experiments), McLean at CUBRC, and NASA Langley (LASTRAC). Our group has requested basic-state solutions from the other participants.

For 3-D boundary layers (e.g. swept wings; Saric, Reed, & White 2003) and also Görtler problems (concave surfaces; Saric 1994), nonlinear distortions of the basic flow may occur early on due to the action of the *stationary* primary instability. These flows are characterized by an extensive distance of nonlinear evolution with eventual saturation of the fundamental disturbance, leading to the strong amplification of very-high-frequency inflectional instabilities and breakdown. Here linear stability theory (LST) is not successful (Reed et al. 1998). However, the NPSE, which have significantly less resource overhead associated with them compared with direct numerical simulations (DNS), have been shown to accurately model transition in a variety of relevant flows when the environment and operating conditions are modeled correctly.

Computationalists Haynes & Reed (2000) and experimentalists Reibert et al. (1996) together systematically studied basic mechanisms and sorted out the effects of curvature, roughness, and nonlinearities in incompressible 3-D boundary layers, and elucidated a very promising strategy for laminar flow control. This team developed and validated the NPSE with experiments on an NLF(2)-0415 swept airfoil. As a baseline case to study the evolution of crossflow vortices, roughness elements with a span-wise spacing of 12 mm were placed on the experimental model. Fig. 7 shows a comparison of the experimental and computational total streamwise velocity

contours at 45% chord; the agreement between the NPSE and the experiments is excellent. Figure 8 shows the comparison of the experimental -factor curves with various linear theories and NPSE. It is clear that the linear theories fail to accurately describe the transitional flow for this situation and that the NPSE does an excellent job of capturing the details for very little computational expense. This work then led to the novel idea of applying subcritically spaced, micron-sized roughness near the leading edge to maintain laminar flow on a swept wing (Saric et al. 1998), and then to supersonic 3-D boundary layers (Saric & Reed 2002).

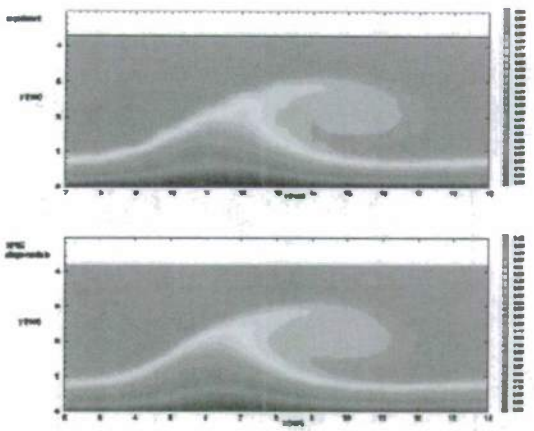

Fig. 2.3.7 Streamwise-velocity contours for NLF (2)-0415 45° - sweep, $R_c = 2.4million, \lambda_z = 12mm$, 45% chord. Excellent agreement between NPSE with curvature and experiments.

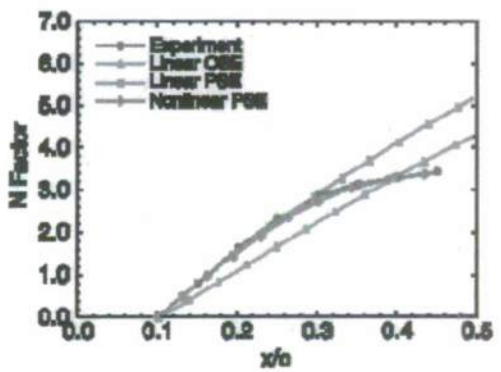

Fig. 2.3.8 N factors for NLF (2)-0415 45° - swept airfoil, $R_c = 2.4million, \lambda_z = 12mm$. Shown is the excellent agreement between NPSE with curvature and the experiments.

An interesting feature of the stationary cross-flow waves is the destabilization of secondary instabilities. The u' distortions created by the stationary wave are time-independent, resulting in a span-wise modulation of the mean streamwise velocity profile. As the distortions grow, the boundary layer develops an alternating pattern of accelerated, decelerated, and doubly inflected profiles. The inflected profiles are inviscidly unstable and subject to a high-frequency secondary instability (Kohama et al 1991; Malik et al 1994). This secondary instability is highly amplified

and leads to rapid local breakdown. Because transition develops locally, the transition front is nonuniform in span and characterized by a 'saw-tooth' pattern of turbulent wedges.

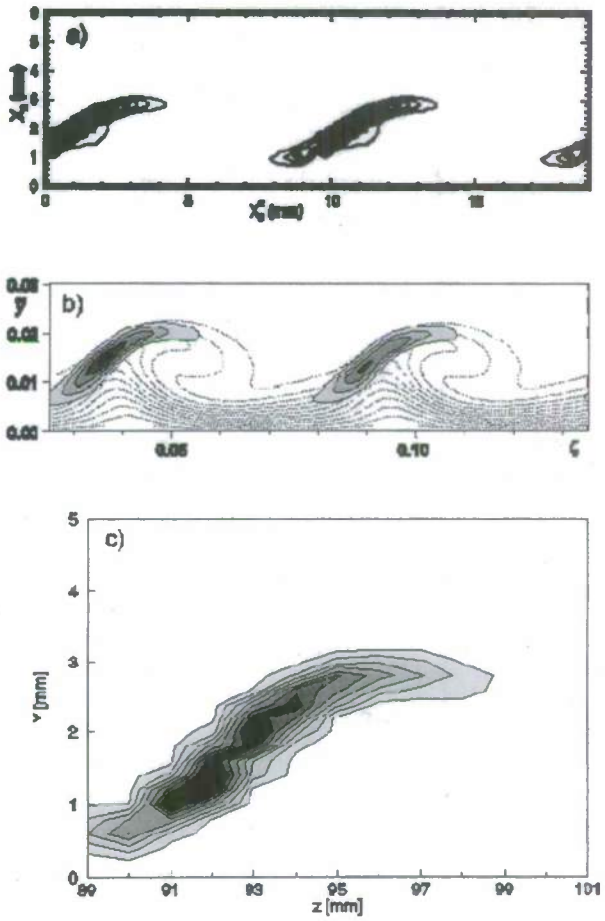

Fig. 2.3.9 Mode-I velocity fluctuation contours (a) Fig. 7 from Malik et al. (1999), (b) Fig. 20b from Wassermann & Kloker (2002), and (c) Fig. 11 from White & Saric (2002).

At this time, various approaches to the secondary instability problem: experimental, NPSE, and DNS, have achieved rather remarkable agreement in terms of identifying the basic mechanisms of the secondary instability, unstable frequencies, mode shapes, and growth rates. The comparison shown in Fig. 9 shows excellent agreement on the location of the breakdown and that it is associated with an inflection point in the span-wise direction (an extremum in $\partial U/\partial z$).

For hypersonic flows, our team has advised the Minnesota team on modeling cross-flow instability physics as stationary because of the extreme dependence on leading-edge roughness per the extensive experiments at Arizona State University, as well as provided details of the numerical NPSE approach above. At present, the Minnesota team has formulated STABL for LST and LPSE for 2-D geometries with chemistry, and has expressed that it would like to continue to work with us in the future to fully implement the NPSE for 3-D geometries. Reed has

traveled to Minnesota to work with Candler and Johnson, and will continue to assist as needed in the implementation of the NPSE.

In the meantime, our team has in-house capability in NPSE for verification in conical flows with ideal gas. However, many geometries in hypersonic applications are non-conical with span-wise variations in the mean flow. Our team is currently refining its tools to study both cross-flow and second-mode instabilities on *general geometries*. We are implementing the group velocity direction for marching, which we feel is key (per earlier work in which one of the co-PIs – Reed was involved). Our team has participated in the regular HIFIRE telecons from last Fall 2008 until this Spring 2009. Basic-state hypersonic-forebody data was provided by Minnesota this Spring 2009 and our stability results should be completed by our team this Fall 2009.

2.3.6 Transitions

The Texas A&M team has leveraged other Air Force programs in which it has participated, namely RATTraP, SWIFT, STAR, SensorCraft/HiLDA and DARPA QSP, to better understand the physics of transition and refine theoretical and computational methodologies.

RATTraP: Reed was a member of the Rapid Assessment Tool for Transition Prediction (RATTraP) team with Lockheed Martin in Fort Worth. Lockheed Martin Aeronautics (LM Aero) was involved in developing, implementing, and validating a computationally efficient and physically accurate method to predict boundary layer transition on laminar flow swept wings for HALE intelligence, surveillance, and reconnaissance (ISR) aircraft. The LM Aero team has developed a low risk technical approach that will efficiently provide AFRL a transition prediction capability that will enable efficient HALE wing design and optimization. This transition method is also applicable to more general aircraft configurations and flow conditions.

The LM Aero RATTraP program plan was devised to efficiently develop a superior transition prediction method for 3-D wing design and optimization. The LM Aero team leveraged existing physics-based transition prediction methods through a comprehensive survey. Experimental and theoretical transition results were surveyed and reliable data sets selected for use in validation and calibration of the final transition prediction methodology. The final RATTP software was designed to ensure computational efficiency, effective parallelization and ease of implementation in multiple flow solvers. The RATTraP software was then implemented in two 3-D Navier-Stokes flow solvers, one of which was selected by AFRL. The software was validated using experimental data and stability theory-based methods. The final thoroughly documented products of the RATTP program were a software design, transition prediction source code modules without any proprietary limitations, an implemented RATTP model in the AFRL code of choice, and a validation database.

SWIFT, SensorCraft/HiLDA: Reed also supports the Flight Research Lab at TEES/Texas A&M generating detailed O-2 flight data for cross-flow validation purposes as well as demonstration of Saric's passive laminar flow technique of span-wise periodically spaced discrete roughness elements. Reed designed the flight test article through stability analysis, and FLUENT and NPSE results show the feasibility of 2-mm spaced roughness elements to control natural cross-flow with a 4-mm wavelength.

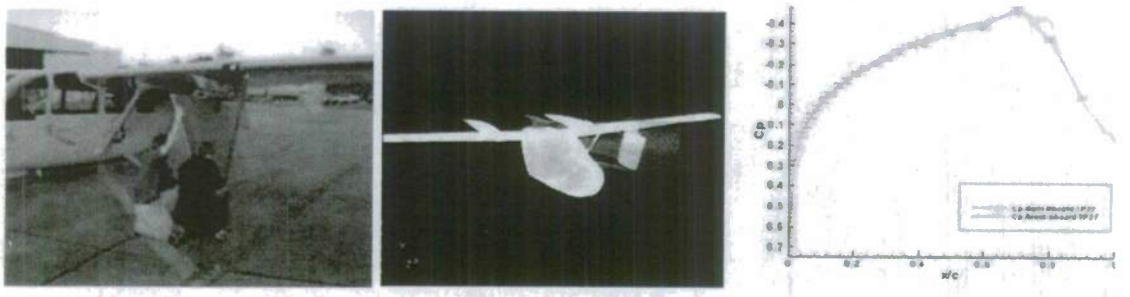

Fig. 2.3.10 SWIFT model mounted on the O-2 at TEES/Texas A&M, FLUENT model of the flight configuration, and a comparison of flight and computational data showing excellent agreement for – Cp.

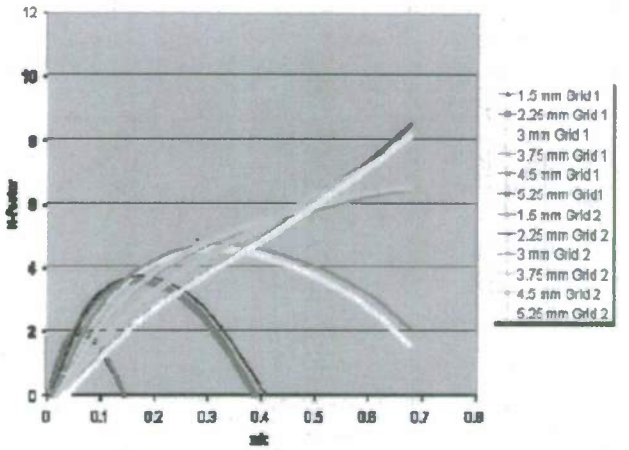

Fig. 2.3.11 Linear stability theory for the SWIFT model shows cross-flow instability wavelength predicted at 4.5 mm. Discrete roughness elements spaced 2.25 mm apart at the leading edge will control the cross-flow (Saric et al. 1998; Saric & Reed 2002).

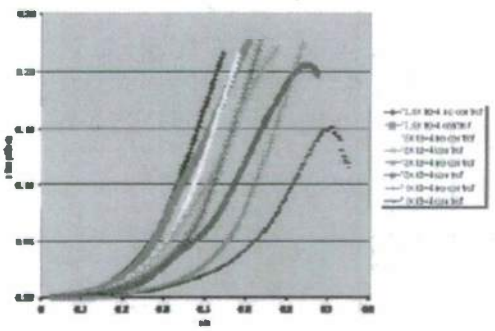

Fig. 2.3.12 NPSE predictions show that if control roughness of 2.25 mm is applied, then 4.5 mm most dangerous wavelength will be damped.

AIAA Professional Development Course: Reed is one of three people who team to offer the AIAA Professional Development Course "Stability and Transition: Theory, Modeling, Experiments, and Applications", first in 2003, then 2006 and 2008, with the next in 2010 at the

Summer AIAA Fluids Meeting. The description of the course is: 'Knowledge of transition is critical for accurate force and heating predictions and effective control (both transition delay and enhancement). This course is intended to present a comprehensive and critical review of current methods used to determine the physics, onset, and extent of transition for a wide variety of 2D and 3D flows, both high- and low-speed. Tools reviewed will include the e^N method based on linear stability theory (LST), Parabolized Stability Equations (PSE), and Direct Numerical Simulations (DNS). Guidelines for experiments and flight tests are reviewed...' Reed is responsible for teaching:

1) Current tools – Linear Stability Theory, Parabolized Stability Equations, Direct Numerical Simulations
2) Verification and Validation for various 2D and 3D flows

Reed has also taught these topics at AFRL in Dayton and Lockheed Martin in Fort Worth.

Reed also team taught RTO course "Advances in Laminar-Turbulent Transition Modeling", 9-12 June 2008, by Saric, Reshotko, Arnal, & Reed, at VKI. This was repeated at AFRL Wright Patterson in January 2009.

2.4 Kinetic-Theory based Schemes (Li-shi Luo)

The task of the group at Old Dominion University (ODU) is two-fold: (a) development of kinetic schemes and numerical procedures for non-thermochemical-equilibrium (NTE) flows and (b) direct numerical simulations (DNS) of isotropic homogeneous NTE turbulence. We will summarize our results and accomplishments in fulfilling the above two objectives set in MURI Topic 19 Project 'Hypersonic Transition and Turbulence with Non-Equilibrium Thermo-chemistry'.

2.4.1 Theoretical Foundation of Kinetic Schemes

Kinetic schemes are derived from the Boltzmann equation written as the following for a mixture of N species:

$$\partial_t f_a + \boldsymbol{\xi} \cdot \nabla f_a = \sum_{b=1}^{N} Q_{ab}, \quad Q_{ab} = \int d\boldsymbol{\xi}_b d\theta d\epsilon B_{ab}(\theta, V)\left[f'_a f'_b - f_a f_b\right], \tag{2.4.1a}$$

$$B_{ab}(\theta, V) = V r_{ba} \left|\frac{\partial r_{ba}}{\partial \theta}\right|, \quad V := \|\boldsymbol{\xi}_a - \boldsymbol{\xi}_b\|. \tag{2.4.1b}$$

where $r_{ba} = \|\boldsymbol{r}_b - \boldsymbol{r}_a\|$ is the trajectory of the particle of species b in the coordinate system centered at the particle of species a, which is fully determined by the interaction potential $\phi_{ab}(r_{ab})$ between the two particles, and θ and ϵ are the azimuthal and polar angles in the collisional coordinate system. The hydrodynamic variables in the system are the moments of distribution functions:

$$\rho = \sum_{a=1}^{N} \rho_a, \quad \rho_a = \int f_a d\boldsymbol{\xi}, \quad \rho \boldsymbol{u} = \sum_{a=1}^{N} \rho_a \boldsymbol{u}_a, \quad \rho_a \boldsymbol{u}_a = \int f_a \boldsymbol{\xi} d\boldsymbol{\xi}, \tag{2.4.2a}$$

$$p = \sum_{a=1}^{N} p_a = n k_B T, \quad n = \sum_{a=1}^{N} n_a = \sum_{a=1}^{N} \rho_a / m_a, \tag{2.4.2b}$$

$$p_a = n_a k_B T = \rho_a R_a T = \int f_a \boldsymbol{c} \cdot \boldsymbol{c} d\boldsymbol{\xi}, \quad \boldsymbol{c} = \boldsymbol{\xi} - \boldsymbol{u}, \tag{2.4.2c}$$

where, $m_a, n_a, \rho_a := m_a n_a$, $\boldsymbol{u}_a$ and p_a are the molecular mass, number density, mass density, flow velocity, and pressure of species a, respectively; $n, \rho, \boldsymbol{u}, p$ and T are the number density, mass density, flow velocity, pressure, and temperature of the mixture, respectively; R_a is the gas constant for of species a and k_B is the Boltzmann constant. The pressure tensor P and the heat flux $\boldsymbol{q}$ are given by:

$$\mathsf{P} = \sum_{a=1}^{N} \mathsf{P}_a, \quad \mathsf{P}_a = \int f_a \boldsymbol{c}\boldsymbol{c} d\boldsymbol{\xi}, \quad \boldsymbol{q} = \sum_{a=1}^{N} \boldsymbol{q}_a, \quad \boldsymbol{q}_a = \int f_a c^2 \boldsymbol{c} d\boldsymbol{\xi}, \quad c^2 := \boldsymbol{c} \cdot \boldsymbol{c}. \tag{2.4.3a}$$

The hydrodynamic equations are obtained as the first three moment equations of the Boltzmann equation (2.4.1):

$$\partial_t \rho_a + \nabla \cdot \rho_a \boldsymbol{u}_a = 0, \quad \partial_t \rho + \nabla \cdot \rho \boldsymbol{u} = 0, \tag{2.4.4a}$$

$$\rho \partial_t \boldsymbol{u} + \rho \boldsymbol{u} \cdot \nabla \boldsymbol{u} + \nabla \cdot \mathsf{P} = 0, \tag{2.4.4b}$$

$$\frac{3}{2} n k_B (\partial_t T + \boldsymbol{u} \cdot \nabla T) + \nabla \cdot \boldsymbol{q} - \frac{3}{2} k_B T \nabla \cdot \sum_{a=1}^{N} n_a (\boldsymbol{u}_a - \boldsymbol{u}) + \mathsf{P} : \nabla \boldsymbol{u} = 0. \tag{2.4.4c}$$

In the framework of Chapman-Enskog analysis, the single particle distribution function f can be expanded formally as a series of the Knudsen number $\mathrm{Kn} := \varepsilon$,

$$f_a = \sum_{n=0}^{\infty} \varepsilon^n f_a^{(n)}, \quad f_a^{(0)} = \rho_a (2\pi k_B T)^{-3/2} e^{-(\boldsymbol{\xi} - \boldsymbol{u})^2 / 2 R_a T}, \tag{2.4.5a}$$

$$\int (1, \boldsymbol{\xi}, c^2) f_a^{(n)} d\boldsymbol{\xi} = (0, \boldsymbol{0}, 0) \quad \forall n > 0. \tag{2.4.5b}$$

Correspondingly, the pressure tensor P and the heat flux $\boldsymbol{q}$ can be written as

$$\mathsf{P} = \sum_{a} \sum_{n=0}^{\infty} \varepsilon^n \mathsf{P}_a^{(n)}, \quad \mathsf{P}_a^{(n)} := \int f_a^{(n)} \boldsymbol{c}\boldsymbol{c} d\boldsymbol{\xi}, \tag{2.4.6a}$$

$$\boldsymbol{q} = \sum_{a} \sum_{n=0}^{\infty} \varepsilon^n \boldsymbol{q}_a^{(n)}, \quad \boldsymbol{q}_a^{(n)} := \int f_a^{(n)} c^2 \boldsymbol{c} d\boldsymbol{\xi}. \tag{2.4.6b}$$

If the distribution function is approximated by the Maxwell equilibrium distribution of Eq. (2.4.5a), i.e., $f_a \approx f_a^{(0)}$, the hydrodynamic equations (2.4.4) become the Euler equations; if $f_a \approx f_a^{(0)} + f_a^{(1)}$, the hydrodynamic equations (2.4.4) become the Navier-Stokes equations, in which the stress-strain constitutive relation and Fourier's law for the heat conduction are derived and the transport coefficients are computed from the microscopic interaction ϕ_{ab}. For non-thermochemical-equilibrium flows, we must consider the effects due to nonequilibrium part of

distribution function $f^{(n)}, n>1$.

Clearly, solving the Boltzmann equation in phase space $(\boldsymbol{x},\boldsymbol{\xi})$ is far more demanding than solving hydrodynamic equation in physical space $\boldsymbol{x}$. Because hydrodynamics is insensitive to the details of molecular dynamics, we can simplify the collision model in order to construct efficient numerical schemes for computational fluid dynamics (CFD). To construct kinetic schemes for CFD, we usually use the linearize collision model, of which the simplest one is the Bhatnagar-Gross-Krook (BGK) model with single relaxation time λ:

$$Q = -\frac{1}{\lambda}\left[f - f^{(0)}\right]. \tag{2.4.7}$$

We will use the Boltzmann equation of one species with the BGK relaxation model for the collision to illustrate construction of various kinetic schemes for CFD.

We can re-write the BGK equation as the following,

$$D_t f = -\frac{1}{\lambda}\left[f - f^{(0)}\right], \quad D_t := \partial_t + \boldsymbol{\xi}\cdot\nabla, \quad f^{(0)} = \frac{\rho}{(2\pi RT)^{3/2}} e^{-(\boldsymbol{\xi}-\boldsymbol{u})^2/2RT}. \tag{2.4.8}$$

Integrating the above equation along characteristics yields the following general solution:

$$f(\boldsymbol{x}+\boldsymbol{\xi}\delta_t, \boldsymbol{\xi}, t+\delta_t) = e^{-\delta_t/\lambda} f(\boldsymbol{x}, \boldsymbol{\xi}, t) + \frac{1}{\lambda} e^{-\delta_t/\lambda} \int_0^{\delta_t} e^{t'/\lambda} f^{(0)}(\boldsymbol{x}+\boldsymbol{\xi}t', \boldsymbol{\xi}, t+t')\, dt'. \tag{2.4.9}$$

Several discretizations of the above solution lead to different kinetic schemes. First, a finite difference discretization and low-Mach-number approximation lead the lattice Boltzmann equation (LBE) for near incompressible flows. Secondly, a finite volume discretization leads to the gas-kinetic scheme (GKS) for fully compressible flows.

2.4.2 Lattice Boltzmann Equation

To obtain the lattice Boltzmann equation, we need to make following approximations. First, a Taylor expansion in δ_t is applied to Eq. (2.4.9):

$$f(\boldsymbol{x}+\boldsymbol{\xi}\delta_t, \boldsymbol{\xi}, t+\delta_t) - f(\boldsymbol{x}, t) = \frac{1}{\tau}\left[f - f^{(0)}\right], \quad \tau := \lambda/\delta_t. \tag{2.4.10}$$

Secondly, the phase space $(\boldsymbol{x},\boldsymbol{\xi})$ is coherently discretized in such way that the physical space $\boldsymbol{x}$ is approximated by a lattice in d dimensional space, $\mathbb{Z}_d$, and the velocity space $\boldsymbol{\xi}$ by a symmetric finite set of Q discrete velocities $\mathrm{V}_Q = -\mathrm{V}_Q$, such that

$$\boldsymbol{x}_j + \boldsymbol{c}_i\delta_t \in \mathbb{Z}_d, \quad \forall \boldsymbol{x}_j \in \mathbb{Z}_d \text{ and } \forall \boldsymbol{c}_i \in \mathrm{V}_Q. \tag{2.4.11}$$

Finally, both the distribution function f and the equilibrium $f^{(0)}$ are approximated by truncated low-Mach-number expansions:

$$f_i^{(0)} = \sum_{n=0}^{2} \frac{1}{n!} \underbrace{\boldsymbol{u}\boldsymbol{u}\cdots\boldsymbol{u}}_{n} : \mathsf{H}^{(n)}(\boldsymbol{c}_i), \quad f_i = \sum_{n=0}^{2} \frac{1}{n!} \mathsf{a}^{(n)} : \mathsf{H}^{(n)}(\boldsymbol{c}_i), \quad \mathsf{a}^{(n)} = \int f \mathsf{H}^{(n)}(\boldsymbol{\xi})\, d\boldsymbol{\xi}. \tag{2.4.12}$$

where $\mathsf{H}^{(n)}$ is the n-th order Hermite polynomial. The lattice Boltzmann equation so derived can be concisely written in a vector form,[1,2]

$$\mathbf{f}(\boldsymbol{x}_j + \boldsymbol{c}\delta_t, t_n + \delta_t) - \mathbf{f}(\boldsymbol{x}_j, t_n) = -\mathsf{M}^{-1}\cdot\mathsf{S}\cdot\left[\mathbf{m} - \mathbf{m}^{(eq)}\right]. \tag{2.4.13}$$

where $\mathbf{f}$ and $\mathbf{m}$ are Q-tuple vectors for the discrete distribution functions and moments,

respectively; $\mathbf{m} = \mathbf{M} \cdot \mathbf{f}$ and $\mathbf{f} = \mathbf{M}^{-1} \cdot \mathbf{m}$; the transform matrix $\mathbf{M}$ can be easily constructed by using the Gram-Schmidt orthogonalization procedure; the equilibrium $\mathbf{m}^{(eq)}$ are second-order polynomials of the conserved variables in the system; and the diagonal relaxation matrix $\mathbf{S}$ has the relaxation rates which determine the values of the transport coefficients in the system.

For nonequilibrium multi-species mixtures, one must consider multi-fluid model which includes the local equilibrium of individual species and the local equilibrium of a mixture. In the BGK presentation, the collision operator of the LBE model for a binary mixture is:

$$Q_i^a = -\frac{1}{\tau_a}\left[f_i^a - f_i^{(eq)}(\rho_a, \boldsymbol{u}_a)\right] - \frac{1}{\tau_D}\left[f_i^a - f_i^{(eq)}(\rho_a, \boldsymbol{u})\right], \tag{2.4.14a}$$

$$f_i^{(eq)}(\rho, \boldsymbol{u}) := w_i \rho \left\{1 + 3\boldsymbol{c}_i \cdot \boldsymbol{u} + \frac{9}{2}(\boldsymbol{c}_i \cdot \boldsymbol{u})^2 + \frac{3}{2}\boldsymbol{u} \cdot \boldsymbol{u}\right\}, \tag{2.4.14b}$$

where $\boldsymbol{u}_a$ and $\boldsymbol{u}$ are the barycentric velocities of an individual species a and the mixture, respectively. The relaxation parameters τ_a and τ_D determine the shear viscosity of species a and the mutual diffusion coefficient, respectively.

2.4.3 Gas Kinetic Scheme for Non-equilibrium Compressible Flows

The gas-kinetic scheme (GKS)[3-7] is a finite volume (FV) scheme based on the BGK equation (2.4.8). The hydrodynamic equations can be written in terms of the conserved variables $\{\Phi_\alpha\}$ and the corresponding fluxes $\{\boldsymbol{J}_\alpha\}$:

$$\partial_t \Phi_\alpha + \nabla \cdot \boldsymbol{J}_\alpha = 0, \quad \Phi_\alpha = \int \phi_\alpha f \, d\boldsymbol{\xi} \in \{\rho, \rho\boldsymbol{u}, \rho e\}, \quad \boldsymbol{J}_\alpha = \int \boldsymbol{\xi}\phi_\alpha f \, d\boldsymbol{\xi}, \tag{2.4.15}$$

where $\phi_\alpha \in \{1, \boldsymbol{\xi}, \boldsymbol{\xi}^2/2\}$ are the collisional invariants. To formulate an FV scheme, Eq. (2.4.15) is integrated over a cell of volume V_i and boundary ∂V_i:

$$\partial_t \int_{V_i} \Phi_\alpha \, dV + \int_{\partial V_i} \hat{\boldsymbol{n}} \cdot \boldsymbol{J}_\alpha \, ds = 0, \tag{2.4.16}$$

where $\hat{\boldsymbol{n}}$ is the unit out-normal vector of the cell surface. The time averaging of Eq. (2.4.16) over one time step leads to:

$$\overline{\Phi}_\alpha^{n+1} - \overline{\Phi}_\alpha^n + \frac{1}{V_i}\int_{t_n}^{t_{n+1}} dt \int_{\partial V_i} ds \, \hat{\boldsymbol{n}} \cdot \boldsymbol{J}_\alpha = 0, \quad \overline{\Phi}_\alpha := \frac{1}{V_i}\int_{V_i} \Phi_\alpha \, dV, \tag{2.4.17}$$

where $\overline{\Phi}_\alpha^n := \overline{\Phi}_\alpha(t_n)$ and $\overline{\Phi}_\alpha$ denotes the volume average of Φ_α.

The key feature that distinguished the GKS from all other FV schemes based on direct discretizations of the Navier-Stokes equations lies in the construction of the fluxes at cell interfaces. In the GKS, the fluxes are evaluated from the distribution function f based on Eq. (2.4.9), as opposed to various numerical differentiation techniques. For *smooth* flows without shocks, f can be approximated at the cell interface $\boldsymbol{x}_{i+1/2}$, as the following:

$$f(\boldsymbol{x}_{i+1/2}, \boldsymbol{\xi}, t) \approx [1 - \lambda\boldsymbol{\xi} \cdot \boldsymbol{a} + (t - t_n)A] f^{(0)}(\boldsymbol{x}_{i+1/2}, \boldsymbol{\xi}, t_n), \tag{2.4.18}$$

where $\boldsymbol{a} = \nabla \ln f^{(0)}$ and $A = \partial_t \ln f^{(0)}$ in 3D can be explicitly given:

$$a = \nabla \ln \rho + \left(\frac{c^2}{2RT} - \frac{3}{2}\right) \nabla \ln T + \frac{1}{RT} c_\alpha \nabla u_\alpha, \tag{2.4.19a}$$

$$A = -\xi \cdot a + \left(\frac{c^2}{2RT} - \frac{5}{2}\right) c \cdot \nabla \ln T + \frac{1}{RT}\left(cc - \frac{1}{3}c^2 \mathsf{I}\right) : \nabla u, \tag{2.4.19b}$$

where the convention for summation over the repeated indexes is used and I is the 3×3 identity matrix. In Eq. (2.4.18), two approximations have been applied. First, f is approximated by its second-order Chapman-Enskog expansion in the context of the BGK equation, *i.e.*, $f \approx (1 - \lambda D_t) f^{(0)}$. And second approximation is that $\partial_t f \approx \partial_t f^{(0)}$, which is consistent with the second-order Chapman-Enskog expansion and includes only the first-order derivatives of the hydrodynamic variables ρ, $\boldsymbol{u}$ and T.

To compute f at the cell boundary $x_{i+1/2}$, one needs $f^{(0)}$ and its derivatives at $x_{i+1/2}$, which in turn are given by the hydrodynamic variables and their derivatives at $x_{i+1/2}$. The hydrodynamic variables and their derivatives at $x_{i+1/2}$ are obtained by interpolations of their averaged values at cell centers $\{x_i\}$ about the cell boundary $x_{i+1/2}$. Consequently, the accuracy of the interpolations determines the accuracy of the GKS method. Once the value of f is known at the cell boundary $x_{i+1/2}$, the fluxes can be easily computed. For compressible flows, discontinuities of hydrodynamic variables at cell interfaces must be explicitly considered in computing f at cell boundaries based on Eqs. (2.4.18) and (2.4.19). For compressible flows with high enough Mach numbers, computing the values of hydrodynamic variables and their derivatives at the both sides of cell boundaries would involve limiters and artificial dissipation to stabilize the code. We usually use van Leer limiter when necessary.

We use the GKS method to simulate the fully compressible Navier-Stokes equations in 3D:

$$\partial_t \rho + \nabla \cdot \rho \boldsymbol{u} = 0, \tag{2.4.20a}$$

$$\partial_t \rho \boldsymbol{u} + \nabla \cdot \rho \boldsymbol{u}\boldsymbol{u} + \frac{1}{\gamma \mathrm{Ma}^2} \nabla p = \frac{1}{\mathrm{Re}} \nabla \cdot \boldsymbol{\sigma}, \tag{2.4.20b}$$

$$\partial_t E + \nabla \cdot E\boldsymbol{u} + \frac{1}{\gamma \mathrm{Ma}^2} \nabla \cdot p\boldsymbol{u} = \frac{1}{\alpha} \nabla \cdot (\kappa \nabla T) + \frac{1}{\mathrm{Re}} \nabla \cdot (\boldsymbol{\sigma} \cdot \boldsymbol{u}), \tag{2.4.20c}$$

$$\sigma_{ij} := \mu \left(\partial_i u_j + \partial_j u_i - \frac{2}{3} \nabla \cdot \boldsymbol{u} \delta_{ij}\right) + \eta \nabla \cdot \boldsymbol{u} \delta_{ij}, \quad \alpha := (\gamma - 1) \mathrm{Pr}\, \mathrm{Re}\, \mathrm{Ma}. \tag{2.4.20d}$$

The ideal-gas equations of state are used: $p = \rho RT$, and $\gamma = c_p / c_v = 7/5$. Sutherland's formula for the viscosity is also used:

$$\mu = \mu_0 \left(\frac{T_0 + C}{T + C}\right) \left(\frac{T}{T_0}\right)^{2/3}, \quad \kappa = \frac{c_p}{\mathrm{Pr}} \mu, \quad c_p = \frac{\gamma R}{(\gamma - 1)}, \tag{2.4.21}$$

where $C = 110°\mathrm{K}$, μ_0 and T_0 are determined by initial Ma_t and Re_λ.

To model nonequilibrium effects due to molecular internal degrees of freedom, we introduce a temperature T_R due to internal degrees of freedom which unequal to the translational temperature T_L, the internal energy is

$$\rho e = \frac{3}{2} RT_L + RT_R = \frac{5}{2} RT. \tag{2.4.22}$$

The collision term in the linearized Boltzmann equation is modified to:[8,9]

$$Q = -\frac{1}{\tau}[f - f_1] - \frac{1}{Z_r \tau}[f_1 - f^{(0)}], \tag{2.4.23a}$$

$$f_1 = \rho(2\pi RT_L)^{-3/2}(2\pi RT_R)^{-1}\exp(-(\xi - u)^2/2RT_L - \zeta^2/2RT_R), \tag{2.4.23b}$$

$$f^{(0)} = \rho(2\pi RT)^{-(3+Z)/2}\exp(-[(\xi - u)^2 + \zeta^2]/2RT), \tag{2.4.23c}$$

$$Z_r = \frac{Z_r^\infty}{1 + (\sqrt[3]{\pi^2}/2)\sqrt{T_*/T} + (\pi + \pi^2/4)(T_*/T)}, \tag{2.4.23d}$$

where $Z_r^\infty = 23.0$ and $T_* = 91.5°\mathrm{K}$. In the lowest-order Chapman-Enskog expansion, the collision term Q leads to a Landau-Teller type relaxation term in the NS equations

$$S = -\frac{\rho R}{Z_r \tau}[T_R - T]. \tag{2.4.24}$$

To model nonequilibrium effects due to finite Knudsen number Kn and rarefaction in gas flows, we modify the relaxation time[4-7]

$$\lambda^* = \frac{\lambda}{1 + \lambda\langle d_i^2 f^{(0)}\rangle / \langle d_i f^{(0)}\rangle}. \tag{2.4.25a}$$

$$\langle d_i f^{(0)}\rangle := \int D_i f^{(0)} \varphi(\xi) f d\Xi. \quad \langle D_i^2 f^{(0)}\rangle := \int D_i^2 f^{(0)} \varphi(\xi) f d\Xi, \quad d\Xi := d\xi d\zeta. \tag{2.4.25b}$$

We use $\varphi(\xi) = c^2$ for the relaxation time corresponding to the viscosity coefficient and $\varphi(\xi) = c_\alpha(c^2 + \zeta^2)$ for relaxation time corresponding to the heat conductivity coefficient in α-direction. In effect, $\langle d^2 f^{(0)}\rangle$ and $\langle df^{(0)}\rangle$ are computed as the functions of hydrodynamic variables as well as their spatial and temporal derivatives up to second order.

2.4.4 Compressible Decaying Isotropic Turbulence

We use a domain of size $L^3 = (2\pi)^3$ with periodic boundary conditions in all three directions and a Cartesian mesh of size N^3. A divergence-free random initial velocity field $\boldsymbol{u}_0(\boldsymbol{x})$ is specified with its root-mean-square (RMS) and the initial energy spectrum $E_0(k)$.[10,11]

$$u' := \frac{1}{\sqrt{3}}\sqrt{\langle \boldsymbol{u}\cdot\boldsymbol{u}\rangle}. \qquad E_0(k) = Ak^4\exp(-2k^2/k_0^2). \tag{2.4.26}$$

We compute one point statistical quantities (the total kinetic energy K, the dissipation rate ε, the energy spectrum $E(k,t)$ and the compensated energy spectrum $\Psi(k,t)$, the skewness S_u and the atness F_u of the velocity field $\boldsymbol{u}$), as well as the probability distribution functions (PDF's) of the two-point longitudinal velocity difference

$$\delta u(\boldsymbol{r}|\delta\boldsymbol{r}) := \delta\hat{\boldsymbol{r}}\cdot[\boldsymbol{u}(\boldsymbol{r}) - \boldsymbol{u}(\boldsymbol{r} + \delta\boldsymbol{r})], \quad \delta\hat{\boldsymbol{r}} := \frac{\delta\boldsymbol{r}}{\|\delta\boldsymbol{r}\|} \tag{2.4.27}$$

and the normal upstream shock Mach number $\mathrm{Ma}_\perp$ and the shock strength χ:[11]

$$\frac{\delta u}{c_*} = -\frac{2}{1+\gamma}\left(\mathrm{Ma}_\perp - \frac{1}{\mathrm{Ma}_\perp}\right), \quad \chi := (\mathrm{Ma}_\perp - 1). \tag{2.4.28}$$

2.4.5 Results and Discussions

Incompressible decaying homogeneous isotropic turbulence

We compare the lattice Boltzmann (LB) method with the pseudo-spectral (PS) method for direct numerical simulations of decaying homogeneous isotropic turbulence with the Taylor Reynolds number $\mathrm{Re}_\lambda = 24.37$ and the system size $N^3 = 128^3$. The simulations are carried out to $t' = t/\tau_0 \approx 30$, where $\tau_0 = K_0/\varepsilon_0$ is the turbulence turnover time.

We first examine a number of statistical quantities, such as the normalized kinetic energy $K(t')/K(0)$, the normalized dissipation rate $\varepsilon(t')/\varepsilon(0)$, the energy spectra $E(k,t')$, the skewness $S_u(t')$, and the flatness $F_u(t')$, as shown in Fig. 2.4.1. We observe that all the statistical quantities obtained by the LBE method agree very well with those obtained by the pseudo-spectral method.

We also compare the instantaneous velocity and vorticity fields obtained by the LBE and pseudo-spectral method, as shown in Fig. 2.4.2. Clearly the flow fields obtained with the two vastly methods agree very well with each other. This is important to note that the LBE method is only second-order accurate in space, while the pseudo-spectral method is exponentially accurate; and we have not seen any detailed comparison between a low-order method against a pseudo-spectral method in literature.

We have also used the LBE model for binary mixtures to simulate decaying turbulence. Our results show that the LBE model for mixtures can reproduce all known results of decaying turbulence and passive species dynamics in turbulence. The LBE model can also model active species dynamics due to difference in molecular weights and transport coefficient.[12]

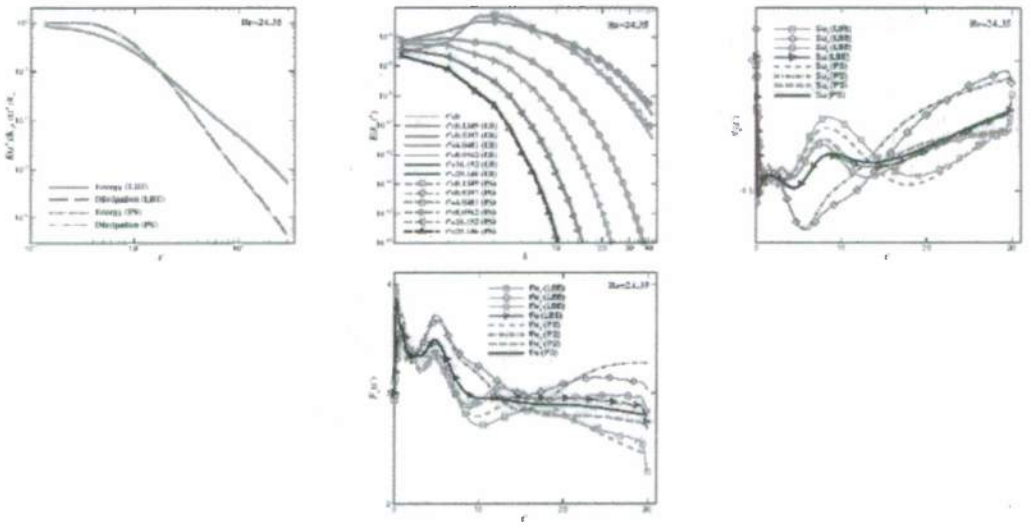

Fig. 2.4.1: The lattice Boltzmann vs. pseudo-spectral method. DNS of decaying homogeneous isotropic turbulence (DHIT) with $\mathrm{Re}_\lambda = 24.37$ and $N^3 = 128^3$. From left to right: the normalized total energy $K(t')/K(0)$ and normalized dissipation rate $\varepsilon(t')/\varepsilon(0)$; the energy spectra $E(k,t')$; the skewness $S_u(t')$; and the flatness $F_u(t')$.

Our systematic investigation shows that the LBE method is one of the most effective and

efficient numerical schemes to carry out accurate DNS for turbulence flows. Our results on multi-species LBE model have been published in Journal of Computational Physics,[12] and a paper on the comparative study of the LBE method versus pseudo-spectral method have submitted to Computers & Fluids.[13]

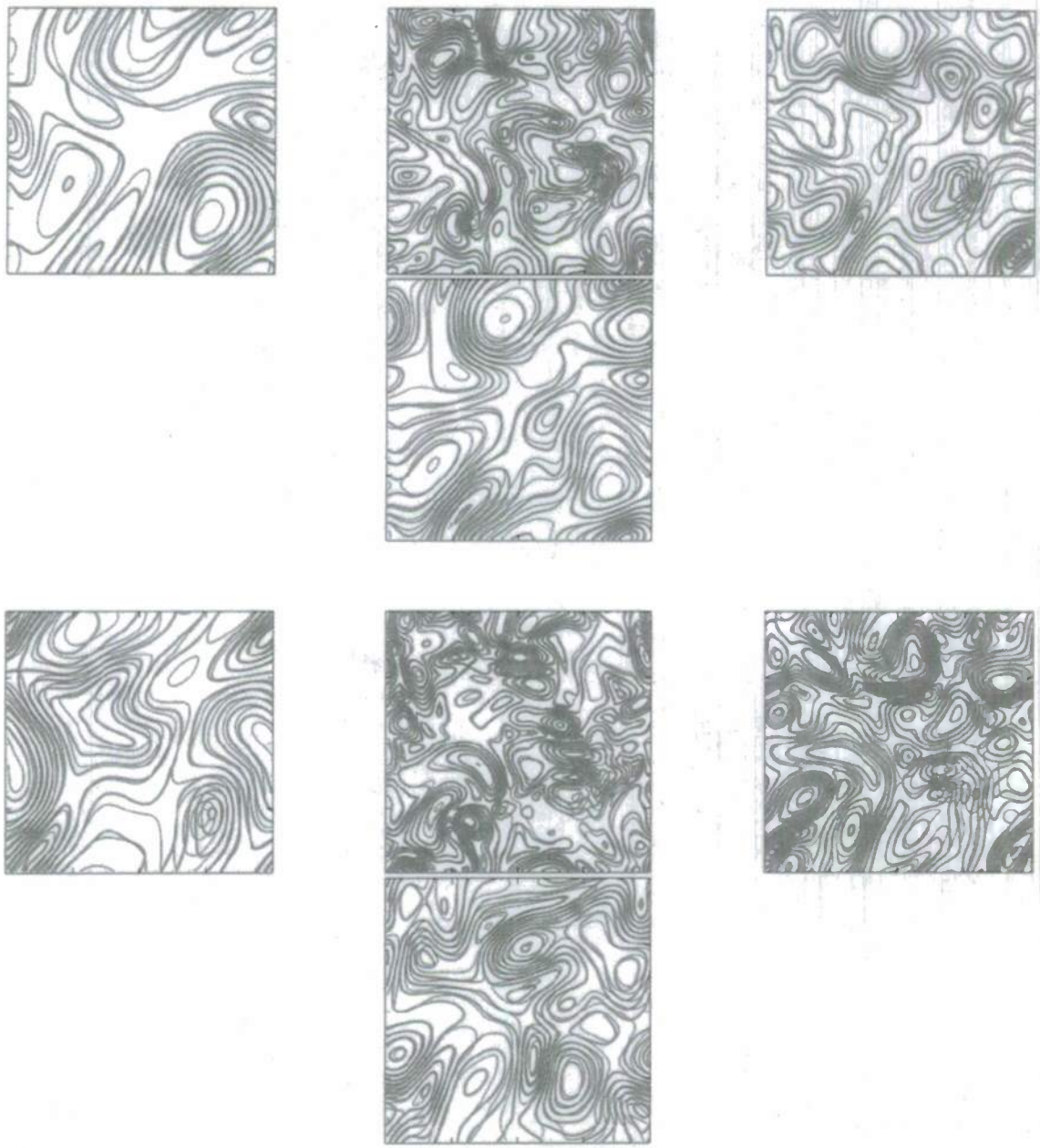

Fig. 2.4.2: The lattice Boltzmann (red) vs. pseudo-spectral method (green), the magnitudes of velocity field $\|u(t')/u'_0\|$ (top) and vorticity field $\|\omega(t')/u'_0\|$ (bottom) at the plane $z = \pi$. $\mathrm{Re}_\lambda = 24.37$ and $N^3 = 128^3$. From left to right: $t' = 4.048169$, 8.095571, 16.18959, and 29.94941.

Compressible decaying homogeneous isotropic turbulence

For the DNS of compressible turbulence,[14,15] we use $N^3 = 128^3$ and 256^3. The initial Taylor-microscale Reynolds number is $\mathrm{Re}_\lambda = 72.0$. The important feature is the generation of shocklets, as shown Fig. 2.4.3, which displays the areas of very sharp gradients in either the density ρ or the local Mach number Ma.

We first show the effect of Ma_t on the kinetic energy $K(t)$ and the dissipation rate $\varepsilon(t)$ in Fig. 2.4.4. To quantify the compressible effect, we apply the Helmholtz decomposition to the velocity field $\boldsymbol{u}$ so that $\boldsymbol{u}$ is decomposed into solenoidal (incompressible) and dilatation (compressible) components,[10]

$$\boldsymbol{u} = \boldsymbol{u}_C + \boldsymbol{u}_I, \quad \nabla \times \boldsymbol{u}_C = 0, \ \nabla \cdot \boldsymbol{u}_C = 0, \tag{2.4.29}$$

and so are the kinetic energy $K = K_C + K_I$ and the dissipation rate $\varepsilon = \varepsilon_C + \varepsilon_I$. While the initial turbulence Mach number Ma_t does not have observable effect on the total kinetic energy $K(t)/K(0)$ and the dissipation rate $\varepsilon(t)/\varepsilon(0)$, it does, however, have a significant effect on $K_C(t)/K(0)$ and $\varepsilon_C(t)/\varepsilon(0)$, the compressible components of $K(t)$ and $\varepsilon(t)$, respectively. As Ma_t increases, the compressible components of both $K(t)$ and $\varepsilon(t)$ increase considerably; when Ma_t increases from 0.1 to 0.625, both $K_C(t)$ and $\varepsilon_C(t)$ increase almost two orders of magnitude, as shown in Fig. 2.4.4. Because $K_C(t)$ and $\varepsilon_C(t)$ are small fractions of $K(t)$ and $\varepsilon(t)$, respectively, this explains the reason why the effects of Ma_t on both $K(t)$ and $\varepsilon(t)$ are difficult to be seen directly.

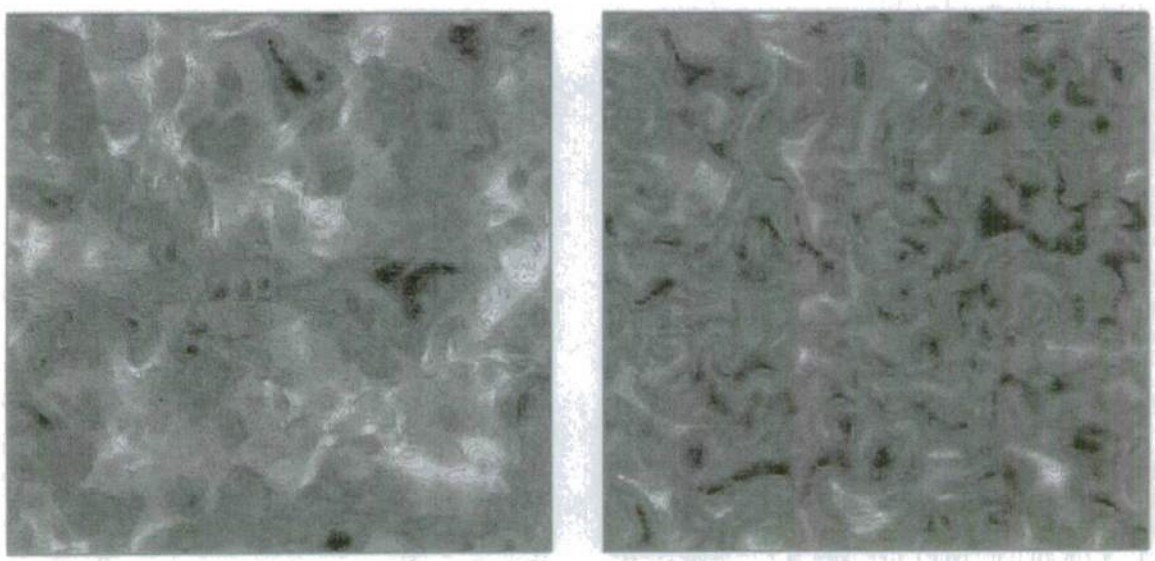

Fig. 2.4.3: Contours of the density (left) and the local Mach number (right) on the xy plane $k = 2$ when $t' = 1.03$. CFL = 0.5, $\mathrm{Ma}_t = 0.5$, $\mathrm{Re}_\lambda = 72.0$ and $N^3 = 128^3$.

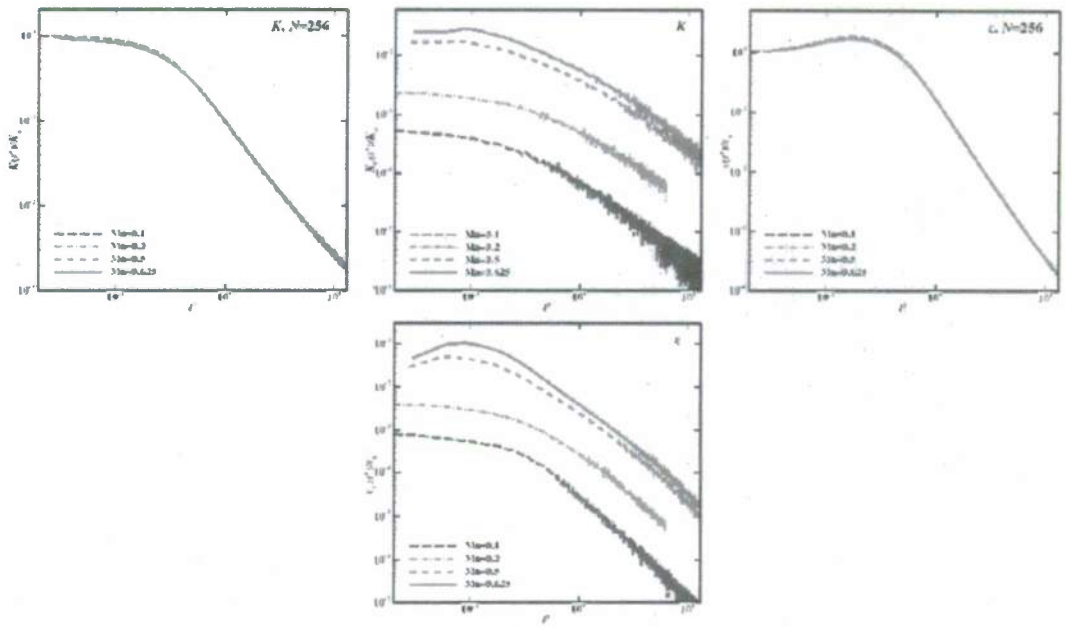

Fig. 2.4.4: Effects of Ma_t on $K(t)$ and $\varepsilon(t)$. The initial $Re_\lambda = 72.0$ and $N^3 = 128^3$, and $Ma_t = 0.1$, 0.2, 0.5 and 0.625. From left to right: $K(t)$, $K_C(t)$, $\varepsilon(t)$, and $\varepsilon_C(t)$.

In Fig. 2.4.5 we show the effects of the initial turbulence Mach number Ma_t on the PDF of the longitudinal velocity difference $\delta u(\delta r)$. Recall that the initial PDF $P(\delta u(\delta r), t = 0)$ is a Gaussian, independent of the separation δr. For a very small separation $\delta r = 1\delta x$, the PDF $P(\delta u(\delta r), t)$ remains very close to a Gaussian, as expected. For larger separations, the PDF $P(\delta u(\delta r), t)$ becomes non-Gaussian, and then evolves to became Gaussian eventually. The duration in which the PDF $P(\delta u(\delta r), t)$ with a given separation δr remains to be non-Gaussian depends on Ma_t. As shown in Fig. 2.4.5, as the initial turbulence Mach number Mat increases, the PDF $P(\delta u(\delta r), t)$ with $\delta r > 1\delta x$ becomes non-Gaussian faster in the initial stage, and then also decays to be Gaussian faster after the initial stage. In short, the increase of the initial turbulence Mach number Ma_t accelerates the evolution of the $P(\delta u(\delta r), t)$.

We also study the evolving statistics of the local Mach number Ma and the shocklet strength χ. In Fig. 2.4.6 and Fig. 2.4.7 we show the PDFs for the local Mach number Ma and the shocklet strength χ, respectively, in different times and with the initial turbulence Mach number Ma_t = 0.2 and 0.5. For the decaying turbulence, the energy decays monotonically in time. The PDF of Ma weakens and its peak approaches to Ma = 0 monotonically in time, shown in Fig. 2.4.6.

The evolution of the PDF of the shock strength χ is not a monotonic decaying process, shown in Fig. 2.4.7. In the initial stage, both its overall intensity and the position of its maximum of PDF(χ) increase in time. After reaching their maxima, both the overall intensity and the position of the maximum of PDF(χ) decay monotonically in time. The overall intensity and the position of its maximum of PDF(χ) increase as the turbulence Mach number Ma_t increases. This is consistent with the development and decay of shocks in the compressible turbulence: the

shocklets are developed in the nonlinear initial stage before the total energy is significantly dissipated, and afterward, shocklets decay in number and intensity monotonically as the energy decays monotonically in time. The stronger the turbulence Mach number Ma_t, the more shocklets with stronger intensities are developed in the initial nonlinear stage.

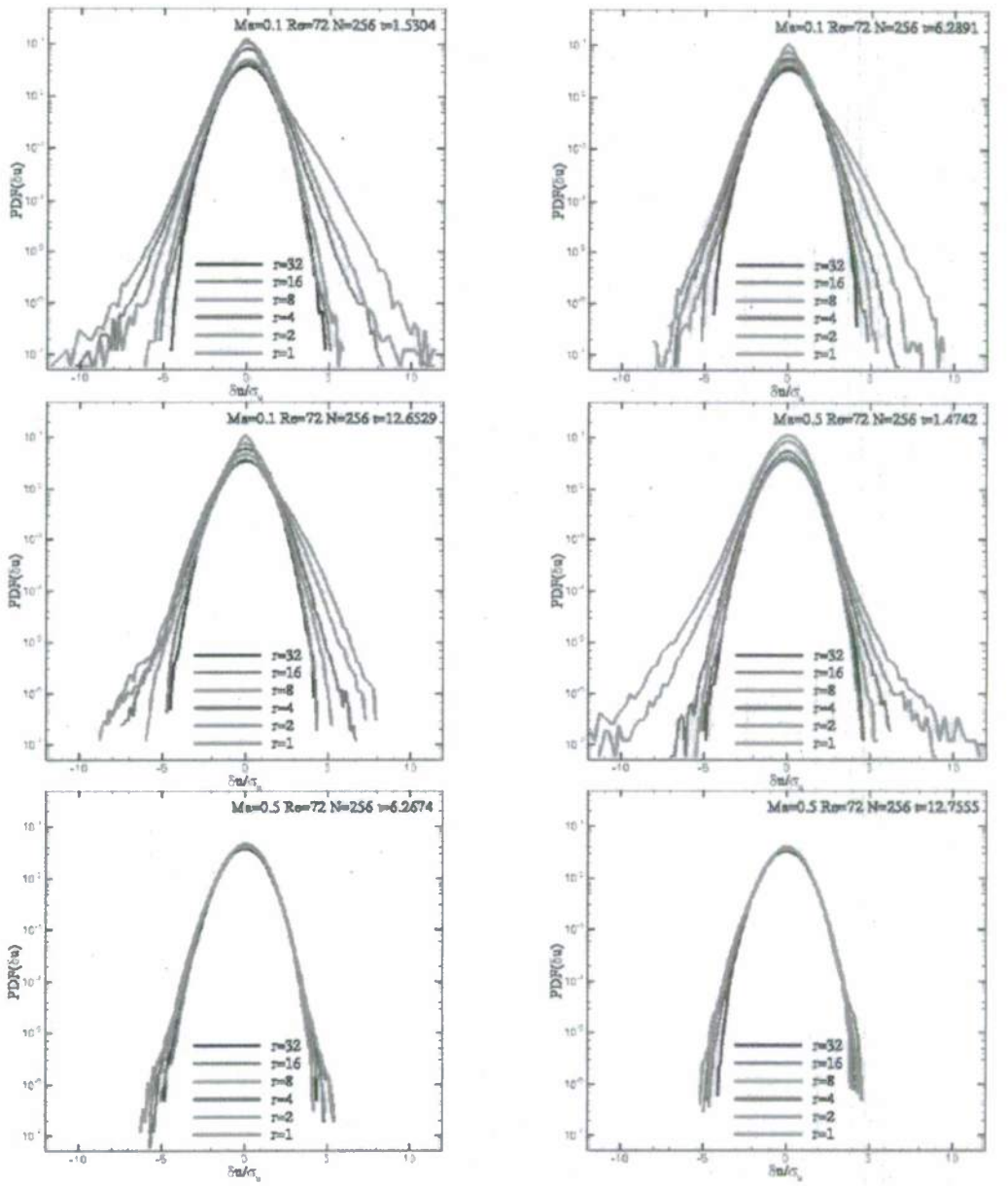

Fig. 2.4.5: Effects of Ma_t on the PDF of $\delta u(\delta r)$. $\mathrm{Ma}_t = 0.1$ (top row) and $\mathrm{Ma}_t = 0.5$ (bottom row), in three different times increasing from left to right.

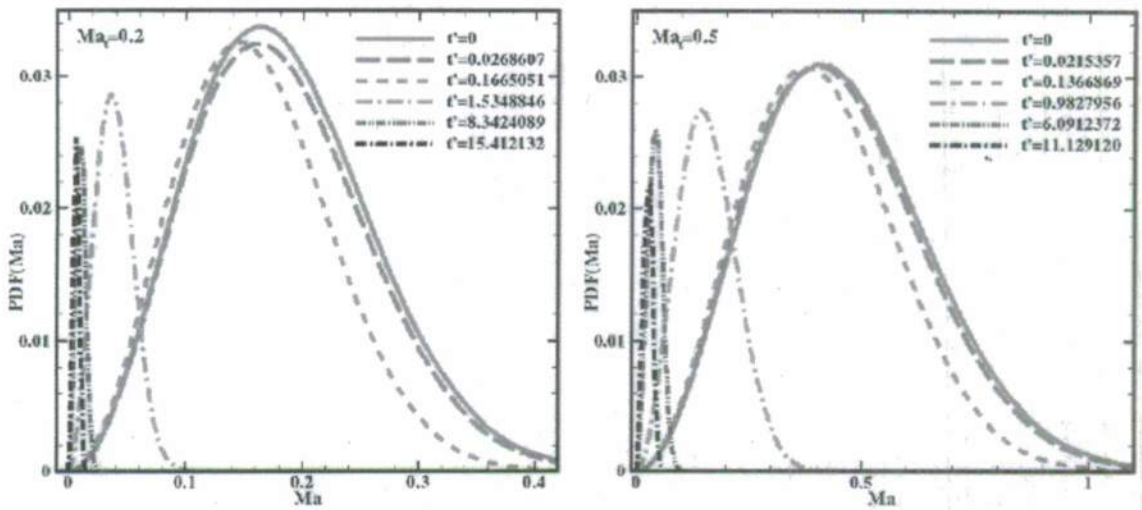

Fig. 2.4.6 The PDFs of the local Mach number Ma with $\mathrm{Ma}_t = 0.2$ (left) and 0.5 (right).

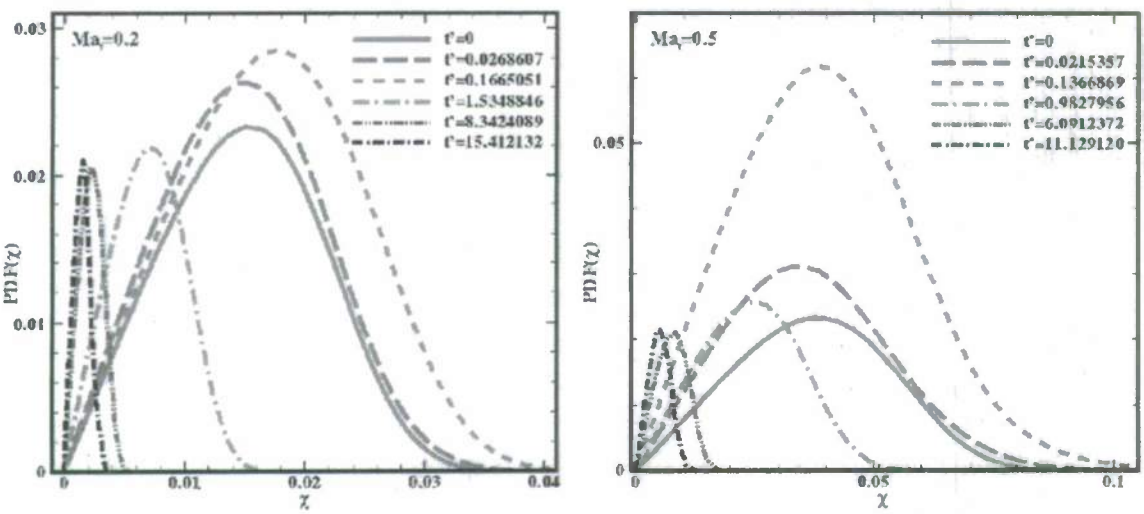

Fig. 2.4.7 The PDFs of the shock strength χ with $\mathrm{Ma}_t = 0.2$ (left) and 0.5 (right).

We rescale the PDFs of Ma and χ such that their maxima are always located at 1 and satisfy the normalization condition that

$$P(x_0) = 1, \quad x_0 = \chi_0 \text{ or } \mathrm{Ma}_0. \tag{2.4.30}$$

where χ_0 and Ma_0 are the maximum values of χ and Ma, observed in the DNS data, respectively. The rescaled PDF's of χ and Ma are shown in Fig. 2.4.8.

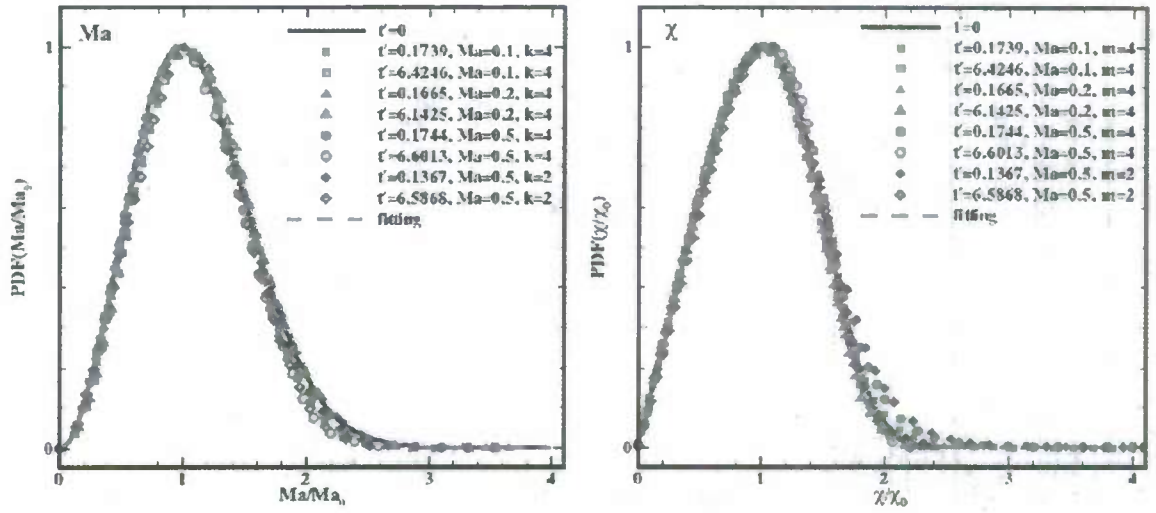

Fig. 2.4.8 The rescaled PDFs of the local Mach number Ma (left) and the shock strength χ (right), with initial Ma_t = 0.1, 0.2, and 0.5.

We note that the rescaled PDFs of χ and Ma in Fig. 2.4.8 all collapse to the distribution of the initial PDFs determined by the initial Gaussian velocity field, independent of Ma_t. This indicates that the PDFs of both χ and Ma obey some universal similarity laws, which have not been observed previously.

Effects of internal degree of freedom

Using the GKS scheme with the internal degrees of freedom T_R, we can quantify the influence of T_R on the turbulence.[16] In Fig. 2.4.9 we show the effect of the non-equilibrium temperature T_R on $K(t)$ and $\varepsilon(t)$ and $S_u(t)$. We set T_R/T_L = 1.0, 1.5, and 3.0 initially. We note that the dilatational components are small fractions in the total energy and the dissipation rate, and as the initial value of T_R/T_L, *i.e.*, the fraction of internal energy increases, the fraction of dilatational components in K and ε decrease monotonically. Indeed, as the initial value of T_R/T_L increases, the behavior of the skewness $S_u(t)$ is closer to that of incompressible decaying turbulence.

We observe that the effect due to nonequilibrium internal degrees of freedom modeled by T_R is similar to the increasing of Ma_t, but in a much more severe manner. For example, the PDF of the longitudinal velocity difference, $P(\delta u(\delta r), t)$, becomes a Gaussian very quickly in time for the case with a nonequilibrium T_R.

We also assess the effect of the coupling parameter Z_r in the multi-temperature model. To simplify the analysis, we set Z_r as a constant and use Z_r = 2.0, 10.0, and 200 in our simulations, with other conditions fixed. The parameter Z_r mainly determines the relaxation time for the temperatures T_L and T_R, as shown in the left plot in Fig. 2.4.10. The larger Z_r is, the longer the relaxation time. Also, as Z_r increases, the RMS velocity divergence $\theta'/\omega'(0) = \|\nabla \cdot \boldsymbol{u}'(t)\|/\|\nabla \times \boldsymbol{u}'(0)\|$ decreases, as shown in the center left plot in Fig. 2.4.10. This is consistent with the multi-temperature collision model. Consequently, as Z_r increases, the flow behavior is

closer to that of incompressible decaying turbulence, as shown in the right plot of $S_u(t)$ in Fig. 2.4.10.

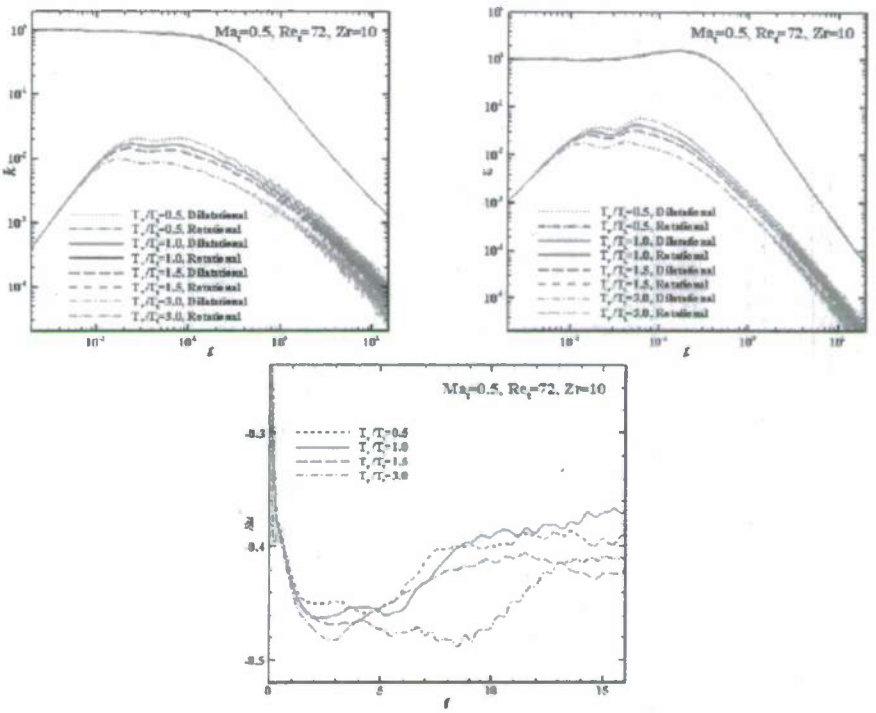

Fig. 2.4.9 The dependence of the dilatational and solenoidal parts of the kinetic energy $K(t')/K(0)$ (left) and the dissipation rate $\varepsilon(t')/\varepsilon(0)$ (center), and the skewness S_u (right) on T_R/T_L . $Ma_t = 0.5$, $Re_\lambda = 72.0$ and $N^3 = 128^3$.

Non-equilibrium flows: Shock-shock and shock-boundary-layer interactions

The hypersonic flow in a hollow flare at Ma = 9.91 and the hypersonic flow past a 25°-55° double-cone at Ma = 9.59 are two canonical flow configurations chosen for validation and verification of numerical schemes for non-equilibrium flows involving shock-shock and shock-boundary-layer interactions. Due to severe effects caused by shock-shock and shock-boundary-layer interactions as well as non-equilibrium rarefaction, it is challenging to simulate these flows. We apply the GKS to simulate these two flows.[6]

The free stream conditions are $Ma_\infty = 9.91$, $p_\infty = 6.3$(Pa), $T_\infty = 51$(°K), Kn = 0.005, and the wall temperature $T_w = 293$(°K). The mesh size used for the flow in a hollow flare is 241 × 161.

We first show the pressure coefficient C_p, the Stanton number St, and the skin friction coefficient C_f,

$$C_p := \frac{(p - p_\infty)}{\frac{1}{2}\rho_\infty U_\infty}, \quad \mathrm{St} := \frac{\kappa \partial_n T|_{\mathrm{wall}}}{\rho_\infty u_\infty (H_0 - H_w)}, \quad C_f := \frac{2\tau_w}{\rho_\infty U_\infty^2}, \tag{2.4.31}$$

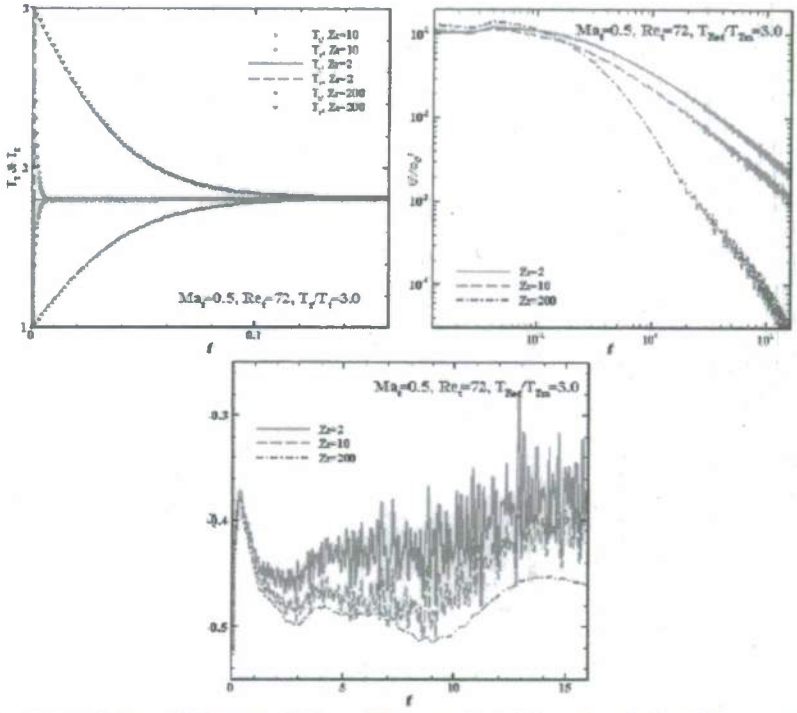

Fig. 2.4.10 The Z_r -dependence of the translational temperature T_L and rotational temperature T_R (left), the RMS velocity divergence $\theta'/\omega'(0)$ (right), and the skewness S_u (right). $Ma_t = 0.5$, $Re_\lambda = 72.0$ and $N^3 = 128^3$.

in Fig. 2.4.11 and density problems in Fig. 2.4.12, and compare the GKS results with existing data obtain experimentally and numerically by using other methods including DSMC and Navier-Stokes (NS) solvers (FLOW and NASCA)[17].We also measure the separation/ reattachment lengths of the flow and the results are given in Table 2.4.1.

Abscissa x/L	NS	DSMC	GKS	Exp.
Separation	0.74–0.75	0.76	0.745	0.76 ± 0.01
Reattachment	1.33	1.32	1.341	1.34 ± 0.01

Table 2.4.1: Flow in a hollow flare. Measurements of separation/reattachment lengths. The experimental, DSMC, NS (FLOW and NASCA) data are taken from Gorchakova *et al.* [17] AIAA J. 40(4):593 (2002).

We next show the results for the hypersonic flow past a double cone. The free stream conditions are: $Ma_\infty = 9.59$, $p_\infty = 36.06$(Pa), $T_\infty = 185.6$(°K), $T_w = 293.3$ (°K), $Re_\infty = 12{,}838$ (based on the length of the first cone L = 3.625"), and $Kn_\infty \approx 1.1\times10^{-3}$. We use a mesh of size 481×201.

Fig. 2.4.13 shows the contours of the Mach number Ma/Ma_∞, the pressure p/p_∞, and the temperature T/T_∞, and Fig. 2.4.14 shows the contours of ρ/ρ_∞ around the recirculation region, p/p_∞ around the strong shock interaction region, and the density Schliere of the GKS simulation compared with experimental one. These figures clearly demonstrate the complexity of

the flow.

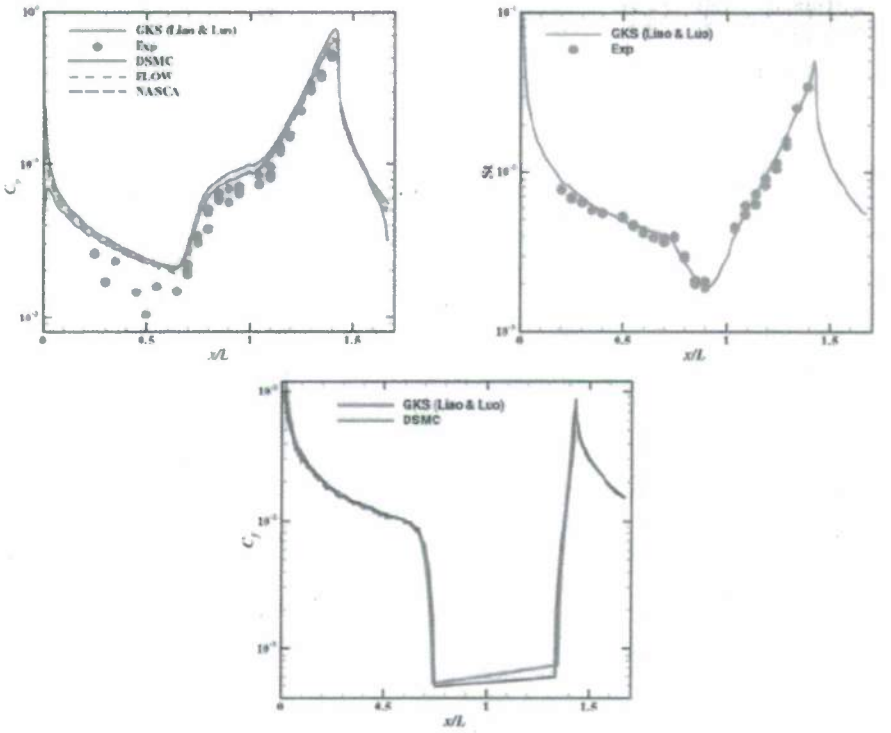

Fig 2.4.11 Flow in a hollow flare. The pressure coefficient C_p, the Stanton number St, and the skin friction coefficient C_f. The experimental, DSMC, FLOW (FE), and NASCA (FV) data are taken from Gorchakova *et al.*[17] AIAA J. 40(4):593 (2002).

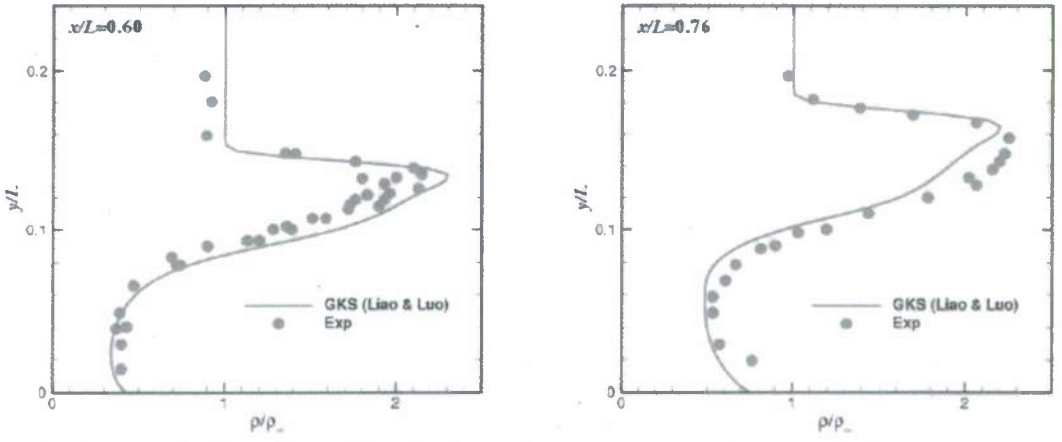

Fig. 2.4.12 Flow in a hollow flare. The density problem ρ / ρ_∞ at x/L = 0.60 (left, pre-separation) and 0.76 (right, post-separation). The experimental data are taken from Gorchakova *et al.* [17] AIAA J. 40(4):593 (2002).

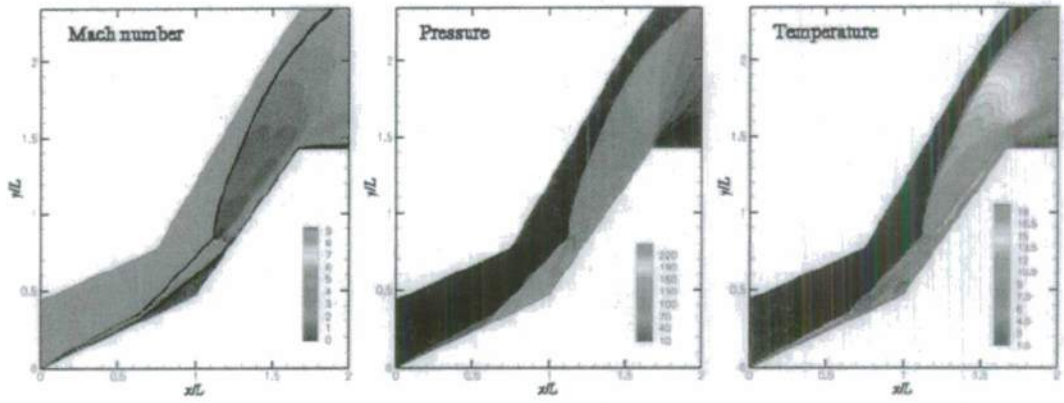

Fig. 2.4.13 Hypersonic flows past a double cone. Left to right: the contours of Mach number $\mathrm{Ma}/\mathrm{Ma}_\infty$, the pressure p/p_∞, and the temperature T/T_∞.

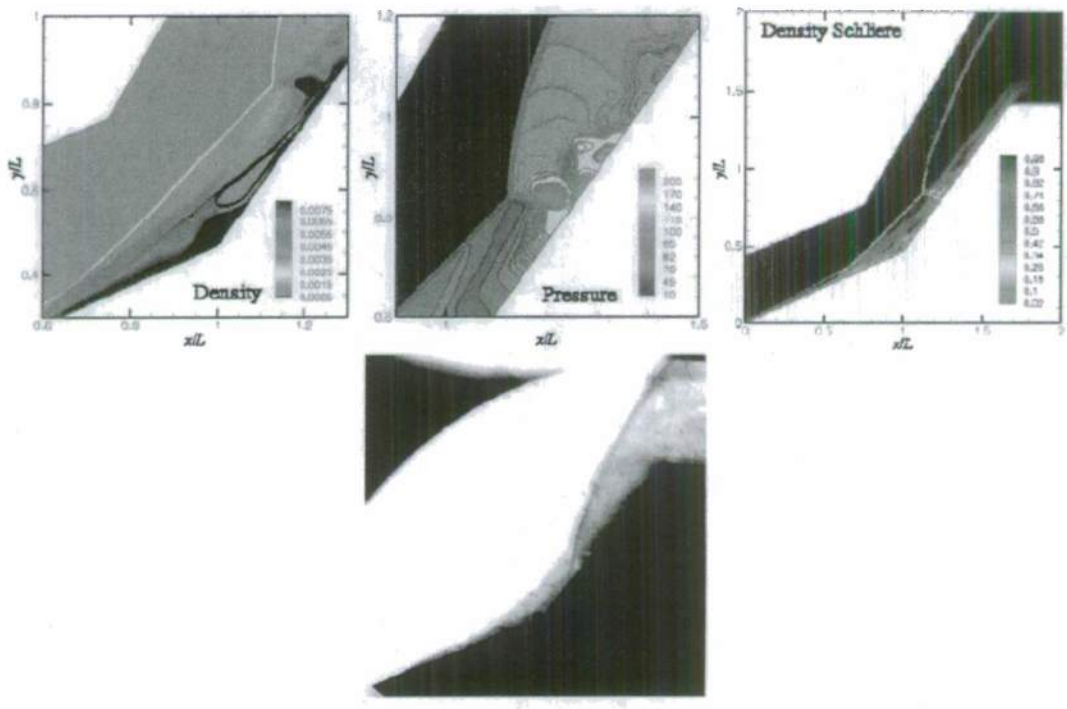

Fig. 2.4.14 Hypersonic flows past a double cone. Left to right: the contours of ρ/ρ_∞ in the recirculation region, p/p_∞ in shock interaction region, the GKS and experimental density Schlieres.

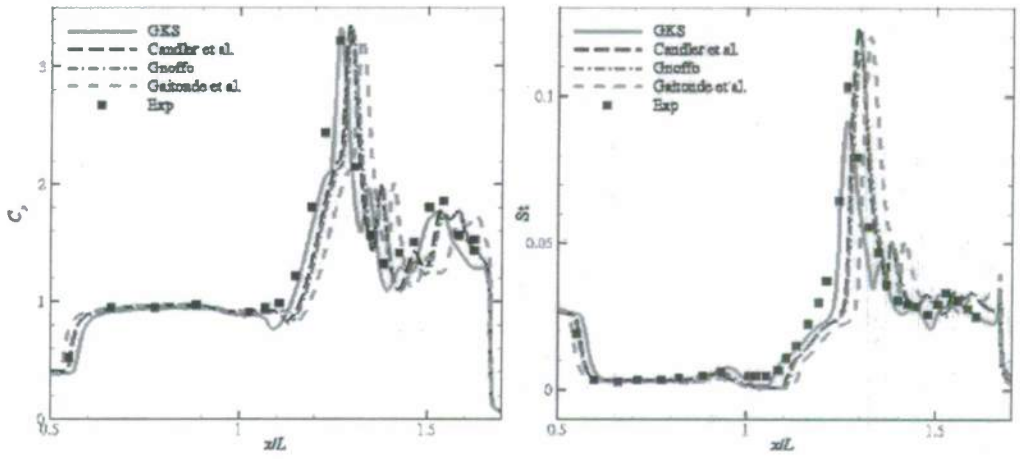

Fig. 2.4.15 Hypersonic flows past a double cone. The pressure coefficient C_p (left) and the Stanton number St (right).

We also compare our results with existing data[18-20] quantitatively. Fig. 2.4.15 shows the pressure coefficient C_p and the Stanton number St. Table 2.4.2 shows the measurements of separation/reattachment lengths[18,21]. The GKS results agree well with existing experimental data and accurate numerical results obtained by other methods. These results clearly show the capability of the GKS method to accurately simulate the hypersonic flows with complicated shock-shock and shock-boundary-layer interactions.

Abscissa x/L	LAURA	NS	GKS
Separation	0.5555	0.5594	0.5755
Reattachment	1.291	1.287	1.263
Length	0.7355	0.7276	0.6875
mesh size	1024×256	1024×256	481×201

Table 2.4.2 Hypersonic flows past a double cone. Measurements of separation/reattachment lengths.

Non-equilibrium flows: Shock structures

The detailed structures within a shock in gases, of which the extend is only a few mean-free paths of the gas molecules, cannot be resolved by the Navier-Stokes equations. The Boltzmann equation is required to resolve shock structures and usually the direct simulation Monte Carlo (DSMC) method, a stochastic method, is used to solve shock structures in gases. We will use the modified GKS method with a relaxation time depending on the local hydrodynamic variables and their derivatives to model shock structures.[7]

We first show the results of the density and temperature problems of monoatomic Argon gas inside a shock of Ma= 8.0 and 9.0 in Fig. 2.4.16,

$$\frac{\delta\rho}{\Delta\rho} := \frac{(\rho-\rho_1)}{(\rho_2-\rho_1)}, \quad \frac{\delta T}{\Delta T} := \frac{(T-T_1)}{(T_2-T_1)}, \quad \lambda_1 := \frac{2\mu(7-2\omega)(5-2\omega)}{15\rho_1\sqrt{2\pi RT_1}}. \tag{2.4.32}$$

We compare the results obtained by using the modified GKS method with the data obtained by experiments[22] and the DSMC method.[23]

The problems of the stress τ_{xx} and the heat-flux q_x for a monoatomic gas inside the shock of Ma= 8.0 are shown in Fig. 2.4.17. The results obtained by the modified GKS method (with a variable relaxation time depending on the hydrodynamic variables and their derivatives) are compared with DSMC data.[23]

In Figs. 2.4.16 and 2.4.17, "GKS-Noneq" and "GKS" indicate data obtained by the GKS method with and without variable relaxation time. The GKS method without the variable relaxation time is practically a Navier-Stokes solver, thus it is incapable of resolving structures within a shock. When compared with DSMC[23] and experimental data[22], our results clearly show that the modified GKS method is capable of resolving shock structures, which is beyond the validity of the Navier-Stokes equations and continuum theory. The modified GKS method is also more efficient than the DSMC method. Our results of the modified GKS method for shock structures have been recognized in the Year in Review of Aerospace America, 2007, published by the American Institute of Aeronautics and Astronautics (AIAA).

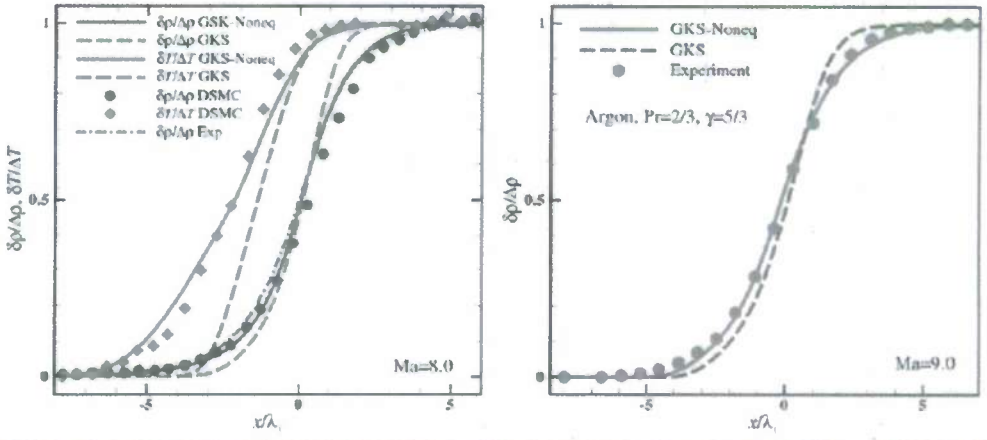

Fig. 2.4.16 The density and temperature profiles of monoatomic Argon gas inside a shock of Ma= 8.0 (left) and 9.0 (right).

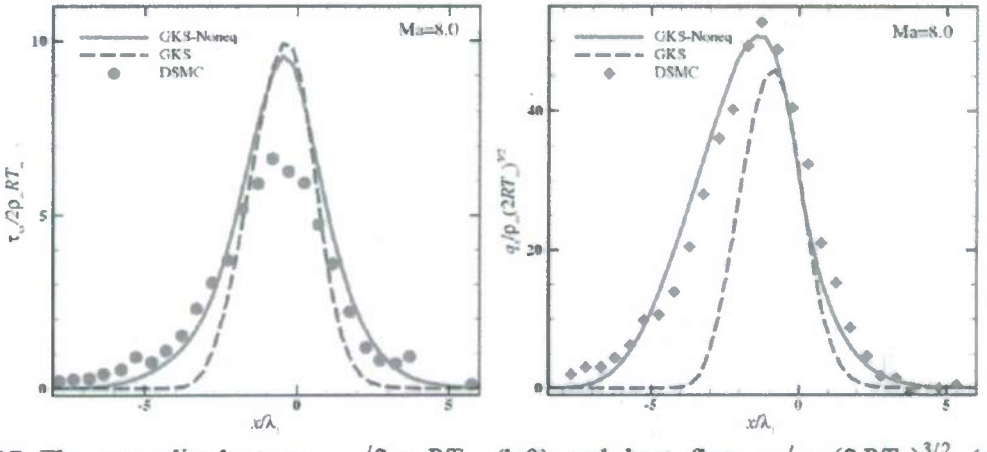

Fig. 2.4.17 The normalized stress $\tau_{xx}/2\rho_\infty RT_\infty$ (left) and heat flux $q_x/\rho_\infty(2RT_\infty)^{3/2}$ (right) of monoatomic Argon gas inside a shock of Ma= 8.0.

Multigrid scheme with textbook-efficiency

Efficient numerical schemes for time integration are crucial to the DNS of turbulence. We envision that implicit time-integration techniques will be important for direct numerical simulations (DNS) for flows at high Reynolds numbers. Therefore, the computational efficiency of implicit flow solvers becomes critically important. The textbook multigrid efficiency (TME), which is the optimal efficiency of a multigrid method, is achieved if accurate solutions of the governing equations are obtained with the total computational work that is a small (less than 10) multiple of the operation counts in one residual evaluation.

We have developed a TME solver for unsteady subsonic compressible Navier-Stokes equations in three dimensions discretized with an implicit, second-order accurate in both space and time, unconditionally stable, and non-conservative scheme. A semi-Lagrangian approach is used to discretize the time-dependent convection part of the equations; viscous terms and the pressure gradient are discretized on a staggered grid. The TME solver for the implicit equations is applied at each time level. The computational efficiency of the solver is designed to be independent of the Reynolds number. Our tests show that the proposed solver maintains its optimal efficiency at high Reynolds numbers and for large time steps.[24]

2.4.6 Summary

Under the MURI project, the accomplishments of the ODU team have developed a suite of kinetic schemes which are efficient and effective to simulate near incompressible and fully compressible non-thermochemical-equilibrium (NTE) flows. Our codes are fully validated. Our codes are capable of simulating flows with multi-species, internal degrees of freedom, and non-zero Knudsen number rarefaction effects. The codes developed under this project are listed below:

1) Lattice-Boltzmann (LB) code with multiple-relaxation-time (MRT) model for single-species low-Mach-number flows in 3D;
2) LB code with MRT model for low-Mach-number flows of multiple-species mixtures in 3D;
3) Gas kinetic scheme (GKS) for flow with strong shock-shock and shock-boundary-layer interactions in 2D and 3D;
4) GKS for flow with non-equilibrium internal degrees of freedom in 3D;
5) GKS for flow with variable relaxation time for non-equilibrium flows with non-zero Knudsen number in 2D;
6) Implicit multi-grid Navier-Stokes solver with textbook multi-grid efficiency for unsteady subsonic compressible Navier-Stokes equations in 3D.

We have used the kinetic schemes to carry out the direct numerical simulations of decaying isotropic homogeneous turbulence (DIHT) with and without non-thermochemical-equilibrium conditions. We investigate the effects on DIHT due to the turbulent Mach number and internal degrees of freedom. We discover universal similarities obeyed the probability distribution functions (PDFs) of the local Mach number and the shock strength incompressible decaying turbulence.

References

1. P. Lallemand and L.-S. Luo, Theory of the lattice Boltzmann method: Dispersion, dissipation, isotropy, Galilean invariance, and stability, Physical Review E **61**:6546-6562 (2000).
2. D. d'Humières, I. Ginzburg, M. Krafczyk, P. Lallemand, and L.-S. Luo, Multiple-relaxation-time lattice Boltzmann models in three-dimensions, Philosophical Transactions of Royal Society of London A **360** (1792):437-451 (2002).
3. K. Xu, , A gas-kinetic BGK scheme for the Navier-Stokes equations and its connection with artificial dissipation and Godunov method, J. Computat. Phys. **171**(1):289-335 (2001).
4. K. Xu, and L. Tang, Nonequilibrium Bhatnagar-Gross-Krook model for nitrogen shock structure, Phys. Fluids **16**(10): 3824-3827 (2004).
5. K. Xu, and E. Josyula, Continuum formulation for non-equilibrium shock structure calculation, Comm. Comput. Phys. **1**(3), 425-450 (2006).
6. W. Liao, L.-S. Luo, and K. Xu. Gas kinetic scheme for continuum and near-continuum hypersonic flows. AIAA J. Rocket and Spacecraft **44**(6):1232-1240 (2007).
7. W. Liao, Y. Peng, L.-S. Luo, and K. Xu. Modified gas-kinetic scheme for shock structures in argon. Prog. Comput. Fluid Dyn. **8**(1-4):97-108 (2008).
8. K. Xu and H. Liu. A multiple temperature kinetic model and its application to near continuum flows. Comm. Comput. Phys. **5**:1069-1085 (2008).
9. K. Xu, X. He, and C. Cai. Multiple temperature kinetic model and gas-kinetic method for hypersonic non-equilibrium flow computations. J. Comput. Phys. **227**:6779-6794 (2008).
10. S. Sarkar, G. Erlebacher, M. Y. Hussaini, and H. O. Kreiss. The analysis and modelling of dilatational terms in compressible turbulence. J. Fluid Mech. **227**:473-493 (1991).
11. R. Samtaney, D.I. Pullin, and B. Kosovi'c. Direct numerical simulation of decaying compressible turbulence and shocklet statistics. Phys. Fluids **13**(5):1415-1430 (2001).
12. P. Asinari and L.-S. Luo. Direct numerical simulation of decaying homogeneous isotropic turbulence for a binary mixture by using a consistent lattice Boltzmann equation. J. Comput. Phys. **227**(8):3878-3895 (2008).
13. Y. Peng, W. Liao, L.-S. Luo, and L.-P. Wang. Comparison of the lattice Boltzmann and pseudo-spectral methods for decaying turbulence. Part I. Low-order statistics. Submitted to Comput. Fluids (2008).
14. W. Liao, Y. Peng, and L.-S. Luo. Gas kinetic schemes for DNS of compressible homogeneous turbulence. Submitted to Phys. Rev. E (2009).
15. W. Liao, Y. Peng, L.-S. Luo, and R. Rubinstein. Mach number effects in statistics of decaying compressible turbulence. To be submitted to J. Fluid Mech. (2009).
16. W. Liao, Y. Peng, and L.-S. Luo. **Decay of compressible homogeneous turbulence with multi-temperature non-equilibrium**, Accepted for 48th AIAA Aerospace Sciences Meeting, Orlando, FL, Jan. 2010.
17. N. Gorchakova, L. Kuznetsov, V. Yarygin, B. Chanetz, T. Pot, R. Bur, J. P. Taran, D. Pignche, D. Schulte, and J. Moss, Progress in hypersonic studies using electronic-beam-excited x-ray detection, AIAA J. **40**(4):593–598 (2002).
18. P. Gnoffo. CFD validation studies for hypersonic flow prediction. AIAA-2001-1025.
19. G. V. Candler, I. Nompelis, and M.-C. Druguet. Navier-Stokes predictions of hypersonic double-cone and cylinder-flare flow fields. AIAA-2001-1024.
20. D. Gaitonde, P. W. Ganupp, and M. S. Holden. Heat transfer predictions in a laminar

hypersonic viscous/inviscid interaction. J. Thermophys. Heat Transf. **16**(4):481-489 (2002).
21. I. Nompelis. Computational study of hypersonic double-cone experiments for code validation. PhD thesis, University of Minnesota, 2004.
22. B. Schmidt, Electron beam density measurements in shock waves in argon, J. Fluid Mech. 39:361-373 (1969).
23. G. A. Bird, Aspects of the structure of strong shock waves, Phys. Fluids **13**(5):1172-1177 (1970).

W. Liao, B. Diskin, Y. Peng, and L.-S. Luo. Textbook-efficiency multigrid solver for three-dimensional

Chapter 3

Progress in Experiments and Diagnostics

The Experimental Team consisted of R. Bowersox and S. North (TAMU), G. Elliott and J. Austin (UIUC) and R. Lucht (Purdue). The TAMU team (Bowersox and North) was responsible for the following tasks:

(1) Create the mathematical framework for the modeling and measurements with emphasis on the coupled non-equilibrium thermodynamics and flow kinematics. *A new internal energy based framework was established* [Bowersox 2009, 2009a, Bowersox et al (2008)]. This is described in more detail in Chapter 2.

(2) Develop facilities to perform NTE experiments for model verification and validation.

- At TAMU, *new RF-Plasma Decaying Mesh and Actively Controlled Expansion Hypersonic Wind Tunnel facilities were developed during this effort.*
- At UIUC, *three new test facilities (expansion tube, blow-down wind tunnel and low pressure jet facility) have been demonstrated and quantified.*

(3) Develop new diagnostic methods to characterize the coupled turbulence and NTE.

- At TAMU, a *new diagnostic method that utilized Vibrationally Enhanced NO Monitoring (VENOM) was developed in this effort.* [Hsu et al (2009, 2009a - 2009c)]. This is the first known technique to allow for coupled molecular tagging velocimetry and internal/external state thermometry. In addition, a combined PIV/PLIF system was developed
  - At Purdue, *a new planar laser-induced fluorescence (PLIF) imaging technique for simultaneous determination of pressure, temperature, and velocity in supersonic and hypersonic flows was developed and tested.* The PLIF images were acquired following laser excitation of nitric oxide (NO) seeded into the flow.
  - At UIUC, *new methods to exploit Doppler shift and broadening characteristics of Rayleigh scattering were developed to determine mean and turbulent flow properties and a single component of velocity from a single laser pulse.* In addition, detailed MTV and PIV measurements were acquired to assess particle lag issues.

(4) Characterize the RF-NTE Plasma.

- At TAMU, *Coherent Anti-Stokes Raman Spectrometry (CARS), high resolution emission spectroscopy, and detailed state-to-state calculations were used to characterized the vibrational state of the nitrogen; the only excited major species within the plasma.*
- *At UIUC, an existing state-resolved three-dimensional forced harmonic oscillator thermochemical model was extended by modifying the molecular-molecular energy transfer rate model to higher collisional energies.* The model was verified experimentally.

(5) Perform the basic model driven experiments.

- At TAMU, Two sets of experiments were planned: decaying mesh turbulence with RF-NTE and a supersonic shear layer with RF-NTE.

  The purpose of the decaying mesh experiments was to provide improved understanding of the effects of vibrational relaxation on basic transport of turbulence.

In the decaying mesh experiments, we demonstrated and characterized mechanisms for the coupling between the vibration relaxation of nitrogen and the basic decay rate of the turbulent kinetic energy.

The purpose of the Shock-Induced-Shear-Layer (SISL) experiment was to provide improved understanding of the turbulent transport of vibrationally active molecules. These data form the basis for model validation [Bowersox (2009a)]. Unfortunately, the wind tunnel facility infrastructure (compressors and dryers) failed, and delayed the project by 12 months. The SISL model was designed and constructed and preliminary tests were performed. *The planned detailed turbulence studies were not accomplished prior to this report.* However, the experiments are currently underway, and will be reported at a later date.

- AT UIUC, experiments were performed in three flows: i) comprehensive velocity field data to compare axisymmetric nitrogen jets produced under various conditions with and without the RF plasma field applied, ii) characterization of the dissociation and thermal relaxation region behind a normal shock, iii) spatial linear stability analysis of a shear layer with a detailed thermochemical modeling, iv) evaluation of the interaction of several types of plasmas/plasma actuators with the supersonic Mach 4 boundary layer.

  A comprehensive set of PIV data was collected comparing axisymmetric nitrogen jets produced under various conditions with and without the RF plasma field applied. A significant effect of the RF-plasma on the jet and converging-diverging exit profiles was observed.

  Vibrational temperature measurements in a post-s hock relaxation region in Mach 7.42 flow were accomplished using emission spectroscopy of NO. The contribution of higher vibrational and rotational levels at the conditions of this study was demonstrated.

  The spatial linear stability of a shock-interaction generated shear layer separating stream of gas with substantially different thermal and chemical properties was examined. A substantial difference in two- and three-dimensional perturbation growth rates was observed among the three models. Dissociation and vibration transfer effects on the perturbation evolution remained closely correlated at all convective Mach numbers.

  RF-plasma interaction with a Mach 4 boundary layer was studied through emission photography, Schlieren imaging, and high-frequency pressure measurements. An unsteady plasma interface was observed to convect upward by buoyant forces, causing the boundary layer to separate immediately downstream of the discharge. The boundary layer reattached shortly thereafter.

3.1 Experiments and Diagnostic Development at TAMU (Bowersox and North)

3.1.1 Experimental Goals

The overarching goals of the experimental studies were to provide measurements for (1) improved understanding of the basic NTE and turbulence coupling mechanisms and (2) model verification and validation.

Decaying mesh turbulence with vibrational non-equilibrium was studied to better appreciate the role of thermal non-equilibrium on the transport of turbulence. The basic question to be addressed was: Does thermal non-equilibrium alter the basic transport of turbulence, and if so, to what extent?

The shock-induced shear layer (SISL) experiment was conceived to provide detailed data to verify and validate models for the transport of a vibrationally relaxing molecule (NO) in a turbulent shear layer. Energy flux models for the processes were described in Chapter 2. One of the defining characteristics of the SISL experiment was well posed inflow and boundary conditions.

For both experiments, the NTE was introduced via a capacitively coupled RF-plasma. This provided the salient non-equilibrium effects, while allowing for detailed measurements in a long duration facilities.

3.1.2 National Aero-thermo-chemistry Laboratory

The Texas A&M University National Aero-thermo-chemistry Laboratory (TAMU-NAL), a new research state-of-the-art facility, was established, as part of this project, in 2005 by Professor R. Bowersox and Dr. J. Schmisseur (AFOSR) to study flows that couple fluid mechanics, chemistry and molecular non-equilibrium in support of National interests and to house National resource facilities. Since then, the TAMU-NAL has grown into an interdisciplinary resource with multiple faculty and student involvement from aerospace engineering and chemistry. The laboratory directors are Professors R. Bowersox (Aerospace Engineering) and S. North (Chemistry). The laboratory is arranged with the instrumentation central to the wind tunnels and test cells. The available wind tunnels and test cells are listed below.

- **Decaying Mesh Tunnel** is a recirculation tunnel, with an RF plasma generator to excite molecular non-equilibrium, for the study turbulence transport mechanisms.
- **Actively Controlled Expansion Hypersonic Tunnel** was developed at TAMU for dynamic actuation of the freestream Mach number from 5.0 to 8.0 during operation. The test section exit dimensions are 35.6 by 22.9 cm. This facility was developed to study basic hypersonic turbulence, unsteady shock interactions and hysteretic phenomena.
- **TAMU/NASA Langley Mach 6 Quiet Tunnel** was developed at NASA Langley Research Center to produce low freestream turbulence for laminar to turbulence transition studies. The facility was relocated to TAMU in 2005. The exit diameter is 18.4 cm and the maximum quiet Reynolds number is ~9.0 million/m.
- **Supersonic Basic Research Tunnel** is a high Reynolds (Re/m = 30 – 70 million) supersonic (M = 2.2-5.0) long duration (30 min) facility, which used for basic studies.
- **High-Temperature Shock Tunnel** is reflection type facility. The available test conditions include true enthalpy tailored operation (5 msec steady run time) to Mach 9. Higher Mach number conditions are available in equilibrium operation mode. This facility was developed for high-temperature gasdynamics studies by NSF-REU students.
- **Laboratory Infrastructure:** The air supply system for tunnels includes two Chicago Pneumatic 160 atm air compressors (14 SCM/min), a 24 m^3 air receiver and a 500 kW Chromalox Brand air heater. This system provides filtered (99% efficient submicron), dry

(-70 deg C), heated (up to 260 deg C) air. A Fox Brand 0.61 m Two-Stage Air Ejector is used to provide the vacuum source. An additional 50 kW, 860K air heater is available.

- **Test Cells.** Areas are established to perform smaller basic study experiments. An example is the ongoing carbon ablation studies that are taking place in a small test cell.

The first two facilities listed above were constructed with funding from this MURI project; these are discussed in more detail in the next two sections. The NASA Langley Mach 6 Quiet tunnel was also installed during the same period of performance. The major laser diagnostic systems are listed below:

- **VENOM/Two-line PLIF systems** consist of two Spectraphysics Model PRO-150-10 Nd:YAG lasers, two Spectraphysics Sirah Dye Lasers and two Andor ICCD cameras, sheet forming optics, in-house data reduction software, photodiodes for calibration and laser frequency monitoring and a Quantum Composer delay generator.
- **Raman and CARS systems** includes a high-resolution 0.66 m, triple grating, SPEX spectrometer fitted with an electron-multiplying (EM) CCD (Andor, DU970N-BV) and both broadband and narrow band dye lasers pumped by a Nd:YAG laser (PRO 290-10).
- **SPIV system** consist of a New Wave Solo 120 PIV laser, two Cooke PCO 1600 interline transfer cameras, and ISSI dPIV software.

The first two instruments were developed with funding from this project. The computational resources within the laboratory include an in-house 32-processor Opteron processor (2.0 GHz) based cluster, with 32 GB of main memory, which was purchased with funding from this project. Various in-house and commercial Navier-Stokes solvers are available.

3.1.3 Decaying Mesh Tunnel Non-Equilibrium Plasma Facility

The Decaying Mesh Turbulence (DMT) wind tunnel was constructed to introduce vibrational non-equilibrium in a decaying mesh turbulent flow field. In this section, a brief overview of the final configuration is described. A more detailed description of the facility development is given in the PhD dissertation of T. Fuller (2009), where a detailed discussion of the failures and successes leading up to the final arrangement are given. The design model for the basic wind-tunnel circuit design is given in Fig. 3.1.1, and a photograph of the final version of the DMT facility is shown in Fig. 3.1.2. The continuous, closed-circuit configuration was chosen due to the nature of the new, untested systems being employed in the facility. Specifically, in addition to providing important information towards understanding the basic coupling between thermal non-equilibrium effects and turbulence, this facility served as the testbed for the new laser diagnostics developed as TAMU as part of this project. The operating conditions for the experiments are listed in Table 3.1.1.

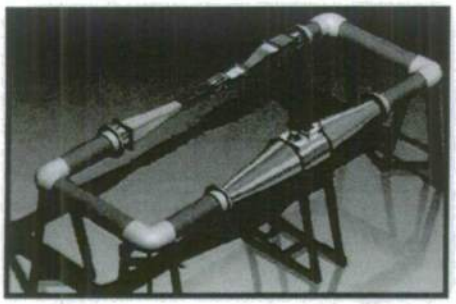

Fig. 3.1.1 DMT SolidWorks design model

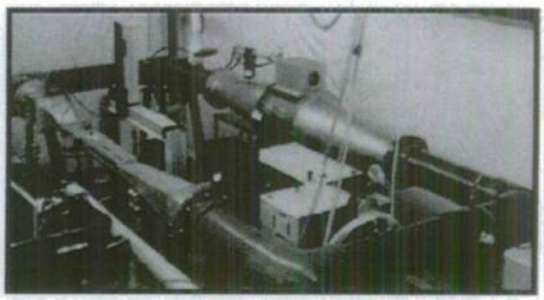

Fig. 3.1.2 DMT facility

Grid #	U (m/s)	Total Pressure (Torr)	Total Temperature (°K)	RF Power (W)
None	40	30	300	0, 150, 300
1	29	30	300	0, 150, 300
2	27	30	300	0, 150, 300

Table 3.1.1: Operating conditions

Tunnel Circuit: The DMT wind-tunnel circuit is 14'-2" x 5'-8" and the centerline is 43" above laboratory floor. The DMT is comprised, in part, of standard 8" schedule 80 PVC (polyvinyl chloride) pipe sections, schedule 80 PVC 90° elbows, and 8" schedule 80 PVC flanges (CorrTech, Inc). These parts are the dark gray segments of the circuit seen in Fig. 3.2. The socket joints were dry fit and sealed with silicone to allow flexibility. The thick walls in the pipe sections readily accept connections from other systems without sacrificing structural integrity. Every interface was sealed using 0.125" rubber sheeting to fabricate gaskets. The four corner elbow fittings contain turning vanes. The center plate (0.125" 6061 aluminum) was cut to fit tight across the center horizontal plane inside the PVC elbow. The vertical vanes (0.0625" 6061 aluminum) were cut to size, bent by hand and welded to the top and bottom surfaces of the center plate. The vane assembly was then slid into place and secured on each side by contact with the mating pipe sections in the elbow sockets.

Tunnel Contraction: A photograph of the contraction section of the DMT facility is given in Fig. 3.1.3. The flow first encountered two aluminum honeycomb sheets cut to fit securely within the 8" PVC pipe section between the elbow and the flange. Each sheet was 2" thick, and each cell had an effective diameter of 0.5". The honeycomb straightened the fluid, resulting in a uniform exit flow. The cells also served to dampen fluctuating velocities, lowering background turbulence. The transition from a circular 8" diameter cross-section to a square 7" x 7" cross-section was accomplished with a conversion segment. The part was 6" long, and each component was fabricated from 0.125" 6061 aluminum sheet metal. The walls were cut to size and hand-formed to shape before being positioned together and tack welded. The upwind flange was 13.5" in diameter, and the inner cross-section was sized to slide onto the outside of the part. This left 0.5" of wall to fit inside the PVC flange, forming a smooth seam with inner surface of the PVC pipe segment. The downwind flange was 10.25" x 10.25" with an inner cross-section fit to the outer dimensions of the part.

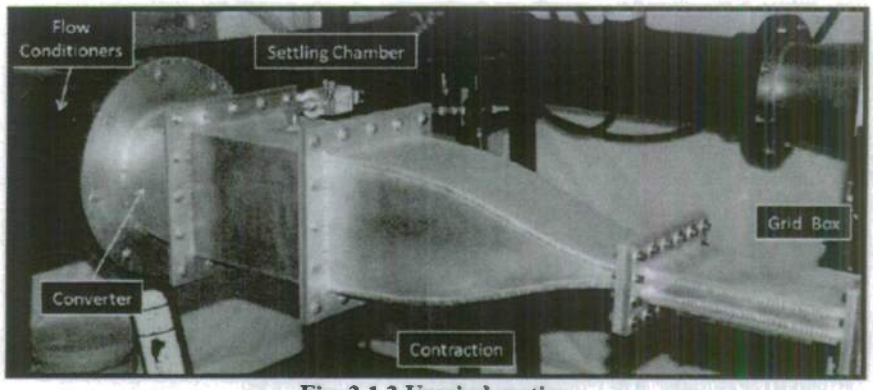

Fig. 3.1.3 Upwind section

Following the converter was the settling chamber. This was simply a box with an internal 7" x 7" cross-section that was designed to allow flexibility in installing any future required hardware upstream of the test section (an active grid, for example, if necessary). Each component of the settling chamber structure was cut to size from 0.125" 6061 aluminum sheet metal. The total length was 10". Each flange was 10.25" x 10.25" with inner cross-sections sized to fit the outer-dimensions of the settling chamber. The parts were assembled, clamped in place and welded. A pitot tube was installed in the settling chamber to measure and monitor DMT total pressure. The 0.03125" tubing was locked by compression into a 0.25" NPT fitting adapter. This fitting was then soldered to a 2" x 2" x 1/16" brass plate. A hole was drilled into the top wall of the settling chamber, and the pitot assembly was installed (with the tube oriented directly upstream) with screws and sealed with silicone. A series 902 piezo vacuum (~0 - 1000 Torr) pressure transducer was connected to the pitot system using a brass 0.25" NPT elbow along with a KF-25 flange to 0.25" NPT adapter and clamp assembly.

The contraction transitioned from a square 7" x 7" cross-section to a 4" x 0.75" cross-section, resulting in a contraction ratio of 16.3 to 1. The total length was 18". The side walls were straight at half angles of 4.76° and fabricated from 0.25" 6061 aluminum sheet metal. The top and bottom controured walls were fabricated from 0.125" 6061 aluminum sheet metal and hand shaped. The upwind (10.25" x 10.25") and downwind (4" x 7.25") flanges were fabricated from 0.375" 6061 aluminum plates. A groove (0.095" wide x 0.051" deep) for a 0.0625" o-ring was cut into the upwind flange to form a static seal with the face of the settling chamber.

Turbulence Generation: A grid-box (see Fig. 3.3) was designed introduce turbulence into the tunnel freestream. The flow cross-section transitions from 4" x 0.75" at the entrance to 4" x 0.8125" at the exit, and the total length of the part is 10". The divergence of the top and bottom walls was designed to counteract the effects of displacement thickness growth. The top and bottom walls, along with the flanges, were milled to size from 0.375" 6061 aluminum stock. Both upwind and downwind flanges were 4" x 7.5". A groove (0.095" wide x 0.051" deep) for a 1/16 inch o-ring was cut into each flange to form a static seal with the mating faces of the contraction and the test-section, respectively . A 4" x 4" access hole was milled into the top wall, and an acces panel (6" x 5" x 0.25" lip; 4" x 4" x 0.375" extrusion) was fabricated from 6061 aluminum stock. Through-holes were drilled to accept ¼-20 screws to secure the access panel to tapped holes in the top wall. The side walls were milled to size, including the 0.18° divergence angle on top and bottom, from 0.5" 6061 aluminum stock. A channel to hold the grids (see Section 3.3) was milled (0.25" wide x 0.125" deep) into each part located 3.5" downwind from

the entrance of the grid-box. The side walls were positioned between the top and bottom walls. Each flange was then slid into place over the wall assembly, and the entire part was welded together.

Turbulence in the DMT facility was generated by passive grids located upwind of the test-section directly downstream of the contraction exit. The most effective approach for turbulence generation was to utilize a square grid comprised of square elements. The iteration process for grid design will be detailed below. The two primary grids that were examined, as listed in Table 3.1.1, are shown Figs. 3.1.4 and 3.1.5.

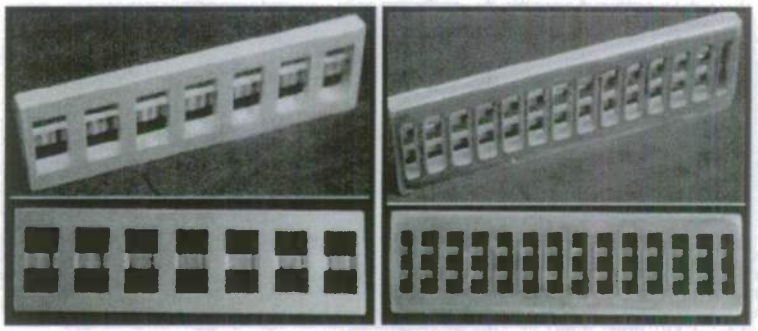

Fig. 3.1.4 Photographs of Grids #1 and #2 (left-to-right)

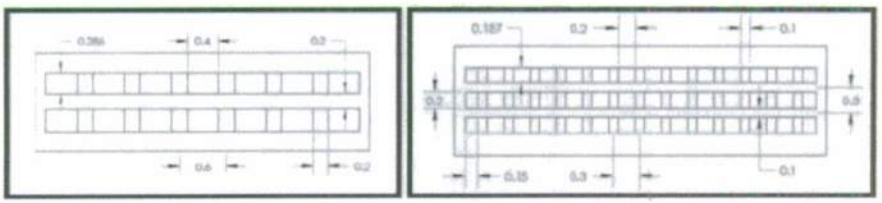

Fig. 3.1.5 Grid #1 and #2 dimensions (inches, left-to-right)

Grid #0 was constructed entirely of brass and designed to be compressed between two rubber sheets located between the downwind contraction flange and the upwind grid-box flange. A brass plate 7.375" x 4.625" x 0.030" with an inner cross-section of 4.5" x 2.0" served as the base for square 0.75" x 0.75" brass bars 2.5" long for the vertical elements and 4.5" long for the horizontal elements. The horizontal bars were soldered to the downwind face of the plate at each end as well as spot-soldered at the contact points with each intersecting vertical bar. The vertical bars were soldered on the upwind face in the same manner. The turbulence generated by Grid #0 was found to be extremely low ($\overline{u'}$ on the order of 0.3-0.5%). This was primarily due to the secondary contraction located downstream. Grid geometry (bar size) also played a role, therefore the following grids were designed for more aggressive turbulence generation. Grids #1 and #2 were designed to provide higher levels. Instead of installing the grids between two flanges, the grids were secured in a slot within the grid-box. An access panel in the grid-box allowed for easy rotation of different grids. Each grid was milled from 6061 aluminum stock to a size of 4.245" x 1.27" x 0.245". The grid elements were generated by milling vertical slots 0.125" deep into the upwind face and horizontal slots 0.125" deep into the downwind face. Therefore, each grid element (regardless of bar size) was 0.125" thick (wind axis). The outer edges of the inner cross-section formed by the pockets (4" x 0.7725") were sized to form a smooth transition with the

wall surfaces. All bar edges were left as sharp as possible. The small radii left in the corners in each slot from the end-mill were then filed square. This construction method was time effective and produced a square mesh array that was structurally rigid, consistent and very accurate to within a small tolerance. The mesh size (M) is the distance between the center-lines of two adjacent parallel grid elements. The bar size (d) is the width of a grid bar (perpendicular to the wind axis). The porosity (β) is the ratio of open flow area to blocked area for the given grid cross-section. A compilation of relevant grid dimensions and characteristics for all three grids can be seen below (Table 3.1.2).

	M (in)	d (in)	β (%)
1	0.60	0.200	51.8
2	0.30	0.100	50.3

Table 3.1.2 Grid properties

Test Section: The test-section was located downstream of the grid-box. Three main versions were constructed throughout the study as improvements were made through multiple design iterations. The first configuration was a simple channel constructed from plexiglass (with limited optical access) designed to implement and test the RF plasma system. The second version was constructed from Lexan and designed for data acquisition as well as final design iterations on the RF plasma system. These first two iterations were constructed from plastic to ensure electrical isolation from the RF-electrodes. However, as we became more familiar with the system, this was deemed unnecessary. The final configuration was constructed from 6061 aluminum and Macor ceramic and was a compilation of all design improvements ascertained from earlier testing configurations. Photographs of the test section are given in Fig. 3.1.6.

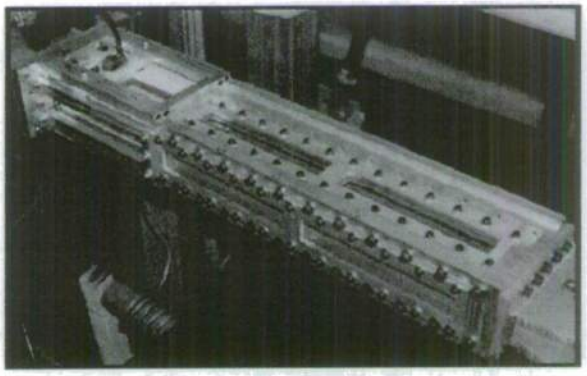

Fig. 3.1.6 Macor-Aluminum test section

The majority of the test section components were fabricated from aluminum to ensure structural rigidity. Ceramic (Macor) slabs were used to form the structure around the plasma discharge to remove any chance of heat damage. Quartz windows were used on all four sides for laser and optical access, which resulted in increased flexibility in choosing measurement locations. The top and bottom walls were positioned to diverge at 0.18° (matching the grid box

divergence) for the entire length to allow for displacement thickness growth. All interfaces (where appropriate) were sealed using 1/16" o-rings, eliminating leaks. The design details are in Fuller (2009).

RF Plasma System: Vibrational non-equilibrium was incited in the DMT flow field utilizing a capacitively-coupled radio-frequency plasma generation system. Advice on setting up the RF system was provided by Dr. Roger Kimmel (Wright-Patterson AFB, OH). The source of the plasma discharge was a Cesar Model 1325 200V Generator (Dressler) (Fig. 3.1.7). Internally, a driver/exciter module generated power at the designated output frequency (13.56 MHz in this case) to drive the main RF sections. RF amplifiers then generated the RF power. The generator was connected through a heavily shield coaxial cable to a Variomatch matching network (2-27 MHz, 700-1500W). The generator and matching network were water-cooled through a re-circulating system of plastic tubing driven by a small water pump and a reservoir. Due to the limited impedance range within the matching network, the output power was passed through a second heavily shielded coaxial cable to an external inductor coil to add additional impedance. The inductor was constructed by coiling 0.25" copper tubing around a dielectric core. The connection from the output coaxial cable to the inductor coil was made using a heavy-duty toothless alligator clip whose jaws gripped the entire circumference of the copper tubing. The location of the connection was adjusted along the length of the coil to maximize forward RF power. The matching network and external inductor coil can be seen below (Fig. 3.1.8).

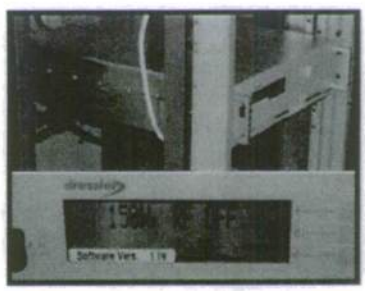

Fig. 3.1.7 RF generator

Fig. 3.1.8 Matching network and inductor coil

The RF plasma was discharged between two electrodes mounted parallel to one another on either side of the test section. There were no sources located with experimental setups comparible to the target configuration for the electrodes in the DMT facility. Because of this, an iterative experimental process was employed to test and evaluate many different electrode prototypes with a range of shapes, materials and configurations. The goal was to discharge a stable, uniform, full-field plasma at as high a forward power as possible. The final electrode was designed with a circular cross-section. It was machined from copper round stock to a diameter of 0.6" and a length of 3". Each end was then rounded (0.3" radius), and a hole was tapped to secure a segment of nickel-copper alloy ¼-20 threaded rod. The entire surface was then polished using a buffing wheel and a standard metal polishing chemical compound. The plasma discharge resulting from this design was uniform and stable. This electrode can be seen in Fig. 3.1.9. The plasma discharge ignition and stability was highly dependant on both test section pressure as well as electrode spacing. The optimal configuration in the DMT facility consisted of an electrode spacing of 1.2" and a pressure of 30 Torr. Several images of the plasma discharge in action can be seen below (Fig. 3.1.10).

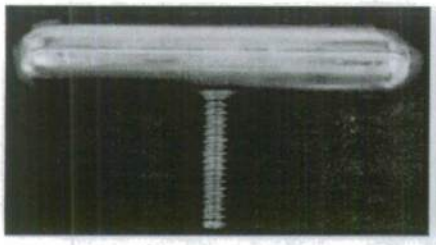

Fig. 3.1.9 Electrode

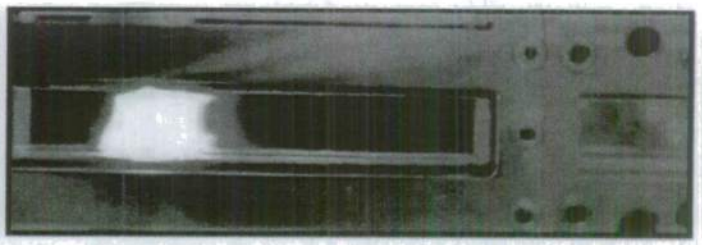

Fig. 3.1.10 Example 30 Torr plasma

Diffuser: Downwind of the test-section was the diffuser. The diffuser was designed to decelerate the flow and recover pressure as efficiently as possible. The optimal half-angle, as a rule, is generally 5° or less. Like the grid-box, there were three different iterations of the diffuser.

Fan System: The DMT flow was driven by a Hartzell 4616DH3 duct-axial fan (Fig. 3.1.2). The fan case was mounted directly into the tunnel circuit via flanges at each end. The case is comprised of 0.125" steel. The propeller is solid cast aluminum and has a diameter of 16". The propeller was secured to the shaft with a bushing, and the shaft rotates in two thrust bearings mounted to the underside of the internal cross plate. This plate was welded to the outer casing and a circular conduit extending from the upper side of the back portion of the center plate to the upper casing. This conduit serves as access to the pulley secured on the back of the drive shaft. The motor is mounted externally on top of the fan casing and provides power to the propeller through a standard v-belt. The belt is tensioned by adjusting a set of nuts and lock washers securing the motor mounting plate to four all-thread posts bolted to the fan casing. An Atlas Copco Tools LZB 33L A060-11 pneumatic motor was used to drive the fan. This type of motor works entirely on compressed air passing over internal vanes, which rotate the shaft and provide power. The largest advantage with this choice was that the drive air would also serve to cool the motor. This model provided the appropriate free speed (within prop speed safety limits), along with an acceptably low maxinum consumption mass flow in order not to overload the compressed air system. Note that the propeller is largely unloaded due the low DMT pressures, which results in the motor operating at, or near, free speed. The motor required only input and exhaust air lines, simplifying the box design required to seal the shaft area. The fan box was constructed out of 0.25" 6061 aluminum plates and welded. The box dimensions were 11.5" x 9" x 8" with a 13.5" x 11" flange. Holes were drilled and tapped in the steel motor mount base. A silicone gasket was applied, allowed to set, and compressed between the base and the flange of the fan box with screws to form the seal. The connections were made by drilling and tapping the wall, then installing 0.5" NPT nipples. A 4" diameter hole was cut into the front wall, and a 4.5" diameter plate of 0.5" thick polycarbonate was installed with silicone in order to facilitate motor and belt visual inspection.

The compressed air system was used to run the pneumatic motor to drive the fan system as well as the atomizer for seed injection. The system was pressurized with a BelAire model 5312D air compressor with a Van Air Systems model RD-100 refrigerant air dryer. The compressor modules were powered by two 10 HP electric motors (208-230/3 phase) and were capable of a mass flow of 74.5 cfm at 100 psi. The tank had a capacity of 120 gallons.

Vacuum System: The DMT facility utilized a Leybold vacuum system comprised of an E250 backing pump and a RUVAC WAU 1001 Roots blower. The two pumps work in tandem with the backing pump first, pulling a "rough vacuum" of at least 20-30 Torr. The blower can then be activated, which will pull an extremely hard vacuum (~0.004 Torr) in an ideal system. During DMT operation, the backing pump alone was required to maintain a system pressure of 30 Torr.

3.1.4 Actively Controlled Hypersonic Wind Tunnel Facility

The Actively Controlled Expansion (ACE) Hypersonic Wind Tunnel was designed to provide a continuously variable Mach number over a range of 5.0 to 8.0. The nozzle exit geometry was chosen to be 9.0 inches by 14.0 inches to accommodate SISL experiment associated with this project. The available flow conditions are summarized in Table 3.1.2. A detailed description of the facility and apparatus is given in the PhD dissertations of M. Semper and N. Tichenor. A summary is available in Semper et al (2009). A brief overview of the facility design and operation is presented here.

Mach No.	Total Pressure (psia)	Total Temperature (°R)	Run Time (sec)	Test Section (sq. in.)
5.0 – 8.0	13 - 150	540 - 960	50	9.0 x 14.0

Table 3.1.2: ACE Hypersonic Wind Tunnel Operating Conditions

Nozzle: A combination of the method of characteristics, with viscous corrections, and CFD were used to design the ACE nozzle. The method of characteristic nozzle design was performed with an in-house written computer program written by Bowersox. The computer program allows for multiple reflections of the expansion fan off of the centerline and upper wall before cancellation at the wall. This measure was included to control the initial expansion angle, which was required to (1) prevent flow separation near the throat and (2) control the rate of acceleration to prevent or minimize the formation of a vortex pair along the centerline on each side of the wind tunnel [see Tilmann and Bowersox (1999)]. This vortex pair results in significant flow distortions and an hourglass shaped uniform flow region. The vortex pair structure is captured with modern finite volume CFD (the CFD methods are described in the next paragraph). The trade-off analysis was centered on minimizing both the nozzle length and the effect of the vortex pair. After numerous iterations, the Mach 7.0 supersonic wall contour shown in Fig. 3.1.11a was designed. The characteristic mesh consisted of 100 characteristics and 7 reflections, followed by the wave cancellation. The dark half diamond structure near the throat in Fig. 3.1.11a shows the intersection points of the characteristic lines. The zoomed images in Figs 3.1.11b and 3.1.11c better show the intersection points. Also visible in Fig. 3.1.11c is the finite radius curvature of the throat. The dashed line in Fig. 3.1.11a shows the estimated boundary layer thickness. As indicated, the maximum core flow region was at $x = 40$ inches. Hence, the nozzle was truncated at this location. The local wall angle is 2.0 degrees at this location. To operate the tunnel at lower Mach numbers, the nozzle planes are rotated up. To adjust the Mach number from 7.0 to 5.0 requires a 0.2° rotation. High fidelity CFD simulations demonstrated the exit flow was uniform over a range of 5.0 to 7.0. A contributing factor to the uniform flow was the large number of expansion reflections. The nozzle planes were designed to float between the side-walls, with O-ring seals. A flexure is connected to the downstream end. These two measures allow for the

nozzle to be actively moved during a tunnel run. The flow response time, estimated as the nozzle length divided by the speed of sound, is on the order of 5 – 10 msec.

The nozzle flow was computed using the GASP [Aerosoft Inc., (2001)] flow solver. GASP is a compressible, structured grid, multi-block code with a suite of turbulence models. The solver has the support for using overlapping grids. Time-accurate solutions can be obtained using either explicit or implicit methods. For the static configuration simulations, three different structured grids corresponding to M = 5, 6 and 7 were generated using Gridgen (1999). The flow domain starts at the throat of the nozzle and includes only one-quarter of the total nozzle cross-section. This is possible due to the symmetry of the nozzle in the lateral and transverse directions. The static flow conditions at the throat were specified at the inlet boundary condition. Adiabatic wall conditions were used on the nozzle internal surfaces and extrapolation boundary conditions were specified at the exit. Symmetry boundary conditions were used on the lateral and transverse symmetry planes. The simulations were performed using both parabolic and elliptic methods. Turbulence effects were simulated using the one-equation [Spalart and Allmaras, (1994)], two-equation models [Menter, (1994)] and Wilcox's stress-ω Reynolds stress transport model [Wilcox, (1998)]. Sample results for the M = 5 and 7 are shown in Fig. 3.1.12. The contours on the exit plane are those of Mach number. The grey scale contours in the lateral and transverse cross-sectional plane shows contours of density gradient. The line plots show the Mach number profile on the exit plane in both directions of symmetry.

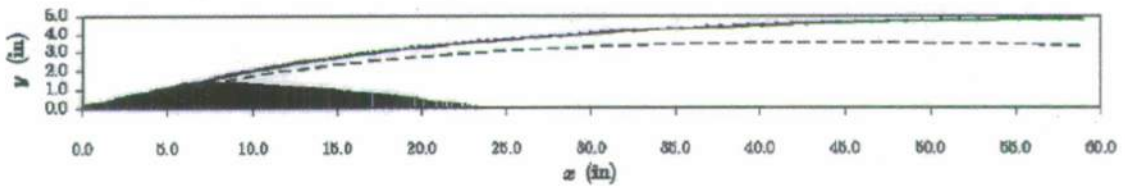

(a) Full Nozzle

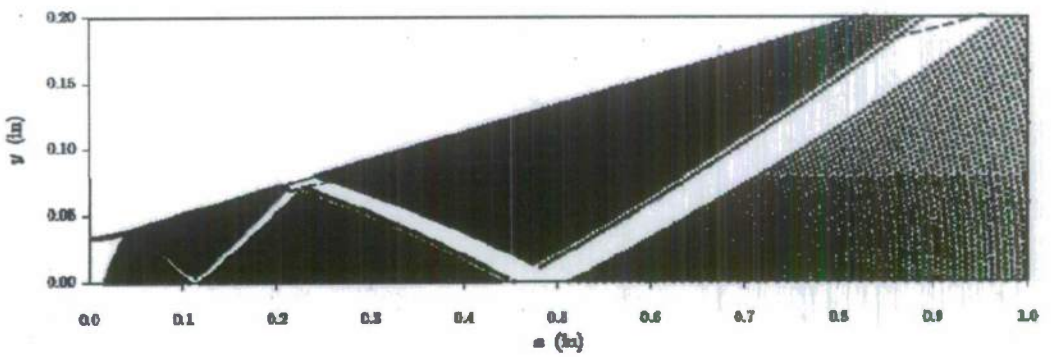

(b) Zoom in on the Throat Region (not to scale)

Fig. 3.1.11 Method of Characteristic Nozzle Design Results (M = 7.0)

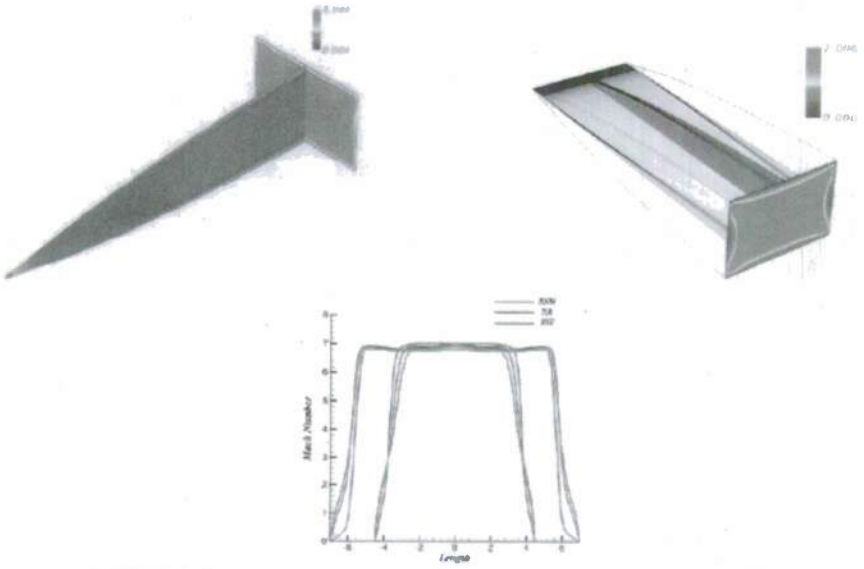

(a) Mach 5.0 (b) Mach 7.0

Fig. 3.1.12 Nozzle CFD Results

The actuating ACE nozzle was also simulated using the GASP flow solver. A two-dimensional grid composed of two blocks was generated using Gridgen. The primary block is the nozzle domain and the second block is the overlapping block used for interpolation. The two blocks are shown in Fig. 3.1.13. Only one half of the nozzle domain is simulated, as the flow is considered symmetric about the nozzle centerline. Choked conditions at the throat were specified at the inlet of the overlapping block. Symmetry conditions were specified for the overlapping block at the tunnel centerline. The corresponding surfaces of the nozzle block were set using interpolation from the overlapping block. Adiabatic wall conditions were used for the nozzle wall and extrapolation was applied at the nozzle exit. Turbulence was modeled using Menter's two-equation SST model (Menter 1994). The implicit method was used for time integration. A sinusoidal oscillation with a frequency of 10 Hz was used in the simulations. New interpolation coefficients were computed at every 10^{th} time step of the simulation.

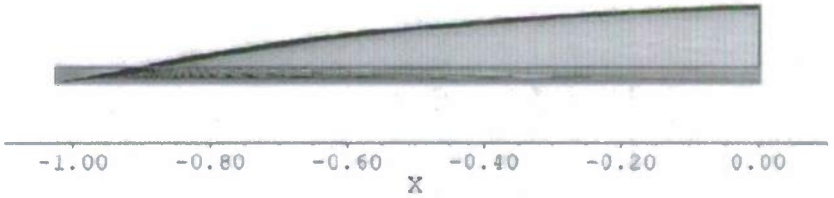

Fig. 3.1.13 2-D grid for the nozzle. The nozzle block is in black and the overlap block in red.

The results from a half-cycle of the simulation are shown in Fig. 4. At the beginning of the cycle, the throat of the nozzle was at the minimum point, i.e., the exit Mach number was at a maximum. As the cycle progressed, the nozzle block was subjected to solid-body rotation, at the specified rate, about the wall point on the exit plane. Information was interpolated between the nozzle block and the overlapping block at each time step. The change in Mach number can be seen in the sequence of images in Fig. 3.1.14. The line plot of the Mach number at the exit plane

of the nozzle is also shown. As expected, the Mach number varied from 7 to 5 during the half-cycle.

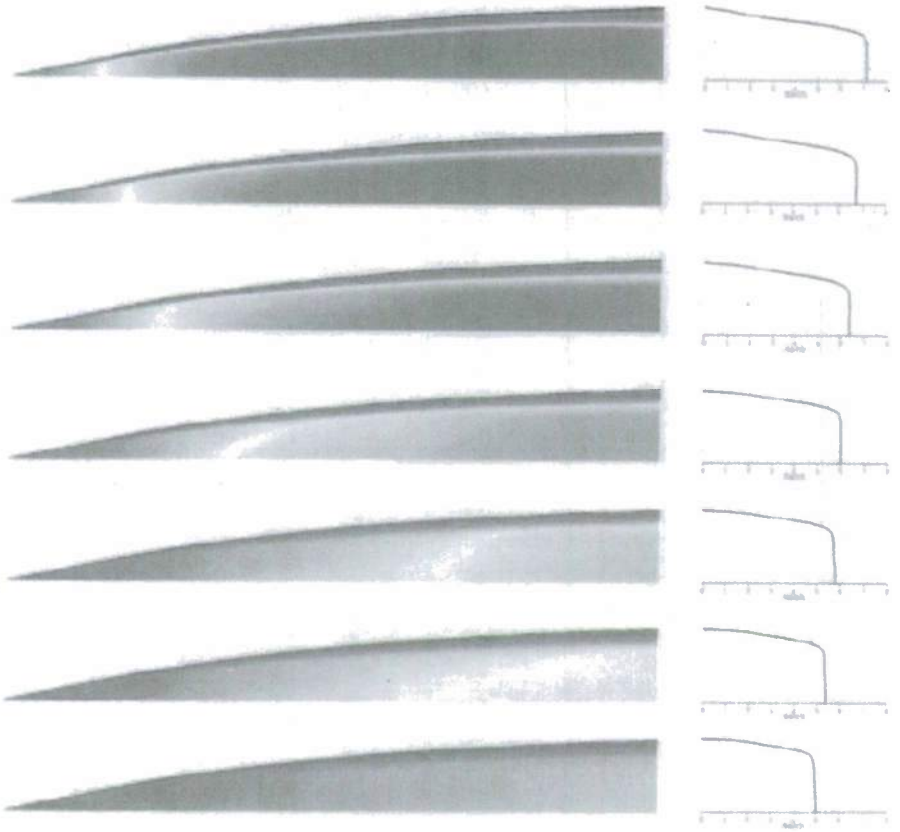

Fig. 3.1.14 Contours of the flow Mach number in the nozzle during actuation. The line plots are the corresponding nozzle exit plane Mach numbers. One-half of a sinusoidal cycle is shown.

The mechanical realization of the CFD results was designed entirely in-house at Texas A&M. The final nozzle geometry was imported directly into a CAD program and the planes were machined from solid plates of stainless steel on a CNC milling machine. After the initial machining, the planes were examined using a 3-dimensional point probe and compared to the original geometry. Any deviations from the original design were then removed with a second fine-machining pass. The sidewalls are stainless steel plates that seal the nozzle by compressing the O-ring embedded in the nozzle planes. The inclusion of the O-ring on the planes themselves allows for movement of the planes when switching Mach number without breaking the seal. To ensure a complete seal and for an added measure of safety, the sidewalls are clamped together using steel tubing and 1.0 in threaded rod. Photographs of the nozzle are given in Fig. 3.1.15a.

The ACE nozzle was designed such that the Mach number is varied by adjusting the throat height of the nozzle; the exit dimensions are constant regardless of the condition being tested. For calibration testing, the nozzle throat is fixed by carefully determining the centerline through laser alignment. At the completion of the current project, a dynamic actuating system will be employed to dynamically actuate over the range of Mach numbers from 5.0 to 8.0 and will allow for a "push-to-set" Mach number configuration. The measured Mach number uniformity across

the nozzle exit flow inviscid core is given in Fig. 3.1.15b. The upper boundary mach number was not mapped to a slight leak in the settling chamber for this configuration.

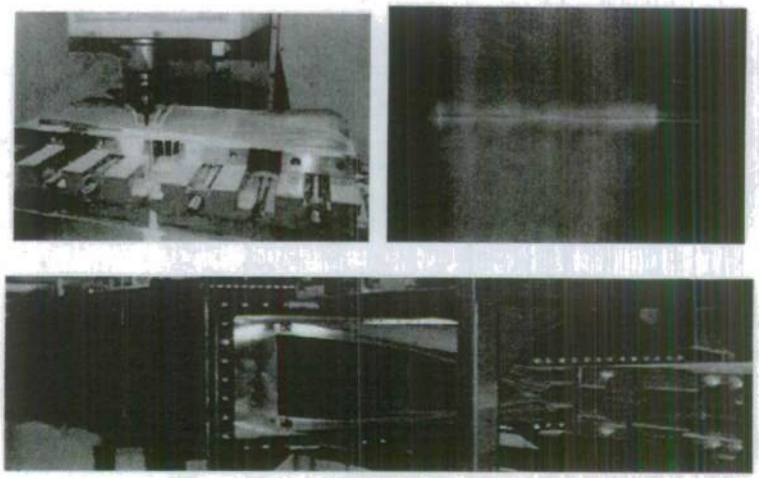

(a) Photographs of the nozzle during construction and installation

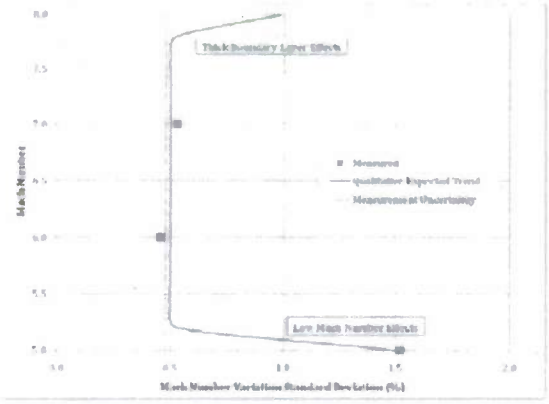

(b) Measured nozzle exit flow uniformity plot
Fig. 3.1.15 ACE Nozzle Results

Diffuser: The diffuser was designed following Wegener and Lobb (1953) and Bertram (1952). The geometry was chosen to match Bertram. A sketch and photograph of the diffuser is given in Fig. 3.1.16a. The throat height can be adjusted continuously from 4.0 inches to 12.0 inches, where the 12.0 inch throat height allows the upper and lower surfaces to be parallel throughout the diffuser length. The measured diffuser performance is given in Fig. 3.1.16b

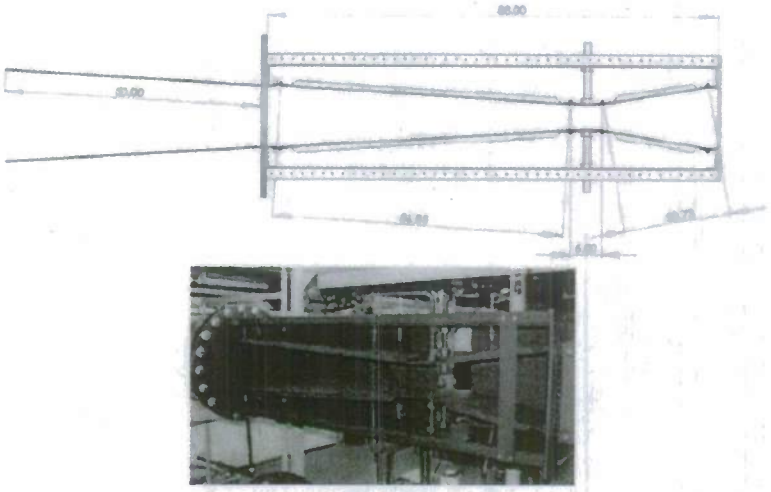

(a) Diffuser dimensions (inches) and photograph

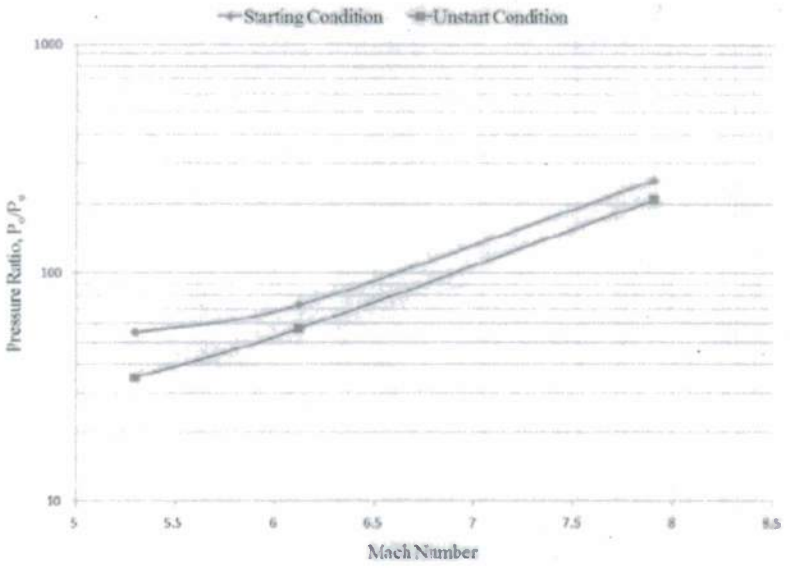

(b) Performance plot

Fig. 3.1.16 Diffuser Results

Infrastructure: The ACE tunnel is housed in the Texas A&M University National Aerothermochemistry Laboratory (TAMU-NAL). The high-speed blow-down tunnels are driven by two 160 atm air compressors (500 SCFM) and an 820 ft^3 air receiver. This system provides filtered (99% efficient submicron), dry (-40°F) air. In addition, a 0.5 MW Chromalox brand heater is available to preheat the air to 500°F. A Fox brand 2-stage air ejector (24.0 inch inlet pipe, 30.0 inch exit diameter) is used to provide the vacuum side to the hypersonic wind tunnels. The ejector requires over 20 kg/sec at nominally 150 psia, which limits the run time to approximately 50 seconds.

3.1.5 SISL Experiment

The concept behind the shock induced shear layer (SISL) experiment is shown in Fig. 3.1.17a. In summary, a shock-shock interaction is used to produce a free shear layer to provide a canonical turbulence model validation test case. This is difficult manner in-which to produce a shear layer. However, we are placed a high weighting factor toward achieving well posed inflow conditions. The RF-plasma instrumentation used in the DMT is to be used here to introduce thermal non-equilibrium effects. The flow path was designed with high fidelity CFD tools, where Reynolds Averaged Navier-Stokes, Detached Eddy Simulation and Direct Numerical Simulations (Dr. Datta Gaitonde, AFRL) methods were employed. Shown in Fig. 3.1.17b are example flow path design results. Example DNS simulation results are given in Fig. 3.1.17c. In addition, stability calculations (Fig. 3.1.17d) were performed to ensure that the shear layer was unstable at the proposed operating conditions. The SISL model was constructed and preliminary flow visualization tests were completed. Unfortunately, detailed turbulence experiments were not completed in time to be included in this document; this was due to the 12 month infrastructure delay mentioned earlier.

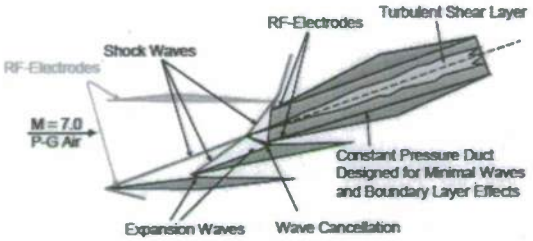

(a) SISL Concept

(b) CFD of SISL model in the ACE tunnel (M = 5.0)

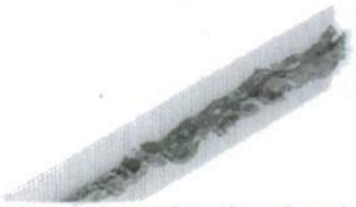

(c) DNS Simulations of the free shear layer

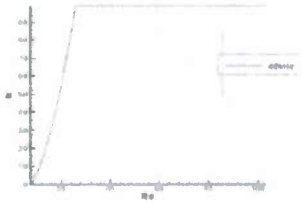

(d) LASTRAC Stability Calculations

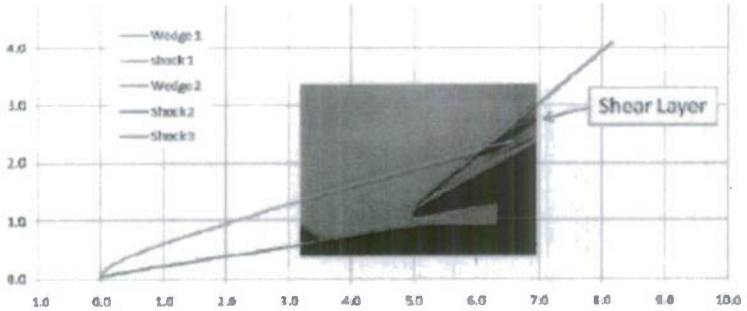

(e) Experimental schlieren of SISL in the ACE tunnel at M = 6.75 (lines are theoretical shock locations)

Fig. 3.1.17 SISL Model

3.1.6 Instrumentation

The primary instrumentation includes particle image velocimetry, planar laser induced fluorescence, coherent anti-Stokes Raman spectroscopy, optical emission spectroscopy, and the newly developed VENOM technique described in the next section. The basic system components for these methods are listed in Section 3.1.2. More complete descriptions can be found in the PhD dissertations of Fuller (2009) and Hsu (2009). A brief overview of the system capabilities is given here for completeness.

Optical Emission Spectroscopy

The RF plasma in the subsonic facility was characterized for species identification using broadband emission spectroscopy and initial rotational and vibrational temperature (of the electronically excited states) of N_2 using narrowband emission spectroscopy. The broadband emission spectra were taken via a fiber-optically coupled Oriel spectrometer (MS 125 1/8m with 2048 pixel linear CCD, 600 line/mm grating, 10 um slit, spectral range 200-1100 nm, resolution ~0.5 nm) adjusted to probe the central region of the plasma. A broadband emission spectrum is shown in Fig. 3.1.18, with room air (red), and room air seeded with NO (blue). These spectra were taken at about 100 W of RF forward power at static pressures of 50 Torr within the test section.

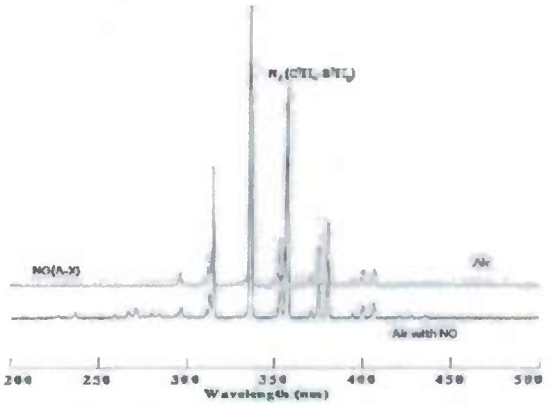

Fig. 3.1.18 Broadband emission spectra for species identification

The broadband emission spectra show several distinct features. First, the absence of emission from NO and OH in the unseeded air case, and of OH in the seeded case verify that the dissociation was minimal. Second, the largest features of the spectra are the $N_2(C^3\prod_u\text{-}B^3\prod_g)$ emission bands from about 320 nm to 400 nm. These features were examined using high resolution spectra were taken of these regions were taken with a fiber optically coupled (Ocean Optics) SPEX 1877 0.6 Triplemate (triple grating with 1800 line/mm final stage grating, resolution ~0.025 nm) adjusted to probe the central region of the plasma. An Andor back-illuminated EMCCD (Newton, DU-970-BV, watercooled to -90 C) detected the emission. A typical spectrum is shown in Fig. 3.1.19, with the fit to theoretical spectrum calculated using custom software graciously provided by DeJoseph (2008):

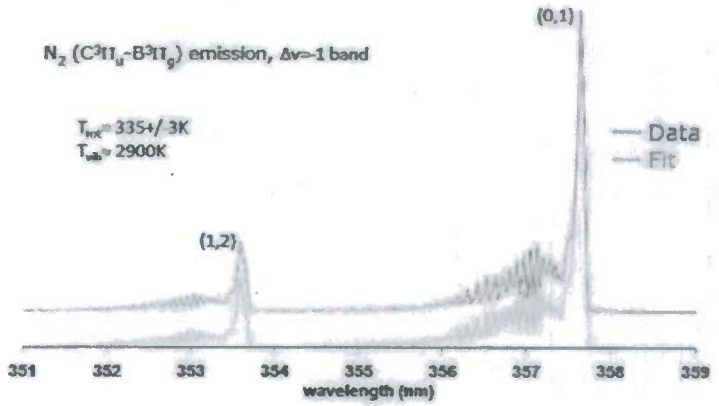

Fig. 3.1.19 Narrowband emission spectra of the $N_2(C^3\prod_u\text{-}B^3\prod_g)$, Δv= -1 band

The experimental data were fitted to the theoretical spectrum through minimization of residuals, to obtain very accurate (335 +/- 3 K) rotational temperatures. This value was obtained very accurately because of the high spectral resolution and signal to noise ratios, and could then be used in the NO PLIF image analysis to calibrate the pair of images to a bulk average temperature, since this value is known more accurately (<1% uncertainty) than the expected flow temperature fluctuations (3-10%). The vibrational temperature (2900 K) is interesting, but in this case, is the vibrational temperature of the N_2 C state, and cannot be linked to the ground state vibrational temperature. Therefore, uncertainty analyses were not conducted on this value.

Velocimetry

The PIV measurements were taken utilizing a dual port/dual head variable frequency New-Wave Solo 120XT PIV laser system. The system provided a stable, high-energy light pulse at 532 nm. The maximum energy output was 120 mJ per head with a pulse width of 4 ns (± 1 ns). The two pulses from each head (laser-one and laser-two) were combined by introducing a half-wave plate made of crystal quartz in the path of laser-one, which induced perpendicular polarization. Each pulse then passed through a high-energy polarizing cube beam-splitter which passed the perpendicularly polarized pulse from laser-one and turned the unmodified pulse from laser-two, combining the beam paths of each laser pulse. The beams were formed into sheets with cylindrical lenses and directed into the test section. The flow was seeded with atomized Sigma-Aldrich brand Bis(2-ethylhexyl) sebacate (DEHS). The liquid particles where produced with a TSI model 9306 six-jet atomizer, which generate DEHS particles with an average diameter of 250 nm. Mie scattering from the particles was captured by a Cooke Corporation PCO 1600 high dynamic 14-bit cooled interline-transfer CCD camera system with 1600x1200 pixel resolution operating in double-shutter mode at 160 MB/s. A Nikon 30-700 mm lens was used along with one 20 mm and one 12 mm extension ring. An F-number of 11 was optimal to maximize signal as well as depth of field. The timing of each laser pulse and the camera was driven by a Quantum Composers, Inc. Model 9618 Digital Delay-Pulse Generator. A photograph of the PIV system in use on the DMT experiment is given in Fig. 3.1.20.

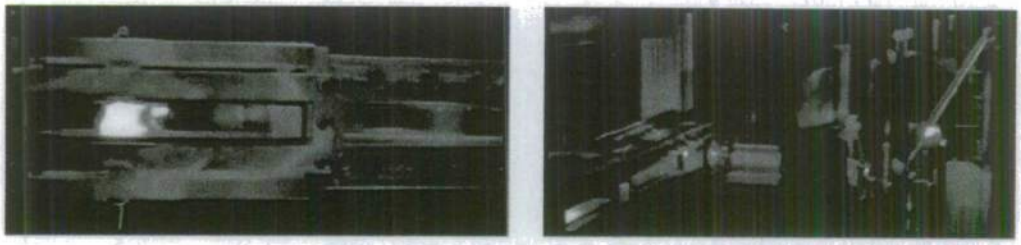

Fig. 3.1.20 PIV (left) and CARS (right) Systems in Action in the DMT

Thermometry

Two-line Nitric-oxide (NO) planar laser induced fluorescence (PLIF) was performed to measure NO rotational and vibrational temperature fields. This was accomplished by relating the temperature to the ratio of the two fluorescence signals generated by two dye-laser pulses tuned to different rotational (or vibrational) bands: This data, along with known calibration (from a reference temperature) and rate constants, allowed the temperature to be computed. The PLIF system consisted of two Nd:YAG pumped dye lasers (Sirah Cobrastretch). Each laser was formed into a sheet and directed into the DMT test section. The fluorescence signal was recorded on two 16-bit Andor iStar ICCD cooled cameras (model DH734) fitted with UG5 Schott filters and Nikon 105mm F/4.0 UV lenses. The images were binned on-chip negating the blurring caused by fluid movement between probe laser pulses. NO concentrations were typically 0.15%. Coherent anti-Stokes Raman spectroscopy (CARS) was performed to measure point-wise N_2 and O_2 vibrational temperatures at the plasma discharge, and at multiple locations downstream. The CARS technique is based on the mixing of two high-powered laser beams, resulting in a coherent beam at a new frequency. This coherent signal is recorded as the two pump beam frequencies are varied, resulting in a CARS spectrum, which is then compared to a theoretical spectrum.

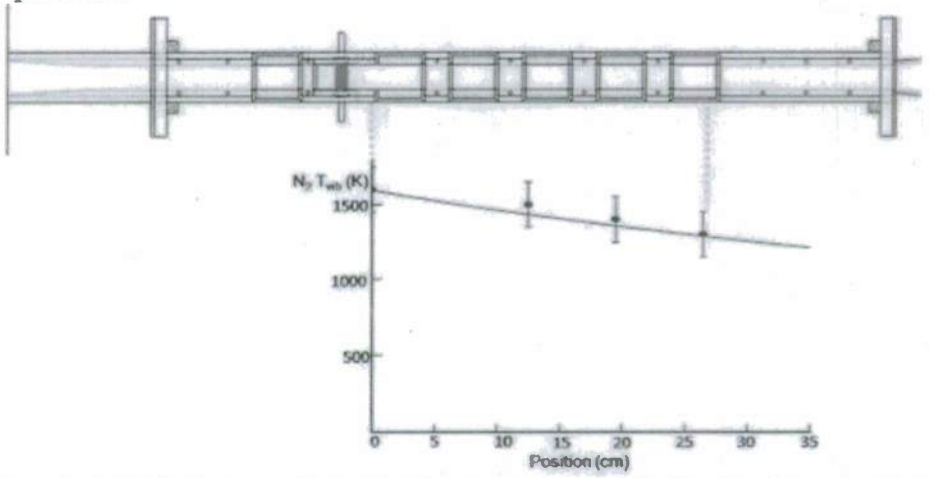

Fig. 3.1.21 CARS schematic for direct measurement of N_2 vibrational temperature

The experimental values of vibrational temperature were obtained using CARSFIT, developed at Sandia National Laboratories, modified for non-equilibrium flows where different rotational and vibrational temperatures could be specified. The rotational temperature was held at 300K for these simulations, while the vibrational temperature was adjusted to fit experimental

data. The CARS data were taken at several locations directly after the plasma and up to about 25 cm downstream of the plasma. The first location was about 1 inch downstream of the plasma. The comparison between the vibrational kinetics model (solid line) and the experimental data (points) is good, and serves to validate the kinetics model (Fig. 3.1.21). The initial starting vibrational temperature of N_2 for the kinetics modeling was set at 1600 K, which was consistent with both the experimental CARS results and calculations estimated from electron collisions cross sections.

Normal Raman spectroscopy relies on collecting spontaneous emission where signal strength is limited by collection optics (solid angle) and initial attempts to measure Raman signals at the low pressures employed in the DMT test section were problematic. Due to its coherent nature, CARS signal is often many orders of magnitude greater than normal Raman scattering.

3.1.7 VENOM Instrumentation

An overview of the newly developed Vibrationally Enhanced NO Monitoring (VENOM) technique for simultaneous velocimetry and thermometry is given this section. The basic system components for these methods are listed in Section 3.1.2. More complete descriptions can be found in the PhD dissertation Hsu (2009) and journal papers by Hsu et al (2009, 2009a). A brief overview of the system capabilities is given here for completeness.

The VENOM technique, recently demonstrated in our laboratory, combines NO_2 photodissociation and NO (v=1) PLIF for molecular tagging velocimetry. The technique exploits the fact that the 355 nm photodissociation of NO_2 results in a 60:40 ratio of NO (v=0) to NO (v=1), corresponding to an effective vibrational temperature of ~7,000K [Harrison et al (1994)]. In the VENOM technique an initial laser pulse 'writes' a grid of nascent vibrationally excited NO into the flowfield. This transient grid of NO is subsequently probed using two temporally separated dye laser pulses with associated ICCD cameras for collection of initial and time-delayed fluorescence images. Displacement of the grid intersection points during the time-delay provides a direct map of the velocity field. The VENOM technique is particularly valuable in slow-moving, high quenching, flowfields since the photolytic NO (v=1) 'tag' is a relatively stable species whose depletion is only governed by very slow recombination reactions (reforming NO_2), diffusion and/or fluid mixing out of the laser probe volume, and vibrational relaxation which is often driven by vibrational quenching through collisions with the coincidently formed O atoms. The technique can also be applied to environments with large ambient NO backgrounds (e.g. combustion or high enthalpy systems) and in environments with high background temperatures such as in combusting flows or ablating boundary layers where the temperatures are typically 2,000-4,000K and the vibrationally excited NO can be easily discriminated.

A schematic diagram of the current VENOM setup, with an inset of the field of view is shown in Fig. 3.1.22. Seeded NO_2 (0.5-5%) is photodissociated at 355 nm (the 'write' laser) using a Spectra Physics LAB 290-10 Nd:YAG split using a 50:50 beam-splitter to generate intersecting laser sheets, formed using combinations of long-focal length cylindrical and spherical lenses. Both sheet pulses are passed through a fine aluminum mesh (and enter the chamber simultaneously, writing a grid of photolytic NO (v=1) into the flowfield. The absorption cross section of NO_2 at 355 nm (σ=4.5x10^{-18} cm^2) results in near saturation of the photodissociation process even at the moderate laser powers (80 mJ/pulse) employed. The first probe ('read') laser consists of a 355 nm pumped (Spectra Physics LAB 150-10 Nd:YAG) dye laser (Sirah Cobrastretch) tuned to probe the R_1+Q_{21}(1.5) transition of NO (v=1). The beam is

formed into a sheet and spatially overlaps the transient grid 100 ns after photodissociation. This initial delay eliminates interference from the 'write' laser scatter and ensures rotational thermalization of the nascent NO. At a time-delay of 400 ns (or longer) after the first probe pulse, a second probe ('read') laser which also consists a 355 nm pumped (Spectra Physics LAB 150-10 Nd:Yag) dye laser (Sirah Cobrastretch) tuned to probe the Q_1(1.5, 2.5, and 3.5) overlapping transitions of NO (v=1) follows the same optical path as the first probe laser sheet. The 226 nm light from the probe lasers is typically 1-2 mJ/pulse. The NO fluorescence resulting from each of the 'read' probe lasers is captured on separate water-cooled Andor iStar ICCD cameras with narrow exposure gates (20 ns). The two probe lasers and the cameras are phase-locked to the excitation pulse so that a single excitation event is imaged for analysis.

Once the images from the two cameras are warped to the same field of view, velocity maps are calculated by locating and tracking the intersection points of the grid. Edge finding procedures have been used to locate the rising and falling edges of the relatively wide laser grid lines, to effectively quadruple the spatial resolution. Such analysis assumes isotropic diffusion of the tagged molecules, also assumed if locating only the grid maxima, and is not unreasonable given the short delay times employed where diffusion is insignificant. A representative VENOM image pair (consisting of 60 co-added single-shot images) applied to a highly underexpanded jet flowfield (Jet Pressure Ratio = 84) is shown in Fig. 3.1.23 (left). The gas mixture consisted of 4% NO_2 in air expanding through a 1 mm diameter orifice. The movement of the grid is subtle between the 400 ns time-delayed images, although the accumulation of signal at the Mach Disk is evident.

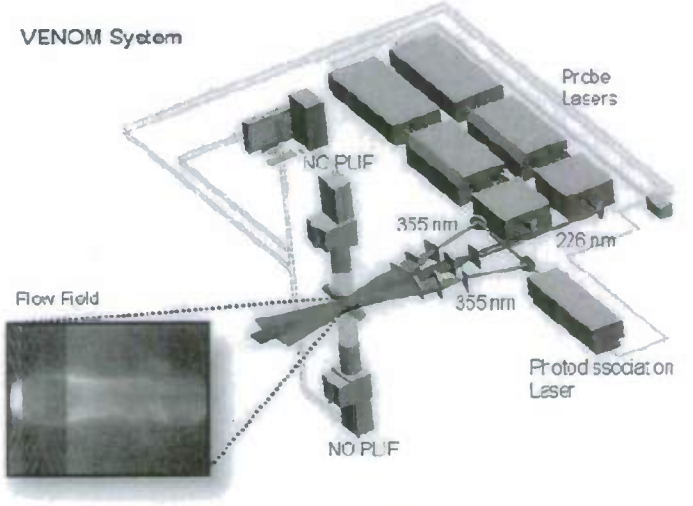

Fig. 3.1.22 Schematic Diagram of the operational TAMU-NAL VENOM system.

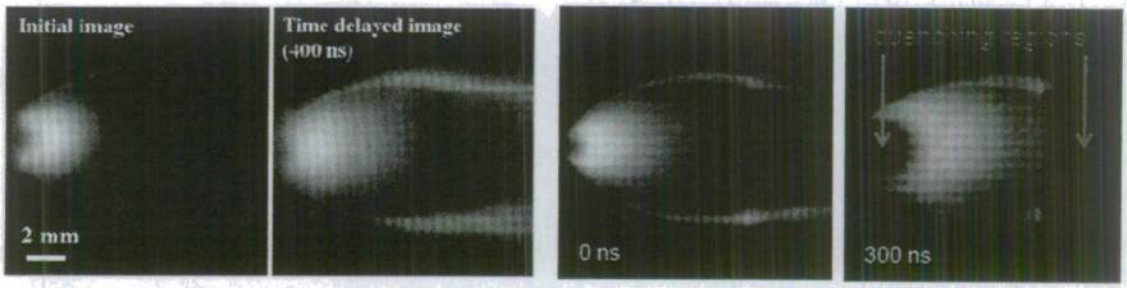

Fig. 3.1.23 VENOM Image pairs on left probing NO (v = 1) and a Fluorescence Image Pair on right probing NO (v = 0)

The interpolated streamwise and radial velocity maps derived from the images in Fig. 3.1.23 (left) are shown in Fig. 3.1.24 (upper panels) with associated CFD simulations (lower panels) using the Cobalt flow solver for comparison. It is clear from Fig. 4 that the agreement between the experimental results and CFD is excellent, both in terms of the overall structure of the flowfield and the magnitudes of the velocities. For comparison, the right panels of Fig. 3.1.23 show a time-delayed image pair acquired using a single laser to electronically excited seed NO (1%) during the fluorescence lifetime. Although this approach is valuable in low-quenching, high-velocity, flowfields, significant quenching results in loss of signal in the time-delayed image particularly in the high pressure regions at the nozzle exit and downstream of the Mach Disk which precludes velocity analysis. This limitation is avoided using the VENOM technique due to the relatively long lifetime of the vibrationally excited NO (v = 1).

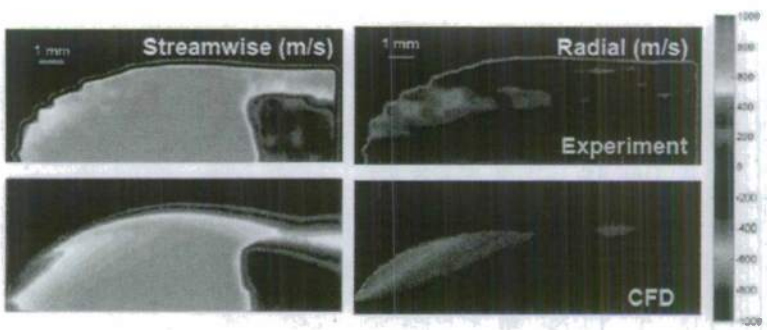

Fig. 3.1.24 Comparison of experimental (upper panels) streamwise and radial velocity maps with CFD simulations (lower panels); units m/s.

3.1.8 Summary of Experimental Results (DMT)

Decaying mesh turbulence with vibrational non-equilibrium was studied to better appreciate the role of thermal non-equilibrium on the transport of turbulence. The basic question to be addressed was: Does thermal non-equilibrium alter the basic transport of turbulence, and if so to what extent? This problem was the subject of the PhD dissertation of T. Fuller (2009). A detailed accounting of the experimental results is given in the 1022 page document. A brief overview of the important conclusions is given here.

To answer the above question, the transport equation set was reduced to appropriate form for one-dimensional nearly homogeneous flow, where it is assumed that the mean velocity gradient,

and Reynolds shear stresses are negligible. To accomplish this, the Reynolds stress tensor and energy flux transport equations were re-derived and simplified with the appropriate state equations. Assuming that $\rho_{(e)} / \rho_{(h)} \ll 1$, which implies that $\rho \approx \rho_{(h)}$, simplifies the operations because this assumption allows the conservation of mass to be written as $\rho_{(h),t} + \left(\rho_{(h)} u_k\right)_{,k} \approx 0$ to eliminate terms when taking the moments.[3] The resulting equations for the energy fluxes and Reynolds axial stresses are summarized below:

$$\frac{D\mathcal{G}^{T(in)}_{(n)t}}{Dt} \approx \tilde{Y}_{(n)} \tau^{T}_{(h)t1} \tilde{e}^{(in)}_{(n),1} + \rho_{(n)} \overline{q^{n(in)}_{(n)} u_t''} - \frac{\tilde{Y}_{(n)} \tilde{R}_{(h)}}{\tilde{C}^{(tr)}_{v(h)}} \rho_{(n)} \overline{e^{n(ex)}_{(h)} e^{n(in)}_{(n),t}}$$

$$\frac{D\mathcal{G}^{T(ex)}_{(h)1}}{Dt} \approx \tau^{T}_{(h)t1} \tilde{e}^{(ex)}_{(h),1} + \rho_{(h)} \overline{q^{n(ex)}_{(h)} u_t''}$$

$$\frac{D\tau^{T}_{(h)(t)(t)}}{Dt} \approx \frac{2\tilde{R}_{(h)}}{\tilde{C}^{(ex)}_{v(h)}} \mathcal{G}^{T(ex)}_{(h)(t),(t)} + \overline{\rho}\varepsilon_{(t)(t)} - \frac{2\tilde{R}_{(h)}}{\tilde{C}^{(tr)}_{v(h)}} \overline{\rho e^{n(ex)}_{(h)} u''_{(t),(t)}}$$

$$\frac{D\overline{\rho}k^{T}}{Dt} \approx -\frac{\tilde{R}_{(h)}}{\tilde{C}^{(ex)}_{v(h)}} \frac{\partial \mathcal{G}^{(ex)T}_{(h)1}}{\partial x_1} - \overline{\rho}\varepsilon$$

The parentheses on the coordinate direction subscript i in the Reynolds stress equation where added to indicate that summation was not implied. The postulated mechanism for the coupling between the internal energy and the turbulence transport is as follows. The molecular relaxations acts as a source or sink for $\mathcal{G}^{T(in)}_{(n)1}$ via the production (first term on the right-hand-side of the first equation above), which in-turn couples into the external energy flux through the exchange terms, and ultimately into the axial stresses and turbulent kinetic energy through the first terms on the right-hand-sides of the last two equations.

A series of experiments were performed at Texas A&M University to provide an empirical database to aid in understanding and model turbulent flows with thermal non-equilibrium. A schematic of the test cell is shown in Fig. 3.1.25a. The flow direction is from left-to-right and the test section height was nominally 19.05 mm, with a slight increase in the axial for boundary layer growth. The test section pressure was 30 Torr and the temperature was nominally 300K. The plasma power was set to 150 W - 500 W, which for the present conditions vibrationally excited nitrogen. The experimental methods included particle image velocimetry, coherent anti-stokes Raman spectroscopy and planar laser induced fluorescence of NO seeded into the flow.

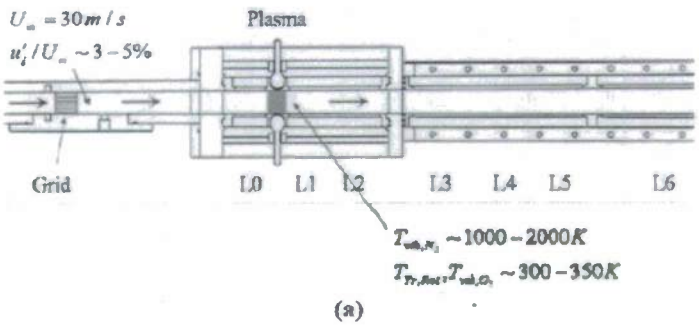

(a)

· This assumption is not required to derive the transport equation.

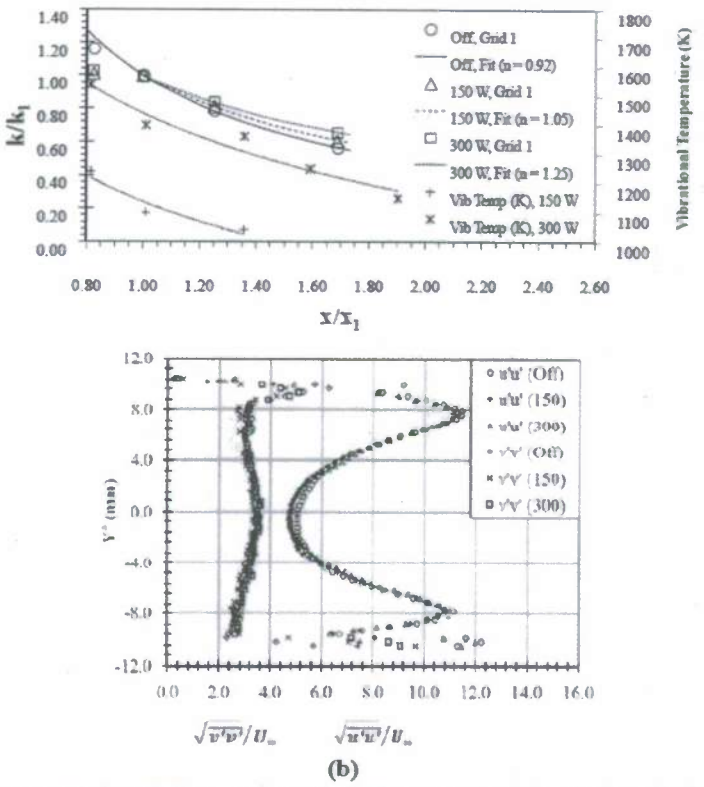

(b)

Fig. 3.1.25 Decaying mesh turbulence plasma experiment. (a) Schematic; (b) Example Results.

The turbulent kinetic energy data in Fig. 3.1.25b show that the decay rate of the turbulence was altered by the presence of the plasma. The Townsend-Batchelor (1943) exponent was observed to increase from 0.92 to 1.25 as the plasma power was increased from 0 to 300 W. Examination of the axial stress profiles (Fig. 3.1.25b) showed that the transverse stress was unaffected, which suggested that transverse axial stress dissipation was unaffected and that $\overline{\rho e_{(k)}^{\prime\prime(\alpha\chi)} u_{2,2}^{\prime\prime}}$ was negligible. If the flow is incompressible, then $\overline{\rho e_{(k)}^{\prime\prime(\alpha\chi)} u_{k,k}^{\prime\prime}}$ is zero. Thus, it is reasonable to drop this term from each of the axial stress components. This simplifies the interpretation of the results and provides confidence in the proposed exchange mechanism. For detailed contour plots, line plots and tabulated data, see Fuller et al (2009).

In summary, relaxation of an internal mode was shown to alter the basic state of turbulence. Hence, algebraic models were derived in Chapter 2 to include these thermal non-equilibrium effects. However, validation data for the models are lacking. The purpose of the SISL experiments, which are still ongoing, is to provide this data.

3.1.9 References

1) Bowersox, R., "Extension of Equilibrium Turbulent Heat Flux models to High-Speed Shear Flows," *Journal of Fluid Mechanics*, Vol. 633, August, 2009, pp. 61-70.
2) Bowersox, R., "Algebraic turbulent energy flux models for hypersonic shear flows: Invited presentation," AIAA-2009-3724, AIAA 39th Fluid Dynamics Conference, San Antonio, TX, June 22-25, 2009a. *Progress in Aerospace Sciences*, In Review.

3) Bowersox, R., North, S. and Srinivasan,R., "High- Speed Free Shear Layers with Molecular Non-Equilibrium: An Example of the Fluids Information Triad (Invited)," AIAA-2008-685, 46th AIAA Aerospace Sciences Meeting and Exhibit, Reno, Nevada, Jan. 2008.
4) Fuller, T., Hsu, A., Bowersox, R. and North, S., "The Effect of Vibrational Non-Equilibrium on the Decay of Grid Generated Turbulence," AIAA-2009-593, 47th AIAA Aerospace Sciences Meeting, Orlando, FL, Jan. 5-8, 2009.
5) Harrison, J., Yang, X., Rosslein, M., Felder, P., Huber, J., "Photodissociation of NO_2 at 355 and 351 nm Investigated by Photofragment Translational Spectroscopy," *Journal of Physical Chemistry*, Vol. 98, 1994, pp. 12260-12269.
6) Hsu, A., Srinivasan, R., Bowersox, R. and North, S., "Two-Component Molecular Tagging Velocimetry Utilizing NO Fluorescence Lifetime and NO2 Photodissociation Techniques in an Underexpanded Jet Flowfield,," *Applied Optics,* Vol. 48, Issue 22, 2009, pp. 4414–4423.
7) Hsu, A., Srinivasan, R., Bowersox, R. and North, S., "Application of Molecular Tagging Towards Simultaneous Vibrational Temperature and Velocity Mapping in an Underexpanded Jet Flowfield ", *AIAA Journal*, 2009a, In-Print.
8) Hsu, A., Srinivasan, R., Bowersox, R. and North, S., "Two-Component Molecular Tagging Velocimetry Utilizing NO Fluorescence Lifetime and NO2 Photodissociation Techniques in an Underexpanded Jet Flowfield,," AIAA-2009-4049, AIAA 39th Fluid Dynamics Conference, San Antonio, TX, June 22-25, 2009b.
9) Hsu, A., Srinivasan, R., Bowersox, R. and North, S., "Application of Molecular Tagging Velocimetry Towards Simultaneous Vibrational Temperature and Velocity Mapping in an Underexpanded Jet Flowfield," AIAA-2009-1447, 47th AIAA Aerospace Sciences Meeting, Orlando, FL, Jan. 5-8, 2009b.
10) Menter, F. R., "Two-Equation Eddy-Viscosity Turbulence Models for Engineering Applications," *AIAA Journal*, Vol. 32, No. 8, August 1994, pp. 1598-1605.
11) Spalart, P. R. and Allmaras, S. R., "A One-Equation Turbulence Model for Aerodynamic Flows," *Recherche Aerospatiale*, No. 1, 1994, pp. 5-21.
12) Semper, M., Tichenor, N. Bowersox, R., Srinivasan, R. and North, S., "On the Design and Calibration of an Actively Controlled Expansion Hypersonic Wind Tunnel," AIAA-2009-799, 47th AIAA Aerospace Sciences Meeting, Orlando, FL, Jan. 5-8, 2009.
13) Tilmann, C., and Bowersox, R., "On the Design and Construction of an Academic Mach 4.9 Wind Tunnel," AIAA-99-0800, AIAA 37th Aerospace Sciences Meeting, Reno, NV, Jan. 11-14, 1999.
14) Wilcox, D., *Turbulence Modeling for CFD*, DCW Industries, La Canada, CA, 2000.

3.2 Diagnostic Development at Purdue (Lucht)

During the course of the AFOSR MURI project, we developed and demonstrated a new planar laser-induced fluorescence (PLIF) imaging technique for simultaneous determination of pressure, temperature, and velocity in supersonic and hypersonic flows. The PLIF images were acquired following laser excitation of nitric oxide (NO) seeded into the flow. Two new, high-spectral-resolution pulsed laser sources have been developed for the measurements, and the technique was demonstrated in a in a highly underexpanded supersonic jet.

Future prospects for the PTV imaging technique are discussed. We have installed a high-spectral-resolution, optical parametric oscillator (OPO) / pulsed dye amplifier (PDA) system in the laboratory of Prof. Greg Elliott at the University of Illinois. We plan to perform NO PLIF imaging experiments to investigate transverse jet injection in a Mach 4 supersonic flow facility in his laboratory.

3.2.1 Underexpanded Jet Studies: Experimental System and Procedure

The experimental system for the underexpanded jet studies was comprised of the laser system to produce the ultraviolet (UV) radiation required for PLIF imaging, the flow system to generate the underexpanded supersonic jet, and the CCD imaging camera and data acquisition system to collect and record the PLIF data. An injection-seeded optical parametric system which produces nearly-transform-limited laser radiation at 452 nm was constructed. This system is depicted in Fig. 3.2.1. An optical parametric oscillator (OPO) stage with two counter-rotating beta-barium borate (β-BBO) crystals was injection-seeded at 1652 nm using a cw distributed feedback (DFB) diode laser. The OPO stage was pumped with the single-frequency 355-nm third harmonic output from an injection-seeded Nd:YAG laser. The signal beam (452 nm) from the OPO stage was amplified in an optical parametric amplifier (OPA) stage consisting of four β-BBO crystals. This beam was then frequency-doubled to produce UV radiation at 226 nm for exciting the selected molecular transition in the A-X (0,0) electronic system of NO.

A specially-contoured convergent nozzle and solenoid valve were connected to high-pressure gas cylinders containing 300 ppm nitric oxide (NO) in buffer nitrogen to produce a highly underexpanded jet at the nozzle exit. The stagnation pressure of the jet was approximately 5 atm. For our experiments, we scanned the temperature of the DFB seed laser of the OPO/OPA system so as to tune the resulting UV beam frequency over the $Q_{22}(5) + R_{12}(5)$ transition at 44,097.53 cm^{-1} in the $A^2\Sigma^+$-$X^2\Pi$ (0,0) system of NO. The seed laser was scanned over approximately 3 cm^{-1} and a PLIF image was obtained at thirty different UV frequencies to construct NO LIF line shapes after carefully processing the raw images recorded using an un-intensified CCD camera (Andor MCD, DU-440). Raw and processed images are shown in Fig. 3.2.2. The images shown in Fig. 3.2.2 were acquired using laser sheets oriented at 90° and 45° to the jet axis. Recording the images for two different angles allows us to measure the velocity of the fluid along the axis of the 45° laser sheet.

3.2.2 Data Analysis

The laser excitation line shape of the nitric oxide molecule is quite sensitive to both temperature and pressure changes. The width of the homogeneous line shape is sensitive to both pressure and temperature through the influence of these parameters on the collision rates in the medium. The Doppler width of the line shape is sensitive only to temperature. For the underexpanded jet flow, the Doppler width is always much less than the homogeneous line width and is neglected in the following analysis. Nitric oxide transitions in the (0,0) band of the $A^2\Sigma^+$-$X^2\Pi$ electronic transition also exhibit a significant pressure shift that provides additional information and allows us to determine the pressure and temperature accurately over the wide range of pressures and temperatures encountered in the supersonic underexpanded jet. The flow velocity is determined from the Doppler shift of the line shape from simultaneous imaging using laser sheets oriented at 45° and 90° to the axis of the jet flow.

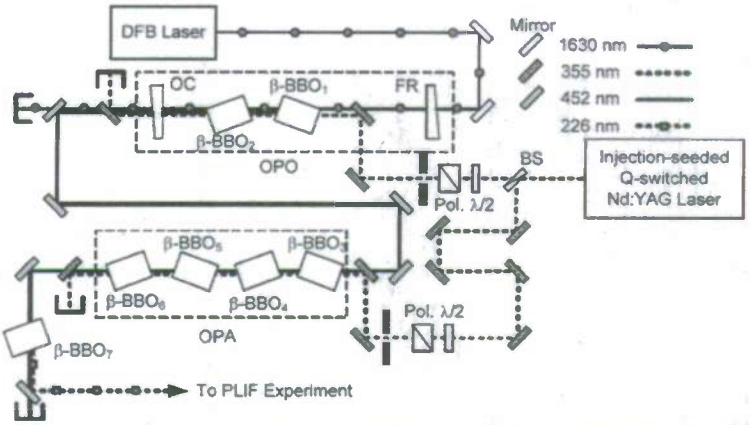

Fig. 3.2.1: Injection-seeded optical parametric system for high-resolution NO-PLIF imaging of an underexpanded supersonic jet using an optical parametric oscillator (OPO)/optical parametric amplifier (OPA) system. BS: beam splitter, FR: full reflector, □/2: half-wave plate, OC: output coupler, Pol: Polarizer.

The LIF line shapes were analyzed using the following equation for signal intensity:

$$S_{LIF} \propto f_B(T) N_{NO} \frac{A}{A+Q(P,T)} \frac{1}{\Delta\omega_a \left\{1+\left[\frac{2(\omega-\omega_a+\delta)}{\Delta\omega_a}\right]^2\right\}} \qquad (1)$$

where $f_B(T)$ is the Boltzmann fraction, N_{NO} is the number density of NO (molecules/cm^3), A is the rate coefficient for spontaneous emission (s^{-1}), $Q(P,T)$ is the collisional quenching rate (s^{-1}), $\Delta\omega_a$ is the collisional line width (cm^{-1}), ω_a is the central frequency of NO transition, and δ is the frequency shift due to pressure (cm^{-1}). For the lowest pressure and temperature in the underexpanded jet right before the normal shock, the collisional line width was 0.18 cm^{-1} while the Doppler line width was 0.06 cm^{-1} [1, 2]. The corresponding Voigt factor, $a = \sqrt{\ln 2}(\Delta\nu_C/\Delta\nu_D)$, has a value of 2.5. After recompression beyond the normal shock, the collisional line width was 0.8 cm^{-1} while the Doppler line width was 0.09 cm^{-1} and the corresponding value of the Voigt factor is 7.1 [1, 2]. Therefore, Doppler broadening was not included in Eqn. (1). We considered contributions from the $Q_{22}(5) + R_{12}(5)$, $R_{22}(2)$, and $P_{22}(12) + Q_{12}(12)$ transitions for our calculations. Pressure and temperature values along the jet centerline were obtained from FLUENT calculations. Collisional quenching rates were calculated using the theoretical pressure and temperature values and available quenching cross-section data [3, 4]. We considered quenching of the NO LIF signal via collisions with NO and N_2. The empirical model of Settersten *et al.* [3] gives a cross-section of 38.8 °A^2 at 300 K and 41.9 °A^2 at 100 K for NO-NO collisions; the average value was used in our calculations. The quenching cross-section for NO-N_2 collisions is less 0.001 °A^2 at 300 K and negligibly small at 100 K [3]. Recent measurements of Settersten show little dependence of NO-N_2 quenching cross-section down to 125 K [5]. Therefore, a constant cross-section with a rate coefficient scaling of $T^{-0.5}$ was assumed for these collisions. The exact frequencies and spontaneous emission coefficients for the relevant NO transitions were obtained from a comprehensive database for the NO A-X electronic system [6]. Collisional broadening and pressure shift

coefficients were calculated using the best fit expressions for absorption line shape data measured in a shock tube [7].

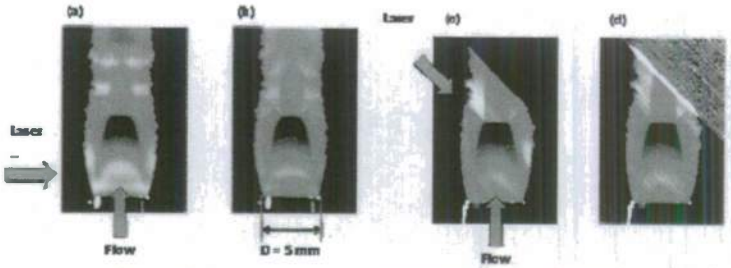

Fig. 3.2.2: NO PLIF images obtained in an underexpanded jet near 44,097.22 cm^{-1}. Panels (a) and (c) show uncorrected images while panels (b) and (d) show corrected images accounting for non-uniformities in the laser sheet using an image processing algorithm. The directions of flow and laser sheet are indicated.

We scanned the DFB laser over a single NO spectral transition. The transition that we selected was the $Q_{22}(5)+R_{12}(5)$ transition at 44,097.53 cm^{-1}. In Fig. 3.2.3, the calculated LIF signal intensities and line shapes just downstream and just upstream of the normal shock are shown for fixed pressure and varying temperature. Fig. 3.2.3(a) shows that the LIF signal intensity depends on temperature in the region before the normal shock. However, the normalized line shapes shown in Fig. 3.2.3(b) essentially collapse to a single curve; thus seemingly indicating that, for a given pressure, the LIF line shape is not very sensitive to temperature. The same trends are observed in the region after the normal shock, as seen from Figs. 3.2.3(c) and 3.2.3(d), respectively. The LIF signal intensities and line shapes just upstream and just downstream of the normal shock for fixed temperature and varying pressure are shown in Fig. 4. As seen from Fig. 3.2.4(a), the LIF signal intensity also depends on pressure in the region before the normal shock. However, the normalized line shapes corresponding to different pressures clearly display frequency shifts for a given temperature, as shown in Fig. 3.2.4(b). Similar trends are observed in the region after the normal shock, as observed from Figs. 3.2.4(c) and 3.2.4(d). We observe that two neighboring NO transitions, viz., $P_{22}(12) + Q_{12}(12)$ at 44,095.70 cm^{-1} and $R_{22}(2)$ at 44,098.09 cm^{-1}, also influence the LIF line shapes. Additional information for determination of temperature and pressure is contained in the pressure shift of the central frequency of the line shape (Figs. 3.2.4(b) and 3.2.4(d)) as well as in the effect of the aforementioned secondary NO transitions that are close in frequency to the main spectral transition $Q_{22}(5) + R_{12}(5)$ at 44,097.57 cm^{-1}. Based on the above observations, we can, therefore, fit the experimental NO LIF line shapes, without knowing the precise value of temperature, to obtain the collisional line width. The collisional line width is proportional to $1/\sqrt{T}$; thus we can obtain good approximation of the pressure using an initial guess value of temperature. The LIF line shapes were fit using a computer program described by Anderson *et al.* [8] to obtain pressure and temperature values. The computer program includes a detailed spectroscopic model for NO and a Voigt profile is used for the line shape function. The collisional line width and temperature were the parameters that were varied to obtain the best fit to the experimental spectra. The fit values of pressure and temperatures, when both collisional line width and temperature were free parameters, were indeed close to those predicted by CFD. For our experiments, we used initial guess values for temperature from FLUENT calculations for more accurate determination of pressure. In practical flow fields, however, such guess values from predictions may not be available.

Therefore, we performed a sensitivity study in which the initial temperature guess was varied from 50 K to 300 K. The corresponding change in the pressure value (or the collisional line width) was approximately ± 25% of the nominal value. The updated value of pressure was then used to determine the temperature. The resulting temperature values were found to be within ± 30 K of the initial guess at most locations. In the low-temperature region of the flow field, the error bars are relatively larger; while the above method gives temperature values within 15% of predicted values above 200 K. More accurate temperature values can presumably be obtained using the ratio of LIF signal intensities from two transitions; however, in the current experiment

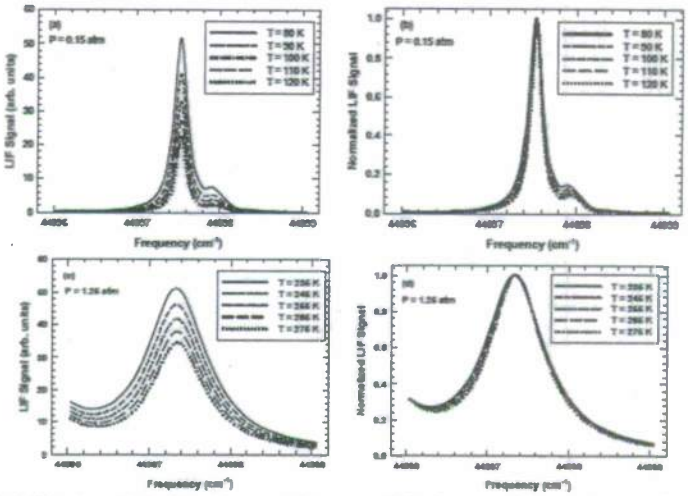

Fig. 3.2.3: Calculated LIF signal intensity variations with temperature at constant pressure, before and after the normal shock in the underexpanded jet.

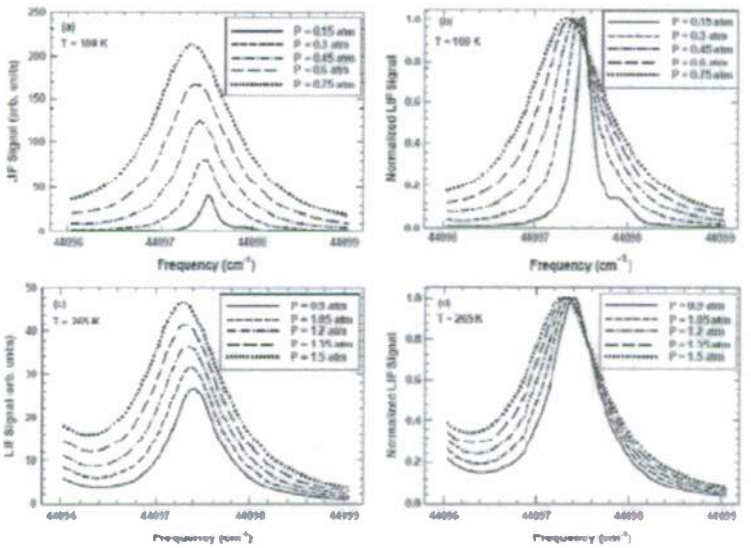

Fig. 3.2.4: Calculated LIF signal intensity variations with pressure at constant temperature, before and after the normal shock in the underexpanded jet.

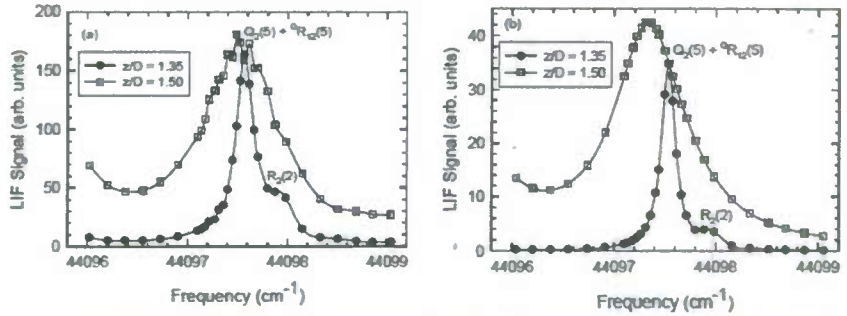

Fig. 3.2.5: Comparison between (a) measured and (b) calculated NO LIF signal intensity before (z/D = 1.35) and after (z/D = 1.50) the normal shock in an underexpanded jet. Part of the $P_{11}(12)$ + $^{Q}P_{12}(12)$ transition is seen on the left side in the region after the normal shock (z/D = 1.50) where the line shape broadens owing to recompression.

we scanned the DFB completely over only one major spectral feature of NO. Yet, as discussed previously, neighboring rotational transitions of NO influence the line shape of the major spectral feature which apparently gives sufficient information for simultaneous determination of pressure and temperature.

Experimental and calculated NO line shapes just upstream and just downstream of the Mach disk are shown in Fig. 3.2.5. In Fig. 3.2.6, we compare the pressure and temperature values measured using NO LIF with previously reported N_2 CARS measurements in the same jet [9] and FLUENT calculations. Clearly, the LIF and CARS measurements are in excellent agreement with one another and computations, except that predicted values are somewhat lower compared to data in the region downstream of the normal shock. The calculated pressure and temperature ratios using isentropic relationships are 10.33 and 2.68, respectively, across the normal shock. The pressure and temperature ratios determined from the PLIF images are 10.36 and 2.65, respectively. These experimental values compare very well with those calculations. Since the collisional line width was determined accurately, conservative error bars of 10% for the pressure measurement are used. The error bars on temperature values were obtained using the sensitivity analysis described above. We should also note here that the LIF measurements are extracted from NO PLIF images acquired using single laser shots while the CARS data is averaged using one hundred single-shot N_2 spectra. The LIF technique offers not only experimental simplicity but also good sensitivity and the capability for extracting accurate thermodynamic information.

For our experimental conditions, we have previously reported that the measured velocity of 500 ± 100 m/s at z/D = 1.35 is in good agreement with isentropic calculations [2]. The measured Doppler shift is 0.05 ± 0.01 cm^{-1} which corresponds to Mach number of 2.5 ± 0.5 just upstream of the normal shock. Fig. 3.2.7 shows the comparison between measured and calculated velocity profile along the jet centerline. In the supersonic region before the normal shock, the computed velocity and temperature values are 625 m/s and 95 K, respectively; the corresponding Mach number of 3.2 compares reasonably well with that obtained from the measured velocity. The measured velocity is within 20% of that calculated using FLUENT at all locations. The agreement between measured and calculated velocities deteriorates closer to nozzle, as expected due to the decreasing frequency shift. The measured Doppler shift values are low for our experimental configuration, with the highest being 0.05 cm^{-1}. The large uncertainty of 100 m/s in the velocity measurement corresponds to Doppler shift of 0.01 cm^{-1}, the minimum value of

which is limited by the resolution of wavemeter used to measure the wavelength of the 452 nm laser beam and by the temperature tuning capability of the DFB laser.

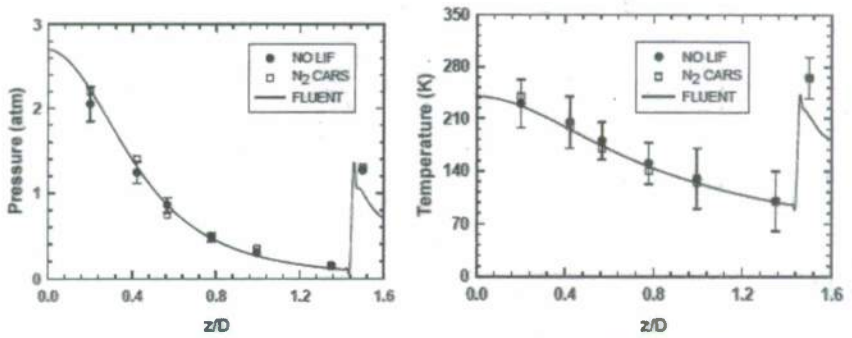

Fig. 3.2.6: Comparison of measured and computed pressure and temperature along the jet centerline.

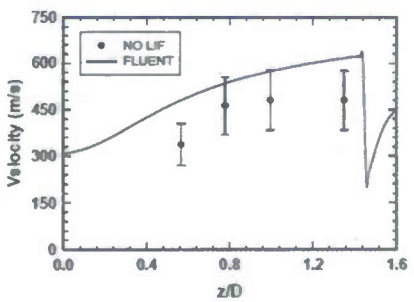

Fig. 3.2.7: Comparison between measured and computed velocity along the jet centerline.

3.2.3 Future Prospects for the PTV Imaging Technique

The PTV imaging technique has been applied to a supersonic underexpanded jet flow field. Conditions in the core of the jet are nearly laminar and thus we have been able to perform the experiments by slowly tuning the excitation wavelength of the laser system and acquiring images from different wavelengths at time intervals that are very long compared to characteristic time scales. For applications in supersonic or hypersonic flows with turbulence, images at several different frequencies will have to be acquired in less than a microsecond. This can be accomplished using fast framing cameras and a system of multiple injection-seeded Nd:YAG lasers and OPO/PDA systems. Each of the OPO/PDA system would need to be injection seeded at a slightly different wavelength. However, it is not clear how many images at different excitation wavelengths would be required to achieve accurate and precise measurements of pressure, temperature, and velocity.

Alternatively, the current system could be used to acquire numerous single laser shot images at a number of different excitation frequencies. The imaging data could be compared to the results of LES computations of the flow by using the computer to simulate the experimental data; the computer would be used to calculate images and statistics for a given excitation frequency using Equation 1. The direct output of the computer code would be the temperature, pressure, and flow velocity, and these terms would then be used to calculate the line shape parameters in Equation 1.

To investigate these potential approaches, we examined the installation of an optical parametric system in Prof. Elliott's laboratory at UIUC was begun. The optical parametric

system is similar to the one implemented at Purdue for measurements in the underexpanded jet. However, amplification of the 452-nm signal beam from the OPO is achieved by using an easy-to-align, cost-effective pulsed dye amplifier (PDA) system. A schematic diagram of the OPO/PDA system is shown in Fig. 3.3.8. Coumarin 450 laser dye in methanol solvent is used and the dye cell in each PDA stage is side-pumped using the third harmonic (~355 nm) output of an injection-seeded Nd:YAG laser. Good spatial and temporal overlap of the signal and pump beams is ensured. The dye cell is tilted at Brewster's angle to allow maximum transmission of the pump and signal beams. In the current system with two PDA stages, the energy output at 452 nm is ~12 mJ/pulse and the frequency-doubled energy at 226 nm is approximately 1 mJ/pulse. The system will be used for measurements of the temperature and pressure field around a laser-induced breakdown shock and for measurements of the flow field for a sonic jet injected into a Mach 4 cross flow. Fig. 3.2.9 shows the laser system in operation in the same room where a laser-generated shock facility and a Mach 4 wind tunnel are located at UIUC.

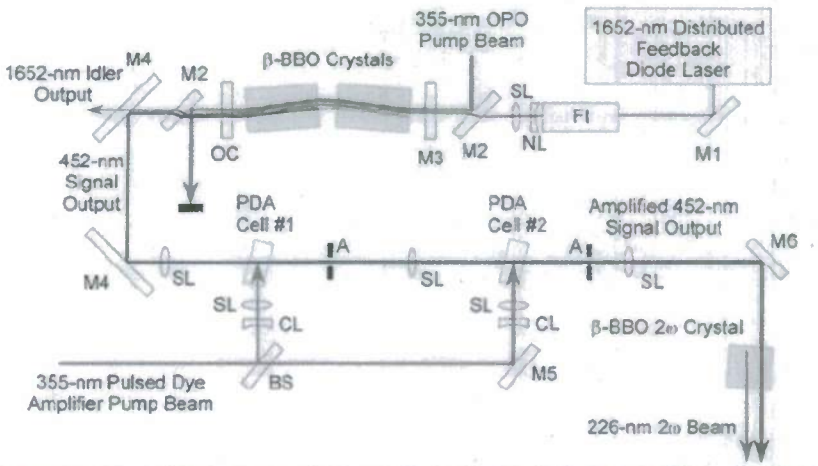

Fig. 3.2.8: Injection-seeded optical parametric oscillator/pulsed dye amplifier (OPO/PDA) system to generate laser radiation near 226 nm for NO PLIF.

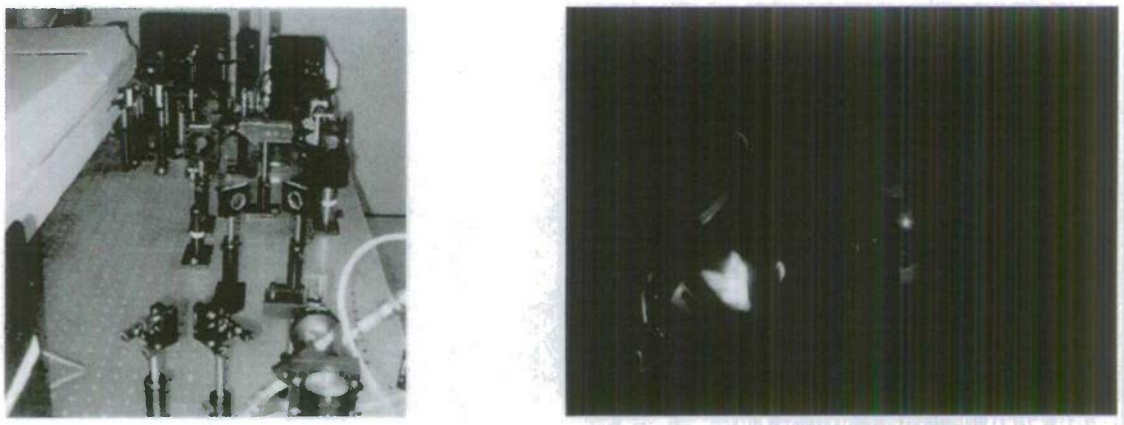

Fig. 3.2.9: Photographs of the 452-nm OPO/PDA system in operation at UIUC.

3.2.4 References

1) Naik, S. V., Kulatilaka, W. D., Venkatesan, K. K., and Lucht, R. P., "Measurements of pressure, temperature and velocity in underexpanded free jets using planar LIF imaging of nitric oxide," *AIAA Journal,* Vol. 47, No. 4, 2009, pp. 839-849.
2) Kulatilaka, W. D., Naik, S. V., and Lucht, R. P., "Development of high-spectral-resolution planar laser-induced fluorescence imaging diagnostics for high-speed gas flows," *AIAA Journal*, Vol. 46, No. 1, 2008, pp. 17-20.
3) Settersten, T. B., Patterson, B. D., and Gray, J. A., "Temperature- and species-dependent quenching of NO $A^2\Sigma^+$ ($v' = 0$) probed by two-photon laser-induced fluorescence using a picosecond laser," *Journal of Chemical Physics*, Vol. 124, No. 23, 2006, pp. 234308-1-234308-14.
4) Settersten, T. B., Patterson, B. D., Kronemayer, H., Sick, V., Schulz, C., and Daily, J. W., "Branching ratios for quenching of nitric oxide $A^2\Sigma^+$ ($v' = 0$) to $X^2\Pi$ ($v'' = 0$)," *Physical Chemistry Chemical Physics*, Vol. 8, No. 45, 2006, pp. 5328-5338.
5) Settersten, T. B., Personal communication, 2008.
6) Reisel, J. R., Carter, C. D., and Laurendeau, N. M., "Einstein coefficients for rotational lines of the (0,0) band of the NO $A^2\Sigma^+$ - $X^2\Pi$ system," *Journal of Quantitative Spectroscopy and Radiative Transfer*, Vol. 47, No. 1, 1992, pp. 43-54.
7) Chang, A. Y., DiRosa, M. D., and Hanson, R. K., "Temperature dependence of collision broadening and shift in the NO A-X (0,0) band in the presence of argon and nitrogen," *Journal of Quantitative Spectroscopy and Raditative Transfer*, Vol. 47, No. 5, 1992, pp. 375-390.
8) Anderson, T. N., Lucht, R. P., Barron-Jimenez, R., Hanna, S. F., Caton, J. A., Walther, T., Roy, S., Brown, M. S., Gord, J. R., Critchley, I., and Flamand, L., "Combustion exhaust measurements of nitric oxide with an ultraviolet diode-laser-based absorption sensor," Applied Optics, Vol. 44, No. 8, 2005, pp. 1491-1502.
9) Woodmansee, M. A., Lucht, R. P., and Dutton, J. C., "Development of high-resolution N_2 coherent anti-Stokes Raman scattering for measuring pressure, temperature, and density in high-speed gas flows," *Applied Optics*, Vol. 39, No. 33, 2000, pp. 6243-6256.

3.3 Experiments and Diagnostic Development at UIUC (Austin and Elliott)

The portion of the MURI project conducted at the University of Illinois at Urbana-Champaign by PIs Austin and Elliott is focused on investigating the effects of thermochemical non-equilibrium on transition and turbulence in canonical flows. Over the course of the MURI program, we have:

- built three high-speed ground testing facilities with complementary capabilities.
- developed and demonstrated a range of advanced laser diagnostics for flow measurement and visualization in these facilities including Filtered Angularly Resolved Rayleigh Scattering, Molecular Tagging Velocimetry, Particle Image Velocimetry and Emission Spectroscopy.
- made measurements and calculations in several canonical flow fields including: i) comprehensive velocity field data to compare axisymmetric nitrogen jets produced under various conditions with and without the RF plasma field applied, ii) characterization of

the dissociation and thermal relaxation region behind a normal shock, iii) spatial linear stability analysis of a shear layer with a detailed thermochemical modeling, iv) evaluation of the interaction of several types of plasmas/plasma actuators with the supersonic Mach 4 boundary layer.

The outcomes of this work include new ground-testing and diagnostic capabilities; quantitative assessment of plasma/plasma actuators on supersonic boundary layer and jet flows; an extension of a state-specific thermochemical model; and a high-quality experimental validation database for canonical hypersonic flows including fluctuating and mean density, pressure, temperature, and velocity measurements; velocity field measurements; and vibrational temperature measurements.

We present a very brief description of the salient features, which serves to establish the framework for the conducted research. The report is organized as follows: the new experimental facilities and their capabilities are described in Section 3.3.1. The development and application advanced laser diagnostics is reported in Section 3.3.2. Results from studies of a shock-generated free shear layer in high enthalpy flow, both experiments and modeling; normal shock relaxation region species identification and temperature measurements; interaction of RF plasma with axisymmetric jets and compressible shear layers; Mach 4 boundary layer plasma interaction experiments are all presented in Section 3.3.3. Publications that were the result of this project and the students involved, together with references to their theses, are listed in Section 3.3.4.

3.3.1 Experimental Facilities

During past five years, three new facilities were constructed at the University of Illinois: the Hypervelocity Expansion Tube, the Reduced Pressure Axisymmetric Jet, and the Mach 4 Supersonic Tunnel. These facilities were designed to have complementary capabilities covering both relatively short and long test times, with non-equilibrium conditions generated via high-enthalpy and via RF plasma. The design, operation, and capabilities of these facilities are described below.

Hypervelocity Expansion Tube Facility. The Hypervelocity Expansion Tube (HET) is a 9.14m 304/304L stainless steel long facility consisting of three sections (driver, driven, and accelerator) all with 150 mm inner bore diameter, Fig. 3.3.1.1. The initial gas pressure and composition can be varied to achieve nominal Mach number operating conditions between 3.0 to 7.5 and stagnation enthalpies of 4.5 to 8.0 MJ/kg. The driver and driven sections are initially separated by a 1.27mm thick 5052-H32 Aluminum primary diaphragm, while the driven and acceleration sections are separated by a 12.7μm Mylar secondary diaphragm. The tube will withstand initial pressures up to 5500kPa and the acceleration section is capable of achieving a vacuum of less than 100mTorr. The facility is mounted on linear bearings for easy access to the diaphragm stations and to allow tube recoil during the experiment. Ten instrumentation ports are located along the tube, of which four are currently instrumented with PCB 113A26 piezoelectric pressure transducers for wave time-of-arrival and pressure profile measurements. Pitot pressure measurements in the test section were made using the same type of pressure sensor mounted normal to the flow field using the sting. The test section shown has a sliding seal and three-way 100mm diameter optical access. The facility was designed using theoretical gas dynamic calculations [Dufrene et al. 2007].

The flow processes in an expansion tube are complex. Nevertheless, simple one-dimensional, inviscid, unsteady wave interactions may be used to calculate the ideal test conditions including thermodynamic state, flow velocity, and test time as a starting point for facility design. A general design procedure was determined for small-scale expansion tube construction, with ideal test conditions calculated based upon unsteady gas dynamics with particular focus upon the problem of short test times associated with expansion tube operation. A sample x-t diagram for a Mach 7.42 test flow is shown in Fig. 3.3.1.2. The driver and driven sections operate as a standard shock tube. The strength of the primary left-facing expansion wave is dependent on the initial pressures, but is in general sufficiently strong to accelerate the gas past sonic velocities. The head of the primary expansion wave will reflect from the upstream end of the tube and the tail will trail the primary contact surface.

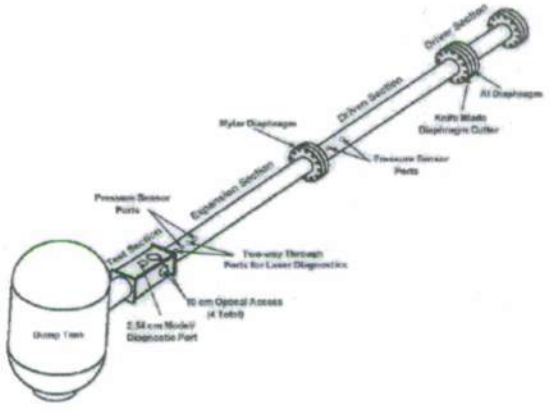

Fig. 3.3.1.1: Schematic of the HET facility.

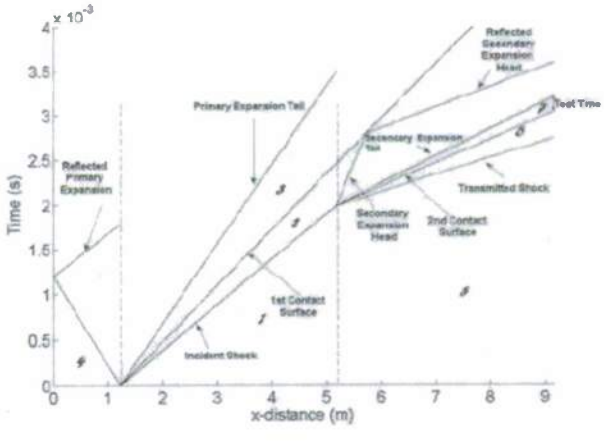

Fig. 3.3.1.2: Sample *x-t* diagram (M = 7.42).

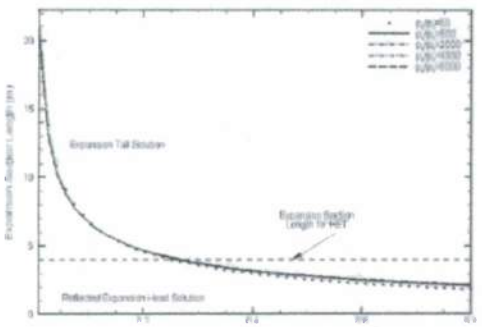

Fig. 3.3.1.3: Optimal acc.-sect. length, L_{EXP}.

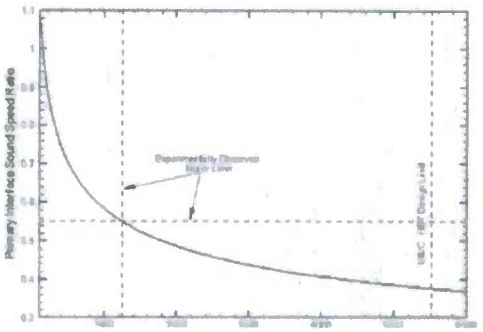

Fig. 3.3.1.4: c_3/c_2 , as a function of p_4/p_1

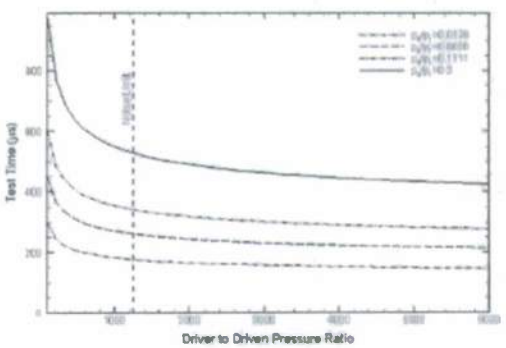

Fig. 3.3.1.5: Test time as a function of p_4/p_1

The secondary diaphragm, assumed in this initial theoretical analysis to be thin and break instantaneously upon arrival of the incident shock, is represented as a contact surface. Pressure-velocity (*p-u*) shock polars are used to calculate states 6 and 7 (see Fig. 3.3.1.2) resulting from incident shock-contact surface interaction. A shock is transmitted and the expansion wave between regions 2 and 7 can be either right-facing or left-facing. The head and tail of the expansion have positive slopes as the flow in state 2 is supersonic and to the right. State 7 is the test gas that has been further accelerated beyond the post-shock state 2 by the unsteady secondary expansion. The secondary expansion wave will interact with the contact surface between states 2 and 3, resulting in reflected and transmitted waves. *p-u* polar calculations show this reflected wave to also be an expansion. The interaction of the incident and reflected secondary expansion waves creates a non-simple region.

Test time varies with the initial conditions of the expansion tube, and can be estimated from an *x-t* diagram. The test time begins with the arrival of the state 6-7 contact surface, and it is terminated by the arrival of either i) the head of the reflected secondary expansion wave, or ii) the tail of the secondary expansion wave, or iii) the arrival of the primary expansion from the driver, which ever occurs first. In HET operation, only cases i) and ii) need to be considered. For these two cases, the maximum test time corresponds to the case in which the reflected head and the tail of the secondary expansion fan arrive at the end of the tube at the same time. For the run condition shown in Fig. 3.3.1.2 the test time is terminated by the expansion tail. The test time is determined using a method of characteristics similarity solution within the complicated non-simple region.

The interaction of the incident and reflected secondary expansion waves creates a non-simple region. We may use the method of characteristics to solve for the trajectory of the leading characteristic of the reflected expansion as it passes through the incident expansion. A more detailed description is given in [Wintenberger et al. 2003]. Assuming an isentropic expansion, an ordinary differential equation for the passage of the first reflected characteristic through a left-facing expansion can be derived in terms of a similarity variable, $\eta = x(t)/c_2 t$. Theoretical results found that there was an error of up to thirty-five percent in calculating the test time for the reflected head limiting case when this correction is neglected. Incorporating this correction, analytical expressions for the maximum test time and optimal length of the facility acceleration section for this maximum test time were also calculated. The derivations for these expressions are presented in our facility paper by Dufrene et al. [Dufrene 2007].

The influence of various expansion tube parameters upon this optimal length was also explored. The optimal expansion section length as a function of the acceleration-driven initial pressure ratio p_5/p_1 is shown in Fig. 3.3.1.3 for different p_4/p_1 values. Lower p_5/p_1 values result in higher test flow Mach numbers and require longer expansion sections for maximum test time. It can be seen that the optimal expansion length parameter is insensitive to the driver-driven initial pressure ratio, p_4/p_1. The horizontal line in Fig. 3.3.1.3 denotes the expansion section length selected for the current HET design. Solutions which fall below this line correspond to the test time being limited by the reflected secondary expansion head and those above it are restricted by the secondary expansion tail.

Previous studies [Paull and Stalker 92] found that significant test flow disturbances rendered the test time unacceptable due to the presence of high-frequency fluctuations, which were minimized by decreasing the ratio of the primary-contact-surface sound speeds, c_3/c_2. Using a derived analytical relationship [Dufrene et al. 2007] for this sound speed ratio in terms of initial conditions and the initial shock Mach number, an operating "envelope" was mapped out for the HET in terms of minimizing this noise criterion. Fig. 3.3.1.4 indicates that the sound speed ratio, and therefore the test flow disturbance, can be reduced by increasing the driver-to-driven gas pressure ratio. The Fig. shows the regime in which the HET facility can operate and is bounded by the experimentally observed acceptable sound speed ratio. The upper bound on the pressure ratio is set by the design yield strength of the driver tube section 5.5MPa, assuming a driven pressure of 1.0kPa.

The dependence of the test time on p_5/p_1 for different p_4/p_1 values is illustrated in Fig. 3.3.1.5. The limit for a sound speed ratio of 0.55 is shown as the vertical line in the Fig.. Acceptable test conditions are to the right of this line. One can see that within this acceptable regime, the dominant influencing factor is that of the p_5/p_1 value rather than the p_4/p_1 value. Thus, the noise limitation tends to dictate the choice of p_4/p_1, rather than test time considerations. For a certain run condition, this vertical line also indicates the maximum allowable test time. Additional theoretical investigation also found that the dominant factor for both expansion tube sizing and test-section Mach number is the p_5/p_1 ratio. Studies also revealed that in order to maintain high Mach number operation, the p_5/p_1 ratio should be kept below 0.3. However, as previously discussed, a decrease in p_5/p_1 reduces the test time. These parametric studies proved to be very useful as they identified key factors for expansion tube

operation which allows a working HET operational balance within the design process that takes into account the limitations and fundamental goals of the facility.

Reduced Pressure Axisymmetric Jet Facility. The reduced pressure axisymmetric jet facility was designed and built specifically to create an axisymmetric jet and shear layer over a range of Mach numbers in an environment which could sustain a uniform RF plasma. This facility allowed us to not only study the effects of the RF plasma on turbulence, but also to evaluate diagnostics to be used in these environments. The RPAJ facility consists of the test section, axisymmetric nozzle, air supply and vacuum system, electrode (anode and cathode) configuration for the RF plasma generation.

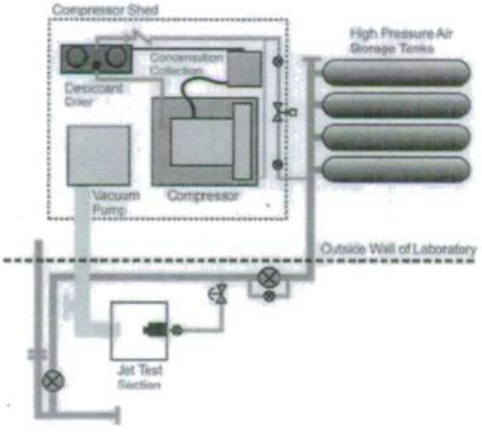

Fig. 3.3.1.6 Schematic of reduced pressure axi-symmetric jet facility layout.

The air/gas handling system illustrated in Fig. 3.3.1.6 consists of a CompAir Mako compressor, capable of producing 3.1 Kg/min. The relative humidity of the compressed air is lowered by a Zander inline drier. Typically, the dew point is roughly -40°C. The air exits the drier and is stored in 4 cylinders with a total volume of 8 m^3 which can store air at 12.1 MPa and 293 K. Although initially the dry air supply in the laboratory was used to run the jet it was later determined that the RF plasma was much more stable when using pure nitrogen instead. For experiments conducted with gasses other than air the supply system was replaced with standard gas cylinders of pure nitrogen or argon. The test section (seen in Fig. 3.3.1.7) is evacuated by a Kinney KT-300 rotary piston vacuum pump.

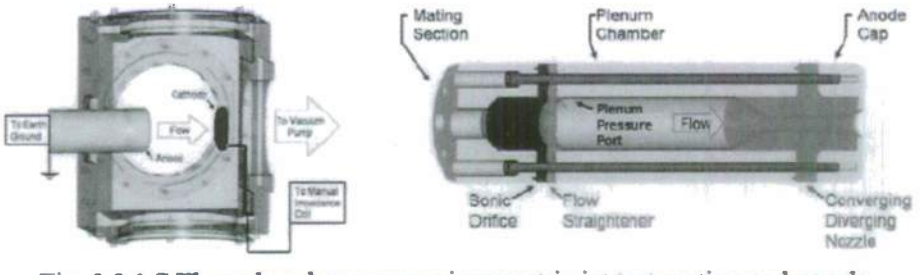

Fig. 3.3.1.7 The reduced pressure axisymmetric jet test section and nozzle.

The nozzle section, including the plenum of the jet, comprised of six separate pieces which mated together, as illustrated in Fig. 3.3.1.7. The nozzle section slid into the test section through a nylon block and was able to adjust the gap distance between the cathode and anode. The flow

straightener provided uniform flow into the plenum chamber, which provided a 15.24 cm long, 3.18 cm diameter long interior cylinder for the flow to be conditioned prior to acceleration through the nozzle. The converging-diverging nozzle section designed was using the method of characteristics. Additionally a constant diameter section 'nozzle' was utilized to produce the increased turbulence found in straight pipe flow.

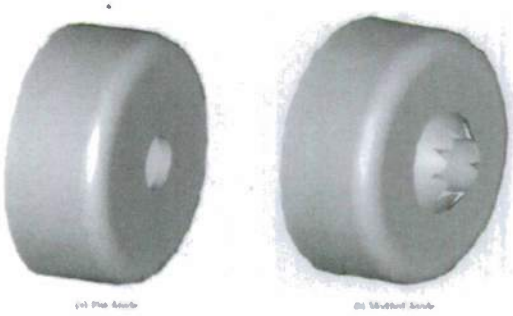

Fig. 3.3.1.8 Flat anode and the anode modified with serrated conical feature.

The final assembly of the nozzle section was the end cap which was grounded to provide the needed electrical connection of the anode for plasma generation. In addition to a flat anode cap arrangement, a modified anode was designed to focus more plasma energy near the exit of the jet. The anode was formed from the conventional flat faced anode described above, by creating a cone segment which came to a lip at the opening drilled for the jet exit. The modification was then altered by filing 8 grooves into the lip to produce a weak corona discharge in the non-uniform electric field formed in the serrations. Fig. 3.3.1.8 is an external view of each anode design, the flat anode and modified anode, clearly showing the serrations of in the conical lip. [Fridman 2004, Raiser 1995]. For the plasmas produced in this study the cathode was formed into a semi-torus disk with a hole in the center for the jet to flow through.

In general, an oscillating electric field provides more effective ionization than a DC field due to the exponential dependence of ionization rate on electric field magnitude. Radio frequency (RF) discharges can be split into two groups based on pressure. Atmospheric (high) pressure RF plasmas are thermal equilibrium plasmas thermal equilibrium plasmas, which are not part of the current research effort interest.. For the moderate pressures (roughly 50 Torr) generated in the RPAJ research facility for this effort, RF plasmas can be generated through inductive or capacitive coupling. A capacitive coupled RF plasma is generated between two electrodes which stimulate an electric field in the gap and produce a plasma. This research effort focused on generation of capacitively coupled plasma (CCP) based on the available equipment and to gain experience with the type of plasma generation which will be applied to larger facilities. [Fridman 2004, Menart 2003, Yano 1999]

The plasma generation system consisted of few components. Most of the system monitoring was provided by the Dressler Cesar 1350 RF generator and accompanying Dressler VarioMatch VM-5000W automatic impedance matching network. The RF generator produced up to 2 KW of power at 13.56 MHz. The generator actively monitored the system impedance and can automatically control the impedance matching network. Impedance matching was critical in RF plasma generation, as reflected power in the transmission lines drastically reduced the power available to the electric field for sustaining the plasma. Typically, to generate a plasma the impedance matching network was augmented with an additional inductance coil. Fig. 3.3.1.9. shows an example of a typical RF plasma created for this study. The jet shown here is formed

from a highly underexpanded jet, created by flow exiting a sonic orifice. This particular jet was used to study the influence of plasma-on strong shocks by measuring the movement of the position of the Mach disk. The goal in plasma tuning for each flow condition was to produce a uniform and symmetric (about the centerline of the jet) visible emission between the cathode and the anode. If the plasma emission did not reach the entire distance from the cathode to the anode, the power was incrementally adjusted to achieve the maximum plasma volume in the electrode gap. When creating a plasma for increasing Mach numbers, the forward power was not able to be fixed at one value. The highest power settings would have transitioned immediately to an arc at the lower jet speeds, while the low power setting used in the subsonic case would not have ignited the plasma for the faster jet.

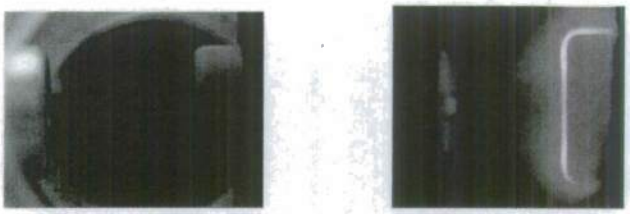

(a) Plasma and Jet Off **(b) Plasma and Jet On**

Fig. 3.3.1.9 Axisymmetric jet anode (left) and cathode (right) with plasma and jet off and on.

Mach 4 Supersonic Tunnel

A Mach 4 supersonic wind tunnel was constructed to facilitate the study of the effects of various types of plasmas and the perturbation on boundary layers in a high-speed flow. The tunnel has a 12.7 cm x 12.7 cm (5" x 5") square test section and optical access on all four walls. For the nominal Mach 4.0 flow, the system is capable of five minutes of run time on a full charge of the storage tanks using the high pressure air storage system described previously. Fig. 3.3.1.10 shows an image of the assembled Mach 4 wind tunnel with the flow characteristics summarized in Table 3.3.1.1.

Fig. 3.3.1.10 Image of the assembled Mach 4 wind tunnel.

Schlieren imaging and pitot probe measurements have been used to gather flow properties of the empty wind tunnel and unperturbed (plasma off) boundary layer. Weak waves emanating from the surface are generally caused by joints in the test section, and the nozzle geometry continues to be adjusted to reduce those due to the profile. By measuring the Mach angle from the schlieren images the Mach number was estimated to be between Mach 3.9 and 4.0. From the Pitot probe profiles the average Mach number in the core was found to be 4.12 ±0.07. The bottom and top 95% boundary layer thicknesses were computed to be 2.15 cm (0.84") and 1.74 cm (0.68"), respectively. More information about the wind tunnel can be found in DeBlauw et al. [2010].

Mach number	Test section size	Boundary layer thickness - 95%		Reynolds number (based on δ)	Stagnation pressure	Stagnation temperature	Test section velocity
	Square	bottom	top				
	cm/in	[cm/in]	[cm/in]	million	MPa/psig	K	m/s
4.12±0.07	12.7 / 5.0	2.15/0.84	1.74/0.68	1.2	1.21 / 175	280	697

Table 3.3.1.1 Summary of significant Mach 4 wind tunnel parameters.

3.3.2 Instrumentation and Diagnostics

One focus of this work is the development and application of advanced diagnostics for challenging hypersonic environments, including Filtered Angularly Resolved Rayleigh Scattering, Molecular Tagging Velocimetry, Particle Image Velocimetry and Emission Spectroscopy. These techniques were used to make fluctuating and mean density, pressure, temperature, and velocity measurements; velocity field measurements; and vibrational temperature measurements. Results obtained using these techniques are reported in Section 3.3.4.

Filtered Angularly Resolved Rayleigh Scattering

One of the first advanced diagnostics considered for the study of the NTE flows in the current investigation was based on the light scattered from molecules termed filtered angularly resolved Rayleigh scattering (FARRS). To describe the technique w start by considering Rayleigh scattering collected from an unseeded gas (which in general includes the effects of the Cabannes line and is also termed Rayleigh-Brillion scattering) which has three characteristics: its radiant intensity, the spectral shape of the scattering profile, and the frequency shift with respect to the incident wave as described in Fig. 3.3.2.1. As a function of the gas properties the intensity of the scattering is a linear function of the gas number density N. The spectral shape of the Rayleigh scattering, $r(x,y)$, can be expressed as a function of two non-dimensional parameters, x the non-dimensional frequency and y the order parameter which is a function of the pressure, laser wavelength, scattering angle measured from the laser propagation direction, and shear viscosity of the fluid which can be expressed as a function of the fluid temperature and molecular mass.[Tenti 1974, Seasholtz 1997, Boguszko 2005, Miles 2001].

The primary frequency shift with respect to the incident laser frequency is due to the Doppler effect of the fluid in motion. The Doppler shift is a function of the orientation of the laser propagation direction and the scattering direction with respect to the flow velocity, and is expressed as

$$\Delta\nu_D = 1/\lambda\ (\kappa_0 - \kappa_L) \cdot V \qquad (3.3.1)$$

where V is the velocity vector, κ_0 being the scattering direction unit vector and κ_L representing the laser direction unit vector, and λ is the laser wavelength. Therefore the Doppler shift changes for each viewing angle relative to the laser direction. For more details on this topic, see the paper by Miles et. al [2001] and Boguszko and Elliott [2005]

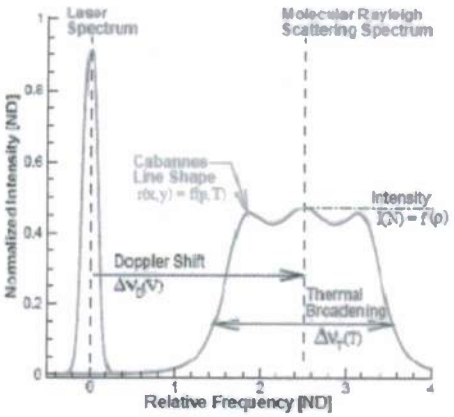

Fig. 3.3.2.1 Spectral characteristics of molecular Rayleigh scattering

For a given gas, all of the primitive variables of interest (pressure, density, temperature and velocity) are contained in the Rayleigh scattering signal. The difficulty lies in decoupling the effects of the primitive variables from the returned signal, which is a conglomerate of the combined effects. Density is easily determined, as the change in intensity of the Rayleigh scattered signal is proportional to fluid density. Fluid under a mean velocity results in a Doppler shift to the signal. Thermal effects are captured in the broadening of the Rayleigh scattered return. And finally, a combination of pressure and density results in a change in the shape of the acoustic sidebands of the scattering.

To use the properties of Rayleigh scattering to measure the fundamental variables Forkey, Finkelstein and Miles[1996] were the first to utilize a molecular absorption filter. Shirley and Winter[1993] modified the technique by introduction of anamorphic optics to measure mass flux. Elliott and Samimy[1996] further improved the technique to measure simultaneous mean flow properties and gave the technique the name: Filtered, Angularly Resolved Rayleigh Scattering (FARRS). This name derives from the fact that the optical set-up records the scattered intensity viewed over a range of observation directions (using anamorphic optics) recording the intensity separately for each direction. The scattered signal is then passed through an iodine absorption cell which acts as a frequency notch filter to the incoming light so that the flow properties (i.e. pressure, density, temperature, and velocity) from the measurement volume can be determined by comparison with a computational model of the scattering process. The goal of the present investigation was to determine the ability of this technique to obtain mean and fluctuating property measurements.

The equipment and techniques used to gather the FARRS images of the supersonic jet studied here are shown in Fig. 3.3.2.2. The FARRS experiment measured a free jet from a nozzle with a measured diameter of 6.5 mm. The collimated light source was an injection seeded Spectra Physics Quanta Ray laser, model number GCR-230 operated at 532 nm. The beam was turned by dichroic mirrors and focused to a point just beyond the interrogation region to prevent camera damage. As the beam exits the laser cavity, a small portion was split off with a dichroic wedge for laser frequency monitoring using a second iodine reference cell.

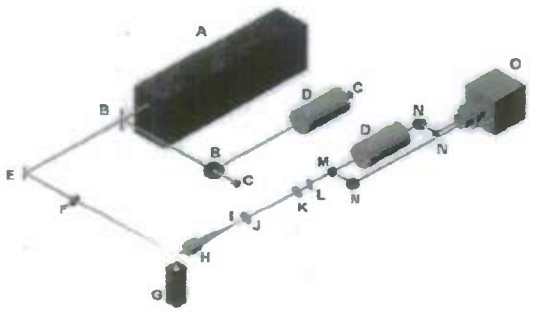

(a) Schematic

A	Spectra Physics Quanta Ray GCR-230 Nd:YAG Laser
B	Beam Splitter
C	Thor Labs Det 210 Photodiode
D	Iodine Cell
E	Dichroic Mirror
F	Spherical Lens, f 500mm
G	Test Nozzle, 5.077mm, Flow Vertically Upward
H	Nikkor 5.C 50mm Camera Lens
I	Thor Labs ID-12 Iris, Field Stop
J	Spherical Lens, f 500mm
K	Spherical Lens, f 500mm
L	Cylindrical Lens, f 1000mm
M	Non-polarizing Prismatic Cube, 25.4mm, $\frac{1}{4}$ wave
N	Silver Coated Mirror
O	Princeton Instruments ICCD-576-S Camera 384x576 pixels

(b) Description

Fig. 3.3.2.2 Typical FARRS layout.

The Rayleigh scattering optical signal was collected by a Nikkor f1.2 50 mm camera lens. The image was focused to a point and passed through a field stop to block the signal received out of the interrogation region. Downstream of the field stop, the image was collimated with a spherical lens and then focused to a line through a cylindrical lens. Then the beam was split through a cube prism and sent down two paths. The first path sent the beam through a calibrated iodine cell and was focused onto the image intensified charge-coupled device (CCD) camera. The second path was routed around the iodine cell and focused onto the same CCD.

After rejecting images from scattered dusted particles based on intensity, the images were reduced to two lines of intensity versus image angle (the filtered signal and unfiltered reference signal). The collapsed image lines were then compared with known flow conditions (jet turned off, pressure and temperature measured). Density was determined directly from relative image intensity which is proportional to air molecule number density in the interrogated flow volume. The flowfield variables of velocity, temperature, and pressure were determined by means of non-linear Levenberg-Marquardt curve-fitting algorithm of a computational model of the scattering process and using the ideal gas law. The algorithm was implemented in MATLAB© and run against the experimental data. To eliminate spurious data from the calculations, further data was rejected based on points which fell outside the range of three standard deviations in the flow and by limiting the curve-fitting residual. Approximately a third of the points were rejected on this basis which were most likely due to unstable laser performance (i.e. beam position and frequency) and remnants of dust particle scattering.

The FARRS measurements were taken over a radial profile (from the quiescent ambient air through the core of the jet) at three downstream locations for the Mach 1.2 axisymmetric jet. Each data point represents the processing of 4000 raw samples of data. Using isentropic equations of a jet issuing from the converging-diverging nozzle the core of the jet has an expected density, temperature, and velocity of 1.54 Kg/m^3, 229 K, and 363 m/s respectively. Fig. 3.3.2.3 shows the radial profiles of the mean property (density, temperature, pressure, and velocity) measurements with the fluctuating property measurements represented by the standard deviation profiles given in Fig. 3.3.2.4.

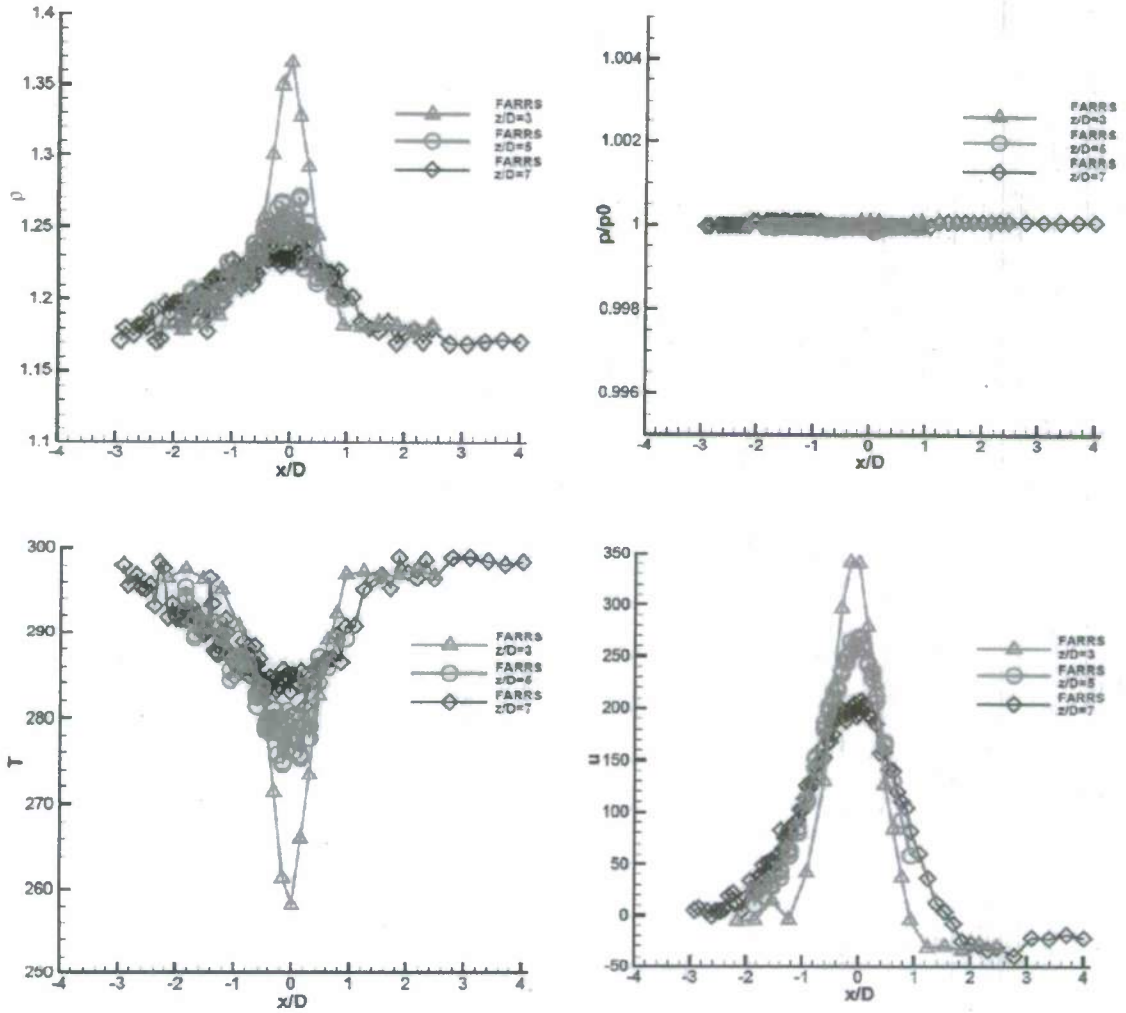

Fig. 3.3.2.3. Density [kg/m^3], pressure [ND], temperature [K], and velocity [m/s] mean radial (x) profiles measured using FARRS in a perfectly expanded jet from a Mach 1.2 converging-diverging nozzle at multiple downstream (z) locations.

The density plots of Fig. 3.3.2.3(a) and 3.3.2.4(a) show an expected decrease between the mean density on the centerline at $z/D = 3$ and the isentropic prediction in Table 3.3.1.1. The core region is marked by decreased turbulent fluctuations on the centerline at three diameters, which then disappear as expected further downstream. In Fig. 3.3.2.3(b) and 3.3.2.4(b), near perfect expansion of the nozzle (variations much less than 0.1% of atmospheric pressure) is evident in the mean pressure. The mean and fluctuating temperature results are presented in Fig. 3.3.2.3(c) and 3.3.2.4(c), and again the mean temperature on the centerline at $z/D = 3$ and the isentropic prediction are in good agreement, given the flow deceleration which occurs by the first measurement station three diameters downstream.

Fig. 3.3.2.3(d) and 3.3.2.4(d) show mean and fluctuating values of streamwise flow speed. The mean flow speed measurements follow the flow features as expected, showing the growth of the shear layer and reduction in peak speed as the flow progresses downstream. The mean flow speed at z/D of 3 and 7 shift to -30 m/s on one side of the jet, where the flow is quiescent. The

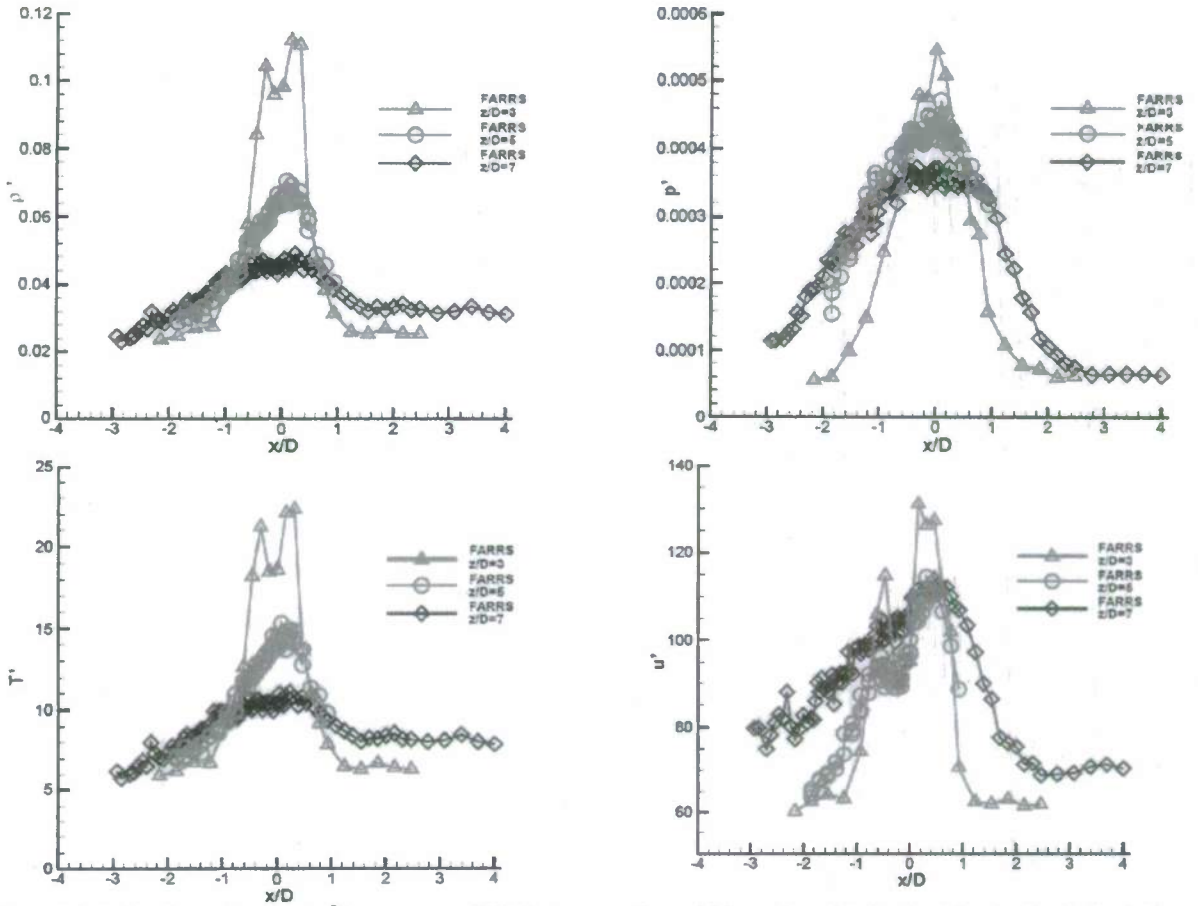

Fig. 3.3.2.4. Density [kg/m^3], pressure [ND], temperature [K], and velocity [m/s] standard deviation radial (x) profiles measured using FARRS in a perfectly expanded jet from a Mach 1.2 converging-diverging nozzle at multiple downstream (z) locations.

lab notes from the $z/D = 7$ sequence document a drastic shift in the position of the piezo which controls the cavity length at the same time as the shift in mean flow speed. From this, it is deduced that the change in cavity length repositioned the beam and therefore no longer correlated to the angular calibration performed at the beginning of the experiment sequence, which was initiated on the opposite side of the jet. It is believed a similar difference between beam position and calibration caused the shift in the $z/D = 3$ line as well. The shape of the fluctuating flow speed profile is generally as expected, with peaks as the measurement crosses the shear layer, and follows the trend of earlier experiments. [Boguszko 2005] However, there is a fluctuating noise floor of 60-80 m/s which is not present in their earlier work. Although the source of this elevated fluctuation level is presently unknown, it is most likely due to the low signal to noise ratio of the intensified camera, or pulse-to-pulse fluctuations of the illuminating laser beam position.

One technique that was incorporated approximately half-way through the testing and was to check the measured flow properties in the core of the jet before testing began for the day. This helps to diagnose any problems with the measurements before completing a full run for the day. Table 3.3.2.1 summarizes the comparison of the 28 baseline points in the jet core with the isentropically predicted values. As demonstrated by the comparison of the FARRS property

measurements and the theoretical (isentropic) values, the mean quantities show excellent agreement although the pressure variation appears to be quite optimistic and the actual value is most likely on the same order (5 to 10%) as the other quantities.

Parameter	Predicted	Measured ($\bar{x}$)	Variation (σ)	Difference
Density, ρ	1.54 Kg/m^3	1.46 Kg/m^3	$\pm$ 0.02 Kg/m^3	5% $\pm$ 1%
Temperature, T	229 K	241 K	$\pm$ 4 K	5% $\pm$ 2%
Pressure, P/P_0	1.0000	1.0003	$\pm$ 0.0001	0.03% $\pm$ 0.01%
Velocity u	363 m/s	357 m/s	$\pm$ 10 m/s	2% $\pm$ 3%

Table 3.3.2.1 Comparison of theoretical and measured values in the Mach 1.2 jet core

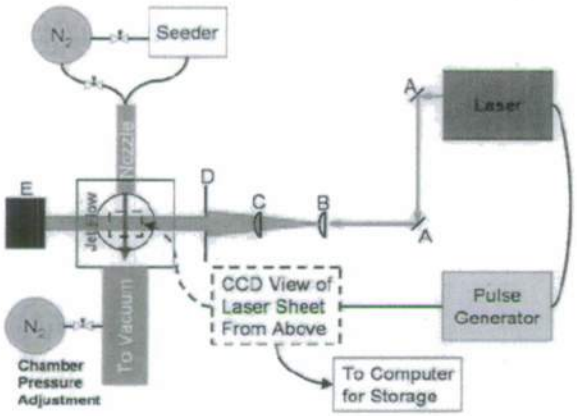

Fig. 3.3.2.5 PIV system.

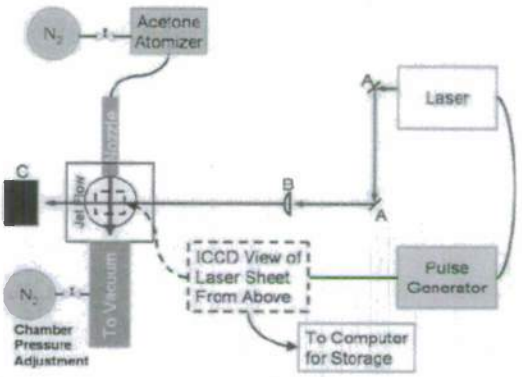

Fig. 3.3.2.6. MTV System

The AIAA paper by Huffman et al. [2007] discusses the FARRS experimental procedure, results, and measurement uncertainty in more detail. Although the results are promising it was determined that the other diagnostic methods described shortly are more suitable for the flow fields to be studied (due to the reduced pressure environment that is needed for the plasma and current uncertainty in the instantaneous measurements) and therefore further research was concentrated on developing them for use in the NTE turbulent flow fields to be studied.

Experimental Investigation of PIV in Rarefied Flows

Although particle image velocimetry (PIV) is a reliable and popular technique, its accuracy can be compromised with poor choices in flow seeding. Therefore before utilizing PIV to analyze the effects of NTE (through the application of various plasmas) on the flow fields to be studied, the ability of PIV to obtain accurate velocity measurements was investigated. Particle lag results when seed particles, which serve as flow markers are too large or too heavy to accurately track the flow field of interest. In the rarefied gas of the test section, quantum molecular collision dynamics govern the particle motion. This effect serves to increase the distance a particle travels before it reaches local conditions, after a sudden change when compared to the continuum dynamics of higher density flows. [Shen 2005, Adrian 2005, Raffel 1998, Loth 2006, Samimy 1991] In addition to a theoretical analysis of the particle tracking process for the flow fields to be studied with PIV (Huffman, 2007) it was also desirable to experimentally verify that PIV could be used to give accurate velocity profiles. To confirm the accuracy of seed particle

tracking, the velocity profiles from supersonic and subsonic axisymmetric jets operated in low pressure environments were compared by measuring exit velocity using PIV and molecular tagging velocimetry (MTV). The MTV data was considered to be the most accurate measurement of velocity, given the measurement tracer was molecular acetone vapor which does not suffer with particle lag problems in tracking the flow. The goal was to indicate if PIV was a viable technique to be utilized in these high speed flows in rarefied environments, and to determine results obtained from PIV are questionable or inaccurate.

Fig. 3.3.2.5 illustrates the setup of the particle image velocimetry system schematically. The laser beam was formed into a sheet by means of a cylindrical plano-convex lens which spread the beam horizontally. Next, the beam was focused vertically by a spherical plano-convex lens with the focal point placed just to the left of the nozzle centerline.

The seed particles were illuminated by the Gemini-15Hz PIV Nd:YAG laser made by New Wave Research. The laser produced two sequential pulses of light at a nominal frequency of 532 nm with the delay time controlled by a delay pulse generator. The PIV images were captured by the PCO.1600 CCD (1200x1600 pixels) camera from Cooke Corp. with a double framing option. Approximately 1000 image pairs were taken for each measurement and correlated using DPIVB software from ISSI Inc.

To provide particle size control, the flowfield was seeded with a Condensation Monodisperse Aerosol Generator (CMAG) model 3475 produced by TSi Inc. The CMAG uses atomized NaCl crystals (nominally 10-100nm in diameter) as a condensation source for heated DEHS oil vapor. The particle size can be adjusted by concentration and flowrate of the airborne salt crystals, as well as through varying the temperature of the oil vapor and the condensation chimney. [Anon 2004, Peters 1993] The setting to produce a given particle size distribution were verified using an Aerodynamic Particle Sizer (APS) model 3321 from TSi Inc. with the assistance of Jongmin Lee and Dr. Yuanhui Zhang.

Molecular tagging velocimetry (MTV) was utilized to determine regions in the flow where the particle seeding methods can give accurate results. Molecular tagging velocimetry (MTV) appears to be first introduced by Miles et. al. [1987] and since then others have seeded liquids with soluble phosphorescent molecules and phosphorescent vapors in gases. [Gendrich 1996, Hu 2002, Hiller 1984, Stier 1999, Lempert 2002].

In MTV the flow, seeded with tracer molecules, is excited by a focused laser line. Then, the tracer molecules are excited. The flow field is then imaged two times. The first image occurs quickly after excitation to capture the phosphorescence as a line. The next image is taken with a delay. The two images are compared and a mean velocity profile is deduced from the distance traveled during the delay time.

Fig. 3.3.2.6 is a schematic of components used in the molecular tagging velocimetry technique. In contrast to PIV, the particle generator is replaced by an atomizer which introduces acetone vapor into the flow. From this arrangement, the Nitrogen gas is saturated with Acetone vapor therefore the mean flow results calculated by this technique are compared to PIV data with the same concentration of Acetone. [Yuen 35, Thurber 1998, Lozano 1993, Nau 1996]

The Spectra Physics GCR-230 Nd:YAG laser provided the beam source, nominally at 266 nm with a pulse width of 8 ns. Images of the Acetone signal were recorded on a Princeton Instruments ICCD-576-S cooled and intensified charge-coupled device (ICCD) gated to 50 ns. 1000 images were taken at each test condition.

A sample of the response of a tagged line of the acetone tracer in a jet flow is given in Fig. 3.3.2.7. This figure shows the structure of a highly underexpanded jet just after the Mach

disk. Here, the flow is subsonic downstream of the normal shock, but the flow which surrounding the disk passed through the reflected oblique shock and is still supersonic. The translation of the tagged line due to flow velocity at increasing time intervals is shown at o and 400 ns after the incident laser excites the acetone vapor. The Mach disk region is located in the center of the image with the flow traveling from the bottom to the top of the figure.

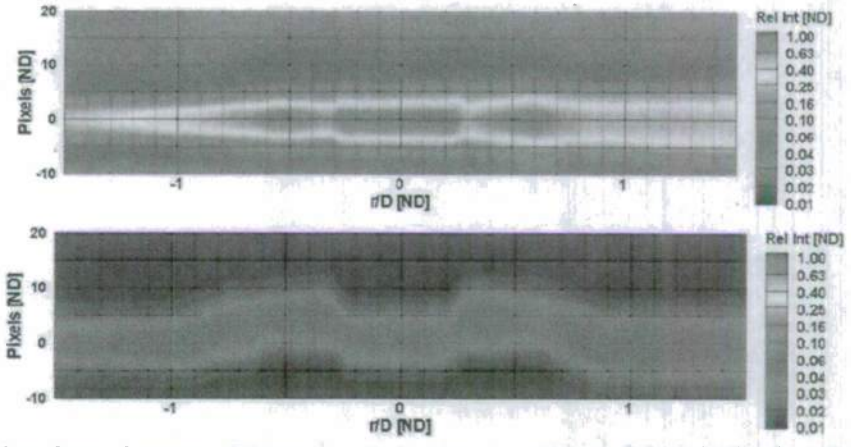

Fig. 3.3.2.7. Time lapse imagery (Upper: t = 0, Lower: t = 400 ns delay) indicating the motion of an acetone seeded flow field (a highly underexpanded jet just downstream of the Mach disk) imaged after being tagged by a UV laser beam at 266nm.

From these images the velocity in the axial direction was obtained by use of a Gaussian curve fitting routine. A MATLAB program based on the "fminsearch" algorithm matched the following equation to the measurement of intensity at each pixel.

$$I_{fit} = a\exp\left(-\left(\frac{x_{pixel}-b}{c}\right)^2\right)+d; \qquad (3.3.2.1)$$

where I_{fit} is the resulting intensity fit for a Gaussian peak centered at b. The constant a represents the maximum value of the peak, and the FWHM is c. A correction for constant floor d was included to improve the fit and never exceeded 1% of the peak value. The use of this curve fit provided sub-pixel accuracy, and assumed the illumination source is Gaussian. The result of the curve fit was a series of values which indicated the location of the peak center, which was calculated individually for each column of pixels and at every frame acquired. Velocity information was easily obtained then by a simple time-of-flight calculation. [Hu 2002, Lempert 2002, Hill 1996, Tran 2006]

Fig. 3.3.2.8 shows contours of axial velocity measurements from PIV, with a white line indicating the location of MTV data used to check the accuracy of the PIV measurements. The jet described in Fig. 3.3.2.8 is formed by developing flow created by a constant-diameter tube 9.5 mm in diameter and 12.7 cm long. The pressure ratio used to drive the flow would result in an isentropic Mach number of 1.9. Although one would expect that the Mach number should not exceed unity in the constant area tube, the presence of an aerodynamic throat at the entrance to the tube creates that converging diverging area needed to enable the supersonic Mach numbers to exist. [Aoki 2005, Dutton 1982, Han 2002]. Shock and expansion structures are present and display as the diamond shaped deceleration along the centerline of the jet in the contour image.

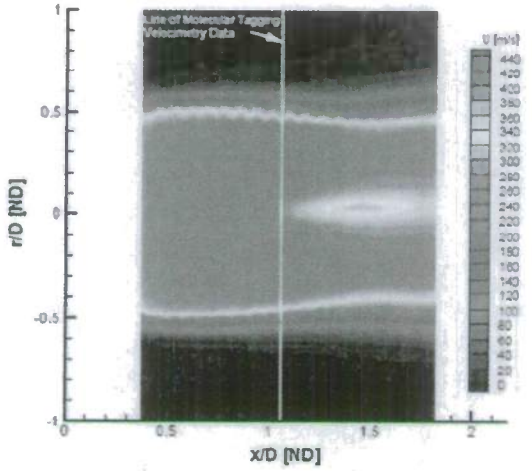

Fig. 3.3.2.8. Contours of axial velocity measured by PIV.

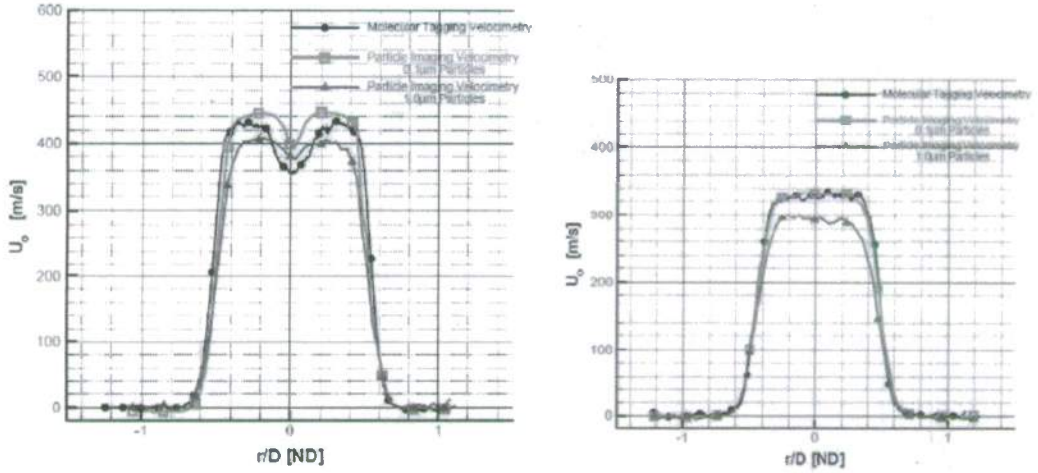

Fig. 3.3.2.9 Comparison of MTV and PIV; Mach number of 1.9 (left) and 1.4 (right).

Fig. 3.3.2.9 is a cross-section of axial velocity at 1.1 diameters from the nozzle cap which compares the MTV measurement to the PIV measurements for two particle sizes at an isentropic Mach number of 1.9. The shock structure is evident in the MTV result as the velocity decrease along the centerline. The $0.1\mu m$ diameter particles appear to track the flow well until the shock structure was encountered, and at this location the PIV results show a 3% higher maximum velocity than the MTV baseline. Conversely, the larger, $1.0\mu m$, particles indicate a 6% lag in peak velocity, having not accelerated to core velocity before encountering the shock. Note that the PIV data shows excellent agreement in the shear layer which is the focus of most of the research into the effects of NTE on turbulence to be discussed shortly.

Fig. 3.3.2.9 also compares MTV data to PIV measurements at the same location, with a pressure ratio equivalent to an isentropic Mach number of 1.4. In this case the $0.1\mu m$ diameter particles show excellent agreement to the MTV baseline, while the $1.0\mu m$ particles are still lagging the flow with now a 10% error. Note that while there are errors in tracking the centerline velocity near the exit of the jet, these represent the worst case tracking errors and that over the

four cases studied the tracking error for the smaller $0.1\mu m$ particles is under 5%. This difference is considered adequate for continued investigation into the mean flow features of rarefied axisymmetric jets in the absence of strong shock-expansion structures.

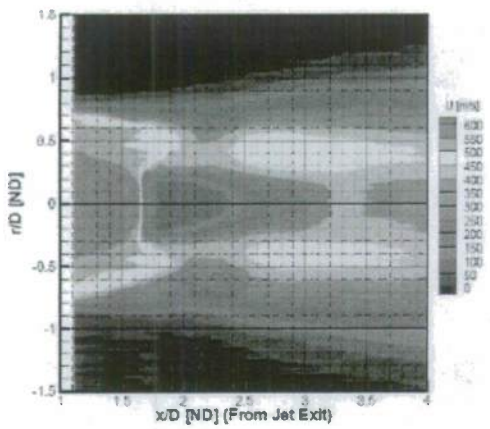

Fig. 3.3.2.10. MTV axial velocity.

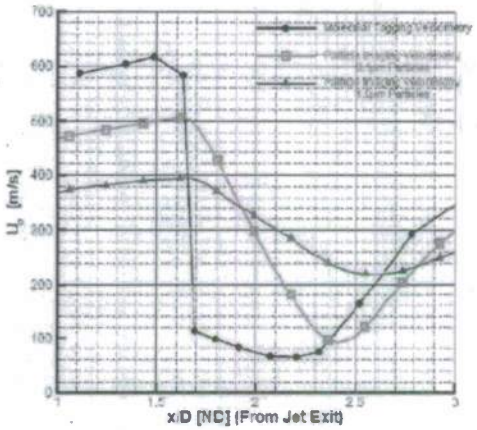

Fig. 3.3.2.11 Comparison of MTV and PIV.

The final case to be investigated was the highly underexpanded jet created by flow exiting a sonic orifice. The ability to track the flow features represented the worst case scenario for particle tracking and it was not expected that the particles would track this flow. The resulting near field flow is left to form its own nozzle with strong reflected shocks and expansions in order to equalize the pressure differential. The near field flow exiting from a sonic orifice contains a barrel shock and Mach disk which has been studied extensively.[Crist 1966, Love 1959, Li 2004, Owen 1948, Arnette 1992].

Fig. 3.3.2.10 shows the contours of axial velocity with the Mach disk clearly indicated by the sharp drop in velocity at 1.7 diameters from the jet exit, where the flow of the jet is from left to right. The flow was mapped with MTV, in a series of 16 lines spaced axially between 0.5 and 4 mm apart, with the tightest spacing occurring at the normal shock. The underexpanded jet was run at a stagnation and static pressure of 76 torr and 8 torr respectively resulting in an equivalent Mach number of 2.8 from the 8.2 mm diameter nozzle.

Fig. 3.3.2.11 compares the centerline axial velocity for the underexpanded jet as measured by MTV and PIV. Two particle sizes (0.1 μm and 1.0 μm)were generated to emphasize the effect of poor particle tracking. While the normal shock location can be determined accurately by all three techniques (by looking for the slope change in PIV curves the shock location can be determined to within a grid point axially), the particle latency in these rarefied flow conditions is extreme although as expected it is slightly better for the smaller particle size. It is clear that accurate velocity information is not available from PIV for rarefied conditions in the presence of strong shocks or expansions and extreme care must be taken in interpreting PIV results if these features are present.

To summarize the results for the PIV particle lag investigation it is found that near the exit of the jet (1.1 diameters downstream of the nozzle cap), the effects of particle latency on mean flow resulted in up to a 5% error in PIV measurements of centerline axial velocity for the 100 nm seed particles. The larger $1.0\mu m$ particles resulted in errors of up to 15%. In general, the 100 nm seed particles showed excellent tracking ability of the mean flow of the jet, which is expected to improve as the flow gradients shallow and the jet core is dissolved. Mean flow tracking for both

100 nm and 1.0μm diameter particles were not acceptable in the presence of strong shocks. Therefore it was determined that the 100 nm seed particles could provide the accuracy needed to study the effects of NTE turbulent flows. More details of these results with a complete uncertainty analysis is given in the dissertation of Huffman [2007] and AIAA paper [Huffman 2009].

Emission Spectroscopy in high enthalpy flow

Emission spectroscopy is used to identify dissociated species and to obtain vibrational temperature measurements using the nitric oxide and hydroxyl radical A-X band sequences. For the spectroscopic measurements, the broadband emission light is collected and collimated at 90 degrees to the vertical axis plane of the test section with a 200 mm focal length, as shown in Fig. 3.3.2.12. The collimated light is then focused for an imaging spectrograph. Two spectrographs were used in this study: an f/2 CP140 Jobin Yvon spectrograph for measurements which will be referred to as "coarse", and a f/4 270M SPEX spectrograph for measurements which will be referred to as "fine". Spectral lines were visualized using a Princeton Instruments PI-MAX MG:512SB intensified CCD camera system and a ST-133 camera controller. For the f/4 270M SPEX spectrograph measurements, a slit size of 43 μm was selected as a compromise between signal strength and resolution. The measured resolution is 1.4 Angstrom. Calibration sources were placed inside the test section and imaging points located with 1 mm spatial precision (with ±0.25 mm uncertainty) via the use of fine-scale translation stages. To assist with data-processing, background intensity and wavelength spectra were also obtained for each shot. As with the schlieren system, the spectrometer acquisition sequence was triggered using the transmitted shock arrival at the test section pitot probe which was located within the core flow, 31.75 mm below the tube centerline.

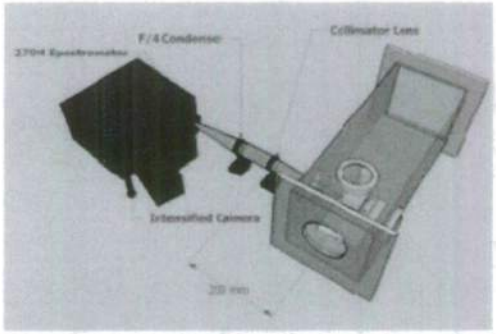

Fig. 3.3.2.12: Three dimensional schematic of imaging spectroscopy collection system

3.3.3 Results and Discussion

The facilities and diagnostic techniques described above were used in a series of investigations of transition and turbulence in canonical high-speed flow fields with nonequilbrium thermochemistry. We focused both on real gas effects occurring naturally at high enthalpy, and on non-equilibrium generated via a plasma. Results from studies of a shock-generated free shear layer in high enthalpy flow, both experiments and modeling; normal shock relaxation region species identification and temperature measurements; interaction of RF plasma with axisymmetric jets and compressible shear layers; Mach 4 boundary layer plasma interaction experiments are presented.

Shock-Interaction Generated Free Shear Layer in High Enthalpy Flow

A Mach reflection in a 7.42 high enthalpy free stream is used to generate i) a normal shock with thermochemical relaxation region, and ii) a triple-point generated free shear layer separating gas streams with significantly different temperatures and chemical composition. Once the free stream is carefully characterized and shock angles are measured from highly resolved schlieren images, this canonical flow provides a useful test bed for experiments and thermochemical model development.

Air-5 Test Condition Characterization

The shock interaction shear layer and emission spectroscopy experiments were conducted in the HET in a Mach 7.42 air freestream test condition, labeled Air-5. This test condition was achieved with a p_4 of 2500kPa (helium), p_1 of 1.5kPa (air) and p_5 of 175mTorr (helium). Table 3.3.3.1 summarizes the test gas freestream condition with a comparison between experimentally measured values and inviscid, one-dimensional, perfect gas calculations. The experimental values presented are ensemble averaged across a total of 28 separate events, consisting of 20 experiments for NO spectra acquisition and 8 experiments for OH spectra acquisition. Across most of the test condition parameters the agreement between theoretical expectation and measurement is very good. The largest discrepancy is seen in the calculated and measured values of the transmitted shock velocity, u_t. However, two-dimensional Navier-Stokes simulations of a very similar run condition (Air-1) have shown that the transmitted shock is considerably attenuated due to viscous effects through the acceleration section. Good agreement was obtained between the numerically predicted and the experimentally measured velocity. The previous run condition, Air-1, differs from Air-5 only by the primary diaphragm burst pressure. Perfect gas predictions indicate that the transmitted shock velocity differs by only 1% for the change in burst pressure. Therefore, u_t is assumed to be invariant with burst pressure and the calculated u_t over-prediction results from the inviscid, one-dimensional assumption. The experimental test gas Mach number is calculated from the measured pitot pressure using the theoretical prediction of the static test gas pressure, p_7. Very low signal-to-noise ratios prevent experimental measurement of p_7 for the current run condition. Despite a lower than theoretically predicted test-time, there is sufficient test time to make spectroscopic measurements.

	M_7	$h_{0,7}$ (MJ/kg)	$P_{7,pitot}$ (kPa)	Test Time (μs)	P_7 (Pa)	u_t (m/s)	u_7 (m/s)	u_s (m/s)	T_7 (K)
Experiment	7.30	-	53.64±6.1	104	-	4148±47	-	2044±42	-
Theory	7.42	7.88	55.6	163	788	5228	3777	1995	644

Table 3.3.3.1: Selected test gas freestream parameters. Theoretical calculations assuming one-dimensional, perfect gas dynamics are compared with experimental measurements.

Asymmetric Mach Reflection

A Mach reflection is created by an asymmetric wedge configuration as shown in the schlieren image of Fig. 3.3.3.1 a), which displays the Mach stem bridging two triple points from which free shear layers emanate. 25 and 35 degree half-angle wedges are used with a tip-to-tip

separation of 25.4mm. In order to avoid three-dimensional effects, inlet aspect ratios of 1.25 and wedge aspect ratios of 5 were used [Skews 1997]. This experimental configuration was chosen to produce well-characterized experimental inflow conditions and to avoid boundary layer complications associated with splitter plate geometries. The shear layers separate a supersonic, relatively cold, gas stream and a subsonic, relatively hot gas stream. The wedge angles were selected using perfect gas shock polar calculations in order to produce only Mach reflection configurations (as opposed to the typical regular reflection).

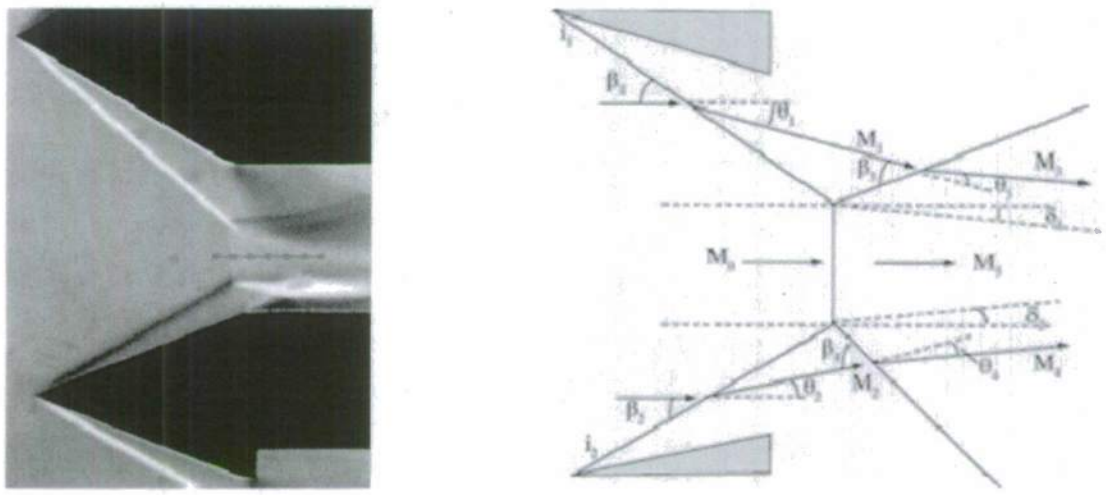

Fig. 3.3.3.1: a) Schlieren image of an asymmetric Mach reflection in Air-5 test condition, nominal freestream Mach number of 7.42. Wedge tip-to-tip spacing is 24.5mm. Emission spectroscopy measurement locations are indicated. b) Schematic of an asymmetric Mach reflection.

The Mach reflection (MR) has been extensively studied throughout the literature as an example of a shock-shock interaction which occurs extensively in aerodynamic applications. With significant thermochemical effects present in the current study, it is important to characterize their anticipated influence upon the Mach reflection configuration. Numerous previous studies have confirmed that the overall MR configuration is displaced forward and the Mach stem height is decreased in the presence of non-equilibrium effects [Gimelschein et al. 1998, Grasso and Pauli 1999, Burtschell et al. 2001, Grasso and Pauli 2000]. The Mach stem height reduction increases the experimental difficulty as the post-shock measurement area is also decreased.

Numerical simulations of the current asymmetric wedge arrangement indicate that the flow field is significantly dependent upon the thermochemical model [McGilvray et al. 2007]. Frozen, finite-rate and equilibrium models were examined. The thermochemical model was seen to change both the location and height of the Mach stem. These results are consistent with the effects of thermochemistry previously observed in the literature. Finite-rate simulations provided the best agreement with experiment. However, the simulation predicted a slightly further recessed and longer Mach stem than experimentally observed from the schlieren imaging. The simulations also indicated that the Mach stem position is stationary 20 microseconds after the passing of the contact surface. For test gas duration of approximately 120 μs this confirms that a

steady Mach reflection exists and ensures, combined with a consistent triggering event, that the steady portion of the test gas is captured.

From schlieren images, the Mach stem is measured to be 3.9mm high, almost perpendicular, located 12.7 mm downstream of the wedge tip plane and 2mm below the tube axial centerline (which also corresponds to the axial centerline of the wedges). As Fig. 3.3.3.1 a) shows, the uniform region behind the Mach stem which is not influenced by the converging shear layer slipstreams is very small (approximately 5mm). It is therefore imperative that the spatial locations of the spectra collection points are known very precisely with respect to the wedge tip plane. This involves determining the repeatability of the Mach stem location and potential shift from experiment-to-experiment. Results found the deviation on both height and location measurements to be ±0.5mm. Considerable care was taken towards the positioning and placement of the calibration stages with respect to the wedge tip plane. This experiment-to-experiment movement of the Mach stem is deemed small enough with respect to the uniform region length and the Mach stem height such that the calibration imaging point (acquired before the experiment) corresponds to the same location within the flowfield during the experiment. Measurements were made along the Mach stem centerline at -1, 0, 1,2,3,4 and 5mm downstream of the Mach stem, locations indicated by the symbols in Fig. 3.3.3.1 a).

The MR configuration geometry has been verified via measurement of shock angles from the schlieren images. The results are presented in Table 3.3.3.2 and compared against perfect gas predictions. The subscripts refer to the Mach reflection schematic depicted in Fig. 3.3.3.1 b). The theoretical reflected-shock angles were determined from shock-polar calculations. Comparisons yield very good agreement between incident shock angles. The differences observed for the lower triple-point reflected-shock and slipstream angles are more pronounced, especially so for the slipstream angle. Whilst the static test gas temperature has not been directly measured, the agreement between test gas pitot pressure, test gas Mach number, primary and transmitted shock speeds and incident shock angles suggests that freestream conditions are well-predicted by perfect gas theory.

Shock Angle (degrees)	Theory	Experiment
β_1	46.6	44.4±0.3
β_2	33.0	32.5±0.3
β_4	40.6	45.1±0.3
δ_2	-7.4	-2.7±0.3

Table 3.3.3.2: Theoretical and measured Mach reflection shock and shear layer angles.

Normal Shock Relaxation Region

Emission spectroscopy is used to measure nitric oxide and hydroxyl radical vibrational temperatures behind a strong normal shock. The stationary normal shock is created via a Mach reflection using an opposing wedge model in a high enthalpy Mach 7.42 air freestream in an expansion tube facility, as described above. The inflow conditions for the normal shock have been experimentally defined by pressure, velocity and shock angle measurements. Experimental spectral data were collected at selected locations, 1 mm apart, behind the Mach stem. OH temperature fits were conducted using simulated spectra generated by LIFBASE, whereas the

NO fits required higher vibrational and rotational levels and the use of an in-house spectral simulation algorithm. A state-resolved thermochemical model was used to model the temperature profile up to 5 mm downstream of the Mach stem. Excellent agreement is obtained between NO vibrational measurements and computations, validating both the experimental technique and the non-equilibrium thermochemical model. These results extend previous studies applying emission spectroscopy for test gas identification in impulse facilities and demonstrate the measurement of species vibrational temperatures in an expansion tube.

Spectroscopic Species Identification

A spectrum obtained 10mm downstream of the Mach stem over the wavelength regime of 200-400nm using the f/2 CP140 Jobin Yvon spectrograph is shown in Fig. 3.3.3.2. Coarse resolution acquisition was undertaken as a means identifying potential temperature-measurement appropriate species. Emission from the OH radical has the strongest signal and dominates the entire spectrum. Certain portions of the spectrum are also magnified in order to show the presence of N_2^+ and NO. Therefore, the identified emitters with temperature-fitting potential in this wavelength regime are NO, OH and N_2^+. Based on these results, the decision was made to concentrate efforts upon the ultraviolet portion of the spectrum. Additional measurements also detected no noticeable signatures in the visible region.

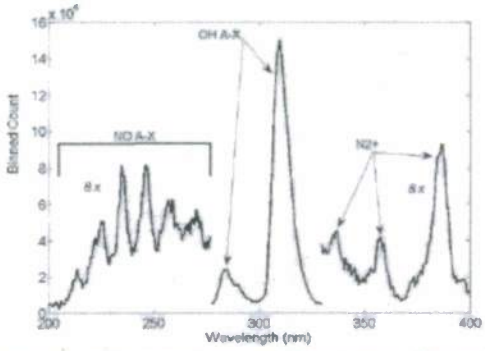

Fig. 3.3.3.2: Spectrum downstream of the Mach stem (50 micron slit and 50 μs exposure time).

Temperature Measurements Using Emission from the Hydroxyl Radical

As a preliminary means of determining the feasibility of applying fine-scale resolution emission spectroscopy to this flow field, initial measurements were conducted using the emission spectra of OH. These data collection locations with respect to the Mach reflection are shown in Fig. 3.3.3.1 a). The OH A-X band was deliberately chosen for initial temperature-fitting as its calibration setup was easier to implement than the NO A-X band as a traditional blackbody radiation source could be used, which has an analytical solution. Additionally, OH is already present in the flow field due to moisture contamination in the test gas. Fine-scale spectra were collected and temperature fits constructed for the $A\,^2\Sigma^+ \rightarrow X\,^2\Pi$ electronic transition in the 307-320nm region.

An example of an emission spectrum for the OH A-X band obtained 4mm downstream of the Mach stem is shown in Fig. 3.3.3.1. Simulated and experimentally observed spectra are compared. At each axial location, LIFBASE was used to generate simulated spectra across a

broad temperature range at coarse temperature increments of 100 K using Lorentzian profiles and a resolution of 0.14nm. Wavelengths were interpolated so that the LIFBASE data points matched up with the experimental points and at each temperature increment a scaling factor was computed which reduces the residual, a value defined to be the sum of the differences between experimental and predicted intensity peak values across the entire spectral range. The smallest residual of the entire temperature range provided the fit temperature. Once the coarse temperature was determined, further optimization was performed such that the final temperature increment was 20K. The results indicate that the intensities across the entire spectrum match up very well and that reasonable temperature fits have been achieved. Spectra collected at 1mm upstream of the Mach stem yielded no signal, confirming the spatial precision of the imaging location technique and lack of freestream dissociation in the facility.

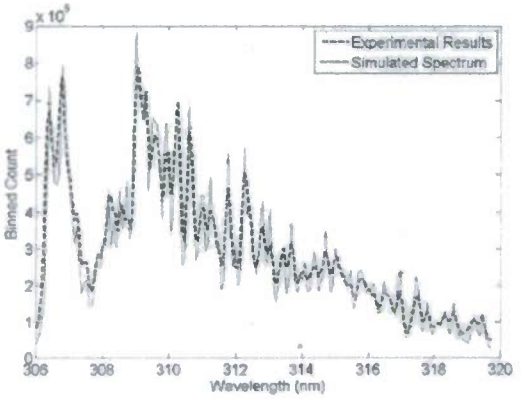

Fig. 3.3.3.3: OH spectra (Tv = 4140K)

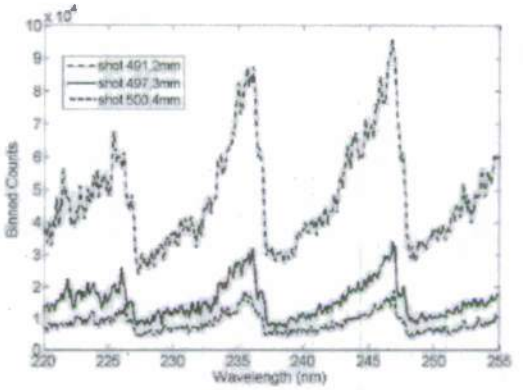

Fig. 3.3.3.4: NO γ band spectra.

Temperature Measurements Using Emission from Nitric Oxide

Experiments were undertaken in order to investigate the NO γ band. Interrogation of the γ band permits comparison with numerical results as the thermochemical model [Massa and Austin 2008] does not include OH as a species. Fig. 3.3.3.4 is an example of three NO spectra at three different streamwise locations of 2, 3 and 4mm downstream from the Mach stem. The graph indicates that the signal strength markedly attenuates with increasing axial distance and suggests that the experimental spatial precision is adequate.

Spectral fitting to the NO data using LIFBASE yielded very high temperatures, possibly due to the LIFBASE rotational and vibrational quantum number limits of 80 and 5 respectively. Calculations across an appropriate temperature range revealed that non-negligible Boltzmann rotational and vibrational populations exist for NO above these limits. Hence, an in-house algorithm developed by Glumac with user-defined maximum limits was used to generate simulated spectra. Vibrational and rotational energies are determined to the third and second-order respectively via Dunham-type potential expansions. For consistency, the spectroscopic constants used in these expansions are taken as those from LIFBASE [Luque 1999]. For the doublet ground state, the lower and upper configuration energies are calculated using the analytical expressions of Kovacs [Kovacs 1969]. The dependence of the spin-orbit parameter, A, upon the vibrational quantum number is taken from Amiot [Amiot 1982]. Line strengths were calculated via multiplication of the Franck-Condon factors and the Hönl-London factors. The Hönl-London factors for the doublet transitions were determined following the expressions of

Kovacs [Kovacs 1969] and the Franck-Condon factors were taken from Ory et al. [Ory et al. 1963]. Conversion from vacuum to air wavelengths is achieved via the Edlen formula. The LIFBASE simulation formulates emission intensity as a function of molecule lifetime, emission co-efficients and predissociation rates. LIFBASE calculates the emission co-efficients by incorporating the Hönl-London factors and the transition probabilities that are calculated using the Rydberg-Klein-Ress (RKR) method. The predissociation phenomena has been observed for the NO γ band and has been experimentally [Luque and Crosley 2000], theoretically [Luque and Crosley 1999] and numerically [Velasco et al. 2005] shown to be dependent upon both vibrational and rotational quantum numbers. Vibrational levels of υ'=4 and 5 can predissociate and for v'=3, rotational levels above N'= 25 can predissociate [Luque and Crosley 2000]. However, for the most part transitions from these levels result in energies outside the current wavelength regime. As identified by Fig. 3.3.3.5, the dominant vibrational transitions which weigh heavily upon the temperature-fitting procedure will not predissociate as explained above. Furthermore, LIFBASE simulations for 220-255nm show no difference between spectra with and without predissociation broadening. Therefore, predissociation is not considered to be a phenomena which needs to be considered for the wavelength range of interest.

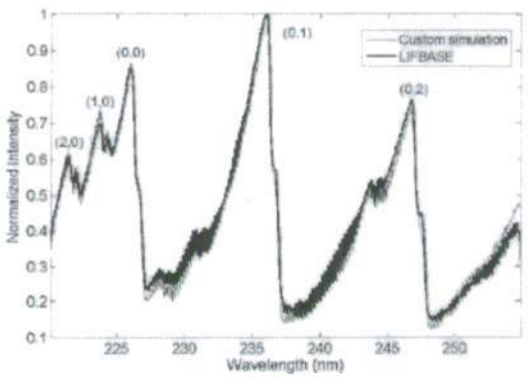

Fig. 3.3.3.5: Simulated Spectra (6200K).

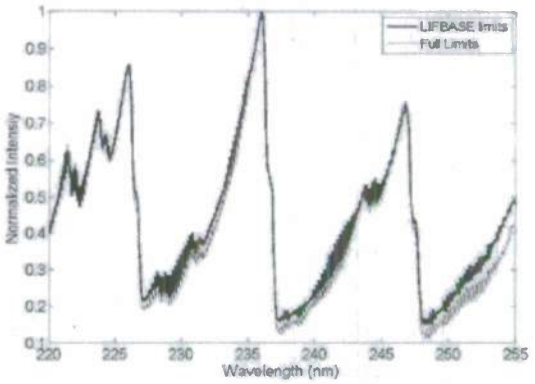

Fig. 3.3.3.6 υ_{max}=5, J_{max}=80 to υ_{max}=20, J_{max}=250.

Fig. 3.3.3.5 shows a comparison between LIFBASE and an in-house simulation for a temperature of 6200K for limits of υ_{max}=5 and J_{max}=80 (limits inherent to LIFBASE). The major vibrational band transitions are also indicated. The spectra are normalized by the maximum intensity in each case, which corresponds to the (0,1) peak value. The agreement between the two simulations is very good and within the experimental spectral resolution. Fig. 3.3.3.6 shows a comparison between the two in-house simulations, one with the lower limits of υ_{max}=5 and J_{max}=80 and the other with the extended limits of of υ_{max}=20 and J_{max}=250. As evident in the Fig., the use of the extended limits alters the intensity distribution across major portions of the spectrum. The extended vibrational limits (and hence larger $\Delta\upsilon$ values) will not influence the simulated spectrum; however the modeling of extra rotational levels will alter the spectrum within the 220-255nm range. Since the intensity distribution is the optimization parameter for the temperature-fitting procedure, the inclusion of additional limits via the in-house simulations is justified.

Fine-scale spectra were collected and temperature fits constructed for the NO $A\,^2\Sigma^+ \rightarrow X^2\Pi$ electronic transition in the 220-255nm region using the extended limits. The temperature fitting

procedure was the same as described for the OH A-X transition. NO spectra were collected at 1,2,3 and 4 mm downstream of the Mach stem. Further downstream spectral acquisition of the relaxation region was restricted by the influence of converging shear layers bounding the measurement region. A sample spectrum, collected at 2 mm behind the Mach stem, is shown in Fig. 3.3.3.7 along with the simulated comparison. The vibrational temperature in this case was determined to be 6900K. Using the LIFBASE limits, the calculated vibrational temperature was 7600K. As exhibited for all imaging locations, the NO spectra are somewhat noisy and the visual fit fidelity is not as pronounced as in the OH spectra. However, the computational algorithm uses the line intensities as the optimizing parameter and as shown in Fig. 3.3.3.7 the major vibrational band transition intensities are all very accurately matched.

The potential of contaminant emission within the 220-255nm range was further investigated. Previous spectroscopic measurements at the TCM2 hypersonic facility have highlighted the importance of reducing test gas contamination. Pilverdier et al. noticed that a Mylar secondary diaphragm displayed significantly less emissive intensity than one made from copper [Pilverdier et al. 2001]. The HET facility operates with a Mylar diaphragm. Ramjuan et al. also emphasized the importance of cleaning the facility [Ramjuan et al. 2001]. As a result, before each shot both the driven and accelerator section were cleaned. No differences in the nitric oxide spectra were observed. Dry air was also used as the test gas in order to see if the trace quantities of OH were contaminating the results. The test location 2mm behind the Mach stem was used to determine the influence of the moisture within the air. At this location five room air shots and six dry air shots were conducted and the temperatures determined. The standard deviation of these determined temperatures was 320K and 140K for the room air and dry air runs respectively. Despite the improvement in shot-to-shot repeatability with dry air as the test gas, no marked change in the experimental spectra was observed. The O_2 Schumann-Runge band system has emission within the investigated spectral regime. Previous studies have identified this O_2 radiation within NO γ band emission, however its presence was overwhelmed by the NO emission [Wurster et al. 1989, Wurster et al. 1990]. As shown in Fig. 3.3.3.7, possible O_2 radiation is less intense than the NO γ signal and hence it is proposed that this interference is not significant enough to seriously hamper the temperature-fitting procedure.

Experimentally measured NO vibrational temperatures are shown in Fig. 3.3.3.8. Data are obtained from three experiments each at 1, 3 and 4 mm and six experiments at the 2 mm location. The repeatability of the measurements is good. The temperature profile calculated using the detailed thermochemical model detailed above is also shown. Very good agreement is achieved between calculated and experimentally measured vibrational temperatures across the relaxation region. The largest discrepancy is observed at the 2mm location, while the temperature measurements at the other three locations are all within experimental error. The equilibrium temperature for this run condition (assuming nitrogen, oxygen and argon air mixture) is calculated to be 3872K from the NASA CEA program [McBride and Gordon 96]. Table 3.3.3.2 compares the ensemble average of the temperature measurement at each location versus the numerical result. The results from the OH temperature fits described above are also presented on the same graph. The OH vibrational temperatures are considerably lower than those of NO and the temperature gradient throughout the relaxation region is much less pronounced and accompanied by a faster relaxation rate. OH error bars are not presented as no thermochemical calculation was conducted and hence no temperature gradient was available. The significant disparity between the experimentally measured OH and NO vibrational temperatures is indicative of the non-equilibrium flow field. Without OH thermochemical calculations, it is

difficult to provide a physical explanation for this disparity. However, the experimentally measured OH vibrational temperatures are included to provide comparative data for any OH thermochemical model.

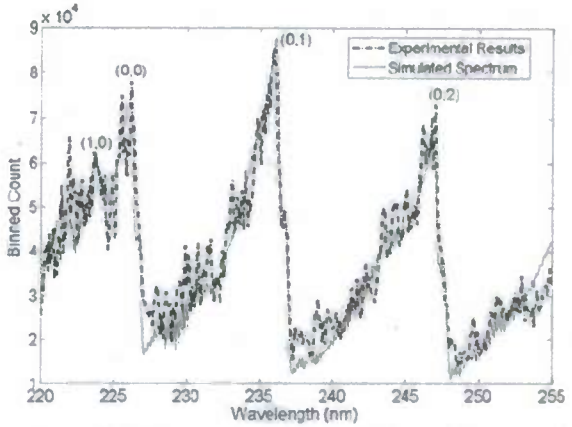

Fig. 3.3.3.7 Simulated and experimental NO spectra obtained 2 mm downstream of the Mach stem for a vibrational temperature of 6900K.

Distance (mm)	Numerical (K)	Experimental (K)
1	7143	7067
2	6356	6917
3	5971	6060
4	5721	6007

Table 3.3.3.2: Comparison of averaged experimental values and numerical results at different locations behind the Mach stem.

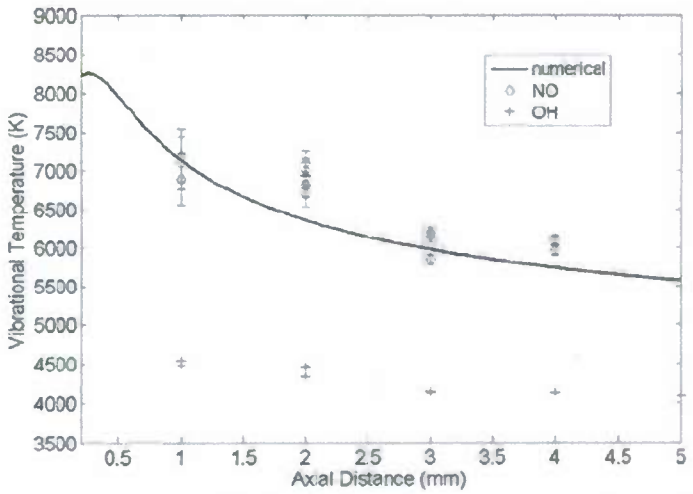

Fig. 3.3.3.8: Measured NO and OH vibrational temperatures in the post-shock region.

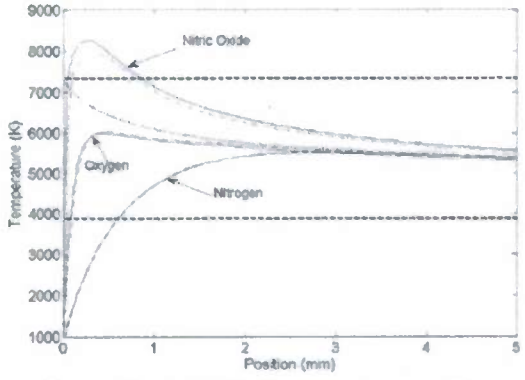

Fig. 3.3.3.8: Temperature profiles.

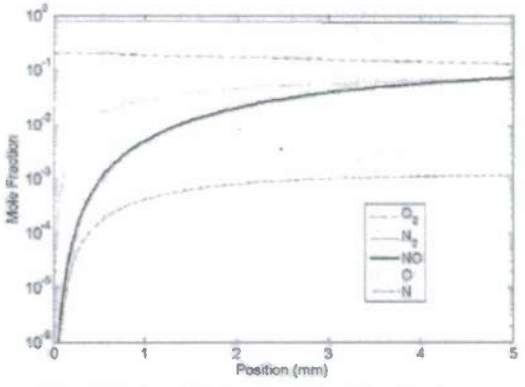

Fig. 3.3.3.9: Mole fraction distribution

Fig. 3.3.3.8 displays the temperature profiles calculated using the thermochemical model up to 5 mm downstream from the Mach stem for nitric oxide, oxygen and nitrogen. The first vibrational temperature T_{v1} is defined as

$$\frac{e_1 - e_0}{k \log\left(\frac{N_0}{N_1}\right)}$$

where N are the mole numbers in the subscripted vibrational levels, (0,1), and k is the Boltzmann constant [Massa and Austin 2008]. Fig. 3.3.3.9 displays the mole fraction profiles of the 5 major species, NO, O_2, N_2, O and N, up to 5 mm downstream of the Mach stem.

Sources of Uncertainty

The temperature measurement sources of error arise from shot-to-shot variation in MR location, the spatial precision of the imaging location, test condition variability, spectroscopic resolution and the temperature increment selection of the fit to simulated spectra. The first two sources are dependent upon the relaxation region temperature gradient, which was determined from numerical calculations. The uncertainties in the imaging location and MR movement are 0.25 mm and 0.5 mm respectively. The spectroscopic resolution in the axial direction is determined by the slit size, which is 43 μm. The freestream static temperature was used as the parameter to gauge test condition variability. For the purpose of the uncertainty analysis, the freestream static temperature is taken to be only dependent upon the HET initial pressures. Theoretically, the freestream static temperature would also be dependent upon the section gas compositions. Moisture within the air is expected to have a negligible influence upon the air test gas and is also not considered. Driver pressures are so large (roughly 25 atm) that any residual air within the helium gas is completely negligible. Therefore, freestream static temperatures are taken to be dependent only upon the initial HET pressures. Table 3.3.3.3. presents the percentage breakdown of each uncertainty source. The temperature measurement error bars at each imaging location, ΔT, based upon the five uncertainty parameters described above is calculated using the following equation

$$\Delta T = \sqrt{\sum_{i=1}^{5}\left[\left(\frac{\partial T}{\partial x_i}\omega_{x_i}\right)^2\right]}$$

where ω_{x_i} denotes the uncertainty in the measurement of a certain parameter, x_i. Values are presented as percentages of the total uncertainty. The largest contribution to the total uncertainty is from the movement of the MR configuration from shot-to-shot. Combined with the imaging location uncertainty these two factors account for more than 70% of the total uncertainty at each spatial location.

Axial Distance (mm)	Spectrometer Resolution	Mach Reflection	Imaging Location	Test Condition	Temperature Increment
1	0.16	77.76	19.44	2.55	0.09
2	0.15	75.45	18.86	5.17	0.37
3	0.13	63.52	15.88	18.67	1.81
4	0.11	56.67	14.17	25.25	2.80

Table 3.3.3.3: Breakdown of the contribution of the different uncertainty sources at each spatial imaging location for the nitric oxide vibrational temperature measurements. Values are given as percentages of the total uncertainty.

Spatial Linear Stability of a Shear Layer with Real Gas Thermochemistry

The goal of this work was for the first time to compare equilibrium, non-equilibrium, and frozen flow models and quantify the impact of high temperature effects on shear layer spatial linear stability. Calculations were performed using the forced harmonic oscillator model of Adamovich and co-workers [Adamovich and Rich 1998, Macheret and Adamovich 2000, Adamovich 2001] with a new extension to higher collisional energies overcoming the complexity of the steepest descent integration of transition probability [Massa and Austin 2008]. The nominal shear layer in this study is based on an experiment in which the shear layer is created at shock triple point. The convective Mach number M_c was varied about the nominal value of 0.683 from 0.341 to 1.707. Mean flow temperature profiles show higher temperatures in the frozen case as expected. All three models show increased viscous heating at the centerline at higher convective Mach number. For oxygen and nitrogen, the first and equivalent vibrational temperature profiles are very similar, Fig. 3.3.3.10. For nitric oxide however, the two temperature profiles are substantially different, indicating departure from log-linear vibrational energy distribution.

Normal velocity and enthalpy eigenfunctions for the most amplified three-dimensional mode show significant difference among the three flow models. The relative importance of non-equilibrium eigenfunctions is dependent on the magnitude of the convective time scale relative to chemical time scale. The equivalent and first vibrational temperature eigenfunctions are similar for oxygen and nitrogen, but very different for nitric oxide, which may be attributed to the departure from log-linear vibrational energy distribution. Vibrational non-equilibrium can be quantified by examining the differences between translational and vibrational temperature eigenfunctions with increased difference indicating increased vibrational non-equilibrium. Vibrational non-equilibrium effects are greatest at higher convective Mach number, with nitric oxide exhibiting the most pronounced temperature differences. A comparison of dissociation and

translational temperature shows significantly different chemical non-equilibrium behavior for the different gases, with oxygen exhibiting a smaller perturbation in equilibrium dissociation temperature than translational temperature while the opposite occurs for nitrogen and nitric oxide. A strong correlation is observed between eigenfunction peaks of equivalent dissociation temperatures in nitrogen, and equivalent vibrational temperature in nitric oxide, Fig. 3.3.3.11, showing a strong dissociation and vibration transfer coupling through the second Zeldovich reaction.

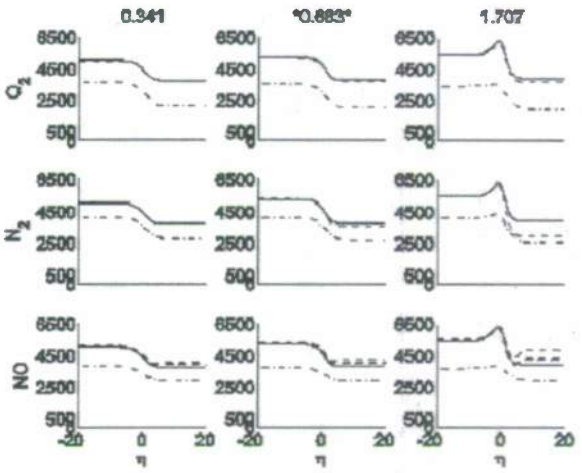

Fig. 3.3.3.10. Shear layer temperature distribution at x=3cm downstream of the triple point for three convective Mach numbers, including the nominal experimental condition M_c=0.683. Translational temperature (solid line), equivalent vibrational temperature (dashed line), equivalent dissociation temperature (dash-dotted line).

Interaction of RF Plasma with Axisymmetric Jets and Compressible Shear Layers

A comprehensive set PIV data was collected comparing axisymmetric nitrogen jets produced under various conditions with and without the RF plasma field applied. Table 3.3.3.4 gives a summary of the flow properties of the jets (stagnation pressure, static pressure, Mach number etc.) studied in this investigation. Cases A, B, C, and E are experiments conducted on converging-diverging nozzles under pressure matched conditions. Case E was tested at 8 torr vice 9 torr to achieve the proper pressure matching. Cases F, G and H were conducted using a constant diameter nozzle. The constant-diameter nozzle was made of a tube, 13.3 diameters long. The goal of these cases was to create a jet with increased turbulence (an effect of the developing pipe flow) in the jet core and thicker shear layer region so that changes in the turbulence profiles may be more obvious. Subsonic and even supersonic exit conditions are achieved with the constant-diameter pipe through an aerodynamic throat caused by a separation at the tube entrance as discussed previously. In addition to these 7 cases an off-nominal, non-pressure matched conditions were examined in Case D which represents an overexpanded jet, using the nozzle from Case C but with a decrease in plenum pressure. This case explored the possibility of plasma field influence on shocks and expansions. Additionally both flat and serrated anodes (indicated by the primed letters) were utilized in the tests. It should be noted that in addition to the data described above experiments were also conducted of baseline cases to compare jets

issuing converging nozzles with those formed after travelling through a long tube with an aerodynamic throat, and to compare the flat and modified anode without the plasma on.

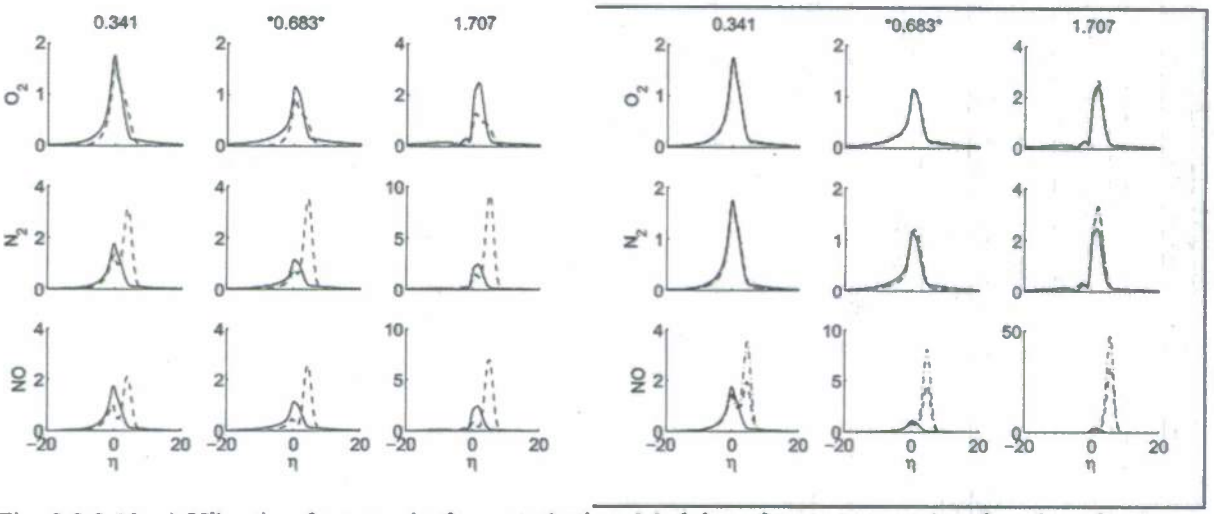

Fig. 3.3.3.11. a) Vibrational energy in the perturbation: Modulus of temperature eigenfunctions for three convective Mach numbers: 0.341, 0.683, and 1.707. Translational temperature (solid line), first vibrational temperature (dashed line), equivalent vibrational temperature (dash-dotted line). b) Dissociation energy in the perturbation: Modulus of temperature eigenfunctions for three convective Mach numbers. Translational temperature (solid line), equivalent dissociation temperature (dash-dotted line).

	P_0 [torr]	P_e [torr]	T_0 [K]	M_i	U_i [m/s]	M_e	U_e [m/s]	D_e [mm]	Re_D
A	12.7	9.15	289	0.70	231	0.69	229	20.8	4470
B	20.5	9.15	293	1.14	353	1.13	350	15.7	8501
C	71.0	8.00	292	2.08	530	2.03	523	11.3	22430
D	62.0	8.00	293	1.99	518	1.94	510	11.3	20208
E'	16.5	5.00	296	1.43	421	1.35	404	9.5	6133
F'	8.2	5.00	293	0.87	283	0.75	247	9.5	2637
G'	16.5	5.00	295	1.43	420	1.27	387	9.5	5605
H'	34.0	5.00	294	1.91	507	1.63	460	9.5	8733
The subscript i refers to value calculated based on assuming the flow is isentropic and the subscript e are the properties based on the measured velocity at the exit of the jet.									

Table 3.3.3.4. Properties of the axisymmetric jets studied

Although planar PIV data was taken, the data was generally reduced to compare the growth rate of the shear layers in the jet and the mean velocity and turbulence profiles at the furthest location downstream. There were many turbulence quantity profiles computed, but generally the turbulent kinetic energy, TKE, [$\sigma_u^2 + \sigma_v^2$ normalized U_0^2] was utilized as a basis of comparison of the flow fields with and without the plasma on. To quantify the plasma field light emission

images were taken for each case along with measurements of the forward power (typically 50 to 150 W), reflected power (0 W), and bias voltage. Also emission spectroscopy was utilized to determine the rotational and vibrational temperature at various points in the plasma utilizing emission spectroscopy of the second positive system of diatomic Nitrogen. Although only a relative few select examples of the study is presented here, the significant data from this study this study can be found in the article by Huffman and Elliott [2010] with a exhaustive set of data, detailed description of the experiments, and complete detailed discussion of all the findings found in the dissertation of Huffman [2007]. Although many of the jets studied showed very little change (generally for the higher exit pressures) due to the presence of the RF plasma [Huffman 2007, 2010], there were cases for the converging-diverging nozzle and constant diameter jet where a significant effect to the profiles was observed. Below are a few select examples for the cases that showed the greatest effect.

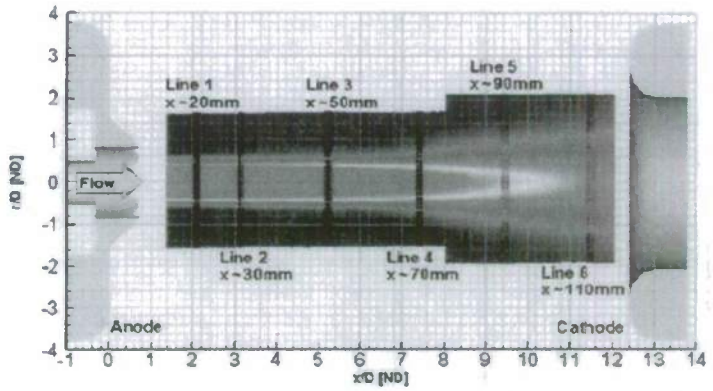

Fig. 3.3.3.11. Measurement locations investigated for the 5 Torr series of nozzles.

Fig. 3.3.3.11 shows the measurement locations in increasing downstream distance from the jet exit, for the 5 torr plasma field cases presented here. The measurements are shown as a sequence of dots, with each dot representing an individual data point. The dots are organized into four columns and are superimposed on the axial velocity contours of a jet to highlight the jet structure at those locations. To report data of large enough sample size, the four adjacent columns of PIV data were combined. Each line consisted of velocity measurements made from 1,056 or 1,150 image pairs (depending on image size used). By combining four adjacent columns, over 4,000 velocity samples were available to perform statistical analysis on. Also note that to eliminate the effect of the tolerance on pressure matching between tests, the plasma-off/plasma-on runs were conducted in one block and were interleaved. In general it was found that the plasma does not begin to influence the flow until after jet core breaks down. The relative weakness of the plasma field near the anode, coupled with the strong shear created at the core interface results in negligible plasma influence on mean and turbulent velocity fluctuations at upstream locations. Therefore for clarity, only the profiles furthest downstream are presented to determine the effects of plasma-on the flow measurements.

Fig. 3.3.3.12 shows the mean centerline axial jet velocity U_o, shear layer thickness δ_{10} (measured as the difference in radial position of the axial velocity between 10% and 90% of the maximum velocity), and mean and TKE profile at 11.3 jet diameters downstream of the anode face for the Mach 1.4 jet issuing from a converging-diverging nozzle perfectly expanded into a 5 torr chamber. The core velocity profile variations in pressure matching and minor nozzle

imperfections combine to form weak waves which show up as oscillations in the core flow of the jet as seen in Fig. 4.22a. As the jet transitions through core breakdown, the decay in velocity picks up the common linear slope. The influence of plasma is seen here, where the green line indicating plasma-off overlays the red plasma-on line in the core, but the plasma-on centerline velocity becomes visible with a slower decay rate. In panel (b), the shear layer thickness between developing jet and self-similar flow at a location between 6 and 7 jet diameters, picking up a linear growth rate. The shear layer growth rate is increased for the plasma-on by 2.7% over the plasma-off case. These effects seem to point to the heating of the shear layer by the plasma field with the subsequent increase in viscosity and speed of sound.[Troutt 1982, Lele 1994, Menart 2003] Turning to the mean velocity profiles of the Mach 1.4 jet the centerline axial velocity increase 5.1% for the plasma-on case over the plasma-off case. This increase is consistent with the decrease in centerline decay for plasma-on discussed previously. Panel (d) shows the TKE which increases by 3.1% in the shear layer and decreases of 5.1% along the centerline for the plasma-on case compared to no plasma cases. These trends support the theory of delayed core breakdown caused by shear layer heating from the plasma[Dimotakis 1993, Menart 2003, Morris 1976].

Fig. 3.3.3.14 shows the same properties, but now for the jet existing a constant diameter pipe operated at an isentropic (sometimes termed equivalent) Mach number of 1.4 issuing into the chamber that is set at 5 torr. First it is observed that the effect of the "more turbulent" jet at the exit produces a jet where the core collapses further upstream and higher turbulence levels observed than the similar jet issuing from a converging diverging nozzle. Again the centerline velocity profile indicates that the plasma the plasma-on centerline velocity has a slower decay rate than the plasma off condition although the shear layer growth rate is approximately the same for both cases. In similar fashion to the previous case, a 9% increase in mean axial velocity occurs at the centerline, when the plasma is turned on. Also TKE decreases by 5% on the centerline and increases by 3% in the shear layer in a similar trend as observed in the jet issuing from the converging-diverging nozzle.

For a subsonic jet (isentropic Mach number of 0.9) operated out of the constant diameter tube the trends are similar for the cases with the plasma on and off when considering the centerline streamwise velocity profile (showing a slower decay rate) and insignificant changes were again observed to the shear layer growth rate. However for the mean and TKE radial profiles more significant changes are observed due to the plasma. Fig. 3.3.3.15 reports an 8% increase in axial velocity for the plasma-on case over the baseline case at the centerline of the jet, 11.4 jet diameters downstream of the anode face. The TKE shows a significant 36% decrease in turbulent kinetic energy along the centerline of 36% with a 29% decrease in TKE in the shear layer. A more complete discussion and catalog of results from the cases run can be found in the dissertation of Huffman [2007] and AIAA paper (Huffman, 2010).

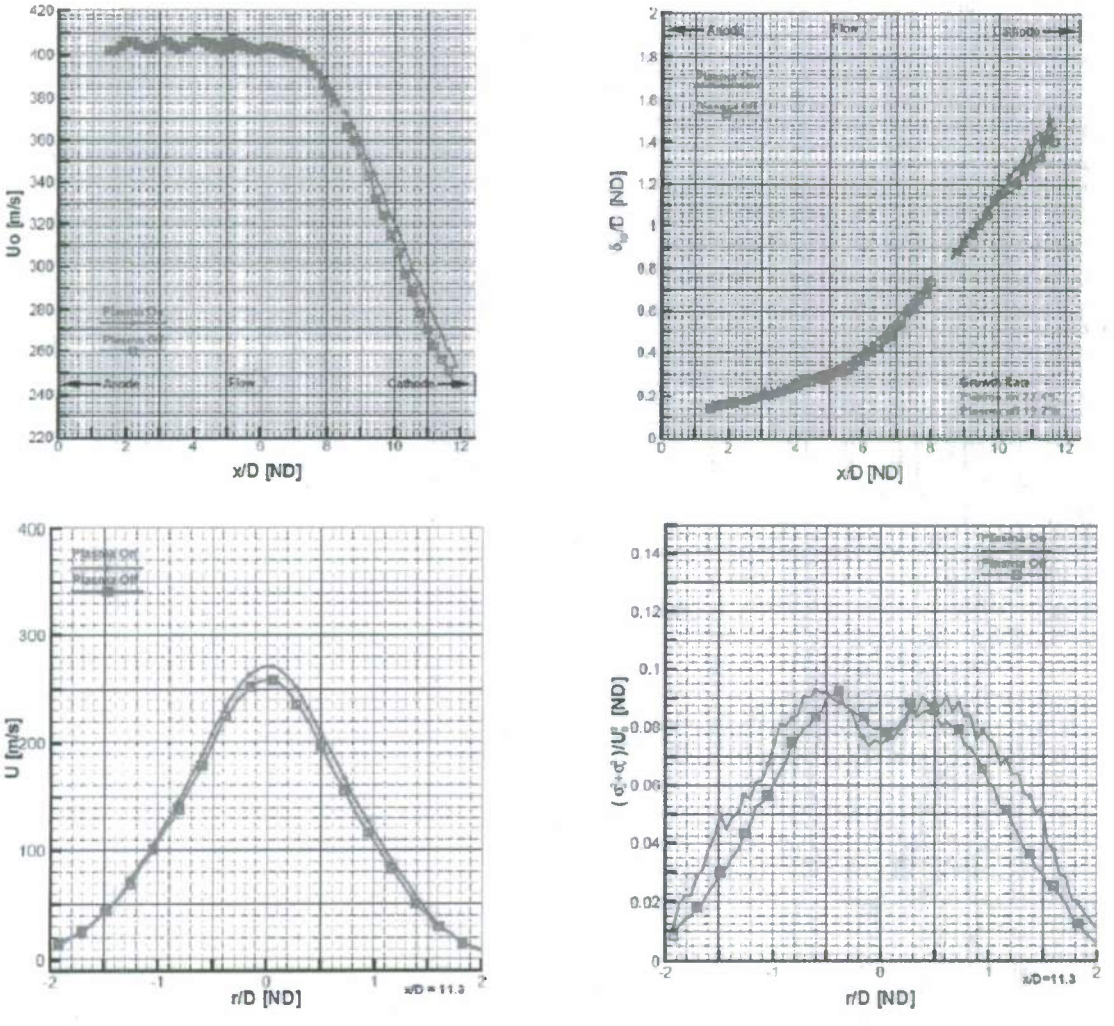

3.3.3.12. Plasma effects on downstream progression of centerline jet velocity, shear layer thickness, and radial profiles of the mean velocity and turbulent kinetic for a jet issuing from a converging diverging nozzle with an isentropic Mach number of 1.4 at 5 Torr.

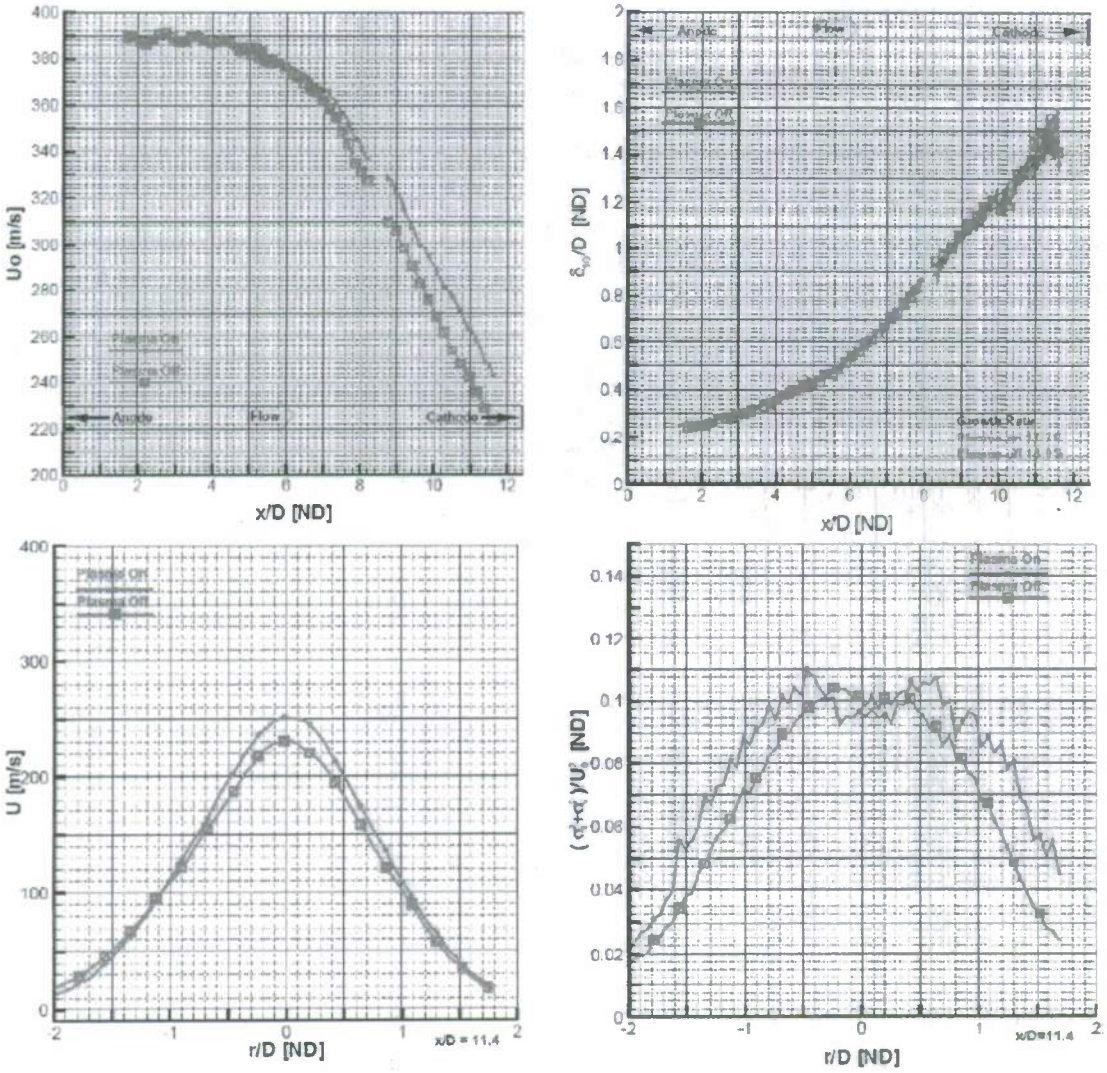

3.3.3.14. Plasma effects on downstream progression of centerline jet velocity, shear layer thickness, and radial profiles of the mean velocity and turbulent kinetic for a jet issuing from a constant diameter tube with an isentropic Mach number of 1.4 at 5 Torr.

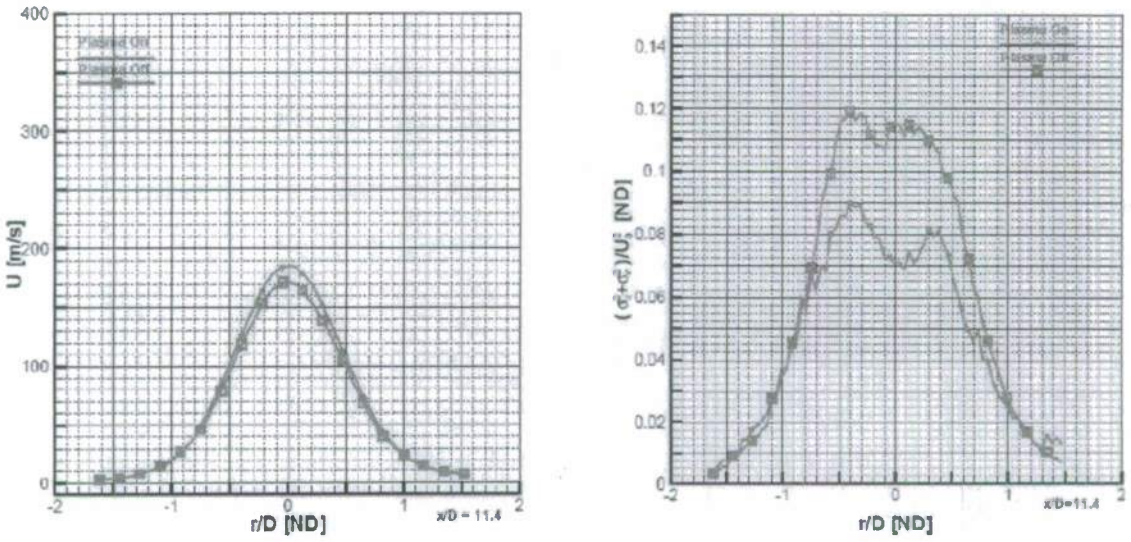

3.3.3.15. Plasma effects on downstream progression of radial profiles of the mean velocity and turbulent kinetic for a jet issuing from a constant diameter tube with an isentropic Mach number of 0.9 at 5 Torr.

Mach 4 Boundary Layer Plasma Interaction Experiments

The focus of the Mach 4 experiments was to investigate the interaction of various types of plasmas with the supersonic boundary layer. Three types of plasmas / plasma actuators were evaluated for their prospective influences: a capactively-coupled radio frequency (RF) discharge providing a 13.56 MHz plasma source, an extended pulsed plasma from an arc discharge providing a plasma pulse lasting approximately 200 μs FWHM and a laser-induced optical breakdown plasma which has a significantly shorter duration (~10 μs FWHM). The potential of each actuator and its effect on the Mach 4 supersonic boundary layer is evaluated through emission photography, Schlieren imaging, and high-frequency pressure measurement at 40 mm (1.57") and 60 mm (2.36") downstream of the discharge which were low pass filtered at 90 kHz.

The RF plasma used in this effort is a non-equilibrium, non-thermal γ-discharge. The RF discharge is similar to a DC glow discharge, but the oscillating electric field provides more effective ionization due to the exponential dependence of ionization rate on electric field magnitude [Fridman 2004]. In contrast the DC arc discharge is a thermal plasma that is self sustaining by thermionic emission (the hot metallic cathode emits electrons from the metal surface) and field electron emission (a strong electric field emits electrons from a cold cathode through tunneling) from the cathode. The laser-induced breakdown initiates by a focused laser beam that achieves a minimum required radiation flux density to break down the gas. [Adelgren 2002] Fig. 3.3.3.16 displays three images of the electrodes or optics used to generate the aforementioned plasmas.

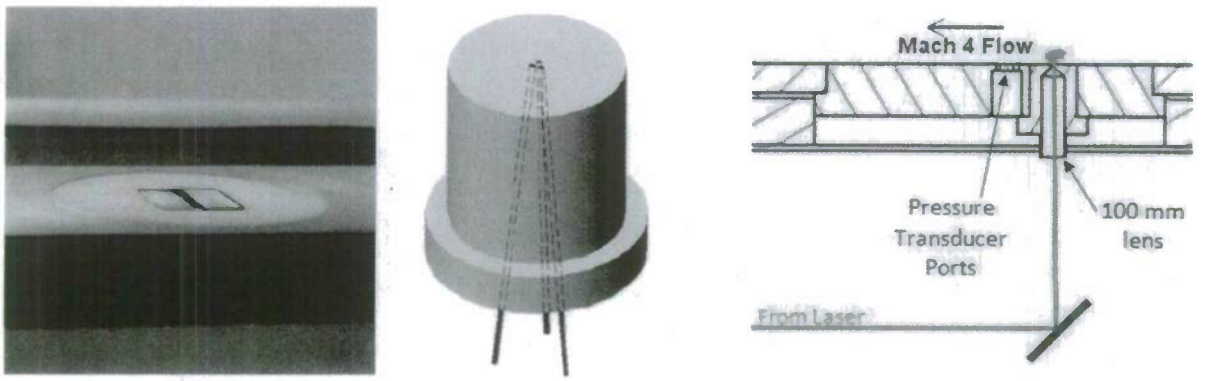

Fig. 3.3.3.16. (left) Photograph of the copper electrodes used in generating the RF plasma, (center) drawing of the Teflon insert with a sketch of the three pin-type electrode paths on top of the image, (right) schematic of the laser-induced breakdown experiments.

The RF discharge plasma results were evaluated using two methods: visible light/emission photographs and Schlieren imaging. These data were acquired at various discharge power levels. Photographs of the RF discharge from the copper plate in the Mach 4 wind tunnel are shown in Fig. 3.3.22. The powers represented by each image are (a) 30 W, (b) 40 W, and (c) 50 W. The acquired Schlieren images show little effect of the RF surface plasma. Furthermore, high-frequency pressure transducer measurements were not taken for the RF discharge for this reason. It is possible that improvements could be made to the electrode configuration in the future so that higher powers could be effectively coupled into the flow.

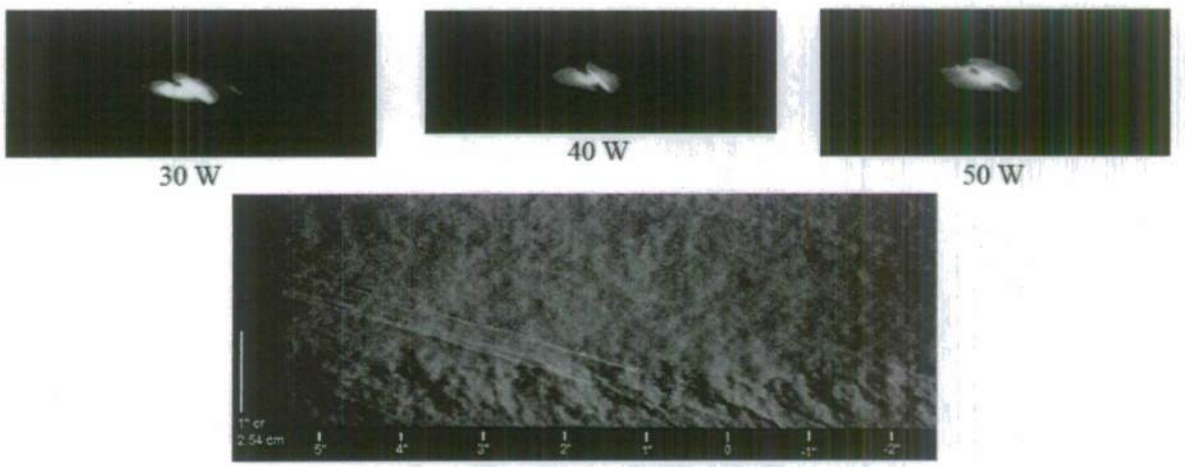

Fig. 3.3.3.17. Photographs of the RF discharge from the copper plate in a Mach 4 flow over a range of powers and an instantaneous schlieren image taken for the 40 W case (below).

The DC arc discharge plasma results were evaluated using three methods: visible light/emission photographs, instantaneous and conditionally averaged Schlieren imaging, and downstream surface static pressure measurements of the perturbed boundary layer. These data were acquired at various delay times measured from the start of the emission. The full width-half maximum and full width-10% maximum of the PMT signal is 175 and 436 μs, respectively.

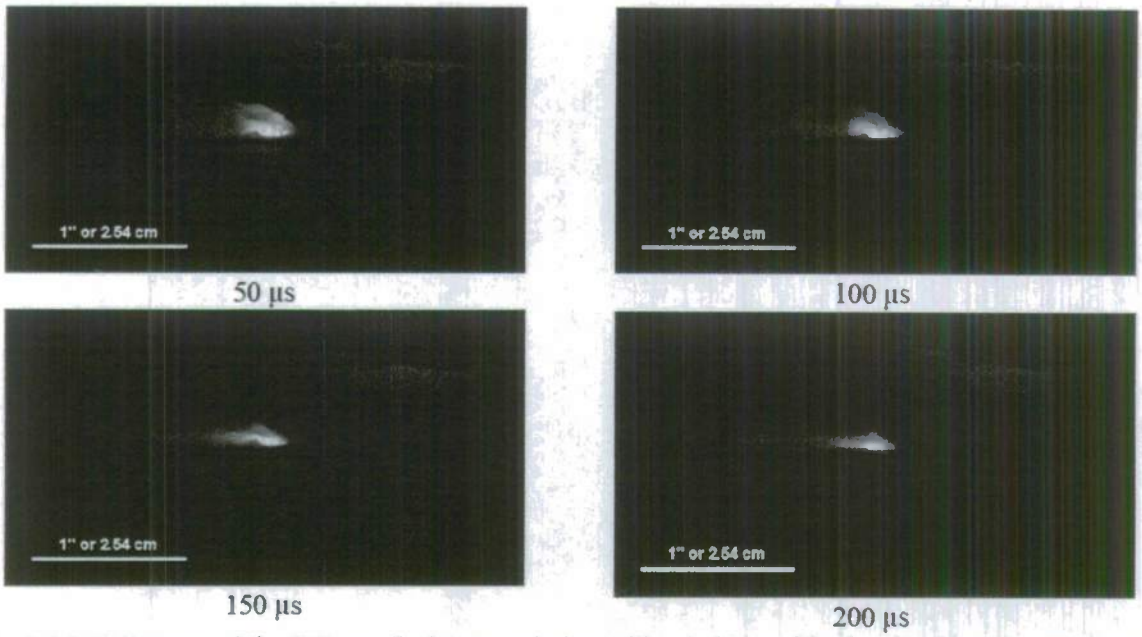

Fig. 3.3.3.18 Images of the DC arc discharge emission with wind tunnel background image superposed. The flow is from right to left of each image.

Photographs of the plasma were taken and superposed to a background image of the wind tunnel for perspective. Four of these images are presented in Fig. 3.3.3.18 for 50, 100, 150, and 200 µs delays. The images show an unsteady plasma interface that seems to convect upward by buoyant forces and causes the boundary layer to separate immediately downstream of the discharge. The boundary layer reattaches shortly thereafter. The plasma has almost completely dissipated after 200 µs. The luminescent plasma is drawn downstream and continues to be visible over 2.5 cm (1") downstream of the electrodes. Schlieren images with the arc discharge actuator active are presented in Fig. 3.3.3.19 for a 50 µs delay. The formation of a bow shock is evident that bends around the plasma and extends downstream. Also apparent is the emission and heated plume of the plasma that convects downstream.

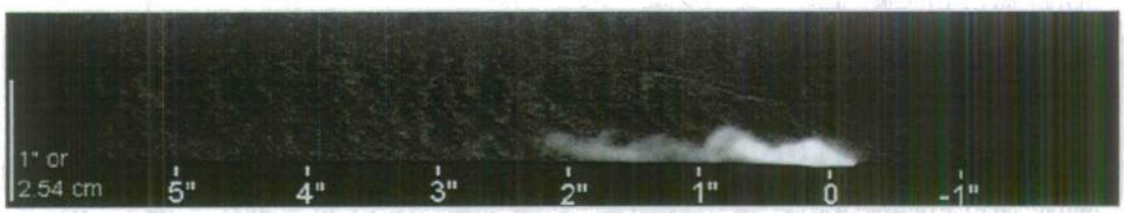

Fig. 3.3.3.19. Schlieren image of DC arc discharge in Mach 4 flow taken at 50 microsec delay.

In Fig. 3.3.3.20 pressure transducer traces are provided for a DC arc discharge 40 mm downstream of the discharge in a Mach 4 flow. One single pressure fluctuation trace is presented with the average of five independent traces plotted over top. For the phase averaged trace the plots were shifted based on the position of the distinct peak due to slight variations in

the triggering of the plasma. The peak amplitude of the fluctuations is as much as 17% of the mean pressure amplitude. Artificial anomalies are present in both images, likely a result of electromagnetic interference and radiative heating. As these oscillations die out, the shock wave and successive expansion arrive sequentially. The time difference between the two transducers indicates a convective velocity of 541 m/s for the DC arc discharge. Before the pulses, the single shots signals are composed oscillations which appear to reduce in frequency after they are affected by the DC arc discharge which produces a small but distinguishable pressure drop and likely represents the passing high-temperature plume.

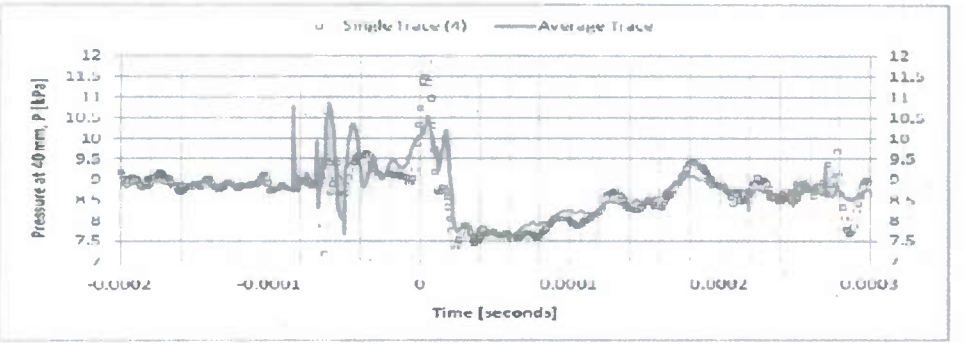

Fig. 3.3.3.20. Pressure fluctuation in kPa as measured 40 mm downstream from a DC arc discharge in a Mach 4 boundary layer.

The laser-induced breakdown plasma results were evaluated using the same three methods as for the DC arc discharge plasma. The average full width-half maximum of the PMT signal with the Mach 4 flow on is 8.0 μs. With the flow on, the discharge has a significantly larger pulse to pulse fluctuation in intensity than with the flow off. Fig. 3.3.3.21 shows two instantaneous images of the plasma emission taken at delay times of 5 and 10 μs and a phased average image taken with a 5 μs delay. Both the initial focused laser beam (which bleeds through due to its high intensity) and emission from the plasma is observed convecting downstream. The 10 μs image shows a significant reduction in the plasma emission as it interacts in the boundary layer and travels further downstream. The 5 μs phase averaged image clearly shows stronger emission higher in the boundary layer and even marks the high shear region near the wall as the line of plasma is stretched.

Thirty-five instantaneous (2 μs) images were acquired for 10, 30, and 50 μs delays and conditionally averaged to produce the resultant images of Fig. 3.3.3.22. A 532 nm notch filter was used to reduce the intensity of the laser wavelength. At 10 μs, a blast wave surrounding the plasma is observed which is deformed by the velocity gradients in the boundary layer. The upstream shock appears more well defined than the downstream one. At 30 μs, the wave has expanded slightly and the higher temperature region continues to grow and be stretched in the boundary layer. These trends continue as the structure convects downstream for the 75 μs case. As time progresses, the light and dark regions continue to coalesce and convect downstream at an approximate convective velocity of 545 m/s. The upstream portion of the blast wave, or bow shock, along with an apparent dark expansion region is also convected downstream and into the core flow once the laser-induced plasma dissipates. The downstream weaker wave appears to be maintained until almost 100 μs, but is deformed into an ellipse as time progresses. It convects at approximately 825 m/s (much higher than the free stream value of 697 m/s). Near 100 μs delay,

the visible effects of the plasma have almost completely been exhausted and the shock is starting to dissipate as well.

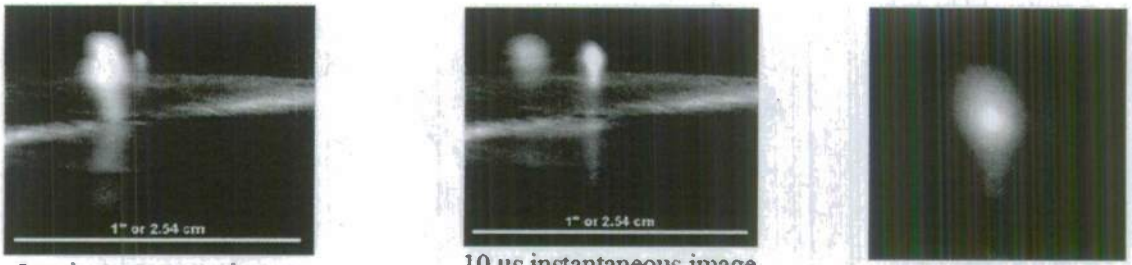

5 μs instantaneous image 10 μs instantaneous image 5 μs average image

Fig. 3.3.3.21. Emission images of plasmas produced by laser-induced optical breakdown in a Mach 4 boundary layer taken at 5 and 10 μs with wind tunnel background image superposed for perspective and a phase average emission image of the 5 μs case. The flow is from right to left.

Fig. 3.3.3.23 shows a plot of the pressure trace from the high frequency transducer placed at 40 mm downstream of the laser induced break down location. Similar to the previous DC arc an individual trace is shown with the average of five traces. The initial peak in the pressure at 13 μs is most likely noise from the plasma formation or initial thermal radiation. The flow signal indicating the pressure start with peak at 56 μs associated with the passage of the first downstream shock. The structure is represented by the lower pressure signal which occurs afterward although there may be some noise created in the transducer which is the cause of the signal ringing after the shock passes. Further analysis, data, and discussion summarized of the plasma effect on the Mach 4 boundary layer can be found in the article by DeBlauw et al. [2010].

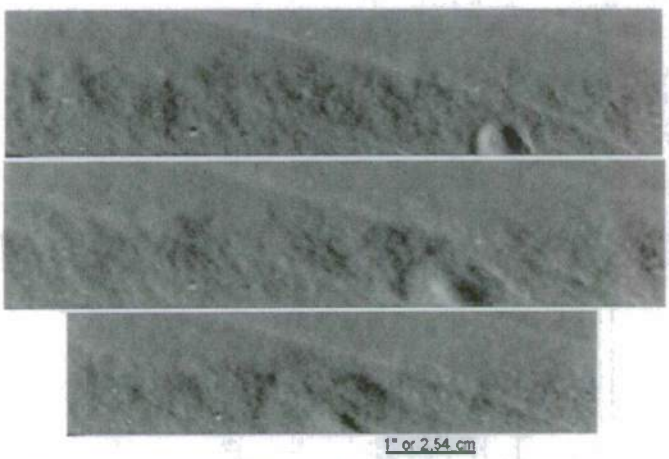

Fig. 3.3.3.22. Averaged Schlieren photography of laser-induced breakdown in a Mach 4 flow. The photographs represent 10, 30, and 75 μs delays from top to bottom.

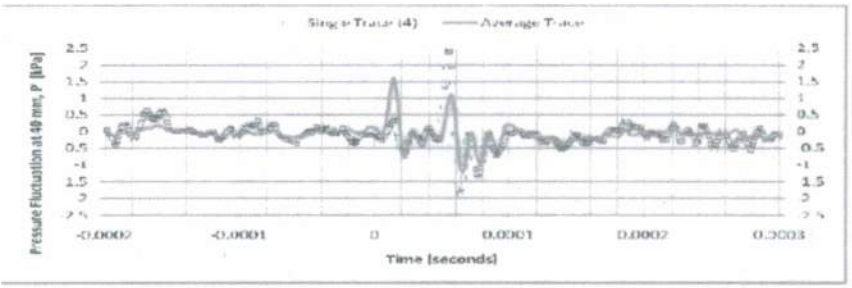

Fig. 3.3.2.23. Pressure fluctuation in kPa as measured 40 mm downstream from (top) a DC arc discharge and (bottom) a laser-induced breakdown in a Mach 4 flow.

3.3.4 References

1) Adamovich, I. and Rich, J., "Three Dimensional Nonperturbative Analytical Model of Vibrational Energy Transfer in Atom-Molecule Collisions," Journal of Chemical Physics, 109 (18): 7711-7724, 1998
2) Adamovich, I., "Three Dimensional Analytical Model of Vibrational Energy Transfer in Molecule-Molecule Collisions," AIAA Journal, 39 (10): 1916-1925, 2001
3) Adelgren, R., Elliott, G., Crawford, J., Carter, C., Donbar, J., and Grosjean, D., "Axisymmetric Jet Shear-Layer Excitation by Laser Energy and Electric Arc Discharges," AIAA Journal, 43 (4): 776–791, 2005.
4) Adrian, R., "Twenty Years of Particle Image Velocimetry," Experiments in Fluids, 39: 159–169, 2005.
5) Amiot, C., "The Infrared Emission Spectrum of NO: Analysis of the v =3 Sequence up to v=22," Journal of Molecular Spectroscopy, 94:150-172, 1982
6) Anon, MODEL 3475 Condensation Monodisperse Aerosol Generator: Instruction Manual, TSI Incorporated, 500 Cardigan Road, Shoreview, MN 55126, 1933475th ed., 2004.
7) Aoki, S., Lee, J., Masuya, G., Kanda, T., and Kudo, K., "Aerodynamic Experiment on an Ejector-Jet," Journal of Propulsion and Power, 21 (3): 496–503, 2005.
8) Arnette, S., Samimy, M., and Elliott, G., "On Streamwise Vortices in High Reynolds Number Supersonic Axisymmetric Jets," Physics of Fluids A, 5 (1): 187–202, 1992.
9) Boguszko, M., and Elliott. G., "Property measurement utilizing atomic/molecular filter-based diagnostics," Progress in Aerospace Sciences, 41: 93–142, 2005.
10) Burtschell, Y., Zeitoun, D. E., and Ben-Dor, G., "Steady shock wave reflection in thermochemical nonequilibrium flows," Shock Waves, 11: 15-21, 2000
11) Crist, S., Sherman, P., and Glass, D., "Study of Highly Underexpanded Sonic Jet," AIAA Journal, 4 (1): 68–71, 1966.
12) DeBlauw, B., Elliott, G., and Dutton, C., " A Mach 4 Wind Tunnel for Plasma / Boundary Layer Interaction Studies," Accepted to 48th AIAA Aerospace sciences Conference and Exhibit, 2010.
13) Dimotakis, P., "Some Issues on Turbulent Mixing and Turbulence," GALCIT Report fm93–1, 1993.
14) Dufrene, A., Sharma, M., and Austin, J. M., "Design and characterization of a hypervelocity expansion tube facility", Journal of Propulsion and Power, 23 (6): 1185-1193, 2007

15) Dutton, J., Mikkelsen, C., and Addy, A., "A Theoretical and Experimental Investigation of the Constant Area Supersonic- Supersonic Ejector," AIAA Journal, 20 (10): 1393–1400, 1982.
16) Elliott, G., and Samimy, M., "Rayleigh scattering technique for simultaneous measurements of velocity and thermodynamic properties," AIAA Journal, 34(11): 2346–2352, 1996.
17) Forkey, J., Finkelstein, N., Lempert, W., and Miles. R., "Demonstration and characterization of filtered Rayleigh scattering for planar velocity measurements," AIAA Journal, 34 (3): 442–448, 1996.
18) Fridman, A., and Kennedy, L., Plasma Physics and Engineering, Taylor & Francis, New York, 2004.
19) Gendrich, C., and Koochesfahani, M., "A Spatial Correlation Technique for Estimating Velocity Fields Using Molecular Tagging Velocimetry," Experiments in Fluids, 22: 67–77, 1996.
20) Gimelschein, S., Markelov, G., and Ivanov, M., "Relaxation and Rarefaction Effects on Shock Wave Reflections," AIAA Paper 1998-2819, 1998.
21) Grasso, F. and Paoli, R., "An Analytical Study of Mach Reflection in Nonequilibrium Steady Flows," Physics of Fluids, 11 (10): 3150-3167, 1999
22) Grasso, F. and Paoli, R., "Simulations of Shock-Wave Reections in Nonequilibrium Flows," Journal of Spacecraft and Rockets, 37 (2): 224-234, 2000
23) Han, S., and Peddieson Jr., J., "One-Dimensional Numerical Study of Compressible Flow Ejector," AIAA Journal, 40 (7): 1469–1472, 2002.
24) Hill, R., and Kiewicki, J., "Data Reduction Methods for Flow-Tagging Velocity Measurements," Experiments in Fluids, 20: 142–152, 1996.
25) Hiller, B., Booman, A., Hassa, C., and Hanson, R., "Velocity Visualization in Gas Flows Using Laser Induced Phosphorescence of Biacetyl," Review of Scientific Instruments, 55(12): 1964–1967, 1984.
26) Hu, H., and Koochesfahani, M., "A Novel Method for Instantaneous, Quantitative Measurement of Molecular Mixing in Gaseous Flows," Experiments in Fluids, 33: 202–209, 2002.
27) Huffman, R., An Experimental Investigation into the Effect of Plasma on the Flow Features of an Axisymmetric Jet, University of Illinois at Urbana-Champaign Dissertation, Urbana IL 61801, 2007.
28) Huffman, R., Elliott, G., and Boguzsko, M. "Turbulence Measurements Using FARRS in a Supersonic Axisymmetric Jet," AIAA Paper 2007-0471, *45th AIAA Aerospace Sciences Meeting and Exhibit*, Reno, Nevada, January, 2007.
29) Huffman, R., Elliott, G. "An Experimental Investigation of Accurate Particle Tracking in Supersonic, Rarefied, Axisymmetric Jets," AIAA Paper 2009-1265, 2009.
30) Huffman, R., Elliott, G., "The Effect of Plasma on the Flow Features of an Axisymmetric Jet Accepted to 48th AIAA Aerspace sciences Conference and Exhibit, 2010.
31) Kovacs, I., Rotational Structure in the Spectra of Diatomic Molecules, 1969.
32) Lele, S., "Compressibility Effects on Turbulence," Annual Review of Fluid Mechanics, 26: 211–254, 1994.
33) Lempert,W., Jiang, N., Sethuram, S., and Samimy, M., "Molecular Tagging Velocimetry Measurements in Supersonic Microjets," AIAA Journal, 40 (6): 1065–1070, 2002.

34) Li, Y., Kirkpatrick, A., Mitchell, C., and Willson, B., "Characteristic and Computational Fluid Dynamics Modeling of High- Pressure Gas Jet Injection," Transactions of the ASME, 126: 192–197, 2004.
35) Loth, E., "Compressibility and Rarefaction Effects on Drag of a Spherical Particle," AIAA Journal, 2007, Submitted for Publication November, 2006.
36) Love, E., Grigsby, C., Lee, L., and Woodling, M., "Experimental and Theoretical Studies of Axisymmetric Free Jets," NASA TR–6, 1959.
37) Lozano, A., Smith, S., Mungal, M., and Hanson, R., "Concentration Measurements in a Transverse Jet by Planar Laser-Induced Fluorescence of Acetone," AIAA Journal, 32 (1): 218–221, 1993.
38) Luque, J. and Crosley, D. R., "LIFBASE: Database and Spectral Simulation Program (Version 1.5," SRI International Report MP 99-009, 1999.
39) Luque, J. and Crosley, D. R., "Transition probabilities and electronic transition moments of the $A\,^2\Sigma^+ \rightarrow X^2\Pi$ and $D\,^2\Sigma^+ \rightarrow X^2\Pi$ systems of nitric oxide," Journal of Chemical Physics, 111 (16): 7405-7415, 1999
40) Luque, J. and Crosley, D. R., "Radiative and predissociative rates for NO $A\,^2\Sigma^+$ v'=0-5 and $D\,^2\Sigma^+$ v'=0-3," Journal of Chemical Physics, 112 (21): 9411-9416, 2000
41) Macheret, S. and Adamovich, I., "Semiclassical Modelling of State Specific Dissociation Rates in Diatomic Gases," Journal of Chemical Physics, 113 (17):7351-7361, 2000
42) Massa, L. and Austin, J. M., "Spatial linear stability of a hypersonic shear layer with nonequilibrium thermochemistry," Physics of Fluids, 20 (8):84-104, 2008
43) McBride, B. J. and Gordon, S., "Computer Program for Calculation of Complex Chemical Equilibrium Compositions and Applications, II. Users Manual and Program Description," NASA CR-1311, 1996.
44) McGilvray, M., Austin, J. M., Sharma, M., Jacobs, P. A., and Morgan, R. G., "Diagnostic modelling of an expansion tube operating condition," Shock Waves, 19: 69-66, 2008
45) McGilvray, M., Austin, J. M., Sharma, M., Jacobs, P. A., and Morgan, R. G., "Diagnostic modelling of an expansion tube operating condition for a hypersonic shear layer experiment," Proceedings of the 16th Australasian Fluid Mechanics Conference, 2007.
46) Menart, J., Shang, J., Henderson, S., Kurpik, A., Kimmel, R., and Hayes, J., "Survey of Plasmas Generated in a Mach 5 Wind Tunnel," Reno: American Institute of Aeronautics and Astronautics, AIAA 2003-1194, 2003.
47) Menart, J., Shang, J., Kurpik, A., Kimmel, R., and Hayes, J., "Survey of Plasmas Generated in a Mach 5 Wind Tunnel," AIAA Paper 03–1194, 2003.
48) Miles, R., Cohen, C., Connors, J., Howard, P., Huang, Markovitz, E., and Russell, G., "Velocity Measurements by Vibrational Tagging and Fluorescent Probing of Oxygen," Optics Letters, 12 (11): 861–863, 1987.
49) Miles, R., Lempert, W., and Forkey, J., "Laser Rayleigh scattering," Measurement Science and Technology, 12: R33–R51, 2001.
50) Morris, P., "Turbulence Measurements in Subsonic and Supersonic Axisymmetric Jets in a Parallel Stream," AIAA Journal, 14 (10): 1468–1475, 1976.
51) Nau,W., and Scaiano, J., "Oxygen Quenching of Excited Aliphatic Ketones and Diketones," Journal of Physical Chemistry, 100: 11360–11367, 1996.
52) Ory, H. A., Gittleman, A. P., and Maddox, J. P., "Franck-Condon Factors for the NO Beta and Gamma Band Systems," Astrophysical Journal, 139 (1): 346-356, 1963

53) Owen, P., and Thornhill, C., "The Flow in an Axially-Symmetric Supersonic Jet from a Nearly-Sonic Orifice into a Vacuum," Aeronautical Research Council, Reports and Memoranda 2616, 1948.
54) Paull, A., and Stalker, R. J., "Test Flow Disturbances in an Expansion Tube," Journal of Fluid Mechanics, 245: 493-521, 1992
55) Peters, C., and Altmann, J., "Monodisperse Aerosol Generation with Rapid Adjustable Particle Size for Inhalation Studies," Journal of Aerosol Medicine, 6 (4): 307–315, 1993.
56) Pilverdier, H., Brun, R., and Dumitrescu, M. P., "Emission and Raman spectroscopy measurements in hypersonic nitrogen flows," Journal of Thermophysics and Heat Transfer, 15 (4):484-490, 2001
57) Raffel, M., Willert, C., and Kompenhans, J., Particle Image Velocimetry: A Practical Guide, Springer-Verlag, Berlin, 1998.
58) Raizer, Y., Shneider, M., and Yatsenko, N., Radio-Frequency Capacitive Discharges, CRC Press, Boca Raton, FL, 1995.
59) Ramjuan, D., Sasoh, A., Ohnishi, Y., and Takayama, K., "Time-resolved spectroscopy in the shock layer of a blunt body placed in an expansion tube flow," 24th International Congress on High-Speed Photography and Photonics, 4183, 2001.
60) Samimy, M., and Lele, S., "Motion of Particles with Inertia in a Compressible Free Shear Layer," Physics of Fluids A, 3 (8): 1915–1923, 1991.
61) Shen, C., Rarefied Gas Dynamics: Fundamentals, Simulations and Micro Flows, Springer-Verlag, Berlin, 2005.
62) Shirley, J. A., and Winter, M., "Air-mass flux measurement system using Doppler-shifted filtered Rayleigh scattering," AIAA Paper 93–0513, 1993.
63) Skews, B. W., "Aspect ratio effects in wind tunnel studies of shock wave reflection transition," Shock Waves, 7: 373-383, 1997
64) Stier, B. and Koochesfahani, M., "Molecular Tagging Velocimetry (MTV) Measurements in Gas Phase Flows," Experiments in Fluids, 26: 297–304, 1999.
65) Tenti, G., Boley, C., and Desai, R., "On the kinetic model description of raleigh-brillouin scattering from molecular gases," Canadian Journal of Physics, 52 (4): 285–290, 1974.
66) Thurber, M., Grisch, F., Kirby, B., Votsmeier, M., and Hanson, R., "Measurements and Modeling of Acetone Laser-Induced Fluorescence with Implications for Temperature-Imaging Diagnostics," Applied Optics, 37 (21): 4963–4978, 1998.
67) Tran, T., Kochar, Y., and Seitzman, J., "Measurements of Acetone Fluorescence and Phosphorescence at High Pressures and Temperatures," AIAA Paper 06–0831, 2006.
68) Troutt, T., and McLaughlin, D., "Experiments on the Flow and Acoustic Properties of a Moderate-Reynolds Number Supersonic Jet," Journal of Fluid Mechanics, 116: 123–156, 1982.
69) Velasco, A. M., Martin, I., Lavin, C., and Bustos, E., "Radiative lifetimes for the $A\,^2\Sigma^+$ (v'=0-7) and $D\,^2\Sigma^+$ (v'=0-5) Rydberg states of NO," Molecular Physics, 103 (10): 1375-1385, 2005
70) Wintenberger, E., Austin, J. M., Cooper, M., Jackson, S., and Shepherd, J. E., "An Analytical Model for the Impulse of a Single-Cycle Pulse Detonation Engine," Journal of Propulsion and Power, 19 (1):22-38, 2003
71) Wurster, W. H., Treanor, C. E., and Williams, M. J., "Nonequilibrium UV Radiation and Kinetics Behind Shock Waves in Air," AIAA Paper 1989-1918, 1989.

72) Wurster, W. H., Treanor, C. E., and Williams, M. J., "Kinetics of UV Production Behind Shock Waves in Air," AIAA Paper 1990-1666, 1990
73) Yano, R., Aithal, S., Subramaniam, V., Contini, V., Palm, P., Merriman, S., Adamovich, I., Lempert, W., and Rich, J., "Experimental Characterization of Shock Dispersions in Weakly Ionized Non-equilibrium Plasmas," AIAA Paper 99–3671, 1999.
74) Yuen, L., Peters, J., and Lucht, R., "Pressure Dependence of Laser-Induced Fluorescence from Acetone," Proceedings of the Indian Academy of Science, 36 (15): 3271–3277, 1997.

Chapter 4

Students and Publications Resulting from this Research

4.1 TAMU

Students	*Degree*	*Department*	*Advisor*	*Current Position*
Sriram Arasinapalai	MS 2008	Aerospace Engr.	Girimaji	Veritas DGC Inc
Michael Belisle	PhD	Aerospace Engr.	Reed	Student
Ravi Bikkani	MS 2005	Aerospace Engr.	Girimaji	Not Known
Andrea Hsu	PhD 2009	Chemistry	North	Sandia National Labs
TJ Fuller	PhD 2009	Aerospace Engr.	Bowersox	Naval Air Command
Jason Garcia	MS 2009	Aerospace Engr.	Bowersox	L3
Sunny Jain	MS 2007	Aerospace Engr.	Girimaji	2H-Offshore, Inc
Johannes Kerimo	Post-Doc	Aerospace Engr.	Girimaji	NASA Contractor
Gaurav Kumar	PhD 2010	Aerospace Engr.	Girimaji	Student
James Lancaster	Undergrad	Aerospace Engr.	Reed	Air Force
Tucker Lavin	MS 2007	Aerospace Engr.	Girimaji	Sandia National Labs
Kumchul Lee	PhD 2007	Aerospace Engr.	Girimaji	S. Korean Def. Lab
Paul Lucas	Undergrad	Aerospace Engr.	Reed	Student
Lasse Maeland	PhD	Aerospace Engr.	Reed	Student
Tyler Neale	MS	Aerospace Engr.	Reed	Student
Richard Rhodes	MS 2007	Aerospace Engr.	Reed	Lockheed Martin
Ben Riley	MS 2006	Aerospace Engr.	Girimaji	US Navy
R. Sanchez-Gonzalez	PhD 2010	Chemistry	North	Student
Sawan Suman	PhD 2009	Aerospace Engr.	Girimaji	Veritas DGC Inc
Michael Semper	PhD 2009	Aerospace Engr.	Bowersox	Student
Ravi Srinivasan	Post-Doc	Aerospace Engr.	Bowersox	Ramgen, LLC
Nathan Tichenor	PhD 2009	Aerospace Engr.	Bowersox	Student
Aaron Tucker	PhD	Aerospace Engr.	Reed	Air Force
Huidan Yu	Post-Doc	Aerospace Engr.	Girimaji	Los Alamos-JHU

Publications

1. K. C. Lee, S. S. Girimaji and J. Kerimo. Effect of compressibility on turbulent velocity gradients and small-scale structure. *Journal of Turbulence,* 9 (10), 1-18 (2009).
2. S. Suman and S.S. Girimaji, `Homogenized Euler Equation: a model for compressible velocity gradient dynamics'. *Journal of Fluid Mechanics*, Vol. 620, pp. 177-194 (2009)
3. B. M. Riley, J. C. Richard and S. S. Girimaji, `Magnetic field effects on axis-switching and instabilities in rectangular plasma jets', To appear in *Flow, Turbulence and Combustion* (2008). Published online November 2008 DOI 10.1007/s10494-008-9182-y
4. K. C. Lee, S. S. Girimaji and J. Kerimo, `Validity of Taylor's dissipation-viscosity independence postulate in variable-viscosity turbulent fluid mixtures', *Physical Review Letters,* Vol. 101, Issue 7, (2008)
5. B. M. Riley, J. C. Richard and S. S. Girimaji, `Assessment of magneto-hydrodynamic Lattice-Boltzmann schemes in turbulence and rectangular jets'. *(IJMPC) Computational Physics and Physical Computation*, Vol. 19, No. 8 (2008) pp. 1211 - 1220.

6. S. S. Girimaji, 'Boltzmann kinetic equation for filtered fluid turbulence', *Physical Review Letters,* Vol. 99, 3 (2007)
7. J. Kerimo and S.S. Girimaji, 'DNS of decaying isotropic turbulence with Boltzmann BGK approach', *Journal of Turbulence*, Volume: 8 Issue: 46 Pages: 1-16 (2007)
8. H. Yu and S.S. Girimaji, 'Extension of compressible ideal gas rapid distortion theory to general mean velocity gradients', *Physics of Fluids,* Vol. 19, 4, (2007).
9. K. C. Lee, D. Yu and S. S. Girimaji, 'Lattice Boltzmann DNS of decaying isotropic turbulence with temperature fluctuations', *International Journal of CFD*, Vol. 20, 6, 401-413 (2006)
10. R. Bikkani and S. S. Girimaji, 'Role of pressure in velocity gradient dynamics'. *Physical Review E* , Vol. 75, 3 (2007).
11. Lex Smits, Pino Martin and Sharath Girimaji. *Current Status of Basic Research in Hypersonic Turbulence.* AIAA-2009-151. 47th AIAA Aerospace Sciences Meeting including The New Horizons Forum and Aerospace Exposition, Orlando, Florida, Jan. 5-8, 2009
12. Sharath S. Girimaji and Ravi Srinivasan. *'Partially-Averaged Navier-Stokes (PANS) Simulations of Ramjet/Scramjet Mixing Environment'.* AIAA-2009-134. 47th AIAA Aerospace Sciences Meeting including The New Horizons Forum and Aerospace Exposition, Orlando, Florida, Jan. 5-8, 2009
13. Suman, S. S. Girimaji and R. Bertsh. *Homogeneously-sheared compressible turbulence at the rapid distortion limit: Interaction between velocity and thermodynamic fluctuations.* THMT'09 - 6th International Symposium on Turbulence, Heat and Mass Transfer, Rome, Italy September 14 – 18, 2009.
14. J. Richard, B.M. Riley and S. S. Girimaji. 'Energy exchange in Magnetohydrodynamic Decaying Isotropic Turbulence'. THMT'09 - 6th International Symposium on Turbulence, Heat and Mass Transfer, Rome, Italy September 14 – 18, 2009
15. Bowersox, R., "Extension of Equilibrium Turbulent Heat Flux models to High-Speed Shear Flows," *Journal of Fluid Mechanics*, Vol. 633, August, 2009, pp. 61-70.
16. Bowersox, R., "Algebraic turbulent energy flux models for hypersonic shear flows: Invited presentation," AIAA-2009-3724, AIAA 39th Fluid Dynamics Conference, San Antonio, TX, June 22-25, 2009a. *Progress in Aerospace Sciences*, In Review.
17. Bowersox, R., North, S. and Srinivasan,R., "High- Speed Free Shear Layers with Molecular Non-Equilibrium: An Example of the Fluids Information Triad (Invited)," AIAA-2008-685, 46th AIAA Aerospace Sciences Meeting and Exhibit, Reno, Nevada, Jan. 2008.
18. Fuller, T., Hsu, A., Bowersox, R. and North, S., "The Effect of Vibrational Non-Equilibrium on the Decay of Grid Generated Turbulence," AIAA-2009-593, 47th AIAA Aerospace Sciences Meeting, Orlando, FL, Jan. 5-8, 2009.
19. Hsu, A., Srinivasan, R., Bowersox, R. and North, S., "Two-Component Molecular Tagging Velocimetry Utilizing NO Fluorescence Lifetime and NO2 Photodissociation Techniques in an Underexpanded Jet Flowfield,," *Applied Optics,* Vol. 48, Issue 22, 2009, pp. 4414–4423.
20. Hsu, A., Srinivasan, R., Bowersox, R. and North, S., "Application of Molecular Tagging Towards Simultaneous Vibrational Temperature and Velocity Mapping in an Underexpanded Jet Flowfield ", *AIAA Journal*, 2009a, In-Print.
21. Hsu, A., Srinivasan, R., Bowersox, R. and North, S., "Two-Component Molecular Tagging Velocimetry Utilizing NO Fluorescence Lifetime and NO2 Photodissociation Techniques in

an Underexpanded Jet Flowfield,," AIAA-2009-4049, AIAA 39th Fluid Dynamics Conference, San Antonio, TX, June 22-25, 2009b.
22. Hsu, A., Srinivasan, R., Bowersox, R. and North, S., "Application of Molecular Tagging Velocimetry Towards Simultaneous Vibrational Temperature and Velocity Mapping in an Underexpanded Jet Flowfield," AIAA-2009-1447, 47th AIAA Aerospace Sciences Meeting, Orlando, FL, Jan. 5-8, 2009b.
23. Semper, M., Tichenor, N. Bowersox, R., Srinivasan, R. and North, S., "On the Design and Calibration of an Actively Controlled Expansion Hypersonic Wind Tunnel," AIAA-2009-799, 47th AIAA Aerospace Sciences Meeting, Orlando, FL, Jan. 5-8, 2009.
24. "Numerical-Experimental Comparisons of Second-Mode Behavior for Blunted Cones," Lyttle, Reed, Shiplyuk, Maslov, Buntin, Schneider, AIAA Journal, Vol. 43, No. 8, 1734-43, Aug 2005.
25. "Sensitivity of 2nd Mode Linear Stability to Constitutive Models in Hypersonic Flow," Lyttle, Reed, AIAA 2005-0889. To be submitted to AIAA Journal.
26. VKI (RTO/NATO) short course on "Transition Modeling" with Saric, Arnal, Reshotko, Reed, June 2008. To be published by VKI.
27. AIAA Professional Development Course Notes on "Stability and Transition: Theory, Modeling Experiments, and Applications," Hassan, Reed, Saric, AIAA Fluid Dynamics Conference, Summers 2006, 2008, 2010.

4.2Purdue

Students
S. Naik
W. Kulatilaka

Publications
1. Naik, S. V., Kulatilaka, W. D., Venkatesan, K. K., and Lucht, R. P., "Measurements of pressure, temperature and velocity in underexpanded free jets using planar LIF imaging of nitric oxide," *AIAA Journal,* Vol. 47, No. 4, 2009, pp. 839-849.
2. Kulatilaka, W. D., Naik, S. V., and Lucht, R. P., "Development of high-spectral-resolution planar laser-induced fluorescence imaging diagnostics for high-speed gas flows," *AIAA Journal*, Vol. 46, No. 1, 2008, pp. 17-20.

4.3 UIUC

Students	*Degree*	*Current Position*
Bradley de Blauw	MS 2008	PhD expected 2011
Aaron Dufrene	MS 2006	Research Scientist CUBRC
Richard Huffman	PhD 2007	Assistant Professor AFIT
Manu Sharma	MS 2007	PhD expected 2010

Publications
1. Boguszko, M., Huffman, R., and Elliott, G., Property and velocity measurements in a supersonic flow, AIAA Paper 2006-1390, *44th AIAA Aerospace Sciences Meeting and Exhibit,* 2006.

2. DeBlauw, B., Elliott, G., and Dutton, C., "A Mach 4 Wind Tunnel for Plasma / Boundary Layer Interaction Studies," *Accepted to 48th AIAA Aerospace Sciences Conference and Exhibit*, 2010.

3. Dufrene A., Sharma M. and Austin, J.M., Design and characterization of a hypervelocity expansion tube facility, *Journal of Propulsion and Power* 23(6):1185-1193, 2007

4. Dufrene A., Sharma M. and Austin, J.M., Design and characterization of a hypervelocity expansion tube facility, AIAA 2007-1327, *44th AIAA Aerospace Sciences Meeting and Exhibit*, Reno NV, January 2007

5. Huffman, R., Elliott, G., and Boguzsko, M. Turbulence Measurements Using FARRS in a Supersonic Axisymmetric Jet, AIAA Paper 2007-0471, *45th AIAA Aerospace Sciences Meeting and Exhibit*, Reno, Nevada, January, 2007.

6. Huffman, R., Elliott, G. "An Experimental Investigation of Accurate Particle Tracking in Supersonic, Rarefied, Axisymmetric Jets," AIAA Paper 2009-1265, 2009.

7. Huffman, R., Elliott, G., "The Effect of Plasma on the Flow Features of an Axisymmetric Jet
8. Accepted to 48th AIAA Aerspace sciences Conference and Exhibit, 2010.

9. Massa L. and Austin, J.M., Spatial linear stability analysis of a hypersonic shear layer with non-equilibrium thermochemistry, *Physics of Fluids* 20(8):084104, 2008

10. McGilvray, M., Austin, J.M., Sharma, M., Jacobs, P.A. and Morgan, R.G., Diagnostic modeling of an expansion tube operating condition, *Int. Journal on Shock Waves* 19(1) 59-66, 2008

11. McGilvray, M., Austin, J.M., Sharma, M., Jacobs, P.A. and. Morgan, R.G, Diagnostic modeling of an expansion tube operating condition for a hypersonic shear layer experiment, *16th Australasian Fluid Mechanics Conference*, Gold Coast Australia, December 2007

12. Sharma, M., Austin, J.M., Glumac, N.G. and Massa, L., NO and OH spectroscopic vibrational temperature measurements in a post-shock relaxation region, submitted to *AIAA Journal* 2009

13. Sharma M., Austin, J.M., Glumac, N.G. and Massa, L., Spectroscopic measurements of a hypervelocity Mach reflection in the presence of thermochemical effects, *AIAA 39th Fluid Dynamics Conference,* San Antonio TX, June 2009

14. Sharma, M., Austin, J.M. and Glumac, N. G., Influence of thermochemical effects on shear layers in hypersonic flow, *44th AIAA/ASME/SAE/ASEE Joint Propulsion Conference and Exhibit*, Hartford CT, July 2008

15. Sharma, M., Massa, L. and Austin, J. M, Triple point shear layers in hypervelocity flow, *26th International Symposium on Shock Waves*, Göttingen, Germany, July 2007

4.4 ODU

Publications

1. W. Liao, Y. Peng, and L.-S. Luo. Effect of multi-temperature non-equilibrium on compressible homogeneous turbulence. To be submitted (2009).
2. W. Liao, Y. Peng, L.-S. Luo, and R. Rubinstein. Mach number effects in statistics of decaying compressible turbulence. To be submitted to J. Fluid Mech. (2009).
3. W. Liao, Y. Peng, and L.-S. Luo. Gas kinetic schemes for DNS of compressible homogeneous turbulence. Submitted to Phys. Rev. E (2009).
4. Y. Peng, W. Liao, L.-S. Luo, and L.-P. Wang. Comparison of the lattice Boltzmann and pseudo-spectral methods for decaying turbulence. Part I. Low-order statistics. Submitted to Comput. Fluids (2008).
5. W. Liao, Y. Peng, L.-S. Luo, and K. Xu. Modified gas-kinetic scheme for shock structures in argon. Prog. Comput. Fluid Dyn. **8**(1-4):97-108 (2008).
6. W. Liao, B. Diskin, Y. Peng, and L.-S. Luo. Textbook-efficiency multigrid solver for three-dimensional unsteady compressible Navier-Stokes equations. J. Comput. Phys. **227**(15): 7160 -7177 (2008).
7. Z.L. Guo, H.W. Liu, L.-S. Luo, and K. Xu. A comparative study of the lattice Boltzmann equation and gas-kinetic scheme for low Mach flows. J. Comput. Phys. **227**(10):4955-4976 (2008).
8. P. Asinari and L.-S. Luo. Direct numerical simulation of decaying homogeneous isotropic turbulence for a binary mixture by using a consistent lattice Boltzmann equation. J. Comput. Phys. **227**(8):3878-3895 (2008).
9. W. Liao, L.-S. Luo, and K. Xu. Gas kinetic scheme for continuum and near-continuum hypersonic flows. AIAA J. Rocket and Spacecraft **44**(6):1232-1240 (2007).
10. W. Liao, Y. Peng, and L.-S. Luo. Decay of compressible homogeneous turbulence with multi-temperature non-equilibrium, Accepted for 48th AIAA Aerospace Sciences Meeting, Orlando, FL, Jan. 2010.
11. W. Liao, Y. Peng, and L.-S. Luo. Gas kinetic scheme for DNS of decaying compressible turbulence, AIAA-2009-0586.
12. Y. Peng, W. Liao, L.-S. Luo, and L.-P. Wang. A comparative study of the lattice Boltzmann and pseudo-spectral methods for decaying homogeneous isotropic turbulence, AIAA-2009-0587.
13. Y. Peng, W. Liao, and L.-S. Luo. A comparative study of the LBE and GKS methods for DNS of decaying turbulence. AIAA-2008-0548.
14. B. Diskin, W. Liao, and L.-S. Luo. Textbook-efficiency multigrid solver for three-dimensional unsteady compressible Navier-Stokes equations. AIAA-2007-4328.
15. W. Liao, L.-S. Luo, and K. Xu. Gas kinetic scheme for continuum and near-continuum hypersonic flows. AIAA-2007-0120.